NOTE TO USERS

This reproduction is the best copy available.

UMI®

UNIVERSITÉ DE MONTRÉAL

ÉTUDE ET MODÉLISATION DU COMPORTEMENT RHÉOLOGIQUE DE SUSPENSIONS DE FIBRES RIGIDES EN RÉGIME NON-DILUÉ

JULIEN FÉREC
DÉPARTEMENT DE GÉNIE CHIMIQUE
ÉCOLE POLYTECHNIQUE DE MONTRÉAL

THÈSE PRÉSENTÉE EN VUE DE L'OBTENTION
DU DIPLÔME DE PHILOSOPHIAE DOCTOR (Ph.D.)
(GÉNIE CHIMIQUE)
FÉVRIER 2008

© Julien Férec, 2008.

Library and Archives Canada

Published Heritage Branch

395 Wellington Street
Ottawa ON K1A 0N4
Canada

Bibliothèque et Archives Canada

Direction du Patrimoine de l'édition

395, rue Wellington
Ottawa ON K1A 0N4
Canada

Your file Votre référence
ISBN: 978-0-494-47717-5
Our file Notre référence
ISBN: 978-0-494-47717-5

NOTICE:
The author has granted a non-exclusive license allowing Library and Archives Canada to reproduce, publish, archive, preserve, conserve, communicate to the public by telecommunication or on the Internet, loan, distribute and sell theses worldwide, for commercial or non-commercial purposes, in microform, paper, electronic and/or any other formats.

The author retains copyright ownership and moral rights in this thesis. Neither the thesis nor substantial extracts from it may be printed or otherwise reproduced without the author's permission.

AVIS:
L'auteur a accordé une licence non exclusive permettant à la Bibliothèque et Archives Canada de reproduire, publier, archiver, sauvegarder, conserver, transmettre au public par télécommunication ou par l'Internet, prêter, distribuer et vendre des thèses partout dans le monde, à des fins commerciales ou autres, sur support microforme, papier, électronique et/ou autres formats.

L'auteur conserve la propriété du droit d'auteur et des droits moraux qui protège cette thèse. Ni la thèse ni des extraits substantiels de celle-ci ne doivent être imprimés ou autrement reproduits sans son autorisation.

In compliance with the Canadian Privacy Act some supporting forms may have been removed from this thesis.

While these forms may be included in the document page count, their removal does not represent any loss of content from the thesis.

Conformément à la loi canadienne sur la protection de la vie privée, quelques formulaires secondaires ont été enlevés de cette thèse.

Bien que ces formulaires aient inclus dans la pagination, il n'y aura aucun contenu manquant.

Canada

UNIVERSITÉ DE MONTRÉAL

ÉCOLE POLYTECHNIQUE DE MONTRÉAL

Cette thèse intitulée:

ÉTUDE ET MODÉLISATION DU COMPORTEMENT RHÉOLOGIQUE DE SUSPENSIONS DE FIBRES RIGIDES EN RÉGIME NON-DILUÉ

présentée par : FÉREC Julien

en vue de l'obtention du diplôme de : Philosophiae Doctor

a été dûment acceptée par le jury d'examen constitué de :

M. BERTRAND François, Ph.D., président

M. CARREAU Pierre J., Ph.D., membre et directeur de recherche

Mme HEUZEY Marie-Claude, Ph.D., membre et codirectrice de recherche

M. AUSIAS Gilles, D.Sc., membre et codirecteur de recherche

M. POITOU Arnaud, Ph.D., membre

M. BAIRD Donald G., Ph.D., membre

À mes parents Marie-Noëlle et Pierre,
À mes grand-mères Catherine et Denise,
À mes frères Nicolas et Hervé.

REMERCIEMENTS

Je tiens en premier lieu à remercier très sincèrement mon directeur de recherche, Monsieur Pierre J. Carreau, de m'avoir accueilli au sein de son groupe de recherche. Malgré ses nombreuses occupations, Monsieur Carreau a toujours su m'accorder de son temps pour entretenir des discussions très enrichissantes et me prodiguer de nombreux conseils.

Ce travail n'aurait pas pu voir le jour sans les multiples implications de Monsieur Gilles Ausias, mon codirecteur. Par la présente, je lui adresse mes remerciements les plus vifs pour nos très nombreuses discussions, de près pendant mes séjours à l'Université de Bretagne Sud et de loin, au-delà de l'Atlantique.

J'exprime ma profonde reconnaissance à Madame Marie-Claude Heuzey qui a acceptée d'être ma codirectrice tout au long de ce projet. Son expérience scientifique ainsi que sa disponibilité m'ont été d'une aide très précieuse. De plus, je la remercie d'avoir pensé à moi pour être son chargé de travaux dirigés du cours de procédés d'extrusion.

Je n'oublierai pas de remercier très chaleureusement tout le personnel du CREPEC, secrétaires, techniciens et associés de recherche particulièrement : Diane Héroux pour sa très grande gentillesse et son dévouement dans toutes les démarches administratives, Mélina Hamdine pour sa sympathie, son aide et les nombreux moments passés dans le laboratoire de rhéologie et enfin Jacques Beausoleil pour sa disponibilité et son aide technique.

Je tiens à remercier également Mourad Heniche qui a patiemment répondu à mes interrogations sur les méthodes numériques de volumes finis.

Merci à tous mes amis, du département de génie chimique ou autre, pour les bons moments passés tout au long de ces années. Je pense en particulier à mes collègues Karen, Christophe, Shant…

Tous mes remerciements vont aussi aux personnes avec qui j'ai eu l'occasion d'entretenir des relations amicales tout au long de mon séjour au Québec : Notamment à mes coéquipiers de l'ASUF et à mes camarades de l'ABYMM qui m'ont supporté dans les deux sens du terme.

Finalement je ne terminerai pas cette section sans omettre d'adresser mes sincères reconnaissances à mes parents pour leur encouragement et leur soutien tout au long de ce projet.

RÉSUMÉ

Le renforcement des polymères thermoplastiques par des fibres bonifie considérablement leurs propriétés mécaniques et thermiques. Leurs procédés de mise en œuvre restent inchangés ce qui permet l'élaboration de pièces en matériaux composites présentant des géométries complexes. L'amélioration ainsi engendrée est étroitement liée à la structure interne définie par l'orientation et la distribution des particules. Cependant à l'état fondu, cette structure est en constante évolution à cause notamment de l'orientation des fibres induite par les nombreuses contraintes générées durant l'écoulement de ces composites. Une description précise de leurs propriétés rhéologiques est alors nécessaire afin de contrôler et d'optimiser leur mise en forme et les performances du produit final. Cette réalisation est d'autant plus complexe que les composites industriels disposent de concentrations de renforts tellement élevées que les interactions fibre-fibre, modifiant leur orientation, ne peuvent être négligées.

De nombreuses recherches se sont intéressées aux comportements rhéologiques des suspensions de fibres en cisaillement simple (transitoire et permanent) et dynamique (petites déformations). Cependant dans la plupart des systèmes de mise en forme, le comportement élongationnel (transitoire et permanent) ne peut être négligé, et dans les procédés d'injection de type « push-pull », la connaissance de leurs propriétés rhéologiques en grandes déformations oscillatoires est d'un grand intérêt. Ainsi une meilleure compréhension du comportement rhéologique de ces fluides, soumis à ce genre de sollicitations, est apportée par ce travail. De plus, l'évaluation de la

performance de certains modèles rhéologiques disponibles dans la littérature et la reconnaissance de leurs lacunes permet de proposer un modèle plus adéquat.

Les résultats oscillatoires en grandes déformations montrent que pour des polypropylènes (PP) renforcés de fibres de verre courtes, l'amplitude de la contrainte en cisaillement diminue graduellement au cours des cycles étudiés. Cependant un comportement inverse est observé pour une matrice en polybutène (PB) renforcée par les mêmes fibres : l'amplitude de la contrainte augmente continuellement pour atteindre une valeur constante au bout de plusieurs cycles. L'accroissement (PB) de même que la diminution (PP) de la contrainte en cisaillement sont d'autant plus prononcés que la concentration en fibres augmente. L'orientation des fibres est à l'origine de ces deux phénomènes. Il a aussi été observé pour ces deux matrices que les premières différences de contraintes normales sont plus sensibles aux phénomènes d'orientation des fibres que les contraintes en cisaillement : les graphes de contrainte normales vs déformation montrent des formes symétriques si la configuration d'orientation des fibres est également symétrique avec la direction de l'écoulement. Également, des analyses du signal brut par transformées de Fourier ont été réalisées pour les systèmes basés sur le PB et le PP : des réponses harmoniques sont observées pour les contraintes de cisaillement tandis que des signaux non harmoniques résultent des premières différences de contraintes normales. De plus, l'énergie de dissipation visqueuse augmente avec le taux de fibres et les composites à base de polypropylène montrent un caractère plus newtonien avec une déformation croissante.

Les observations réalisées en écoulement élongationnel nous indiquent que la présence des fibres dans un polypropylène augmente considérablement sa viscosité. En régime transitoire, différentes orientations initiales des fibres ont été préparées : planaire aléatoire, perpendiculaire et parallèle à la direction de l'étirement. Ce dernier cas exhibe la viscosité élongationnelle transitoire la plus élevée à cause de la résistance des fibres à l'étirement. Pour les deux autres cas, la dynamique d'orientation des charges provoque un léger comportement rhéoépaississant sous déformation. En régime établi, la viscosité élongationnelle en fonction du taux effectif de déformation a été comparée pour trois appareillages différents (l'unité SER montée sur un rhéomètre rotationnel ARES, un système de rhéomètre capillaire Rheotens et l'entrée convergente d'une filière hyperbolique planaire). Le comportement à de faibles taux d'élongation montre des désaccords entre les trois appareils, expliqués par l'histoire du pré-cisaillement des échantillons et des taux de déformation non homogènes. Néanmoins, à des taux d'élongation modérés et élevés, les résultats sont comparables : la matrice de PP et ses composites deviennent rhéofluidifiants.

Le modèle Folgar-Tucker-Lipscomb (FTL) est basé sur l'équation constitutive de Lipscomb et al. (1988), où l'évolution de l'orientation des fibres est donnée par l'expression de Folgar et Tucker (1984). Dans le cadre de ce travail, il a été utilisé pour prédire avec succès le comportement d'un polybutène chargé à 20% en masse de fibres de verre et soumis à de grandes déformations oscillatoires. Il a également pu prédire de façon qualitative les phénomènes de rhéoépaississement sous déformation observés en

élongation transitoire pour un polypropylène renforcé de fibres. Étant donné que le modèle FTL a été développé pour une matrice newtonienne, une nouvelle équation constitutive est proposée pour des suspensions de fibres dans un fluide newtonien généralisé décrit par le modèle de Carreau. Cette loi de comportement estime avec justesse les comportements rhéofluidifiants observés pour la viscosité élongationnelle en fonction du taux de déformation.

Afin d'utiliser les principaux modèles rhéologiques applicables aux suspensions de fibres disponibles dans la littérature, il est nécessaire de connaître le tenseur d'orientation d'ordre quatre $\mathbf{a}_4$. On a alors recours à des approximations de fermeture et ceci génère des erreurs implicites. En contrepartie, la résolution numérique de la fonction de distribution d'orientation ψ donne de meilleurs résultats mais consomme énormément de temps de calcul. Dans ce travail, une méthode basée sur les volumes finis a été utilisée pour résoudre numériquement l'équation de Fokker-Planck pour ψ. Les résultats sont tels que les temps de calcul sont réduits de façon considérable et qu'une large gamme de nombre de Péclet est maintenant envisageable.

Le dernier point abordé dans ce travail présente le développement mathématique d'un modèle rhéologique pour des suspensions de fibres où l'attention est portée sur une modélisation plus précise des interactions fibre-fibre. Cette loi de comportement est considérée comme une extension du modèle de Dinh et Armstrong (1984). En plus de la contribution hydrodynamique des fibres, la contrainte totale comprend un terme additionnel dû aux interactions fibre-fibre. De nouveaux tenseurs d'interaction d'ordre

deux et quatre sont introduits. De plus, une nouvelle équation d'évolution est proposée, où le terme de diffusion est proportionnel au nombre moyen de contacts entre les fibres. Le modèle a été validé par des mesures expérimentales en cisaillement transitoire et permanent pour des suspensions concentrées de fibres dans une matrice newtonienne en polybutène. La viscosité réduite et la différence des contraintes normales mesurées exhibent des fonctions quadratiques, comme prédits par le modèle. Les comportements transitoires sont également bien estimés, considérant que le modèle ne requiert que trois paramètres pour représenter le comportement des suspensions sur une large gamme de concentration de fibres.

ABSTRACT

The reinforcement of thermoplastic polymers by short fibers improves considerably their mechanical and thermal properties. In addition their processing methods remain unchanged with respect to processing of unfilled polymers, which allow the development of composite material parts having complex geometries. Properties enhancement is closely related to the internal structure defined by the orientation and the distribution of the particles. In the molten state this structure is in constant evolution, in particular because of the fiber orientation induced by many constraints present during the flow of these composites. A precise description of their rheological properties is therefore necessary in order to control and to optimize their processing and the performance of the final products. This is particularly complex as industrial composites contain high reinforcement loading that may induce fiber-fiber interactions that may influence fiber orientation.

Several studies have investigated the rheological behavior of fiber suspensions in simple shear (transient and steady) and oscillatory shear (small deformations) flow. However in many transformation processes, the elongational component of the flow cannot be neglected, while in a process such as push-pull injection, knowledge of the rheological properties in large amplitude oscillatory shear (LAOS) may be of great interest. Thus, a thorough study of the rheological behavior of fiber-filled fluids subjected to elongational and LAOS flows is presented in this work. The second

objective is to evaluate the performances of rheological models available in the literature and highlight their drawbacks in order to propose a more adequate approach.

Results from large amplitude oscillatory shear flow showed that for short glass fiber reinforced polypropylene (PP) the shear stress amplitude decreased gradually over the cycles investigated. However, an opposite behavior was observed for a reinforced polybutene matrix (PB) containing the same fibers: the stress amplitude increased continuously until reaching a constant value after several cycles. The shear stress increase (PB) and decrease (PP) are especially pronounced as the fiber loading increases. Fiber orientation is at the origin of these two phenomena. It was observed that the primary normal stress differences of the two matrices are more sensitive to fiber orientation than the shear stresses: the normal stress-strain loops showed a symmetrical shape if the fiber orientation was also symmetric with respect to the flow direction. Fast Fourier Transforms were also performed for the PB- and PP-based systems: harmonic responses were observed for shear stress, whereas non-harmonic signals were obtained for the primary normal stress differences. In addition the viscous dissipation energy increased with increasing fiber content, and composites based on polypropylene showed an increased Newtonian character with increasing deformation.

The observations carried out in elongational flow indicated that the presence of fibers in polypropylene increased considerably its viscosity. For transient tests, various initial fiber orientations were prepared: planar random, perpendicular and parallel with the stretching direction. The latter case exhibited the highest transient elongational

viscosity because of the fiber resistance to stretching. For the two other cases, the fiber orientation dynamics caused a slight strain hardening behavior. The steady state elongational viscosity data as a function of the effective strain rate obtained using three different equipments (an SER unit mounted on a rotational rheometer ARES, a capillary rheometer-Rheotens device, and a planar slit die with a hyperbolic entrance) have been compared. At low strain rates, the elongational viscosity showed discrepancies that are tentatively explained by the pre-shearing history of the sample, differences in flow kinematics and non-homogeneous strain rates. Nevertheless, from moderate to high strain rates, the results were comparable and the PP matrix and composites showed strain thinning.

The Folgar-Tucker-Lipscomb (FTL) model is based on the constitutive equation of Lipscomb et al. (1988), where the fiber orientation evolution is given by the expression of Folgar and Tucker (1984). It was used in this work to predict successfully the behavior of a polybutene filled with 20% wt. of glass fibers and subjected to large oscillatory deformation in shear. It could also predict qualitatively the strain hardening behavior observed in transient elongation of fiber reinforced polypropylenes. Since the FTL model has been developed for a Newtonian matrix, a new constitutive equation was proposed for fiber suspensions in generalized Newtonian fluids described by the Carreau model. This model predicts accurately the experimentally observed strain thinning of the elongational viscosity as a function of strain rate.

In order to use the principal rheological models designed for fiber suspensions and available in the literature, it is necessary to know the fourth order orientation tensor $\mathbf{a}_4$. In this case, the use of closure approximations is required, but this generates implicit errors. On the other hand, the numerical resolution of the probability distribution function ψ is more reliable but requires large computational times. In this work a finite volume method has been used to solve numerically the Fokker-Planck equation for ψ. The results are such that the computational time is considerably reduced, and this approach also allows calculations over a wide range of the Peclet number.

The last point tackled in this work concerns the mathematical development of a rheological model for fiber suspensions with a more precise modeling of fiber-fiber interactions. This constitutive equation consists in an extension of the Dinh and Armstrong (1984) model. In addition to the hydrodynamic contribution of the fibers, the total stress results from an additional component due to fiber-fiber interactions. Accordingly, novel second and fourth order interaction tensors are defined. Moreover, a new time evolution equation is proposed, where the diffusion term is proportional to the average number of contacts between fibers. The model is validated using experimental data in transient and steady shear flows for concentrated fiber suspensions in a polybutene. Measured reduced viscosity and primary normal stress differences exhibit quadratic functions, as predicted by the model. The transient behaviour is also fairly well estimated, considering that the model only requires three parameters to fit the behavior of suspensions over a wide range of fiber concentrations.

TABLE DES MATIÈRES

DÉDICACE iv

REMERCIEMENTS v

RÉSUMÉ vii

ABSTRACT xii

TABLE DES MATIÈRES xvi

LISTE DES TABLEAUX xxi

LISTE DES FIGURES xxii

LISTE DES ANNEXES xxix

LISTE DES SIGLES ET ABRÉVIATIONS xxx

CHAPITRE 1 - INTRODUCTION ET OBJECTIF 1

CHAPITRE 2 - ÉTUDE BIBLIOGRAPHIQUE 7

2.1. PROPRIÉTÉS DES FIBRES 7

2.2. COMPORTEMENTS RHÉOLOGIQUES DES SUSPENSIONS DE FIBRES 10

2.3. MODÉLISATION DE LA DYNAMIQUE D'ORIENTATION DES FIBRES 21

2.4. LOIS DE COMPORTEMENT DES SUSPENSIONS DE FIBRES 31

2.5. CALCUL DE LA FONCTION DE DISTRIBUTION D'ORIENTATION ET APPROXIMATIONS DE FERMETURE 37

2.6. CONCLUSION 46

CHAPITRE 3 - SYNTHÈSE DES ARTICLES 48

3.1. ARTICLE 1 (CHAPITRE 4) 48

3.2. ARTICLE 2 (CHAPITRE 5) 49

3.3. ARTICLE 3 (CHAPITRE 6) 51

3.4. ARTICLE 4 (CHAPITRE 7) 52

CHAPITRE 4 - ARTICLE: RHEOLOGICAL BEHAVIOR OF FIBER-FILLED POLYMERS UNDER LARGE AMPLITUDE OSCILLATORY SHEAR FLOW 54

4.1. INTRODUCTION 56

4.2. EXPERIMENTAL 60

4.3. MODELING 65

4.4. RESULTS AND DISCUSSION 68

4.5. CONCLUSIONS 80

4.6. ACKNOWLEDGEMENTS 81

CHAPITRE 5 - ARTICLE: INVESTIGATION OF THE RHEOLOGICAL PROPERTIES OF SHORT GLASS FIBER FILLED POLYPROPYLENE IN EXTENSIONAL FLOW 99

5.1. INTRODUCTION 101

5.2. MODELING 107

5.3. EXPERIMENTS 111

5.4. RESULTS AND DISCUSSION 117

5.5. CONCLUDING REMARKS 125

5.6. ACKNOWLEDGEMENTS 126

5.7. APPENDIX 1 128

5.8. APPENDIX 2 129

5.9. APPENDIX 3 130

CHAPITRE 6 - ARTICLE: NUMERICAL SOLUTION OF THE FOKKER-PLANCK EQUATION FOR FIBER SUSPENSIONS: APPLICATION TO THE FOLGAR-TUCKER-LIPSCOMB MODEL 145

6.1. INTRODUCTION 147

6.2. CALCULATION OF THE ORIENTATION DISTRIBUTION FUNCTION 153

6.3. INVESTIGATION OF THE FOURTH-ORDER ORIENTATION TENSOR COMPONENTS IN SIMPLE SHEAR FLOW 158

6.4. COMPARISON OF EXPERIMENTAL DATA WITH FOLGAR-TUCKER-LIPSCOMB MODEL PREDICTIONS 161

6.5. DISCUSSION 164

6.6. CONCLUDING REMARKS 165

6.7. ACKNOWLEDGEMENTS 166

6.8. APPENDIX 167

CHAPITRE 7 - ARTICLE: MODELING FIBER INTERACTIONS IN NON-DILUTE FIBER SUSPENSIONS 180

7.1. INTRODUCTION 182

7.2. MODEL FORMULATION 186

7.3. STRESS DETERMINATION 194

7.4. APPROXIMATIONS 196

7.5. ONSAGER AND MAIER-SAUPE POTENTIALS 196

7.6. PREDICTIONS AND COMPARISON WITH EXPERIMENTAL DATA 198

7.7. CONCLUSIONS 205

7.8. ACKNOWLEDGEMENTS 206

7.9. APPENDIX 1: FIBER MASS CENTER VELOCITY 207

7.10. APPENDIX 2: EVALUATION OF INTERACTION TENSORS WITH MAIER-SAUPE APPROXIMATION 209

CHAPITRE 8 - DISCUSSION GÉNÉRALE 222

8.1. DÉGRADATION ET STABILITÉ THERMIQUE 222

8.2. CONDITIONNEMENT INITIAL DES ÉCHANTILLONS 223

8.3. HOMOGÉNÉITÉ DANS LA DÉFORMATION 223

8.4. PROGRAMME FORTRAN DE LA RÉSOLUTION NUMÉRIQUE DE LA FONCTION DE DISTRIBUTION D'ORIENTATION 224

8.5. MODÈLE RHÉOLOGIQUE 224

CHAPITRE 9 - CONCLUSIONS 226

PERSPECTIVES 230

RÉFÉRENCES 233

ANNEXES 254

LISTE DES TABLEAUX

Tableau 2.1 : Critères et limites des solutions diluées et non-diluées de fibres. 8

Tableau 2.2 : Paramètres matériaux pour la loi de comportement [Éq. (2.22)].....34

Tableau 2.3 : Équivalences entre les indices des tenseurs.....42

Table 5.1 : Sample nomenclature, fiber content and density. 131

Table 5.2 : Elongational parameter values for Eq. (5.11). 131

Table 5.3 : Calculated average distance between fibers.....131

Table 6.1 : Calculation CPU time for different spatial schemes, time schemes and Peclet numbers. 168

Table 7.1 : Calculated values of f and g for different fiber orientations. 210

Tableau A.1 : Caractéristiques dimensionnelles des fibres dans les polypropylènes...254

LISTE DES FIGURES

Figure 1.1 : Orientation d'une fibre isolée lors d'un écoulement de cisaillement simple. 2

Figure 1.2 : Orientation d'une fibre isolée lors d'un écoulement élongationnel. 3

Figure 1.3 : Lignes de courant dans une contraction brusque axisymétrique (4.5 : 1) d'un fluide newtonien : À droite, la matrice vierge ; À gauche, la même matrice renforcée par une fraction volumique de 0.045% en fibre (Lipscomb et al., 1988). 4

Figure 1.4 : Profil du front de matière pendant le remplissage d'un moule d'injection avec un taux massique de fibres respectivement de 40% (en haut) et 50% (en bas) (Akay & Barkley, 1993). 5

Figure 2.1 : Représentation des régimes de concentration. La zone rectangulaire hachurée montre l'emplacement des principaux composites utilisés (Advani 1994). 9

Figure 2.2 : Orientation d'une fibre axisymétrique décrite par deux angles θ et φ ou par un vecteur unitaire **p** de direction principale l'axe de symétrie. 23

Figure 2.3 : Exemples de trois états d'orientation : (a) orientation isotrope ; (b) orientation aléatoire dans un plan ; (c) orientation des fibres totalement alignées suivant la direction (1). 25

Figure 4.1 : (a) Torque and (b) normal force as functions of the rim shear rate for the neat PP and based polypropylene composites. 83

Figure 4.2 : Complex viscosity as a function of strain for PB0 and PB20. PB20 has been pre-sheared at 10 s^{-1} during 1000 s. 84

Figure 4.3 : Complex viscosity as a function of strain for PP0 and PP30. 85

Figure 4.4 : Shear stress versus strain for 3 LAOS cycles, with γ_R = 7 and f = 0.1 Hz: (a) PB0; (b) PB20. 86

Figure 4.5 : PB20 primary normal stress differences versus strain for 3 LAOS cycles, with γ_R = 7 and f = 0.1 Hz. 87

Figure 4.6 : FFT analysis at γ_R = 7 and f = 0.1 Hz of cycles 200-250: Primary normal stress difference responses for PB20. 88

Figure 4.7 : Time evolution of the primary normal stress differences of PB20 in LAOS test (γ_R = 7 and f = 0.1 Hz), for which the sample was previously pre-sheared at 10 s^{-1} during 1000 s: (a) 2nd; (b) 6th; and (c) 14th cycles. 90

Figure 4.8 : Shear stress versus strain after 3 different LAOS cycles, where γ_R = 3 and f = 0.005 Hz for PP30. 91

Figure 4.9 : Primary normal stress differences versus strain after 3 different LAOS cycles, where γ_R = 3 and f = 0.005 Hz: (a) PP0; (b) PP30. 92

Figure 4.10 : FFT analysis of the PP30 (PP0 in insert) primary normal stress difference responses at γ_R = 3 and f = 0.005 Hz, cycles 7-12. 93

Figure 4.11 : Effect of pre-shear before LAOS tests on the normal stress Lissajous figures for PP30: (a) Pre-shear in CW direction at 0.08 s^{-1} during 1000 s; (b) Pre-shear in CCW direction at 0.08 s^{-1} during 1000 s. 94

Figure 4.12 : Fundamental shift angle as a function of strain for PP0, PP10 and PP30. 95

Figure 4.13 : Comparison of model predictions and shear data for PB20 in LAOS for γ_R = 7 and f = 0.01 Hz. The ORW closure approximation and C_I = 0.0005 and A = 90 have been used for the predictions. The initial fiber orientation is given by Eq.

(13): (a) Shear stress as a function of time; (b) Shear stress as a function of deformation. 96

Figure 4.14 : Comparison of model predictions and normal stress data for PB20 in LAOS for $\gamma_R = 7$ and $f = 0.01$ Hz. The ORW closure approximation, $C_I = 0.0005$ and $A = 90$ have been used for the predictions: (a) Normal stress differences as a function of time for an initial planar random fiber orientation [Eq. (4.13)]; (b) Normal stress differences as a function of time for initial aligned fibers [Eq. (4.14)]. ... 97

Figure 4.15 : Simulation of the second-order orientation tensor for PB20 in LAOS for $\gamma_R = 7$ and $f = 0.01$ Hz using the ORW closure approximation ($C_I = 0.0005$, $A = 90$): (a) Variations of $\mathbf{a_2}$ components with strain: initial orientation given by Eq. (4.13); (b) Variations of $\mathbf{a_2}$ components with strain: initial orientation given by Eq. (4.14). 98

Figure 5.1 : Schematic representation of the three different initial fiber orientations used with the SER unit: (a) PRO: planar random orientation, (b) PARA: fibers aligned parallel to the extensional flow direction and (c) PERP: fibers oriented perpendicularly to the elongational flow direction. The arrows indicate the stretching flow direction. 132

Figure 5.2 : Hencky strain rate as measured by a video camera for the unfilled matrix (PP0), for 30 wt % fiber filled polypropylene with fibers aligned parallel to the flow (PP30 – PARA) and perpendicular (PP30 – PERP) to the stretching direction. The nominal Hencky strain rate was 0.1 s^{-1}. Also shown in the insert are the width changes for PP30 - PERP in the middle of the sample (A-B), and close to the left (C-D) and right (E-F) of the rotary clamps. 133

Figure 5.3 : Transient elongational viscosity of the unfilled matrix PP0 and the glass bead filled polypropylene PPB11 (values multiplied by 10) at 200 °C for Hencky strain rates ranging from 0.05 to 20 s^{-1} obtained with the SER unit. Also

shown is the predicted LVE behavior as determined from the shear relaxation modulus after a step strain.....134

Figure 5.4 : Comparison of the transient elongational viscosity of the 30 wt % fiber filled polypropylene with fiber parallel (PP30 – PARA) and perpendicular (PP30 – PER) to the stretching direction obtained with the SER unit (at Hencky rates of 0.05 and 0.1 s^{-1}) and with the RME (at the corrected Hencky rates).....135

Figure 5.5 : Transient elongational viscosity at a Hencky strain rate of 0.05 s^{-1} for PP30 with different initial fiber orientations: (a) parallel to the stretching direction, PARA, (b) planar random orientation, PRO and (c) perpendicular to the stretching, PERP. Also shown is the transient elongational viscosity for PPB11 and the LVE regime of PP0 for the purpose of comparison. The dashed lines represent the model predictions (Eqs. 5, 6 and 20) for the different initial fiber orientations. 136

Figure 5.6 : Transient elongational viscosity as a function of Hencky deformation at different strain rates for PP30 with the initial fiber orientation perpendicular to the stretching direction.....137

Figure 5.7 : Shear and elongational viscosities of PP0. Also shown are the elongational viscosity data of fiber filled PP when the fibers are aligned (obtained from PARA data in elongation). The dashed lines represent the model predictions. 138

Figure 5.8 : Schematic illustration of microscopic distortions produced by aligned fibers in uniaxial elongation: (a) initial state with length L_0 and (b) elongated state with $L = 2L_0$ [taken from Laun (1984)].....139

Figure 5.9 : Specific elongational viscosity of polypropylene systems. Also shown are the predictions of various models for the uniaxial elongational viscosity. 140

Figure 5.10 : Matrix characteristic time and power-law index as functions of fiber volume fraction. The lines represent the best fits (linear for λ_m and quadratic for m). .141

Figure 5.11 : Coupling coefficient μ_2 as a function of the power-law index m. 142

Figure 5.12 : Comparison of the reduced "steady" elongational viscosity of PP and its composites from measurements using three different instruments: (a) PP0, (b) PP10 and (c) PP30 144

Figure 6.1 : Control volume used to perform flux balances for the probability distribution function. The faces of the control volume labelled as e, w, n and s refers to east, west, north and south directions. 169

Figure 6.2 : Schematic representation of the periodic boundary conditions on the total meshed domain. 170

Figure 6.3 : Comparison of calculation results in simple shear flow (1: velocity direction; 2: gradient direction) with $r = \infty$; (▪▪) Advani results; (○) Bay results; (□) Bay results; (△) Bay results (r = 10 instead of infinity for all previous cases), adapted from Advani (1987) and Bay (1991): (a) a_{11} component; (b) a_{22} component; and (c) a_{12} component vs. deformation. 172

Figure 6.4 : Comparison of calculated results in simple shear flow (1: velocity direction; 2: gradient direction, $r = \infty$) for the attractive components of $\mathbf{a_2}$: (△) Fokker-Planck analytical solution without diffusion [Eq. (6.13)]; (·····) Central scheme; (------) Power law scheme. 173

Figure 6.5 : Comparisons of a_{1212}, a_{1112}, a_{1222} and a_{1233} components obtained by solving the orientation distribution function and the ORW3 closure approximation in simple shear (forward direction) at different Pe numbers 175

Figure 6.6 : Comparisons of a_{1212}, a_{1112}, a_{1222} and a_{1233} components obtained by solving the orientation distribution function computation or the ORW3 closure approximation in simple shear (reverse direction) for different Pe numbers 177

Figure 6.7 : Experimental stress growth data for PP30 as compared to model predictions from the orientation distribution function computation (DFC) and from the ORW3 closure approximation for forward flow (CW) at $\dot{\gamma}$ = 0.1 s^{-1}: (a) Transient viscosity, and (b) transient normal stress difference as functions of strain. ..178

Figure 6.8 : Experimental stress growth data for PP30 as compared to model predictions from the orientation distribution function computation (DFC) and from the ORW3 closure approximation for reverse flow (CCW) at $\dot{\gamma}$ = 0.1 s^{-1}: (a) Transient viscosity and (b) transient normal stress differences as functions of strain...179

Figure 7.1 : Schematic representation of two interacting fibers. Superscript α represents the test fiber, superscript β refers to the neighboring fiber. 211

Figure 7.2 : Predicted stress growth functions for forward flow (CW); ORW3 and IQUA closure approximations, $\dot{\gamma}$ = 1 s-1 and q = 0.5: (a) transient viscosity; (b) transient primary normal stress differences as functions of strain. 212

Figure 7.3 : Predicted stress growth functions for reverse flow (CCW); ORW3 and IQUA closure approximations, $|\dot{\gamma}|$ = 1 s^{-1} and q = 0.5: (a) transient viscosity; (b) transient primary normal stress differences as functions of strain. 213

Figure 7.4 : Predicted stress growth functions for forward flow (CW); ORW3 and IQUA closure approximations, $\dot{\gamma}$ = 1 s^{-1} and k = 0.3: (a) transient viscosity; (b) transient primary normal stress differences as functions of strain. 214

Figure 7.5 : Predicted stress growth functions for reverse flow (CCW); ORW3 and IQUA closure approximations, $|\dot{\gamma}|$ = 1 s^{-1} and k= 0.3: (a) transient viscosity; (b) transient primary normal stress differences as functions of strain. 215

Figure 7.6 : Predicted variations for key components of $\mathbf{a_2}$ (a_{11}, a_{22} and a_{12}) and for the scalar f as functions of deformation for forward flow (ORW3 and IQUA closure approximations, $\dot{\gamma} = 1\ s^{-1}$, $X_A = 1$, $k = 0.3$ and $q = 0.5$). 216

Figure 7.7 : Predicted variations for key components of $\mathbf{a_2}$ (a_{11}, a_{22} and a_{12}) and for the scalar f as functions of deformation for reverse flow (ORW3 and IQUA closure approximations, $|\dot{\gamma}| = 1\ s^{-1}$, $X_A = 1$, $k = 0.3$ and $q = 0.5$). 217

Figure 7.8 : Predicted reduced steady shear viscosity and normal stress differences compared to experimental data as functions of fiber volume fraction (ORW3 and IQUA closure approximations). ($|\dot{\gamma}| = 10\ s^{-1}$, $X_A = 17.116$, $k = 0.112$ and $q = 0.220$). σ_{12} represents the shear stress component of the matrix. 218

Figure 7.9 : Stress growth data compared to model predictions for reverse flow (CCW) performed with the ORW3 and IQUA closure approximations. ($|\dot{\gamma}| = 10\ s^{-1}$, $X_A = 17.116$, $k = 0.112$ and $q = 0.220$): (a) transient viscosity; (b) transient normal stress differences as a functions of strain. 219

Figure 7.10 : Comparison of values of C_I obtained with the new model (ORW3 and IQUA closure approximations) with Bay model and Phan-Thien et al. model. 220

Figure 7.11 : Predictions of the average contact number per fiber as a function of deformation in reverse flow (CCW) at a shear rate of 10 s^{-1} (ORW3 and IQUA closure approximations). 221

Figure B.1 : Courbes de viscosité du PP0, PP10, PP20 et PP30.....255

LISTE DES ANNEXES

ANNEXE A : Étude morphologique 254

ANNEXE B : Courbes de viscosité 255

LISTE DES SIGLES ET ABRÉVIATIONS

Alphabet Grec

β	Multiplicateur de Lagrange
β_i	Coefficients de l'approximation de fermeture naturelle
γ_R	Amplitude de déformation
$\boldsymbol{\gamma}^{[0]}$	Tenseur des déformations finies
$\dot{\boldsymbol{\gamma}}$ ou $\dot{\gamma}_{ij}$	Tenseur des vitesses de déformation
$\dot{\boldsymbol{\gamma}}^*$	Tenseur des vitesses de déformation sans dimension
$\dot{\gamma}$	Taux de cisaillement
$\dot{\gamma}_R$	Taux de cisaillement au bord de la géométrie
$\dot{\gamma}_{RMS}$	Taux de cisaillement effectif
$\lvert\dot{\gamma}\rvert$	Mesure scalaire du tenseur des vitesses de déformation
$\Delta\theta$	Longueur élémentaire suivant la direction θ
$\Delta\rho$	Différence des masses volumiques
$\Delta\varphi$	Longueur élémentaire suivant la direction φ
ΔA	Surface élémentaire
$\Delta\dot{\mathbf{r}}$	Vitesse relative en deux fibres au point de contact
$\boldsymbol{\delta}$ ou δ_{ij}	Tenseur unitaire d'ordre deux ou delta de Kronecker
δ	Angle de déphasage
δ_1	Angle de déphasage pour l'harmonique fondamentale
δ_σ	Angle de déphasage de la contrainte
δ_{γ_R}	Angle de déphasage de la déformation
$\boldsymbol{\varepsilon}$	Tenseur de permutation
$\dot{\varepsilon}$	Taux d'élongation
$\dot{\varepsilon}_H$	Taux d'élongation Hencky

η	Viscosité en cisaillement
$\eta(\dot{\gamma})$	Viscosité du polymère
η_0	Viscosité newtonienne de la matrice
$\eta_0^{composite}$	Viscosité au plateau du composite
$\eta_0^{matrice}$	Viscosité au plateau de la matrice
η_E	Viscosité élongationnelle
η_r	Viscosité relative
η^*	Viscosité complexe
η_E^+	Viscosité transitoire en élongation
η_E^{SP}	Viscosité spécifique en élongation
$\eta^{composite}$	Viscosité en cisaillement du composite
$\eta^{matrice}$	Viscosité en cisaillement de la matrice
$\langle\eta(\mathbf{a}_4)\rangle$	Viscosité de la suspension pour une orientation moyennée des fibres sur une période
θ	Angle azimutal d'Euler
$\dot{\theta}$	Vitesse suivant la direction θ
θ_{max}	Angle maximum de déformation
$\boldsymbol{\kappa}^\dagger$	Tenseur des gradients de vitesse
$\boldsymbol{\Lambda}$	Tenseur des mobilités
Λ_0	Constante de mobilité
λ	Facteur de forme de la fibre
λ_f	Temps caractéristique des fibres
λ_i	Valeurs propres de $\mathbf{a_2}$
λ_m	Temps de relaxation du polymère
λ_s	Longueur d'onde en cisaillement
μ_1, μ_2, μ_3 et μ_4 ou μ_i	Constantes du matériau (ou parfois : *A*, *B*, *C* et *F*)

ρ_b	Densité des billes de verre
ρ_f	Densité des fibres de verre
ρ_{PB0}	Densité de la matrice en polybutène
σ	Coefficient de couplage entre le polymère et les fibres
$\boldsymbol{\sigma}$	Tenseur des contraintes totales
σ_1	Amplitude de la contrainte en cisaillement du signal fondamental
σ_{11}	Composante 11 du tenseur des contraintes
σ_{22}	Composante 22 du tenseur des contraintes
σ_{33}	Composante 33 du tenseur des contraintes
$\sigma_{\theta\theta}$	Composante $\theta\theta$ du tenseur des contraintes
σ_E	Contrainte uniaxiale
σ_E^+	Contrainte uniaxiale transitoire
$\sigma_{z\theta}$	Contrainte en cisaillement du tenseur des contraintes
σ_{zz}	Contrainte zz du tenseur des contraintes
σ^{sim}	Contrainte en cisaillement simulée
$\boldsymbol{\tau}$	Partie déviatorique du tenseur des contraintes
$\boldsymbol{\tau}^f$	Contribution des fibres
$\boldsymbol{\tau}^m$	Contribution de la matrice
τ	Temps sans dimension
ϕ	Fraction volumique des fibres
φ	Angle polaire d'Euler
$\dot{\varphi}$	Vitesse suivant la direction φ
ψ ou $\psi(\mathbf{p})$	Fonction de distribution d'orientation
$\psi_{\mathbf{p}}$	Fonction de distribution d'orientation donnée par la direction $\mathbf{p}$
$\psi_{\mathbf{p}^\alpha}$	Fonction de distribution d'orientation donnée par la direction $\mathbf{p}^\alpha$
$\psi_{\mathbf{p}^\beta}$	Fonction de distribution d'orientation donnée par la direction $\mathbf{p}^\beta$
$\boldsymbol{\Omega}^\infty$	Vitesse angulaire du fluide

$\boldsymbol{\omega}$ ou ω_{ij}	Tenseur des vitesses de rotation
$\boldsymbol{\omega}^*$	Tenseur des vitesses de rotation sans dimension
ω	Fréquence d'oscillation
$\boldsymbol{\varpi}^\alpha$	Vecteur des vitesses angulaires de la fibre α

Alphabet Latin

$\boldsymbol{A}$	Tenseur de résistance en translation
A	Constante
$A(t)$	Aire instantanée de la section
A_{mm}	Tenseur $\mathbf{a_4}$ en notation contractée dans le repère global
A^*_{mm}	Tenseur $\mathbf{a_4}$ en notation contractée dans le repère principal
$\mathbf{a_2}$ ou a_{ij}	Tenseur d'orientation d'ordre 2
$\dot{\mathbf{a}}_2$	Évolution temporelle du tenseur d'orientation d'ordre 2
$\mathbf{a_4}$ ou a_{ijkl}	Tenseur d'orientation d'ordre 4
$\mathbf{a}_4^{Hyb}$	Approximation de fermeture hybride
$\mathbf{a}_4^{Lin}$	Approximation de fermeture linéaire
$\mathbf{a}_4^{Nat}$	Approximation de fermeture naturelle
$\mathbf{a}_4^{Ort}$	Approximation de fermeture orthotrope
$\mathbf{a}_4^{Qua}$	Approximation de fermeture quadratique
$\mathbf{a_6}$ ou a_{ijklmn}	Tenseur d'orientation d'ordre 6
a_I, a_{II} et a_{III}	Invariants de $\mathbf{a_2}$
a	- Paramètre d'orientation
	- Paramètre du modèle de Carreau-Yasuda
a_E, a_W, a_N, a_S, a_M, a_P	Coefficients issus de la méthode des volumes finis
$\mathbf{B}$	Tenseur de conformation adimensionnel d'une macromolécule
B	Constante
$\mathbf{b_2}$ ou b_{ij}	Tenseur d'interaction d'ordre 2

$\mathbf{b}_4$ ou b_{ijkl}	Tenseur d'interaction d'ordre 4
$\mathbf{b}_4^L$ ou b_{ijkl}^L	Approximation de fermeture linéaire
$\mathbf{b}_4^Q$ ou b_{ijkl}^Q	Approximation de fermeture quadratique
b	Extensibilité adimensionnelle maximale d'une macromolécule
b_i	Fonctions de l'approximation de fermeture de Bay
$\mathbf{c}$	Tenseur de conformation d'une chaîne macromoléculaire
$\mathbf{C}$	Tenseur de résistance en rotation
$\boldsymbol{C_I}$	Tenseur d'interaction
C_m^i	Coefficients de l'approximation de fermeture orthotrope
C_I	Coefficient d'interaction
C_I^*	Constante d'interaction du modèle de Ramazani
Cr	Nombre de Courant (ou CFL)
$\boldsymbol{D_r}$	Tenseur de diffusion
D	- Diamètre du capillaire
	- Diamètre d'une fibre
D_R	Ratio d'étirement
D_r	Coefficient de diffusion
$d\mathbf{f}_I$	Force élémentaire de la force d'interaction
$d\mathbf{T}_I$	Moment élémentaire du couple global
$\mathbf{E}$	Tenseur des gradients de déformation
E_σ	Dissipation visqueuse par unité de volume pour un cycle
E_Y	Module d'Young
e	Paramètre ajustable de l'extrapolation de Petrie
$F(t)$	Force instantanée d'étirement
F_z	Force normale
$\mathbf{f}_I$	Force d'interaction
f	- Fréquence
	- Trace du tenseur d'interaction d'ordre 2

f^*	Mesure scalaire de l'orientation
G	Énergie libre de Gibbs
G'	Module élastique
G''	Module visqueux
$\mathbf{H}$	Tenseur de résistance
H	Entrefer de la géométrie des plaques parallèles
g	Constante universelle de gravitation
h	Distance moyenne entre les fibres
h_{ali}	Distance moyenne entre les fibres quand elles sont alignées
h_{iso}	Distance moyenne entre les fibres quand leur orientation est isotrope
Id4	Tenseur identité d'ordre 4 en notation contractée
I	Moment d'inertie de surface axial
K	- Consistance de la matrice - Constante universelle de proportionnalité
k	Facteur géométrique adimensionnel
k_{B}	Constante de Boltzmann
L	- Longueur du capillaire - Longueur d'une fibre
$\overline{L}$	Longueur moyenne d'une fibre
L_σ	Écart-type de la longueur d'une fibre
L_i	Longueur de la fibre i
$\overline{L}_n$	Longueur moyenne en nombre
$\overline{L}_w$	Longueur moyenne en masse
$\tilde{M}$	Scalaire adimensionnel
m	- Dimension de l'espace - Indice de rhéofluidifiance
N_1	Première différence des contraintes normales

N_1^{sim}	Première différence des contraintes normales simulée
N_2	Deuxième différence des contraintes normales
N_C	Nombre moyen de contact
n	Nombre de fibres par unité de volume
n_0	Concentration maximale en tassement des fibres
n_i	Nombre de fibres ayant la longueur L_i
P	- Pression hydrostatique
	- Probabilité de la présence d'une fibre
P_C	Probabilité de contact
Pe	Nombre de Péclet
$\mathbf{p}$	Vecteur unitaire dans la direction de l'axe principal de la fibre
$\mathbf{p}^{\alpha}$	Vecteur d'orientation de la fibre α
$\mathbf{p}^{\beta}$	Vecteur d'orientation de la fibre β
$\dot{\mathbf{p}}$	Évolution temporelle du vecteur unitaire $\mathbf{p}$
$\dot{\mathbf{p}}^{\alpha}$	Évolution temporelle de la fibre α
$\dot{\mathbf{p}}^{\beta}$	Évolution temporelle de la fibre β
$\dot{\mathbf{p}}_{\mathrm{H}}$	Évolution temporelle de $\mathbf{p}$ (contribution hydrodynamique)
$\dot{\mathbf{p}}_{\mathrm{Jeffery}}$	Évolution temporelle de $\mathbf{p}$ (équation de Jeffery)
$\dot{\mathbf{p}}_{\mathrm{H}}^{*}$	Évolution temporelle hydrodynamique de $\mathbf{p}$ sans dimension
p_1, p_2 et p_3	Composantes cartésiennes du vecteur unitaire $\mathbf{p}$
q	Coefficient d'interaction adimensionnel
$\mathbf{R}$	Matrice de rotation contractée
R	Rayon de la plaque parallèle
Re^*	Nombre de Reynolds pour une viscosité complexe
$\mathbf{r}_C^{\alpha}$	Vecteur position du centre de gravité de la fibre α
$\mathbf{r}_C^{\beta}$	Vecteur position du centre de gravité de la fibre β
r	- Position radiale

	- Rapport de forme ou élancement d'une fibre
S_B	Contribution dissipative de Boltzmann
S_{eff}	Rigidité effective d'une fibre
S_L	Contribution de Lifshitz
S_O	Contribution d'Onsager
s^α	Position suivant la longueur de la fibre α
s^β	Position suivant la longueur de la fibre β
$\mathbf{T}_I$	Couple global d'interaction
T_r	Période de rotation d'un sphéroïde
T_r	Rapport de Trouton
T	- Couple
	- Température absolue
T_{OSC}	Période du signal d'oscillation
t	Temps
t_s	Temps de sédimentation
$\mathbf{v}$	Vecteur vitesse
$\mathbf{v}^\infty$	Vecteur vitesse du fluide
v	Vitesse moyenne d'extrusion
v_0	Vitesse instantanée d'étirement
w	Largeur instantanée de l'échantillon
w_0	Largeur initiale de l'échantillon
X_A	Coefficient de frottement parallèle en translation
X_C	Coefficient de frottement parallèle en rotation
Y_A	Coefficient de frottement transverse en translation
Y_C	Coefficient de frottement transverse en rotation
Y_H	Coefficient de frottement
Z	Opérateur non linéaire relié à la conformation d'une macromolécule

CHAPITRE 1 - INTRODUCTION ET OBJECTIF

De nos jours, les matières plastiques sont largement répandues dans le monde industriel puisqu'elles sont fréquemment utilisées comme substituts de matériaux traditionnels (bois, métal, céramique...) au vu notamment de leurs faibles masses volumiques et de leurs prix attractifs. L'introduction de renforts aux polymères vierges augmente considérablement leurs propriétés mécaniques. Les fibres courtes, de longueurs inférieures au millimètre, sont généralement les charges de renfort utilisées pour les composites à matrice thermoplastique. De plus, ces matériaux nécessitent peu de modifications des procédés conventionnels de mise en forme (injection, extrusion...) et les pièces ainsi fabriquées peuvent présenter des formes complexes.

Les propriétés de ces polymères chargés dépendent principalement de la quantité, du type, de la taille et surtout de l'orientation des particules. À l'inverse des composites structuraux où les fibres sont placées adéquatement avant de les imprégner de polymère, les thermoplastiques renforcés sont des suspensions qui s'écoulent lors d'un procédé de mise en œuvre. Ainsi les fibres se déplacent et s'orientent en fonction de la cinématique de l'écoulement.

Dans les procédés industriels, les écoulements sont complexes puisqu'ils sont issus de la combinaison plus ou moins importante de cisaillements et d'élongations. Le cisaillement simple, tel qu'illustré sur la **Figure 1.1**, anime une fibre isolée dans un fluide newtonien d'un mouvement périodique de rotation, avec un temps de séjour

privilégié dans la direction principale de l'écoulement. Au cours d'un écoulement en élongation, tel que schématisé sur la **Figure 1.2**, la fibre s'oriente perpendiculairement à la direction d'étirement. De ce fait, l'orientation des fibres est induite par l'écoulement du polymère dans l'outillage de mise en forme. Après leur refroidissement, ces polymères renforcés présentent des propriétés physiques anisotropes à cause des dispositions finales des fibres dans l'espace. Ainsi la pièce manufacturée exhibe de meilleures caractéristiques selon l'orientation dominante des fibres qui doit correspondre à la direction principale des sollicitations mécaniques.

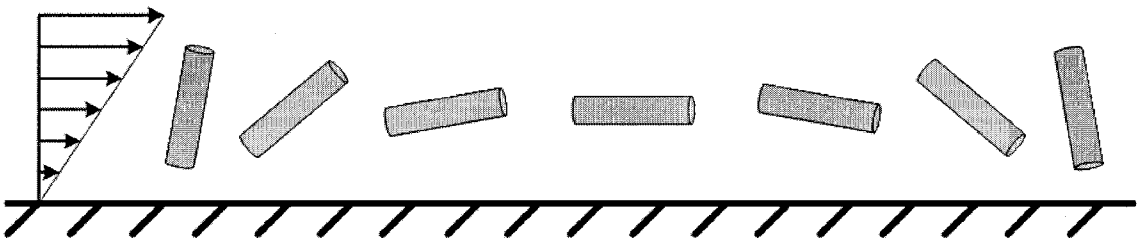

Figure 1.1 : Orientation d'une fibre isolée lors d'un écoulement de cisaillement simple.

Néanmoins les particules modifient également le comportement rhéologique du système. En règle générale, elles induisent une augmentation de la viscosité mais également une modification du champ de vitesse de l'écoulement. En visualisant les lignes de courant dans une contraction brusque axisymétrique (4.5 : 1), Lipscomb et al. (1988) montrent que, même à de faible concentration de particules (la fraction volumique étant de 0.045%), l'ajout des fibres augmente considérablement la taille des recirculations (**Figure 1.3**). Akay et Barkley (1993) prennent des clichés des fronts de matière lors d'un remplissage d'un moule d'injection pour deux polyamides respectivement chargés de 40% et 50% en masse de fibres de verre. La **Figure 1.4**

montre clairement que la forme du front de matière en injection est altérée par la présence des particules.

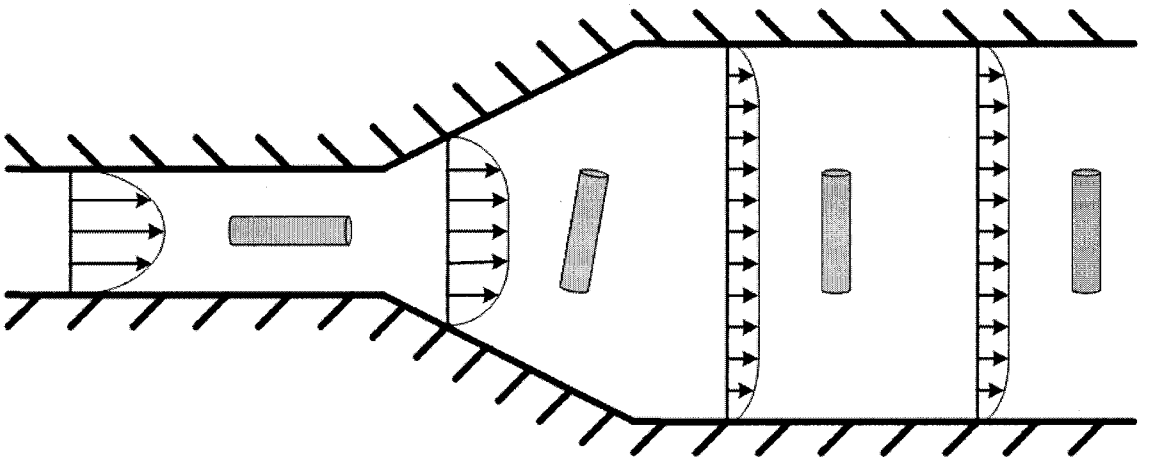

Figure 1.2 : Orientation d'une fibre isolée lors d'un écoulement élongationnel.

Ces quelques illustrations révèlent que manifestement il existe un couplage : les propriétés rhéologiques sont modifiées par la présence des fibres et inversement, l'écoulement induit l'orientation des particules. Dans son livre, Advani (1994) propose une démarche simple pour concevoir une pièce composite renforcée de fibres. Après avoir déterminé les caractéristiques à respecter, le procédé de la mise en forme est simulé. Les données ainsi obtenues permettent d'estimer l'orientation globale des fibres et servent à prédire les propriétés physiques en tous points de la pièce à fabriquer. Suivra ensuite une analyse qui jugera si le cahier des charges est respecté, et en fonction des données issues de la simulation, il sera possible d'ajuster au mieux les paramètres de la mise en œuvre.

La connaissance de la dynamique d'orientation des fibres est donc d'une importance majeure pour le concepteur qui souhaite optimiser les propriétés physiques

du produit final. C'est à ce stade que la rhéologie entre en jeu et aide à élucider certains problèmes. L'état d'orientation des renforts dans le composite est essentiellement déterminé par la rhéologie du polymère fondu, la distribution initiale des fibres et la cinématique de l'écoulement. De plus, les matériaux industriels utilisent principalement des systèmes fortement chargés, ce qui engendre des problèmes supplémentaires comme les interactions entre les fibres.

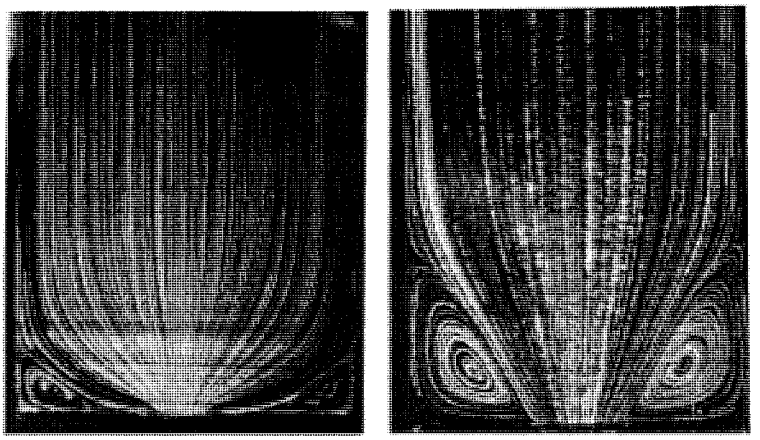

Figure 1.3 : Lignes de courant dans une contraction brusque axisymétrique (4.5 : 1) d'un fluide newtonien : À droite, la matrice vierge ; À gauche, la même matrice renforcée par une fraction volumique de 0.045% en fibre (Lipscomb et al., 1988).

L'objectif majeur de cette thèse consistera dans un premier temps en une meilleure compréhension du comportement rhéologique des polymères fortement chargés de fibres. Notamment l'orientation des fibres pour des écoulements simples (cisaillement, élongation) sera investiguée. Par la suite, il s'agira de proposer un modèle rhéologique qui prendra en compte les principales interactions que subissent ces suspensions concentrées.

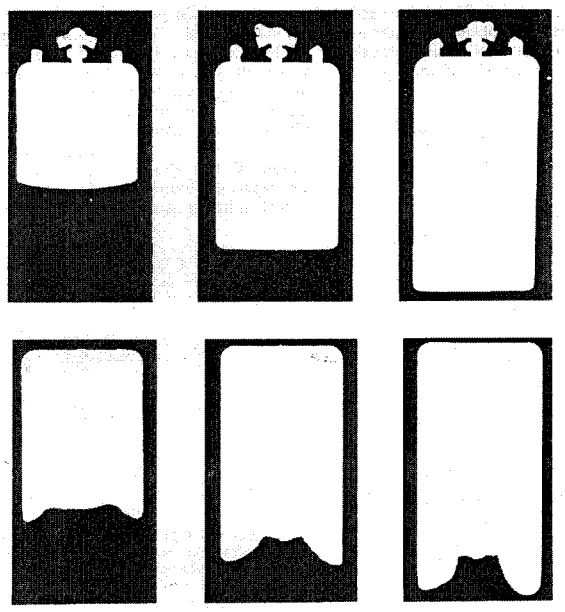

Figure 1.4 : Profil du front de matière pendant le remplissage d'un moule d'injection avec un taux massique de fibres respectivement de 40% (en haut) et 50% (en bas) (Akay & Barkley, 1993).

Dans ce contexte, cet ouvrage se décompose en plusieurs chapitres :

Le chapitre 2 synthétise les observations expérimentales effectuées au cours des dernières décennies sur les suspensions de fibres. Il vise également à faire l'état de l'art en matière de modélisation des lois de comportement. Le tout sert à mettre en évidence le manque d'informations sur certains tests expérimentaux et les lacunes des modèles rhéologiques actuellement utilisées.

Le chapitre 3 résume les principaux résultats de chaque article dont chacun sera la substance d'un chapitre au complet dans cette thèse.

Le chapitre 4 est une partie principalement expérimentale qui porte sur la compréhension du comportement rhéologique de suspensions de fibres lorsque ces dernières subissent de grandes déformations dynamiques.

Le chapitre 5 porte sur une analyse expérimentale du comportement rhéologique de matériaux industriels (polypropylènes renforcés jusqu'à 30% en masse de fibres de verre courtes) soumis à des écoulements élongationnels. Plus particulièrement, les régimes transitoires et permanents sont étudiés.

Le chapitre 6 présente une nouvelle approche numérique, basée sur la méthode des volumes finis, qui permet de réduire considérablement le temps de calcul nécessaire à la résolution de l'équation de Fokker-Planck appliquée aux suspensions de fibres. On obtient ainsi un état d'orientation des fibres plus précis que par le biais des tenseurs d'orientation.

Le chapitre 7 expose le développement théorique d'une loi de comportement pour une suspension non-diluée de fibres en prenant en compte les interactions entres les particules. Cette modélisation plus précise fait intervenir une nouvelle notion que sont les tenseurs d'interaction.

Suivra finalement une discussion générale au chapitre 8, de même que des conclusions et perspectives présentées au chapitre 9.

CHAPITRE 2 - ÉTUDE BIBLIOGRAPHIQUE

Un certain nombre de caractéristiques physiques doivent être connus pour pouvoir comprendre et prédire le comportement rhéologique à l'état fondu d'un polymère chargé :

- La forme géométrique du renfort est l'une d'entre elles. Habituellement, le renfort peut être fibreux (fibre de carbone, de bore, de Kevlar®, de verre), sphérique (bille de verre) ou plaquettaire (mica, talc, argile). Dans cette thèse, l'intérêt est principalement porté aux suspensions de fibres.

- La fraction volumique ϕ des particules en est une autre. Du point de vue du rhéologue, elle représente le volume occupé par la charge et est reliée au nombre de particules par unité de volume n.

La quantité de particules ajoutée au polymère ainsi que leur géométrie sont des paramètres pertinents.

2.1. Propriétés des fibres

Une fibre est généralement représentée par un cylindre de longueur L et un diamètre D. Son rapport de forme ou son élancement est alors défini par $r = L / D$. Les composites ainsi formés par ces renforts sont souvent considérés comme des suspensions de cylindres de longueurs uniformes (Advani, 1994). Cependant au cours d'un procédé de mise en forme, la rupture des fibres engendrent une redistribution en longueur des

fibres et par conséquent une modification de l'élancement des particules (Franzen et al., 1989). Ce point ne sera pas couvert dans ce travail.

La forme et la quantité de fibres permettent de déterminer dans lequel de ces trois régimes de concentration se trouve une suspension (Doi & Edwards, 1978a, b) : dilué, semi-dilué ou concentré (**Tableau 2.1**). Dans le premier cas (dilué), les particules sont hydrodynamiquement indépendantes c'est-à-dire que les champs de vitesse des différentes particules ne se chevauchent pas. Pour le deuxième régime (semi-dilué), les fibres se touchent rarement, mais des interactions hydrodynamiques existent, issues des perturbations de la vitesse du fluide causée par les particules voisines. Au-delà d'une certaine fraction volumique, le régime concentré est atteint : la distance moyenne entre les fibres est alors de l'ordre du diamètre. Chaque fibre peut donc toucher ses voisines induisant des forces de contact entre elles. La **Figure 2.1** montre les différents régimes et nous indique que la plupart des composites commerciaux se situent dans le régime concentré.

Tableau 2.1 : Critères et limites des solutions diluées et non-diluées de fibres.

Critère		Régime	Description
$\phi << r^{-2}$	$n << 1/L^3$	Dilué	Fibres éloignées les unes des autres. Pas d'interaction
$r^{-2} << \phi << r^{-1}$	$1/L^3 << n << 1/L^2 D$	Semi-dilué	Quelques interactions hydrodynamiques
$\phi >> r^{-1}$	$n >> 1/L^2 D$	Concentré	De nombreux contacts entre particules

Les fibres courtes se distinguent des fibres longues par le fait que leur longueur moyenne L est comprise entre 200 et 500 μm et leur diamètre D entre de 10 et 15 μm (Vincent, 2003). Kumar et al. (2007) stipulent quant à eux que $r < 100$. Ainsi les fibres

courtes se distinguent des fibres longues par le fait qu'elles ne fléchissent quasiment pas lors d'un écoulement.

À cause de la différence des masses volumiques $\Delta\rho$ des deux constituants, les fibres en suspension dans un fluide de viscosité η_0 sont soumises à de la sédimentation. Chaouche et Koch (2001) calcule le temps nécessaire pour qu'une fibre orientée parallèlement à la direction verticale parcourt une distance équivalente à sa longueur par : $t_s = 8\eta_0 L / \Delta\rho g D^2 \left[\ln(r) - 0.72\right]$. Ce temps caractéristique est à prendre en compte lors des travaux expérimentaux.

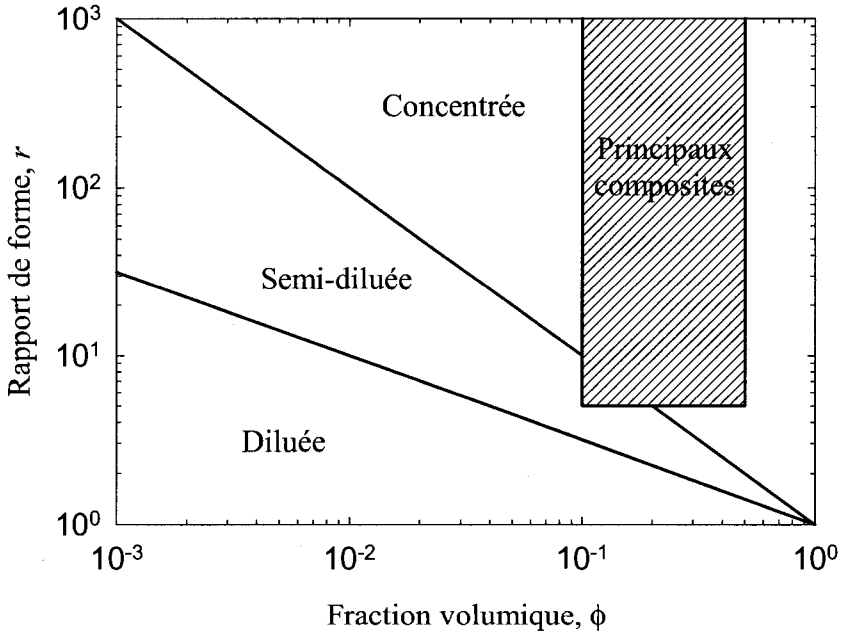

Figure 2.1 : Représentation des régimes de concentration. La zone rectangulaire hachurée montre l'emplacement des principaux composites utilisés (Advani 1994).

Le nombre de Péclet, défini comme le rapport entre les forces hydrodynamiques et browniennes, permet de déterminer si les fibres sont sujettes au mouvement brownien. Chaouche et Koch (2001) estiment ce nombre par : $P_e = \eta_0 \dot{\gamma} \pi L^3 / 3k_B T \ln(r)$. $\dot{\gamma}$ est le taux de cisaillement, k_B est la constante de Boltzmann et T est la température absolue. Pour des nombres de Péclet élevés, le mouvement brownien est négligeable ce qui est très souvent le cas pour les suspensions de fibres.

La fibre peut se courber sous l'effet des contraintes induites par l'écoulement. En cisaillement simple, sa flexibilité est souvent reliée à la rigidité effective S_{eff}. Ce nombre adimensionnel est défini par : $S_{eff} = E_Y I / \eta_0 \dot{\gamma} L^4$ (Switzer & Klingenberg, 2003), où E_Y est le module de Young et I est le moment d'inertie de surface axial. Pour des suspensions de fibres de verre courtes, $S_{eff} \rightarrow \infty$, justifiant ainsi leur rigidité et la conservation de leur forme durant un écoulement.

La géométrie des plaques parallèles est généralement utilisée pour mesurer les fonctions rhéologiques d'une suspension. Ainsi, l'entrefer doit être assez important par rapport à la longueur des fibres. Au regard des récents travaux (Mobuchon, 2002; Sepehr, 2003), un entrefer minimum de trois pour un (c'est-à-dire de trois fois la longueur d'un fibre) a été jugé suffisant pour ne pas nuire à l'orientation des fibres.

2.2. Comportements rhéologiques des suspensions de fibres

Les systèmes chargés de fibres exhibent des comportements non newtoniens et sont à ce titre classés dans la catégorie des fluides complexes. Leurs propriétés

rhéologiques sont fortement dépendantes de la concentration, de l'élancement et de l'orientation des fibres. Les interactions fibre-fibre et fibre-matrice sont également non négligeables. De nombreuses investigations ont alors été réalisées et leurs résultats sont synthétisés ci-après.

2.2.1. En régimes établis

En régimes permanents, les fibres en suspension dans des fluides newtoniens ou viscoélastiques augmentent leur dissipation visqueuse et leur composante élastique.

Viscosité en cisaillement simple

Que ce soit dans un fluide newtonien ou viscoélastique, la présence des fibres accroît la viscosité en cisaillement, particulièrement à des faibles taux de cisaillement $\dot{\gamma}$ (Kitano & Kataoka, 1981a, b; Nicodemo & Nicolais, 1974). La viscosité relative ($\eta_r = \eta / \eta_0$ avec respectivement η et η_0 les viscosités de la suspension et de la matrice) est une fonction linéaire de la fraction volumique des fibres pour des suspensions diluées à semi-diluées (Bibbo et al., 1985; Kitano & Kataoka, 1981a; Sepehr et al., 2004d) et devient quadratique pour des systèmes plus concentrés (Djalili-Moghaddam & Toll, 2005). L'augmentation est plus prononcée pour des élancements de fibre plus importants (Djalili-Moghaddam & Toll, 2005; Ganani & Powell, 1986; Huq & Azaiez, 2005) tandis qu'une diminution est constatée pour des taux de cisaillement plus élevés (Goto et al., 1986a; Kitano & Kataoka, 1981a, b). En utilisant un viscosimètre à bille tombante, les auteurs Milliken et al. (1989) déterminent la viscosité relative d'une suspension de fibres orientées aléatoirement dans un fluide newtonien. Ils montrent que η_r varie linéairement

pour de faibles concentrations ($\phi < 12.5\%$) et η_r augmente de façon cubique pour des concentrations plus élevées ($12.5\% < \phi < 23.15\%$). En utilisant la même technique et le même composite, Mondy et al. (1990) montrent que pour une même concentration ($\phi = 5\%$) $\eta_r = 1.52$ pour des particules alignées alors que $\eta_r = 2.37$ pour une orientation isotrope des fibres. Cette expérience démontre que l'orientation des fibres modifie la viscosité des suspensions. En cisaillement simple, une orientation isotrope des fibres génère une dissipation visqueuse plus importante que le cas des fibres alignées suivant la direction de l'écoulement.

En révisant la littérature dans le domaine des suspensions de fibres dans une matrice newtonienne, Ganani et Powell (1985) trouvent que leur viscosité est dépendante de la fraction des fibres ainsi que de leur rapport de forme. Pour un tel composite au-delà du régime dilué, un léger comportement rhéofluidifiant est mesuré par certains scientifiques (Kitano & Kataoka, 1981a; Petrich et al., 2000a; Sepehr et al., 2004d) mais il n'est pas observé par Ganani et Powell (1985). Ce phénomène est expliqué soit par la destruction d'un réseau de fibres à taux de cisaillement croissant (Zirnsak et al., 1994), soit par des mesures effectuées légèrement en dessous du plateau newtonien (Petrich et al., 2000a).

Cette dernière hypothèse peut être confirmée par l'apparition anticipée de la zone rhéofluidifiante pour des polymères fondus chargés de fibres comparativement à la matrice pure (Czarnecki & White, 1980; Greene & Wilkes, 1995; Kitano et al., 1984b; Mobuchon et al., 2005; Mutel & Kamal, 1984; Ramazani et al., 2001). Dans la zone de

la loi de puissance, la viscosité des composites rejoint celle de la matrice vierge indiquant la faible influence des fibres à des forts taux de cisaillement (Czarnecki & White, 1980; Kitano & Kataoka, 1980, 1981b; Mutel & Kamal, 1984; Ramazani et al., 2001). À de faibles taux de cisaillement, les polymères renforcés de fibres sont fortement fonctions de la fraction volumique des charges (Becraft & Metzner, 1992; Greene & Wilkes, 1995; Mobuchon et al., 2005). Pour les suspensions de fibres courtes étudiées au sein de notre groupe de recherche, leur viscosité à de faibles taux de cisaillement tend vers un plateau newtonien (Ausias et al., 1992; Mobuchon et al., 2005). Ce résultat est confirmé par d'autres auteurs (Crowson & Folkes, 1980; Greene & Wilkes, 1995; Guo et al., 2005; Kitano et al., 1984b). Des contraintes seuils apparaissent pour des systèmes chargés de fibres longues (Thomasset et al., 2005). Cependant Laun (1984) mesure également des contraintes seuils pour des polymères renforcés de fibres courtes. Dans son papier, Laun (1984) ne mentionne aucun traitement de surface de leurs renforts alors que les fibres courtes utilisées dans notre groupe sont recouvertes d'une formulation à base de silane. Kamal et Mutel (1985) remarquent qu'un tel traitement de surface réduit considérablement la viscosité et la contrainte seuil à de faibles $\dot{\gamma}$, là où les particules ont une grande influence sur les propriétés rhéologiques.

Différences des contraintes normales

Comme pour la viscosité, la première différence des contraintes normales N_1 augmente avec la fraction volumique et le rapport de forme des fibres (Chan et al., 1978; Goto et al., 1986a; Mobuchon et al., 2005; Zirnsak et al., 1994) alors que la deuxième différence des contraintes normales N_2 devient nulle (Chan et al., 1978). D'ailleurs, N_2

est souvent négligée (Hypothèse de Weissenberg) puisque $N_2 \approx -10$ % de N_1 (Bird et al., 1987a). Ce résultat est confirmé pour un fluide newtonien (Sepehr et al., 2004d) et pour un polymère fondu (Chan et al., 1978), les deux systèmes étant renforcés de fibres de verre.

Les suspensions de fibres à base d'un fluide newtonien exhibent une première différence des contraintes normales importantes (Goto et al., 1986b; Kitano & Kataoka, 1981a) alors que théoriquement pour la matrice vierge, $N_1 = 0$. Ce comportement est attribué aux interactions fibre-fibre (Sepehr et al., 2004d; Zirnsak et al., 1994). Pour ces systèmes, N_1 varie linéairement avec le taux de cisaillement et la concentration des fibres (Sepehr et al., 2004d; Zirnsak et al., 1994). Le rapport de forme ou la flexibilité des fibres (Zirnsak et al., 1994) génèrent également une hausse de N_1.

Sepehr et al. (2004d) ont préparé des suspensions modèles de fibre de verre à base d'un polybutène (noté PB avec un comportement quasi newtonien) et d'un fluide de Boger (noté B avec une viscosité quasi constante et une élasticité non nulle) (Boger & Binnington, 1977). Étrangement à de faibles taux de cisaillement, $N_1 - N_2$ des trois systèmes chargés à base de PB est supérieure à $N_1 - N_2$ des composites à base de B, pour les mêmes concentrations de fibres. Il semble que l'élasticité du fluide de Boger rivalise avec les interactions fibre-fibres (Iso et al., 1996a; Iso et al., 1996b). Aussi la différence de contraintes normales $N_1 - N_2$ pour les suspensions à base de PB a une pente de 1 alors que les suspensions à base de B, la pente est de 2.

La présence des fibres dans les polymères fondus augmente considérablement la première différence des contraintes normales puisque la matrice pure est déjà élastique (Chan et al., 1978; Kitano & Kataoka, 1981b; Mobuchon et al., 2005; Mutel & Kamal, 1984). La dépendance avec le taux de cisaillement des polymères renforcées de fibres est très proche de celle du polymère vierge [$N_1 \propto \dot{\gamma}^2$, selon la théorie de Lodge (1964)].

L'augmentation des contraintes normales est donc liée aux interactions entre les fibres, et non à l'accroissement de l'élasticité de la matrice. Cependant en sortie de filière, la présence des fibres réduit le gonflement (Chan et al., 1978; Crowson et al., 1980; Kalaprasad et al., 2003; Knutsson et al., 1981).

Viscosité élongationnelle

Les propriétés élongationnelles ont suscité beaucoup d'intérêts à cause de leurs importances dans les applications industrielles mais restent difficiles à mesurer. En écoulement uniaxial, les fibres résistent au champ de déformation induisant, dans le matériau, une contrainte σ_E élevée qui augmente en fonction de leur concentration et leur rapport de forme (Mewis & Metzner, 1974; Zirnsak et al., 1994).

Pour un fluide newtonien, les chercheurs (Mewis & Metzner, 1974; Ooi & Sridhar, 2004; Weinberger & Goddard, 1974) montrent que la viscosité élongationnelle η_E de la matrice ainsi que celle de ces composites est indépendante du taux d'élongation $\dot{\varepsilon}$. À titre d'exemple, Weinberger et Goddard (1974) obtiennent un rapport de Trouton

($T_r = \eta_E / \eta$) de l'ordre de 23 pour des fibres courtes de verre (L = 200 μm et $r \approx 57$) en suspension dans un polybutène (PB).

Pour des suspensions de fibres dans un fluide non newtonien, leur viscosité élongationnelle η_E exhibe un comportement rhéofluidifiant tout comme la matrice vierge (Kamal et al., 1984). Pour Chan et al. (1978), les mêmes phénomènes sont observés pour les composites bien que leur première matrice en PS (Polystyrène) montre un comportement rhéoépaississant et leur seconde matrice en HDPE (Polyéthylène haute densité) présente une viscosité élongationnelle η_E constante en fonction du taux d'extension $\dot{\varepsilon}$. En utilisant un Rheotens, Lin et Hu (1997) mesurent des viscosités élongationnelles légèrement rhéofluidifiantes à de faibles taux d'étirement ($\dot{\varepsilon} < 0.5 s^{-1}$) et croissantes avec la fraction des fibres, mais trouvent qu'au-delà d'une concentration critique (i.e. 20% en masse) η_E chute. Cependant les suspensions de fibres longues présentent un caractère rhéofluidifiant (Creasy et al., 1996b; Thomasset et al., 2005). En élongation planaire, Mobuchon et al. (2005) trouvent un caractère rhéofluidifiant pour un PP (Polypropylène) avec respectivement une augmentation de la viscosité élongationnelle d'environ 5 et 35 % pour ses composites renforcés de 10 et 30% en masse de fibres de verre.

2.2.2. En régimes dynamiques

Pour des cisaillements oscillatoires, l'amplitude des déformations modifie le comportement viscoélastique. Dans la zone linéaire (petites déformations), les propriétés

et la structure du polymère sont peu affectées ce qui n'est pas le cas dans la zone non-linéaire (grandes déformations).

Petites déformations (SAOS : « Small Amplitude Oscillatory Shear »)

Tout comme en cisaillement simple, l'addition des fibres ainsi que leur rapport de forme haussent les propriétés viscoélastiques du polymère, l'accroissement étant largement plus prononcé pour des régimes concentrés (Mobuchon et al., 2005). À hautes fréquences ω, les modules élastiques G' et visqueux G'' tendent à rejoindre ceux de la matrice tandis qu'à de faibles fréquences, G' augmente plus que G'' (Greene & Wilkes, 1995; Kitano et al., 1984a).

Ces observations indiquent que l'angle de déphasage δ ($\tan \delta = G'' / G'$) décroit avec la fraction volumique des fibres à de faibles ω, mais devient constant pour des ω croissantes (Guo et al., 2005). Cependant, Mobuchon et al. (2005) montrent que l'angle de déphasage δ est indépendant de la concentration et de l'orientation des fibres sur une plage de fréquence de trois décades. Ils en déduisent que l'élasticité des suspensions est la même que celle de la matrice.

Les suspensions de fibres dans un fluide newtonien ne génère pas ou très peu d'élasticité en régime dynamique bien qu'elles font apparaître des contraintes normales en cisaillement simple (Ganani & Powell, 1986).

Le principe empirique de Cox-Merz (1958) ne semble pas s'appliquer aux polymères renforcés de fibres. En effet l'orientation des fibres induite par un

cisaillement simple diffère de celle d'un cisaillement dynamique (Guo et al., 2005; Kamal & Mutel, 1989). En effectuant le pré-cisaillant d'un échantillon de polypropylène chargé de fibres avant de mesurer sa viscosité complexe η^*, Mobuchon et al. (2005) appliquent avec succès la règle de Cox-Merz indiquant que la macrostructure des fibres doit être très semblable lors des mesures. Cependant, la loi de Cox-Merz échoue au-delà d'un taux de cisaillement supérieur à 10 s^{-1} (Mobuchon et al., 2005).

Deux tests de fluage à 500 et 1000 Pa ont été réalisés sur des polypropylènes fortement chargés en fibre avant de mesurer leur viscosité complexe. Par comparaison avec un même échantillon non pré-cisaillé, Mobuchon et al. (2005) montrent une réduction significative de η^* respectivement de 32% et 57%.

Grandes déformations (LAOS : « Large Amplitude Oscillatory Shear »)

En investiguant les effets de l'amplitude de déformation γ_R et du temps de pré-cisaillement, Kim et Song (1997) ont conclu que l'orientation des fibres diminue la viscosité complexe η^* : Plus l'amplitude de cisaillement augmente, plus les fibres s'alignent suivant la direction de l'écoulement. En modélisant le comportement non-linéaire d'une suspension diluée de fibres dans un fluide d'Oldroyd B, Harlen et Koch (1997) indiquent un changement de l'orientation des fibres au cours d'un cycle.

Mutel (1989) remarque des réponses non-harmoniques pour des suspensions concentrées de fibres même lorsqu'elles sont sollicitées dynamiquement par de faibles amplitudes de déformation. Dès lors Mutel et Kamal (1986) observent un signal non fondamental pour un polypropylène chargé à 10% en masse de fibres ($\omega = 0.1$ rad/s et γ_R

= 2.4) de même pour un polypropylène fortement renforcé en fibres (ω = 0.2 rad/s et γ_R = 1.4).

2.2.3. En régimes transitoires

Le comportement rhéologique des systèmes chargés de fibres en régime transitoire est fortement affecté par la distribution d'orientation des particules, spécialement pour de fortes concentrations de fibres (Ausias et al., 1992; Laun, 1984; Mobuchon et al., 2005; Sepehr et al., 2004c; Sepehr et al., 2004d).

Viscosité transitoire

Lorsqu'une suspension de fibres est cisaillée à un $\dot{\gamma}$ constant, l'orientation initialement désordonnée des particules évolue pour atteindre un régime permanent où la plupart des fibres sont alignées suivant la direction de l'écoulement. Ce changement de structure se traduit par l'apparition d'un pic de viscosité qui dépend de la fraction volumique et du rapport de forme des charges fibres (Ausias et al., 1992; Laun, 1984; Mobuchon et al., 2005; Sepehr et al., 2004c; Sepehr et al., 2004d). Pour un polymère vierge ou renforcé de billes, cet extrémum est inexistant (Laun, 1984; Sepehr et al., 2004c). De même, à la suite d'un pré-cisaillement ou d'un second démarrage dans le même sens (sans délai), aucun pic de viscosité n'est observé puisque les fibres sont déjà orientées (Mutel & Kamal, 1987; Sepehr et al., 2004c; Sepehr et al., 2004d).

Lors d'un second démarrage dans le sens contraire, un second pic de viscosité (pic retour) est observé. Il est causé par un basculement des fibres dans la nouvelle direction de l'écoulement (Barbosa et al., 1994; Ramazani et al., 2001; Sepehr et al.,

2004c; Sepehr et al., 2004d). Pour des suspensions modèles (fluide PB et B), un pic de viscosité reproductible a été observé à chaque inversion de l'écoulement (Sepehr et al., 2004d). Aussi des tests successifs dans la même direction mettent en évidence un pseudo-plateau, inférieur à celui du régime établi pour les systèmes à base de PB, qui est attribué à la formation d'un réseau par les fibres (Sepehr et al., 2004d). En laissant un temps de relaxation suffisamment long à la matrice élastique (fluide B), un pic de viscosité, très similaire à celui du premier démarrage, est observé (Sepehr et al., 2004d). Ces auteurs suggèrent que les chaînes de haut poids moléculaire du polyisobutylène, adsorbées sur les fibres de verre, se relaxent entrainant avec elle la désorientation des particules. Finalement la présence des fibres n'influence pas le temps de relaxation de la matrice (Laun, 1984; Sepehr et al., 2004d).

Différences des contraintes normales transitoires

De même que pour la viscosité, un pic pour les contraintes normales est observé lorsqu'une suspension de fibres est cisaillée à une vitesse constante (Laun, 1984; Sepehr et al., 2004c; Sepehr et al., 2004d). Ce pic des contraintes normales est plus prononcé que celui de la viscosité et est également fonction de ϕ et de r.

Lors d'un inversement du sens de rotation (sans délai), les contraintes normales montrent au préalable des valeurs négatives pour ensuite exhiber un pic positif (correspondant au pic de viscosité) avant d'atteindre le régime permanent (Sepehr et al., 2004c; Sepehr et al., 2004d). Tout comme la viscosité, le temps de relaxation des contraintes normales n'est pas modifié par les fibres (Laun, 1984; Sepehr et al., 2004d).

Viscosité élongationnelle transitoire

Pour des composites à base de fluides newtoniens ou viscoélastiques, les fibres haussent leur viscosité élongationnelle transitoire (Chan et al., 1978; Kamal et al., 1984). Laun (1984) mesure la viscosité élongationnelle transitoire d'un HDPE renforcé de fibre de verre pour différentes orientations initiales de fibres. Les charges orientées parallèlement à la direction de l'étirement génèrent la contrainte élongationnelle la plus importante en régime établi, tandis que les charges orientées aléatoirement engendrent une contrainte élongationnelle σ_E^+ qui tend à rejoindre la σ_E maximale. Ce phénomène est attribué à une orientation des fibres suivant la direction de l'élongation et est également observé par Wagner et al. (2003).

En élongation uniaxiale, les régimes permanents sont atteints plus rapidement pour les composites renforcés de fibres que pour leur matrice pure (Kamal et al., 1984).

2.3. Modélisation de la dynamique d'orientation des fibres

De nombreux travaux ont été réalisés pour prédire le comportement rhéologique des suspensions de fibres. Ce qui suit synthétise les principales formulations théoriques de modèles décrivant l'orientation d'une population de fibres. Il sera également question de savoir comment la déformation du polymère modifie l'orientation des fibres.

2.3.1. Description de l'orientation d'une population de fibres

Dans un repère sphérique, l'orientation d'une fibre rigide peut être représentée par un vecteur unitaire **p** ayant comme direction principale l'axe de symétrie de la

particule. Sa projection dans un repère fixe fait apparaître la paire d'angle d'Euler φ et θ reliée aux coordonnées Cartésiennes (p_1, p_2 et p_3) selon (**Figure 2.2**) :

$$\mathbf{p} = \begin{cases} p_1 = \sin\theta\cos\varphi \\ p_2 = \sin\theta\sin\varphi \\ p_3 = \cos\theta \end{cases}. \tag{2.1}$$

Comme les deux extrémités d'une fibre sont indissociables, le sens du vecteur **p** est arbitraire, d'où : $\mathbf{p} \rightarrow -\mathbf{p}$. Dans certains composites, la flexibilité des fibres devient prépondérante et leurs descriptions nécessitent plus de détails (Joung et al., 2001; Ross & Klingenberg, 1997; Schmid et al., 2000). Ce point de vue de représentation est largement utilisé dans les techniques numériques de simulations directes, où généralement 500 à 1000 fibres sont générées pour représenter les écoulements simples à l'état fondu de ces composites. Cependant dans les milieux industriels, l'important nombre de particules et la complexité des écoulements font que cette description devient rapidement contraignante.

La fonction de distribution d'orientation ψ permet de décrire plus globalement l'état d'orientation d'une population de fibres en un point matériel (Advani & Tucker, 1987). Ce point de vue plus réaliste représente la fraction de particules ayant la même orientation à l'intérieur d'un volume élémentaire. Elle est définie de telle sorte que la probabilité P de trouver des fibres alignées suivant le secteur d'angle φ_1 et $\varphi_1 + d\varphi$ et θ_1 et $\theta_1 + d\theta$ soit donnée par :

$$P(\varphi_1 \le \varphi \le \varphi_1 + d\varphi, \theta_1 \le \theta \le \theta_1 + d\theta) = \psi(\varphi_1, \theta_1)\sin\theta_1 d\theta d\varphi. \tag{2.2}$$

La périodicité de cette fonction de distribution d'orientation donne $\psi(\mathbf{p}) = \psi(-\mathbf{p})$. Sur toute la surface d'une sphère de rayon unitaire, la probabilité de trouver une particule est l'unité. Ainsi la condition de normalisation implique que :

$$\int_{\varphi=0}^{2\pi} \int_{\theta=0}^{\pi} \psi(\varphi,\theta) \sin\theta \, d\theta \, d\varphi = \int_{\mathbf{p}} \psi \, d\mathbf{p} = 1 , \tag{2.3}$$

où l'intégration est calculée suivant toutes les directions pointées par **p**.

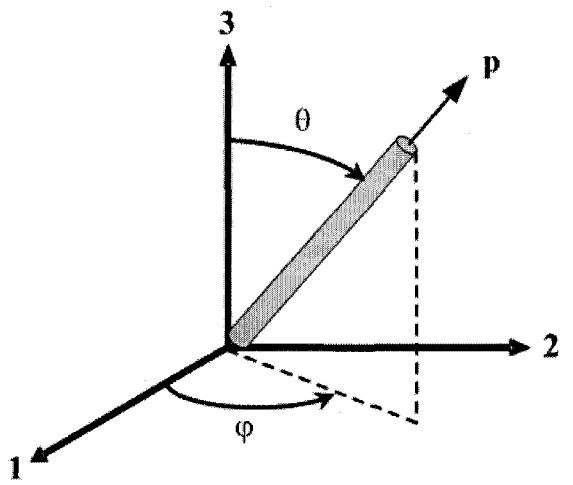

Figure 2.2 : Orientation d'une fibre axisymétrique décrite par deux angles θ et φ ou par un vecteur unitaire **p** de direction principale l'axe de symétrie.

Néanmoins, une description plus compacte de l'état d'orientation des fibres dans un composite est obtenue par une troncature des moments de la fonction de distribution. Ces moments sont dénommés tenseurs d'orientation (Advani & Tucker, 1987). Les produits dyadiques du vecteur unitaire **p**, pondérés par la fonction de distribution ψ, sont intégrés suivant toutes les directions pour former les tenseurs d'orientation du second et du quatrième ordre respectivement :

$$\mathbf{a}_2 = \langle \mathbf{pp} \rangle = \int_{\mathbf{p}} \mathbf{pp}\psi \, d\mathbf{p} \,, \tag{2.4}$$

$$\mathbf{a}_4 = \langle \mathbf{pppp} \rangle = \int_{\mathbf{p}} \mathbf{pppp}\psi \, d\mathbf{p} \,. \tag{2.5}$$

Étant donné que la fonction de distribution est paire, les tenseurs d'orientation d'ordre impair sont tous nuls. Aussi, plus l'ordre du tenseur est élevé, meilleure est la description de l'état d'orientation des fibres. Il en découle de la condition de normalisation que :

$$\mathrm{tr}\, \mathbf{a}_2 = a_{\mathrm{ii}} = 1 \,, \tag{2.6}$$

$$a_{\mathrm{ijkk}} = a_{\mathrm{ij}} \,, \tag{2.7}$$

où la sommation suivant l'indice répété a été omise. Également la symétrie des tenseurs d'orientation implique que :

$$a_{\mathrm{ij}} = a_{\mathrm{ji}} \,, \tag{2.8}$$

$$a_{\mathrm{ijkl}} = a_{\mathrm{jikl}} = a_{\mathrm{kijl}} = a_{\mathrm{lijk}} = a_{\mathrm{klij}} = \ldots \tag{2.9}$$

Il en résulte que seulement cinq et quinze composantes suffisent à déterminer entièrement $\mathbf{a}_2$ et $\mathbf{a}_4$, respectivement.

Les composantes du tenseur d'orientation $\mathbf{a}_2$ présentent des interprétations physiques compréhensibles. La **Figure 2.3a** représente un état d'orientation isotrope. Dans le cas où les fibres sont orientées aléatoirement dans le plan (1-2) comme schématisé sur la **Figure 2.3b**, l'orientation est considérée aléatoire dans un plan. Finalement la **Figure 2.3c** montre un alignement parfait des fibres suivant la direction 1.

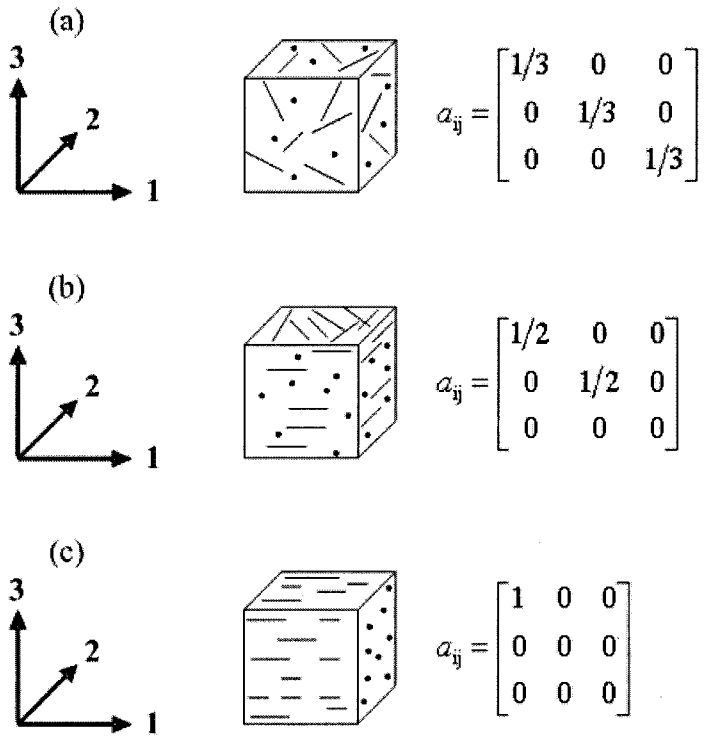

Figure 2.3 : Exemples de trois états d'orientation : (a) orientation isotrope ; (b) orientation aléatoire dans un plan ; (c) orientation des fibres totalement alignées suivant la direction (1).

2.3.2. Dynamique d'orientation d'une population de fibres

Sachant maintenant comment représenter l'état d'orientation des fibres, la présente section explique brièvement les modèles mathématiques élaborés pour décrire leur dynamique d'orientation. En suspension dans un milieu liquide en écoulement, les fibres sont sujettes à de nombreuses forces.

Dynamique d'une fibre

L'une des premières théories est celle de Jeffery (1922) qui détermine le mouvement d'une fibre isolée en suspension dans un fluide newtonien. Représentée par un sphéroïde rigide, la fibre est uniquement soumise à des forces hydrodynamiques en

l'absence de forces inertielles. Le facteur de forme de la particule $\lambda = (r^2-1) / (r^2+1)$, avec r l'élancement de la particule, induit une rotation cyclique lorsque cette dernière est sujette à un cisaillement simple (**Figure 1.1**). La période de rotation vaut alors :

$$T_r = \frac{2\pi}{\dot{\gamma}}\left(r + r^{-1}\right). \tag{2.10}$$

Le rapport de forme r est occasionnellement substitué par un rapport de forme effectif afin de corriger la forme réelle de la particule (Burgers, 1938; Cox, 1971; Nawab & Mason, 1958; Trevelyan & Mason, 1951). L'équation de Jeffery (1922) décrit relativement bien le mouvement d'une particule pour des suspensions diluées car la fibre se meut librement sans être soumise à des interactions mécaniques et hydrodynamiques notamment. Dans le monde industriel, les suspensions sont tellement concentrées que les fibres ne peuvent plus être considérées séparément. Néanmoins pour de tels systèmes, la théorie de Jeffery (1922) prédit qualitativement la dynamique d'orientation mais le niveau d'alignement diffère et ceci sans exhiber des rotations périodiques. Ces effets sont principalement attribués aux interactions entre les fibres, d'où l'idée de Folgar et Tucker (1984) d'étendre l'équation de Jeffery (1922) pour incorporer une diffusion. Issu d'un concept phénoménologique, ce terme de diffusion est donné par $D_r \nabla \ln \psi = C_I \, |\dot{\gamma}| \, \nabla \ln \psi$. D_r et C_I sont respectivement les coefficients de diffusion en rotation et d'interaction, tandis que $|\dot{\gamma}|$ est le second invariant du tenseur des vitesses de déformation. ∇ est l'opérateur gradient. Dans cette configuration, quand l'écoulement est arrêté, aucune réorganisation spatiale des particules ne se produit et les fibres

conservent alors leurs inclinaisons finales. Un modèle générique donnant l'évolution du vecteur unitaire **p** s'écrit sous la forme (Advani & Tucker, 1987) :

$$\frac{D\mathbf{p}}{Dt} = \dot{\mathbf{p}} = -\frac{1}{2}\boldsymbol{\omega}\cdot\mathbf{p} + \frac{\lambda}{2}(\dot{\boldsymbol{\gamma}}\cdot\mathbf{p} - \dot{\boldsymbol{\gamma}}:\mathbf{ppp}) - D_r\cdot\nabla\ln\psi, \tag{2.11}$$

où $\boldsymbol{\omega} = \boldsymbol{\kappa} - \boldsymbol{\kappa}^{\dagger}$ et $\dot{\boldsymbol{\gamma}} = \boldsymbol{\kappa} + \boldsymbol{\kappa}^{\dagger}$ sont respectivement les tenseurs de vorticité et des taux de déformation avec $\boldsymbol{\kappa}^{\dagger}$ le tenseur des gradients de vitesse.

Évolution d'une population de fibres

L'évolution temporelle de la fonction de distribution d'orientation répond à une équation de continuité dans le sens où, une particule qui quitte une orientation doit réapparaître dans une autre. Dès lors, un bilan des flux conduit à (Bird et al., 1987b) :

$$\frac{D\psi}{Dt} = -\nabla\cdot(\dot{\mathbf{p}}\psi). \tag{2.12}$$

Connaissant l'évolution du vecteur unitaire **p**, cette dernière expression donne l'évolution de la fonction de distribution d'orientation. L'équation de Fokker-Planck est ainsi obtenue à partir de l'équation généralisée de Jeffery (Advani & Tucker, 1987).

Évolution du tenseur d'orientation

Grâce à l'évolution temporelle de la fonction de distribution d'orientation ψ, donnée par l'équation (2.12), et aux définitions des tenseurs d'orientation, équations (2.4) et (2.5), Advani et Tucker (1987) dérivent l'évolution du tenseur d'orientation $\mathbf{a_2}$. Ce résultat s'exprime sous la forme suivante :

$$\frac{D\mathbf{a}_2}{Dt} = \dot{\mathbf{a}}_2 = -\frac{1}{2}(\boldsymbol{\omega}\cdot\mathbf{a}_2 - \mathbf{a}_2\cdot\boldsymbol{\omega}) + \frac{\lambda}{2}(\dot{\boldsymbol{\gamma}}\cdot\mathbf{a}_2 + \mathbf{a}_2\cdot\dot{\boldsymbol{\gamma}} - 2\mathbf{a}_4:\dot{\boldsymbol{\gamma}}) + 2D_r(\boldsymbol{\delta} - m\mathbf{a}_2), \tag{2.13}$$

où $\boldsymbol{\delta}$ est le tenseur identité et m =2 ou 3 respectivement pour un problème 2D ou 3D. Sous cette notation tensorielle, l'équation donnant l'évolution d'orientation d'une population de fibres possède une forme compacte et efficace, ce qui explique pourquoi elle est largement implantée dans les logiciels de simulation. Également dans leur papier, Advani et Tucker (1987) dérivent l'évolution du tenseur d'orientation d'ordre quatre $\mathbf{a}_4$.

Des idées ont émergé pour introduire une diffusion anisotrope $\boldsymbol{D}_r$. Koch (1995) fait intervenir les tenseurs d'ordre quatre et six dans son terme de diffusion, ce qui n'est pas très pragmatique. Les auteurs (Fan et al., 1998; Phan-Thien et al., 2002) suggèrent que le tenseur de diffusion $\boldsymbol{D}_r = \boldsymbol{C}_I \, |\dot{\gamma}|$ soit proportionnel à la cinématique de l'écoulement et au tenseur d'interaction $\boldsymbol{C}_I$. En 3D, l'évolution du tenseur d'orientation $\mathbf{a}_2$ devient :

$$\begin{aligned}\dot{\mathbf{a}}_2 = &-\frac{1}{2}(\boldsymbol{\omega}\cdot\mathbf{a}_2 - \mathbf{a}_2\cdot\boldsymbol{\omega}) + \frac{\lambda}{2}(\dot{\boldsymbol{\gamma}}\cdot\mathbf{a}_2 + \mathbf{a}_2\cdot\dot{\boldsymbol{\gamma}} - 2\mathbf{a}_4 : \dot{\boldsymbol{\gamma}}) \\ &+ |\dot{\gamma}|\left(2\boldsymbol{C}_I - 3\boldsymbol{C}_I\cdot\mathbf{a}_2 - 3\mathbf{a}_2\cdot\boldsymbol{C}_I - 2\boldsymbol{\delta} : \boldsymbol{C}_I\mathbf{a}_2 + 6\mathbf{a}_4 : \boldsymbol{C}_I\right)\end{aligned}, \tag{2.14}$$

où les composantes du tenseur d'interaction $\boldsymbol{C}_I$ sont déterminées en les ajustant aux données expérimentales obtenues en régime établi. Néanmoins cette loi d'évolution est très peu usitée.

Hormis les travaux de Koch (1995), les théories proposées indiquent que le coefficient d'interaction ne dépend pas explicitement de la fraction volumique des fibres

ϕ et du rapport de forme r. Dans sa thèse, Bay (1991) suggère l'équation empirique suivante :

$$C_I = A\exp(-Br\phi). \tag{2.15}$$

Cette expression provient de la résolution de la fonction de distribution où les valeurs de C_I ont été déterminées en ajustant les composantes de $\mathbf{a}_2$ avec des données expérimentales obtenues par l'injection de thermoplastiques. Ainsi, Bay (1991) rapporte que $A = 0.0184$ et $B = 0.7148$. Pour un rapport de forme donné, la limite supérieure ($\phi \rightarrow 0$) indique que $C_I = 0.0184$ et la limite inférieure ($\phi \rightarrow \infty$) donne $C_I = 0$, ce qui est contradictoire avec la théorie de Jeffery (1922). Afin que C_I augmente de façon monotone, Phan-Thien et al. (2002) (2002) proposent :

$$C_I = A\left[1-\exp(-Br\phi)\right]. \tag{2.16}$$

En variant le rapport de forme r, Phan-Thien et al. (2002) obtiennent que $A = 0.030$ et $B = 0.224$ grâce à une méthode de minimisation entre l'équation (2.16) et des simulations directes. Ranganathan et Advani (1991) ont quant à eux exprimé la dépendance du coefficient d'interaction C_I est fonction de l'espace moyen entre les fibres h sous la forme :

$$C_I = KL/h, \tag{2.17}$$

où K est une constante universelle de proportionnalité. Les observations expérimentales de Ramazani et al. (2001) leur indiquent que l'orientation des chaînes macromolécules suivant la direction de l'écoulement favorise l'alignement des fibres. Ramazani et al. (2001) modifient alors le coefficient d'interaction :

$$C_l = \frac{LC_l^*}{h\left[tr\left(\mathbf{a}_2 \cdot \mathbf{c}\right)\right]^n}, \tag{2.18}$$

où C_l^* est une constante et $\mathbf{c}$ est le tenseur de conformation d'une macromolécule (Carreau et al., 1997).

2.3.3. Approche thermodynamique

Par une approche thermodynamique basée sur la structure Hamiltonienne (Grmela, 1986; Grmela & Carreau, 1987), les auteurs (Ghosh, 1993; Ghosh et al., 1995) présentent une alternative pour décrire l'évolution de l'orientation d'une population de fibres. La démarche consiste en la dérivation du tenseur de conformation d'une macromolécule pour représenter l'orientation des fibres. Ce changement de l'orientation des fibres s'écrit donc :

$$\dot{\mathbf{a}}_2 = -\frac{1}{2}\left(\boldsymbol{\omega} \cdot \mathbf{a}_2 - \mathbf{a}_2 \cdot \boldsymbol{\omega}\right) + \frac{1}{2}\left(\dot{\boldsymbol{\gamma}} \cdot \mathbf{a}_2 + \mathbf{a}_2 \cdot \dot{\boldsymbol{\gamma}}\right) - \boldsymbol{\Lambda} \cdot \mathbf{a}_2 \cdot \frac{\delta G}{\delta \mathbf{a}_2}, \tag{2.19}$$

où $\delta / \delta \mathbf{a}_2$ est la dérivée de Volterra, $\boldsymbol{\Lambda}$ est le tenseur des mobilités et G est l'énergie libre de Gibbs. La dérivée de ce potentiel thermodynamique est exprimée pour des particules axisymétriques par :

$$\frac{\delta G}{\delta \mathbf{a}_2} = \frac{k_B T}{2}\left[\beta \boldsymbol{\delta} - S_B \mathbf{a}_2^{-1} - L^2 S_L \mathbf{a}_2^{-1} \cdot \mathbf{a}_2^{-1} + 2\frac{S_O}{L^2}\left(\boldsymbol{\delta} - \frac{\mathbf{a}_2}{L^2}\right)\right], \tag{2.20}$$

avec k_B la constante de Boltzmann et T la température absolue. β est le multiplicateur Lagrangien qui garde constante la trace du tenseur d'orientation $\mathbf{a}_2$ au cours d'une déformation (les fibres sont inextensibles). Le terme S_B est la contribution dissipative de

Boltzmann nivelant l'ordre de l'orientation. S_L est un coefficient qui pondère la contribution de Lifshitz caractérisant la semi flexibilité des fibres. Enfin le paramètre S_O a été introduit par Onsager pour tenir compte des interactions topologiques ou en d'autres termes du volume exclu. Dans leur papier, Ghosh et al. (1995) présentent un tenseur isotrope des mobilités par l'expression suivante :

$$\mathbf{\Lambda} = \Lambda_0 \frac{\left(1 - \dfrac{n^2}{n_0^2}\right)}{\left[1 - a\,\mathrm{tr}\left(\dfrac{\mathbf{a}_2 \cdot \mathbf{a}_2}{L^4}\right)\right]^2} \boldsymbol{\delta}, \tag{2.21}$$

où Λ_0 est la constante de mobilité et n_0 la concentration maximale en tassement des fibres. Enfin le paramètre d'orientation a apporte une correction sur l'effet de l'orientation des fibres ($0 \leq a \leq 1$). Dans sa thèse, Ghosh (1993) propose un tenseur anisotrope des mobilités.

2.4. Lois de comportement des suspensions de fibres

Une loi de comportement ou une équation constitutive exprime mathématiquement les contraintes en fonction de l'histoire de la déformation et/ou des taux de déformation pour un matériau donné (Carreau et al., 1997). Pour modéliser correctement un procédé de mise en forme, il est donc important de disposer d'une équation constitutive globale, qui représente au mieux le comportement du matériau pour une multitude de sollicitations (cisaillement simple, élongation ou combinaison des deux) et pour des régimes particuliers (établi ou transitoire). Pour le cas des suspensions

de particules axisymétriques, il semble important de tenir compte des effets de l'orientation des fibres.

En considérant le composite incompressible (fibres et fluide), la contrainte totale $\boldsymbol{\sigma}$ dans le matériau est la contribution d'une pression hydrostatique P et d'une partie déviatorique représentant le champ des extras contraintes $\boldsymbol{\tau}$. Généralement, la pression hydrostatique est négligeable. Pour un composite, il est d'usage de décomposer le champ des contraintes en une somme des contributions provenant de la matrice $\boldsymbol{\tau}^m$ et des fibres $\boldsymbol{\tau}^f$.

2.4.1. Fibres en suspension dans un fluide newtonien

Une multitude de théories existent pour prédire la contribution des fibres dans un fluide newtonien. Les chercheurs (Batchelor, 1971; Burgers, 1938; Dinh & Armstrong, 1984; Shaqfeh & Fredrickson, 1990) ont employé la mécanique des milieux continus avec la théorie sur les corps minces ($r >> 1$), tandis que les auteurs (Giesekus, Hanswalter, 1962; Hand, 1961) relient le tenseur des contraintes avec la microstructure déterminée par les travaux de Jeffery (1922). Dès lors, les scientifiques (Hinch & Leal, 1973; Lipscomb et al., 1988) ont développé une équation générique qui se présente sous la forme :

$$\boldsymbol{\sigma} = -P\boldsymbol{\delta} + \eta_0\dot{\boldsymbol{\gamma}} + \eta_0\phi\left[\mu_1\dot{\boldsymbol{\gamma}} + \mu_2\mathbf{a}_4 : \dot{\boldsymbol{\gamma}} + \mu_3\left(\dot{\boldsymbol{\gamma}}\cdot\mathbf{a}_2 + \mathbf{a}_2\cdot\dot{\boldsymbol{\gamma}}\right) + 2\mu_4\mathbf{a}_2 D_r\right]. \tag{2.22}$$

Dans cette expression, η_0 est la viscosité newtonienne du fluide, D_r est le coefficient de diffusion causé par le mouvement brownien et μ_1, μ_2, μ_3 et μ_4 sont les

constantes du matériel. Le **Tableau 2.2** recense les constantes matérielles μ_i rencontrées dans la littérature (pour une présentation plus claire, uniquement les μ_i non nuls sont présentées). Il est à noter que les fibres sont souvent considérées comme des corps minces, d'où $\mu_1 = \mu_3 = 0$ et non sujettes au mouvement brownien (Chaouche & Koch, 2001), ce qui entraîne que $\mu_4 = 0$.

La loi de comportement de Dinh et Armstrong (1984) fait intervenir l'espacement moyen entre deux fibres h. Cette distance moyenne est encadrée par une borne supérieure $h_{\text{ali}} = D\sqrt{\pi/\phi}/2$, cas où les fibres sont parfaitement alignées et par une borne inférieure $h_{\text{iso}} = D\pi/4\phi r$, cas où l'orientation des fibres est isotrope (Doi & Edwards, 1978a, b). Du fait que la distance moyenne h évolue en fonction de l'orientation des fibres, les chercheurs (Chung & Kwon, 1995; Chung & Kwon, 2002a) utilisent la mesure scalaire du tenseur d'orientation, $f^* = 1 - 27\ \det(\mathbf{a}_2)$ (Advani & Tucker, 1990a) pour déterminer des distances moyennes intermédiaires.

Tableau 2.2 : Paramètres matériaux pour la loi de comportement [Éq. (2.22)].

Modèle	Paramètres matériaux	Solution
Batchelor (1971)	$\mu_2 = \dfrac{8r^2}{3\ln(r)}$	Très diluée
Batchelor (1970a)	$\mu_2 = \mu_2^{\text{dilué}} = \dfrac{8r^2}{3\ln(2r)}\left(\dfrac{\ln(2r)+0.64}{\ln(2r)-1.5}+\dfrac{1.659}{\ln^2(2r)}\right)$	Diluée
Mackaplow et Shaqfeh (1996)	$\mu_2 = \mu_2^{\text{dilué}} + \dfrac{C_1\phi r^4}{\ln^3(2r)}$ $C_1 = 1.399$ pour fibres alignées $C_1 = 1.508$ pour fibres aléatoires	Diluée (interaction de deux corps)
Hinch et Leal (1972)	$\mu_1 = 2$; $\mu_2 = \dfrac{r^2}{2\left[\ln(2r)-1.5\right]}$; $\mu_3 = \dfrac{6\ln(2r)-11}{r^2}$	Semi-diluée
Shaqfeh et Fredrickson (1990)	$\mu_2 = \dfrac{16r^2}{3\left(\ln(1/\phi)+\ln\ln(1/\phi)+C_2\right)}$ $C_2 = 0.1585$ pour fibres alignées $C_2 = -0.6634$ pour fibres aléatoires	Semi-diluée
Lipscomb et al. (1988)	$\mu_1 = 2$; $\mu_2 = r^2/2\ln(r)$	Semi-diluée
Dinh et Amrstrong (1984)	$\mu_2 = \dfrac{r^2}{3\ln(2h/D)}$ $h = h_{\text{ali}} = \dfrac{D}{2}\sqrt{\dfrac{\pi}{\phi}}$ pour des fibres alignées $h = h_{\text{iso}} = \pi D/4\phi r$ pour des fibres aléatoires	Semi-concentrée
Chung et Kwon (2002a)	$\mu_2 = \dfrac{r^2}{3\ln(2h/D)}$ $h = (1-f^*)h_{\text{iso}} + f^* h_{\text{ali}}$ $f^* = 1 - 27\det(\mathbf{a}_2)$	Semi-concentrée

2.4.2. Fibres en suspension dans un fluide rhéofluidifiant

Grâce à un modèle cellulaire, Souloumiac et Vincent (1998) ont dérivé la contrainte totale pour une suspension de fibres dans un fluide rhéofluidifiant. La matrice

est caractérisée par une loi puissance de consistance K et d'indice de rhéofluidifiance m. Leur expression finale s'écrit :

$$\boldsymbol{\sigma} = -P\boldsymbol{\delta} + K\left|\dot{\boldsymbol{\gamma}}\right|^{m-1}\dot{\boldsymbol{\gamma}} + K\phi\mu_2 \int_{\mathbf{p}} \dot{\boldsymbol{\gamma}} : \mathbf{pppp} \left|\dot{\boldsymbol{\gamma}} : \mathbf{pp}\right|^{m-1} \psi \, d\mathbf{p} \,, \tag{2.23}$$

avec le coefficient de couplage μ_2 exprimé par :

$$\mu_2 = \frac{r^{m+1}}{2^{m-1}(m+2)} \left[\frac{1-m}{m\left[1-(D/2h)^{(1-m)/m}\right]} \right]^m . \tag{2.24}$$

Pour m = 1, l'expression de Dinh et Armstrong (1984) est retrouvée (**Tableau 2.2**).

2.4.3. Fibres en suspension dans un fluide viscoélastique

Deux démarches différentes, l'une mécanique, l'autre thermodynamique, sont suggérées dans la littérature pour décrire le comportement de suspensions de fibres dans un milieu viscoélastique. Ces deux approches convergent vers des résultats analogues.

Approche mécanique

Azaiez (1996) a développé une équation constitutive pour des fibres en suspension dans un milieu viscoélastique. La chaîne macromoléculaire du polymère est matérialisée par une altère élastique : deux billes identiques et sans masse sont reliées entre elles par un ressort (Bird et al., 1987b). Le modèle FENE-P (« Finitely Extensible Non-linear Elastic - Peterlin ») est utilisé pour exprimer la force d'un tel connecteur. Ainsi la contrainte totale dans le composite s'écrit (Azaiez, 1996) :

$$\boldsymbol{\sigma} = \boldsymbol{\tau}^{m} + \boldsymbol{\tau}^{f} = -P\boldsymbol{\delta} + \frac{\eta_0}{\lambda_m}(Z\mathbf{B} - \boldsymbol{\delta})\dot{\boldsymbol{\gamma}} + \eta(\dot{\gamma})\phi(\mu_1\dot{\boldsymbol{\gamma}} + \mu_2\mathbf{a}_4 : \dot{\boldsymbol{\gamma}}), \tag{2.25}$$

où η_0 et $\eta(\dot{\gamma})$ sont respectivement les viscosités au plateau newtonien et du polymère (la viscosité du solvant a été négligée). λ_m est le temps de relaxation de la matrice. La fonction Z prend la forme $Z = b / (b - \mathrm{tr}\ \mathbf{B})$ avec b un paramètre adimensionnel mesurant l'extensibilité du ressort. Finalement **B** représente le tenseur de conformation adimensionnel **B** de la macromolécule, son équation d'évolution temporelle étant donnée par :

$$\begin{aligned}\dot{\mathbf{B}} = &-\frac{1}{2}(\boldsymbol{\omega}\cdot\mathbf{B} - \mathbf{B}\cdot\boldsymbol{\omega}) + \frac{1}{2}(\dot{\boldsymbol{\gamma}}\cdot\mathbf{B} + \mathbf{B}\cdot\dot{\boldsymbol{\gamma}}) \\ &-\frac{Z}{\lambda_m}\left[\sigma\mathbf{B} + \frac{m(1-\sigma)}{2}(\mathbf{a}_2\cdot\mathbf{B} + \mathbf{B}\cdot\mathbf{a}_2)\right] + \frac{1}{\lambda_m}\left[\sigma\,\boldsymbol{\delta} + m(1-\sigma)\mathbf{a}_2\right]\end{aligned}, \tag{2.26}$$

où m est la dimension du problème. Un point intéressant dans les travaux d'Azaiez (1996) est que le modèle prend en compte les interactions fibre-polymère par le coefficient de couplage σ. En testant ce modèle sur des thermoplastiques (LLDPE) renforcés de fibres de verre jusqu'à une fraction volumique de 35%, Guo et al. (2005) montrent la nécessité du couplage fibre-matrice. Les modèles d'Oldroyd-B, de Giesekus, de FENE-CR et de Phan-Thien - Tanner sont également utilisés pour représenter le comportement de la matrice (Azaiez, 1996; Azaiez et al., 1997; Azaiez, 2000).

Approche thermodynamique

En s'appuyant sur les travaux d'Ait-Kadi et Gremla (1994), Ramazani et al. (1997) modélisent le comportement rhéologique de composites thermoplastiques à fibres

courtes, l'approche décrivant l'orientation des fibres étant donné par l'équation (2.13). Ils y introduisent les interactions fibre-matrice dans la formulation du tenseur des mobilités. Dans le cas d'un fluide FENE-P, ils obtiennent ainsi une loi constitutive très similaire aux travaux d'Azaiez (1996). Ramazani et al. (2001) présentent les possibilités du modèle à prédire le comportement d'une suspension de fibres dans un fluide de Boger.

2.5. Calcul de la fonction de distribution d'orientation et approximations de fermeture

Au regard des équations donnant l'évolution de $\mathbf{a_2}$ et des lois de comportement, il est nécessaire de connaître le tenseur d'orientation $\mathbf{a_4}$. Généralement le tenseur d'orientation $\mathbf{a_2}$ est utilisé pour représenter l'état d'orientation tandis que le tenseur $\mathbf{a_4}$ reste inconnu. Cependant l'évolution de $\mathbf{a_4}$ fait intervenir le tenseur d'orientation $\mathbf{a_6}$ (Advani & Tucker, 1987) et ce schéma se répète ainsi pour les tenseurs d'ordre supérieur. Ce problème est évité en utilisant les approximations de fermeture : elles permettent d'évaluer un tenseur d'ordre (2i+2) par un tenseur d'ordre (2i). Les relations de fermetures les plus répandues estiment $\mathbf{a_4}$ en fonction de $\mathbf{a_2}$.

2.5.1. Résolution de la fonction de distribution d'orientation

L'équation de Fokker-Planck possède des solutions analytiques uniquement pour deux cas extrêmes. Dans les cas intermédiaires, il est nécessaire de recourir à des méthodes numériques en remarquant que les temps de calcul peuvent devenir exorbitants. Si la diffusion prévaut ($C_I \rightarrow \infty$), Bird (1987b) présentent la résolution. À

l'opposé pour une diffusion nulle ($C_I = 0$), l'équation de Fokker-Planck possède une solution analytique (Dinh, 1981; Dinh & Armstrong, 1984). Le facteur de forme λ apparaissant de façon implicite, les chercheurs (Lipscomb, 1986; Lipscomb et al., 1988) expriment cette solution sous la forme :

$$\psi = \frac{1}{4\pi}\left[1 + \boldsymbol{\gamma}^{[0]} : \mathbf{pp}\right]^{-3/2}, \tag{2.27}$$

où $\boldsymbol{\gamma}^{[0]}$ est le tenseur des déformations finies et est relié à celui des gradients de déformation par $\boldsymbol{\gamma}^{[0]} = \left(\mathbf{E}^{-1}\right)^{\dagger} \cdot \mathbf{E}^{-1} - \boldsymbol{\delta}$ (Dinh & Armstrong, 1984). Ce dernier tenseur $\mathbf{E}$ satisfait l'équation différentielle suivante (Lipscomb, 1986; Lipscomb et al., 1988) :

$$\frac{D\mathbf{E}}{Dt} = \frac{1}{2}\left(-\boldsymbol{\omega} + \lambda\dot{\boldsymbol{\gamma}}\right) \cdot \mathbf{E}. \tag{2.28}$$

Pour que l'orientation initiale des fibres soit isotrope, il faut que $\mathbf{E} = \boldsymbol{\delta}$. À partir de la solution de l'équation de Fokker-Planck pour des écoulements convectifs transitoires, il est possible de déterminer les évolutions des tenseurs d'orientation. Avec une orientation initiale isotrope des fibres, les tenseurs $\mathbf{a}_2$ et $\mathbf{a}_4$ s'écrivent respectivement (Lipscomb, 1986; Lipscomb et al., 1988) :

$$\mathbf{a}_2 = \frac{1}{4\pi}\int_{\mathbf{p}} \mathbf{pp}\left[1 + \boldsymbol{\gamma}^{[0]} : \mathbf{pp}\right]^{-3/2} d\mathbf{p}, \tag{2.29}$$

$$\mathbf{a}_4 = \frac{1}{4\pi}\int_{\mathbf{p}} \mathbf{pppp}\left[1 + \boldsymbol{\gamma}^{[0]} : \mathbf{pp}\right]^{-3/2} d\mathbf{p}. \tag{2.30}$$

Dès lors pour des écoulements purement convectifs, les composantes de ces tenseurs d'orientation sont aisément calculées. Ainsi, cette procédure est à l'origine d'approximations de fermeture.

2.5.2. Approximations de fermeture basiques

L'approximation de fermeture hybride $\mathbf{a}_4^{\mathrm{Hyb}}$ (Advani & Tucker, 1990b) est largement utilisée dans les logiciels de simulation numérique puisque elle exhibe un comportement stable de l'orientation des fibres en ayant recours à peu de ressource informatique. Son expression est donnée par :

$$a_{\mathrm{ijkl}}^{\mathrm{Hyb}} = (1 - f^*)\, a_{\mathrm{ijkl}}^{\mathrm{Lin}} + f^*\, a_{\mathrm{ijkl}}^{\mathrm{Qua}}, \tag{2.31}$$

où l'approximation linéaire $\mathbf{a}_4^{\mathrm{Lin}}$ (exacte pour une configuration isotrope des fibres) est formulée par (Hand, 1962) :

$$\begin{aligned} a_{\mathrm{ijkl}}^{\mathrm{Lin}} = & -\frac{1}{35}\left(\delta_{\mathrm{ij}}\delta_{\mathrm{kl}} + \delta_{\mathrm{ik}}\delta_{\mathrm{jl}} + \delta_{\mathrm{il}}\delta_{\mathrm{jk}}\right) \\ & + \frac{1}{7}\left(a_{\mathrm{ij}}\delta_{\mathrm{kl}} + a_{\mathrm{ik}}\delta_{\mathrm{jl}} + a_{\mathrm{il}}\delta_{\mathrm{jk}} + a_{\mathrm{kl}}\delta_{\mathrm{ij}} + a_{\mathrm{jl}}\delta_{\mathrm{ik}} + a_{\mathrm{jk}}\delta_{\mathrm{il}}\right) \end{aligned}, \tag{2.32}$$

et où la relation de fermeture quadratique $\mathbf{a}_4^{\mathrm{Qua}}$ (juste pour une orientation parfaitement alignée des fibres) s'écrit (Lipscomb et al., 1988) :

$$a_{\mathrm{ijkl}}^{\mathrm{Qua}} = a_{\mathrm{ij}} a_{\mathrm{kl}}. \tag{2.33}$$

Cette approximation hybride fait intervenir la mesure scalaire de l'orientation $f^* = 1 - 27\det(\mathbf{a}_2)$. Généralement, la relation de fermeture hybride tend à surestimer l'orientation réelle des fibres (Advani & Tucker, 1990b).

2.5.3. Approximations de fermeture ajustables

Plus sophistiquées, ces relations de fermeture contiennent des paramètres ajustables qui sont définis en minimisant des solutions particulières de différents champs d'écoulement (5 à l'origine) obtenues par la résolution de ψ avec des fonctions scalaires de $\mathbf{a}_2$. Ainsi deux familles se distinguent par le choix de ces fonctions scalaires et leur jeu de paramètres : les orthotropes (Cintra & Tucker, 1995) et les naturelles (Verleye et al., 1994).

Approximations orthotropes

Cintra et Tucker (1995) sont à l'origine du développement des approximations de fermeture orthotropes $\mathbf{a}_4^{\mathrm{Ort}}$. Elles sont définies de façon à satisfaire la condition d'orthotropie du tenseur $\mathbf{a}_4$ dans le repère principal orthonormé formé par les vecteurs propres de $\mathbf{a}_2$. Dans cette base, les deux valeurs propres indépendantes de $\mathbf{a}_2$ sont notées λ_1 et λ_2 avec $\lambda_1 \geq \lambda_2$ (la somme des valeurs propres étant égale à 1). Comme chaque axe principal est un axe de symétrie pour la population de fibres, seulement six coefficients sont non nuls. Cintra et Tucker (1995) suggèrent donc d'utiliser une notation contractée : $a_{\mathrm{ijkl}}^{\mathrm{Ort}} \Leftrightarrow A_{\mathrm{mn}}$, où chaque paire d'indices est remplacée par un indice unique allant de 1 à 6 suivant le **Tableau 2.3**.

La condition de normalisation de $\mathbf{a}_4$ réduit à trois le nombre de termes indépendants (A_{11}, A_{22} et A_{33}). Afin d'exprimer A_{mn} en fonction ses valeurs propres, il est nécessaire d'avoir recours à un changement de base :

$$A_{mn} = R_{mq} Id4_{qr} A^*_{rs} R_{st}^{-1} Id4_{tn}^{-1}, \tag{2.34}$$

où **R** et **Id4** représentent respectivement la matrice contractée de rotation (ou de passage) d'un tenseur symétrique et le tenseur identité contracté d'ordre 4. Dès lors, les trois composantes A^*_{11}, A^*_{22} et A^*_{33}, exprimées dans leur repère principal, sont entièrement fonctions de leurs valeurs propres λ_1 et λ_2. En utilisant des interpolations polynomiales, les auteurs (Wetzel & Tucker, 1999; Wetzel, 1999) donnent l'expression générale pour A^*_{mm} (il n'y a pas de somme suivant m) :

$$\begin{aligned} A^*_{mm} = {} & C_m^1 + C_m^2 \lambda_1 + C_m^3 \lambda_2 + C_m^4 \lambda_1\lambda_2 + C_m^5 \lambda_1^2 + C_m^6 \lambda_2^2 \\ & + C_m^7 \lambda_1^2\lambda_2 + C_m^8 \lambda_1\lambda_2^2 + C_m^9 \lambda_1^3 + C_m^{10} \lambda_2^3 \\ & + C_m^{11} \lambda_1^2\lambda_2^2 + C_m^{12} \lambda_1^3\lambda_2 + C_m^{13} \lambda_1\lambda_2^3 + C_m^{14} \lambda_1^4 + C_m^{15} \lambda_2^4 \end{aligned} . \tag{2.35}$$

Ainsi Cintra et Tucker (1995) proposent les valeurs que doivent prendre les coefficients C_m^i pour former les approximations de fermeture ORF et ORL (obtenues par des interpolations polynomiales quadratiques). Ces relations apportent des améliorations signifiantes par rapport aux approximations précédentes mais engendrent des oscillations non physiques, notamment pour des faibles coefficients d'interaction C_I en cisaillement simple (écoulement homogène) et en écoulement radial (écoulement non homogène).

Il est à noter que tous les états d'orientation possibles des fibres sont inclus dans un triangle UTB (Cintra & Tucker, 1995) où les sommets correspondent aux états d'orientation limite tels que uniaxial (U), biaxial (B) et isotrope (T). En adoptant une interpolation polynomiale d'ordre 4 [Éq. (2.35)], VerWeyst (1998) construit l'approximation de fermeture ORT en se basant sur les travaux des chercheurs (Wetzel

& Tucker, 1999; Wetzel, 1999). L'ORT est ajustée aux résultats de la fonction de distribution ψ (avec $C_I = 0$ et $\lambda = 1$) pour une multitude de points uniformément répartis dans le triangle UTB. De plus, des contraintes imposent que la procédure de minimisation respecte les valeurs exactes aux trois états d'orientation limite. De ce fait, les oscillations observées pour ORF et ORL sont maitrisées.

Tableau 2.3 : Équivalences entre les indices des tenseurs.

m ou n	ij ou kl
1	11
2	22
3	33
4	23 ou 32
5	31 ou 13
6	12 ou 21

Une autre alternative pour réduire ces instabilités consiste à introduire des écoulements supplémentaires pour couvrir un plus vaste état d'orientation des fibres (Chung & Kwon, 2001). Les fonctionnelles de l'ORW sont les mêmes que pour les approximations ORF et ORL, tandis que l'ORW3 est basée sur une interpolation d'ordre supérieur (i.e. 3). La fermeture ORW3 est plus performante que l'approximation ORW particulièrement pour l'écoulement non homogène (Chung & Kwon, 2001).

Approximations naturelles

Les approximations naturelles établissent une relation générale pour les composantes de $\mathbf{a}_4$ en fonction du tenseur unitaire $\boldsymbol{\delta}$, du tenseur d'orientation $\mathbf{a}_2$ et ses invariants sous la forme générale (Verleye et al., 1994) :

$$a_{ijkl}^{Nat} = \beta_1\, S\left(\delta_{ij}\delta_{kl}\right) + \beta_2\, S\left(\delta_{ij}a_{kl}\right) + \beta_3\, S\left(\delta_{ij}a_{km}a_{ml}\right) + \beta_4\, S\left(a_{ij}a_{kl}\right) \\ + \beta_5\, S\left(a_{ij}a_{km}a_{ml}\right) + \beta_6\, S\left(a_{im}a_{mj}a_{kn}a_{nl}\right), \tag{2.36}$$

où l'opérateur S transforme un tenseur d'ordre 4 en un tenseur du même ordre complètement symétrique :

$$S\left(T_{ijkl}\right) = \frac{1}{24}\left(T_{ijkl} + T_{jikl} + T_{ijlk} + \ldots\right), \tag{2.37}$$

avec un total de 24 termes dans la sommation. Pour être indépendant du repère choisi (et ainsi d'éviter de calculer la matrice de passage), les coefficients β_i sont des fonctions polynomiales du 2nd et du 3ième invariant de $\mathbf{a_2}$ (a_{II} et a_{III}), le premier invariant a_I étant égal à un. Les coefficients de ces fonctions sont ajustés pour minimiser les écarts de a_{ijkl} prédits par l'approximation naturelle (NAT) et les solutions analytiques de la fonction de distribution d'orientation [Éq. (2.30)]. Cette relation de fermeture prédit de bons comportements transitoires, très similaires à ceux obtenus par l'approximation ORE, mais surestime légèrement l'état d'orientation en régimes permanents. Néanmoins, des attentions particulières sont à considérer pour le traitement des singularités générées par l'approximation naturelle (NAT) quand elle est utilisée pour des écoulements combinés (Dupret & Verleye, 1999). C'est à ce titre que la fermeture IBOF (« Invariant Based Optimal Fitting») a été proposée où la minimisation est effectuée à partir des solutions numériques de la fonction de distribution d'orientation (Chung & Kwon, 2002b).

2.5.4. Approximations de fermeture diverses

Le terme $\mathbf{a}_4 : \dot{\boldsymbol{\gamma}}$ apparaît simultanément dans l'équation d'évolution de $\mathbf{a}_2$ et dans les lois de comportement. Une alternative d'approximation de fermeture consiste donc à évaluer le tenseur d'ordre deux $\mathbf{a}_4 : \dot{\boldsymbol{\gamma}}$.

Approche de Bay (1991)

En utilisant les propriétés de $\mathbf{a}_2$ et du tenseur des taux de déformation, le chercheur (Bay, 1991) a proposé l'expression suivante basée sur les travaux de Hand (1962) :

$$\begin{aligned} a_{ijkl}\dot{\gamma}_{kl} &= a_{ij}a_{kl}\dot{\gamma}_{kl} + b_8\left|\dot{\gamma}\right|\left(\delta_{ij} - 3a_{ij}\right) - \frac{1}{2}b_2\dot{\gamma}_{ij} \\ &+ b_6\left(\frac{1}{2}\left(\dot{\gamma}_{im}a_{mn}a_{nj} + a_{im}a_{mn}\dot{\gamma}_{nj}\right) - \frac{a_{mn}a_{no}\dot{\gamma}_{om}}{a_{mn}a_{nm}}a_{im}a_{mj}\right) \end{aligned} \tag{2.38}$$

Pour un coefficient d'interaction C_I donné, les fonctions b_2, b_6 et b_8 sont ajustées avec la fonction de distribution d'orientation afin de prédire au mieux la configuration des fibres en régime permanent. Ainsi pour $10^{-4} \leq C_I \leq 10^{-1}$, Bay (1991) donne les relations pour b_2, b_6 et b_8 et montre que cette approche donne des résultats légèrement meilleurs que la fermeture hybride.

Approche de Dhont et Briels (2003)

Leur idée consiste à exprimer le terme contracté d'ordre 2, $\mathbf{a}_4 : \dot{\boldsymbol{\gamma}}$, en fonction des deux tenseurs symétriques $\dot{\boldsymbol{\gamma}}$, $\mathbf{a}_2$ et d'une combinaison de leurs invariants. Dhont et Briels (2003) utilisent une expansion polynomiale jusqu'à l'ordre 2, les ordres

supérieurs se ramenant aux premiers ordres grâce au théorème de Cayley-Hamilton. Ces fonctions dépendant des invariants sont déterminées pour des cas limites d'orientation de fibres. Ainsi pour une orientation isotrope, l'approximation linéaire permet de déterminer certaines fonctions et pour une orientation totalement alignée des fibres, l'approximation quadratique donne le reste. Dhont et Briels (2003) obtiennent alors :

$$\mathbf{a}_4 : \dot{\boldsymbol{\gamma}} = \frac{1}{5}\left(\mathbf{a}_2 \cdot \dot{\boldsymbol{\gamma}} + \dot{\boldsymbol{\gamma}} \cdot \mathbf{a}_2 - \mathbf{a}_2 \cdot \mathbf{a}_2 \cdot \dot{\boldsymbol{\gamma}} - \dot{\boldsymbol{\gamma}} \cdot \mathbf{a}_2 \cdot \mathbf{a}_2 + 2\mathbf{a}_2 \cdot \dot{\boldsymbol{\gamma}} \cdot \mathbf{a}_2 + 3\mathbf{a}_2 : \dot{\boldsymbol{\gamma}}\, \mathbf{a}_2\right). \tag{2.39}$$

Des comparaisons avec la fonction de distribution d'orientation ($C_I = 0$ et $\lambda = 1$) montrent que cette approximation est précise à environ 10 % (Dhont & Briels, 2003).

Approche thermodynamique

Currie (1982) a observé qu'un potentiel thermodynamique décrit bien le comportement des polymères tout en étant indépendant des constantes du matériau. Il exprime alors ce potentiel thermodynamique en fonction des valeurs propres du tenseur de Finger. Ainsi Malamatris et Papanastasiou (1991) montrent que l'approximation du terme contracté $\mathbf{a}_4 : \dot{\boldsymbol{\gamma}}$ donne des résultats très proches de l'équation (2.30), surtout en cisaillement.

Conclusion

Des approximations de fermeture du tenseur d'orientation $\mathbf{a}_6$ sont également disponibles dans la littérature (Altan et al., 1989). Récemment, le tenseur d'orientation $\mathbf{a}_6$ a été approximé en fonction des scalaires de $\mathbf{a}_2$ en suivant les démarches similaires aux fermetures orthotropes (Jack & Smith, 2006) ou naturelles (Jack & Smith, 2005).

Pour résumer, plusieurs stratégies sont envisageables pour dériver une approximation de fermeture. Mais comme son nom l'indique, les solutions obtenues sont plus ou moins précises.

2.6. Conclusion

Que se soit pour un fluide newtonien ou non-newtonien, l'ajout de fibres accroit considérablement leur viscosité en élongation ou en cisaillement. En outre des propriétés intrinsèques des polymères vierges, la rhéologie des composites renforcés de fibres dépendant fortement de leur fraction volumique, leur rapport de forme et leur orientation. Par rapport à la direction de l'écoulement, un alignement des fibres donne lieu à la viscosité élongationnelle la plus élevée tandis qu'une orientation des fibres à 45° génère la viscosité en cisaillement la plus importante. Pour des taux de déformation élevés, la viscosité en cisaillement ou en élongation d'un fluide rhéofluidifiant chargé de fluide tend à rejoindre celle de la matrice vierge.

Dans une optique contraire, l'élasticité d'une matrice semble inchangée par la présence des fibres, au vu des observations en cisaillement oscillatoire et en relaxation. Pourtant la première différence des contraintes normales devient non négligeable pour un fluide newtonien et augmente pour un fluide viscoélastique. Ce phénomène serait donc attribué aux interactions entre les fibres bien que l'on note une réduction du gonflement de l'extrudat en sortie de filière.

En régime transitoire, la viscosité et la première différence des contraintes normales exhibent des pics induits par l'évolution d'orientation des fibres. Le maximum pour la viscosité se situe à une déformation plus faible que celui de la première différence des contraintes normales. L'amplitude de ces pics est une fonction croissante de la concentration volumique des fibres.

La modélisation d'une suspension de fibres résulte d'un couplage entre une loi constitutive donnant la contrainte totale dans le matériau, et d'une équation décrivant l'orientation des fibres au cours de la déformation. Ces équations d'évolution ont été principalement développées pour un fluide newtonien et pour des systèmes non-concentrés. Les lois constitutives ont quant à elles suscitées plus d'intérêt pour les étendre à différents fluides (newtonien, rhéofluidifiant et viscoélastique). Dans tous les cas de figure, la modélisation d'une suspension de fibres fait également appel à des approximations de fermeture, qui génèrent implicitement des erreurs.

CHAPITRE 3 - SYNTHÈSE DES ARTICLES

Cette thèse est présentée par article, chacun faisant l'objet d'un chapitre. Les quatre sections introduisent respectivement les quatre articles.

3.1. Article 1 (Chapitre 4)

En cisaillement simple ou dynamique à de petites déformations, les propriétés rhéologiques de polymères renforcés de fibres ont suscité de nombreuses études. Leur comportement oscillatoire en grandes déformations reste peu investigué et est pourtant un phénomène rencontré dans les procédés d'injection « push-pull ». Ce mode de sollicitation est également une méthode de caractérisation et fait l'objet du premier article intitulé « Comportement rhéologique de polymères renforcés de fibres sous écoulement en cisaillement oscillatoire à de grandes déformations ».

À des amplitudes de déformation croissante, la réponse d'un matériau à une sollicitation sinusoïdale peut se mettre sous la forme d'une somme de sinusoïdes. Ainsi sur un rhéomètre à vitesse imposée (ARES), les signaux bruts du couple, de la déformation et de la force normale sont numérisés en temps réel. Une analyse de ces données permet de déterminer les fonctions matérielles telles que la contrainte en cisaillement et la première différence des contraintes normales en utilisant les caractéristiques géométriques des plaques parallèles. Dans le régime linéaire, la concentration des fibres affecte uniquement l'amplitude de la sinusoïde du couple tandis que le signal de la force normale est trop faible pour être mesuré. En augmentant la

déformation, l'amplitude du couple devient une fonction du temps. En fonction du taux de cisaillement, la contrainte en cisaillement d'un polybutène chargé de fibres s'intensifie avec le temps tandis que le comportement inverse est observé pour un polypropylène renforcé (matrice viscoélastique). Ces effets sont plus prononcés pour des fortes concentrations de fibre. De plus, la première différence des contraintes normales ne devient plus négligeable et manifeste une réponse périodique non sinusoïdale. Une analyse par les transformées de Fourier est effectuée. Le spectre résultant de même que les figures de Lissajous des contraintes en cisaillement et des premières différences de contraintes normales sont expliqués en fonction de l'orientation des fibres. Finalement, le modèle de Folgar-Tucker-Lipscomb (FTL) prédit correctement les résultats expérimentaux des suspensions à base de polybutène.

3.2. Article 2 (Chapitre 5)

Au cours de la mise en forme d'un polymère fondu renforcé de fibres, le matériel est principalement soumis à des contraintes en cisaillement et en élongation. La première ayant déjà fait l'objet de nombreuses publications dans la littérature, son comportement en élongation reste néanmoins inusité à cause des difficultés expérimentales rencontrées pour générer ce type d'écoulement. C'est sur ce dernier type de sollicitation que le second article, intitulé « Étude sur les propriétés rhéologiques de polypropylènes chargés de fibres courtes en écoulement élongationnel », porte attention.

Le comportement en écoulement élongationnel de fibres de verre courtes en suspension dans un polypropylène a été étudié en utilisant trois instruments différents :

une géométrie basée sur un mécanisme de tambours (Système de Rhéologie Extensionnel) et montée sur un rhéomètre rotationnel à déformation imposée, un rhéomètre de Meissner (ou RME qui est la version commerciale chez Rheometric Scientific) et un Rheotens. De plus, les résultats des essais en tension uniaxiale sont comparés avec des données préalablement obtenues en utilisant l'entrée convergente d'une filière hyperbolique. Les effets de trois orientations initiales des fibres ont été investigués : aléatoire dans un plan, parfaitement aligné et perpendiculaire à la direction d'étirement. Pour les expériences avec le Rheotens, les conséquences d'un pré-cisaillement sur le comportement élongationnel a été étudié. Une augmentation de la viscosité élongationnelle avec l'accroissement de la fraction volumique des fibres a été observée. De plus, l'orientation des fibres en fonction de la direction de l'écoulement affecte la viscosité élongationnelle des composites : plus les fibres sont orientées, plus la viscosité est importante. Le comportement à de faibles taux d'élongation montre des différences parmi les divers systèmes expérimentaux, ce qui est en partie expliqué par l'histoire du pré-cisaillement des échantillons et des taux de déformation non homogènes. Cependant à des taux d'élongation modérés et élevés, les résultats sont comparables et le comportement devient rhéofluidifiant. Finalement une nouvelle équation constitutive pour des fibres en suspension dans un fluide obéissant au modèle de Carreau est utilisée pour prédire la viscosité élongationnelle et démontre de bons accords avec les données expérimentales.

3.3. Article 3 (Chapitre 6)

La prédiction des modèles pour déterminer l'orientation des fibres fait appel aux approximations de fermeture afin d'estimer le tenseur d'orientation d'ordre quatre $\mathbf{a}_4$. Ce point de vue de description est moins précis que celui de la fonction de distribution d'orientation mais permet d'économiser du temps de calcul. Le but de l'article 3, titré « Amélioration de la résolution numérique de la fonction de probabilité d'orientation : Application au modèle de Folgar-Tucker-Lipscomb » est de proposer une méthode de résolution numérique de la fonction de distribution d'orientation qui puisse réduire ces temps de calcul. De plus, cela permettra de lever l'ambiguïté induite par l'emploi des relations de fermeture.

La fonction de probabilité d'orientation a été résolue numériquement par la méthode des volumes finis. Différents schémas temporels et spatiaux ont été testés pour réduire considérablement le temps de calcul et pour couvrir une large gamme de nombres de Péclet (Pe). Pour Pe $\leq$ 1000, les résultats sont comparés avec des données disponibles dans la littérature et pour Pe $\geq$ 1000, ils sont confrontés à une solution analytique. Les accords sont très bons et nous permettent ainsi de suivre l'évolution des composantes d'intérêt de $\mathbf{a}_4$ en cisaillement simple pour des écoulements aller et retour, et de les comparer avec celle prédite par l'approximation de fermeture ORW3. Finalement, le modèle de Folgar-Tucker-Lipscomb est utilisé pour prédire le comportement rhéologique d'un polypropylène chargé de fibres courtes en cisaillement simple. Aucune approximation n'a été employée. L'exactitude des approximations de

fermeture habituellement employées est discutée, et les points clés du modèle de Folgar-Tucker-Lipscomb sont mis en avant dans le but d'améliorer les prédictions du comportement des suspensions de fibres.

3.4. Article 4 (Chapitre 7)

Les travaux précédents ont permis de mettre en évidence que les modèles de Folgar-Tucker-Lipscomb (FTL) ou de Dinh et Armstrong (DA) prédisent qualitativement l'ensemble des résultats observés par des mesures expérimentales sur des suspensions de fibres. Néanmoins, des divergences perdurent et sont attribuées aux interactions entre les fibres. C'est à ce titre que l'article quatre, intitulé « Modélisation de l'interaction des fibres pour des suspensions non diluées de fibres », présente un modèle rhéologique basé sur les travaux de Dinh et Armstrong qui prend en compte une description plus précise et plus physique des interactions fibre-fibre.

Un jeu d'équations rhéologiques a été développé pour des suspensions non diluées de fibres rigides dans un fluide newtonien en prenant en compte les interactions hydrodynamiques et fibre-fibre. La force générée par les interactions des fibres est modélisée en utilisant un coefficient de friction hydrodynamique linéaire proportionnel à la vitesse relative des deux fibres au point de contact, et est ensuite pondérée par la probabilité que ce contact ait lieu. L'équation d'évolution du tenseur d'orientation d'ordre deux, composée de termes convectif et diffusif causé par les interactions des fibres, est dérivée pour prédire l'orientation des fibres sous écoulement. Le bien connu tenseur d'orientation d'ordre quatre, relié à la contribution hydrodynamique, et un

tenseur d'interaction d'ordre quatre, proposé dans cet article, sont utilisés pour déterminer la contrainte totale dans le composite. Des approximations de fermeture linéaire et quadratique ont été formulées pour décrire le tenseur d'interaction du quatrième ordre. Les résultats sont présentés en utilisant la forme quadratique qui a été trouvée plus précise que la relation linéaire. Le modèle décrit correctement l'évolution de la viscosité et de la différence de contraintes normales dans un écoulement retour en cisaillement simple. De plus, l'orientation des fibres et le nombre moyen de contacts par fibre sont prédits. Le nouveau coefficient d'interaction proposé varie avec l'orientation des fibres, ce qui semble réaliste.

CHAPITRE 4 - ARTICLE: RHEOLOGICAL BEHAVIOR OF FIBER-FILLED POLYMERS UNDER LARGE AMPLITUDE OSCILLATORY SHEAR FLOW*

J. Férec [a, b], M.C. Heuzey [a], G. Ausias [b] and P.J. Carreau [a]

[a] *Center for Applied Research on Polymers and Composites (CREPEC), Chemical Engineering Department, École Polytechnique de Montréal, PO Box 6079, Stn Centre-Ville, Montreal, QC, Canada H3C3A7*

[b] *Laboratoire d'Ingénierie des MATériaux de Bretagne (LIMATB) Université de Bretagne Sud, rue de St Maudé, 56325 Lorient, France*

Abstract

Small and large amplitude oscillatory shear measurements (SAOS and LAOS) were used to investigate the rheological behavior of short glass fibers suspended in polybutene and molten polypropylene. Raw torque and normal force signals obtained from a strain controlled instrument (ARES rheometer) were digitized using an ADC (Analog to Digital Converter) card to allow more precise data analysis. The fiber concentration did not affect the torque signal in the SAOS mode, except for its magnitude, whereas the normal force signal was too low to be measurable. With increasing strain amplitude, the magnitude of the torque became a function of time. Depending on the applied frequency and strain rate, the stress in the filled polybutene increased with time, whereas for reinforced polypropylene (viscoelastic matrix), the behavior was opposite, i.e. the stress decreased with time. These effects were more

---

* Cet article a été accepté au Journal of Non-Newtonian Fluid Mechanics.

pronounced at high fiber content. In addition the primary normal stress differences were no longer negligible at large deformation amplitude and exhibited a non-sinusoidal periodic response. Fast Fourier-transform (FFT) analysis was performed and the resulting spectra, along with Lissajous figures of the shear stress and the primary normal stress differences, are explained in terms of fiber orientation. The experimental results for the suspensions in polybutene are well predicted by the Folgar-Tucker-Lipscomb (FTL) model.

4.1. Introduction

Composite materials are now widely present in the manufacturing industry, especially those involving short glass fibers suspended in thermoplastic matrices. Adding these fibers enhance considerably the physical properties of the products, without requiring any substantial modifications of the processing machines. Improvements are strongly related to the internal structure characterized by the fiber orientation and dispersion. The bulk rheological properties of fiber suspensions are functions of the filler as well as the matrix, and knowledge of these properties is important to determine the internal structure. The rheological behavior of filled systems is generally quite complex, and the relationships between the fiber at the microstructural level and the macroscopic properties are still not fully understood.

Oscillatory shear experiments are commonly used to investigate polymeric viscoelastic properties in order to have insight of the microstructure (Ferry, 1980). Numerous studies have been performed on the rheological behavior of filled polymers, which manifest remarkable non linear viscoelasticity even at very low deformation amplitude. Generally the addition of a filler increases the storage and loss moduli of the neat resin kitano (Greene & Wilkes, 1995; Kitano et al., 1984a; Mobuchon et al., 2005; Mutel & Kamal, 1986), especially when the fiber aspect ratio (length/diameter) is large (Kitano et al., 1984a). Greene and Wilkes (1995) demonstrated that the elastic modulus G' increases more than the loss modulus G'' at low frequencies and less at higher frequencies, a behavior also observed by Kitano et al. (1984a). On the other hand,

Mobuchon et al. (2005) showed that from the examination of the loss angle (δ), the matrix elasticity was unchanged by the presence of the fibers and this has been confirmed by several authors (Laun, 1984; Sepehr et al., 2004d; Zirnsak et al., 1994). On their part, Zirnsak et al. (1994) have related a normal stress enhancement to fiber-fiber interactions, which induce an anisotropic fiber orientation. By performing stress relaxation experiments, Sepehr et al. (2004d) observed that the elasticity of their suspensions was that of the matrix. Numerous investigations report no yield stress for short fiber filled polymers (Chan et al., 1978; Kitano et al., 1980; Kitano et al., 1984b; Mobuchon et al., 2005), which is not the case for long fibers (Servais & Manson, 1999; Thomasset et al., 2005). Finally, the Cox-Merz rule does not generally apply to fiber suspensions, as noted by Kitano et al. (1984a) and Mobuchon et al. (2005). This has been explained by a different fiber orientation induced during simple shear flow (Mobuchon et al., 2005).

In terms of pre-shearing effects, Onogi et al. (1977) reported an increase of G' and G'' for titanate fibers suspended in a polystyrene solution, and related this effect to a structure re-formation following pre-shearing. Mobuchon et al. (2005) also looked at the effect of pre-shearing in the case of a 30 wt % short glass fiber reinforced polypropylene. Creep tests were performed under two different stresses before carrying out frequency sweep tests, and they observed that the complex viscosity decreased with increasing stress values due to strong fiber alignment during the pre-shearing.

Kim and Song (1997) investigated the influence of time, frequency and strain amplitude on the dynamic moduli of a short glass fiber reinforced polystyrene. At a constant angular frequency, they found that the complex viscosity for a deformation of 0.3 dropped more rapidly than for a deformation of 0.02. They explained this behavior by assuming that more fibers were aligned in the flow direction. A similar phenomenon has been observed for block copolymers containing lamellar micro-domains (Gupta et al., 1996). Kim and Song (1997) also looked at the effect of pre-shearing in oscillatory mode at a constant strain amplitude. They noticed that the initial value of the complex viscosity was not recovered and was smaller for the larger pre-oscillatory frequency. Furthermore, Kim and Song (1997) performed subsequent frequency sweeps and showed that the complex viscosity decreased to reach a constant value at low frequency. They concluded that the fiber orientation induced a drop of the complex viscosity, especially at high fiber content. This hypothesis has been confirmed by the results of Harlen and Koch (1997) who have modeled the small amplitude oscillatory shear flow of fibers suspended in an Oldroyd-B fluid, and predicted a slow orientation of the fibers in the flow direction. Petrich et al. (2000b) also confirmed these findings through experiments on cellulose acetate propionate filaments and carbon fibers suspended in a Boger fluid.

Large amplitude oscillatory shear (LAOS) flow is particularly helpful to investigate complex fluids that exhibit microstructures that depend on the deformation history. Increasing the deformation in oscillatory shear flow increases the non-linear

properties of filled polymers, and in the non-linear viscoelastic region, the stress response is no longer harmonic (Giacomin & Dealy, 1993). Using a sliding plate rheometer, Ericsson et al. (1997) have investigated the dynamic properties of a glass fiber-filled polypropylene. They showed that the loops of the shear stress vs. shear rate, or Lissajous curves, became skewed for an applied strain of 0.1, indicating the presence of higher harmonics. Mutel and Kamal (1986) have characterized the behavior of a 10 wt % fiber filled polypropylene under oscillatory shear flow using parallel plates in rotational flow. Even if at low deformation the loss and storage moduli exhibited strong strain dependence, they found that the stress response presented no higher harmonics. By increasing the fiber concentration up to 40 wt %, Mutel (1989) observed a slight third harmonic for a strain amplitude of 2.1.

It is also possible to measure the normal stress differences for large amplitude oscillatory shear flow, as done by Endo and Nagasawa (1970) for concentrated polystyrene solutions in chlorinated diphenyl. They showed that the normal stress differences oscillated at twice the applied frequency, as predicted by the theory on elastic liquids (Lodge, 1964).

The overall objective of this work is to investigate the effect of fiber orientation on the rheological behavior of two short glass fiber suspensions under large amplitude oscillatory shear flow. The first suspension is based on a Newtonian polybutene matrix (PB), whereas the second one is polypropylene (PP)-based. Results are mainly presented using Lissajous figures, while Fast Fourier Transforms (FFT) are also performed to

analyze the material responses. Furthermore, the time-dependent behavior of the polybutene composites is compared to predictions of the Folgar-Tucker-Lipscomb (FTL) model.

4.2. Experimental

4.2.1. Materials

The first type of suspensions is a model system composed of a polybutene matrix (PB0, Stanchem Indopol H100), while the second one is a commercial composite based on a polypropylene matrix (PP0, Basell Hostacom). The polypropylene composites were provided by Basell with, respectively, 10 (PP10) and 30 (PP30) wt % of glass fibers, which corresponds to 3.3 and 11.5 in terms of vol %, respectively. To prepare the samples required for rheometry, the polypropylenes were blended in an internal mixer (Brabender) with 1 wt % of stabilizer (Irganox B225) in order to reduce thermal degradation (Sepehr et al., 2004c). As a consequence of this blending, some fiber breakage occurred and the final average length was L = 320 μm, while the polydispersity (weight average over number average, $\bar{L}_w / \bar{L}_n$) was 1.16 (for measurements over 500 fibers using an optical microscope). The aspect ratio r, defined by L/D, was equal to 20 (diameter D = 16 μm). For the PP composites, all tests were performed at a temperature of 200 °C under a nitrogen atmosphere.

At the test temperature of 20 °C, the polybutene matrix (PB0) has a constant viscosity of η_0 = 37 Pa·s. The glass fibers to be incorporated to the PB-based composites

were obtained from the calcination at 600 °C for 40 min of the 30 wt % filled polypropylene (PP30) sample in order to keep the same fiber aspect ratio for both matrices. The PB composites were prepared by incorporating the appropriate fiber content into the polybutene and the suspensions were gently hand-mixed in order to achieve proper wetting of the fibers and to avoid further fiber breakage. Two composites materials were prepared with 10 and 20 wt % of fibers (PB10 and PB20), or 3.8 and 8.1 vol %, respectively. Noting that the polybutene matrix density is ρ_{PB0} = 880 kg/m^3, whereas the fiber density is ρ_f = 2500 kg/m^3, it was important to prevent fiber sedimentation and to homogenize the PB-based suspensions prior to rheological measurements. For this purpose the suspensions were periodically hand mixed and stored under vacuum to remove rapidly the air bubbles introduced during mixing. According to the definition of the fiber concentration regimes(Doi & Edwards, 1978a), PP10 and PB10 were semi-dilute with $1/r^2 << \phi << 1/r$, while PP30 and PB20 were concentrated with $\phi > 1/r$.

4.2.2. Rheometry

Measurements of viscoelastic properties were carried out using two different rotational rheometers (TA-Instruments ARES and Anton Paar Physica MCR 501) using parallel plates. This geometry is advantageous for particle suspensions measurements since the gap can be set to be larger than the fiber length. The parallel plates used had a diameter of 25 mm for the polypropylene and 50 mm for the polybutene composites, respectively, as done in previous studies (Sepehr et al., 2004c; Sepehr et al., 2004d). The

preparation of PP samples of a diameter of 50 mm for rheometric measurements presented experimental difficulties, while using 25 mm plates for the PB samples did not provide good response signals in the measurements. For all experiments, the gap H was set to 1.5 mm, which provided a maximum deformation of 4.3 and 8.3 depending on the geometry used ($\gamma_R = R\theta_{max} / H$). This allowed the gap to fiber length ratio to be larger than 3 (Attanasio et al., 1972).

The strain controlled rheometer (ARES) was used to perform the LAOS measurements and allowed a maximum amplitude deformation of θ_{max} = 0.5 rad. This rheometer is equipped with a standard 2KFRTN1 force transducer, which can measure a maximum torque of 200 mN·m and a maximal normal force of 20 N (as specified by the manufacturer). The raw data, collected from the signal panel, were digitized using a 12-bit 16 channel USB-based Analog to Digital Converter (ADC) with a 100 ksamples/s rate (National Instruments DAQ-Pad 6020E). This ADC card was plugged into the ARES computer that contains a home-written LabView routine to handle the raw data. Three channels were used to sample simultaneously the strain, the torque and the normal force. For all tests, the scan rate was fixed to 10000 data per second and then averages for each 1000 data were used to generate 10 average values per second. To reduce the mechanical and electronical noises, the rheometer was placed on a stable environmental table and the connections made with double shielded BNC cables. Oscillatory time sweep tests were performed up to 2500 s. For the systems based on polybutene, the strain amplitude varied from 0.1 to 7 under three different frequencies (0.01, 0.1 and 1

Hz), while smaller deformations (0.1 to 3) were used for the polypropylene composites at two frequencies (0.005 and 0.01 Hz).

From Carreau et al. (1997), the torque T and the normal force F_z that the fluid exerts on the upper disk are expressed, respectively, by:

$$T = 2\pi \int_0^R \sigma_{z\theta}(r)\, r^2 dr, \tag{4.1}$$

$$F_z = \pi \int_0^R \left[N_1(r) - N_2(r) \right] r\, dr, \tag{4.2}$$

where $\sigma_{z\theta}(r)$ is the shear stress, and $N_1(r)$ and $N_2(r)$ are respectively the primary and secondary normal stress differences evaluated at the radial position r. In the following development, the Weissenberg hypothesis is used, i.e. N_2 is assumed to be negligible. To compare experimental results for the shear stress, $\sigma_{z\theta}$, and the primary normal stress differences, N_1, with the model predictions, these quantities have to be evaluated in a similar manner. From Carreau et al. (1997), the two materials functions are related to the torque and the normal force, respectively, by:

$$\sigma_{z\theta} = \eta(\dot{\gamma}_R)\dot{\gamma}_R = \frac{T}{2\pi R^3}\left[3 + \frac{d\ln\left(\frac{T}{2\pi R^3}\right)}{d\ln\dot{\gamma}_R} \right], \tag{4.3}$$

$$N_1 = -\frac{2F_z}{\pi R^2}\left(1 + \frac{1}{2}\frac{d\ln F_z}{d\ln\dot{\gamma}_R} \right). \tag{4.4}$$

To calculate the experimental shear stress and the primary normal stress differences, the derivatives in Eqs. (4.3) and (4.4) were obtained by plotting ln $T/2\pi R^3$ versus $\ln\dot{\gamma}_R$ and ln F_z versus $\ln\dot{\gamma}_R$, respectively, for the various suspensions. It is worth

mentioning that these expressions were developed for steady shear flow, while no analytical solution exits for large amplitude oscillatory shear flow. Therefore, Eqs. (4.3) and (4.4) were used as approximations in the case of LAOS. For the model predictions, macroscopic quantities were calculated from the shear stress component $\sigma_{z\theta}(r)$, the $\theta\theta$-component $\sigma_{\theta\theta}(r)$ and the zz-component $\sigma_{zz}(r)$ of the total stress tensor, combining expressions (4.1) and (4.2) with Eqs. (4.3) and (4.4), to provide the simulated stress σ^{sim} and primary normal stress differences N_1^{sim}:

$$\sigma^{\text{sim}} = \left[3 + \frac{d \ln\left(\dfrac{T}{2\pi R^3}\right)}{d \ln \dot{\gamma}_R} \right] \frac{1}{R^3} \int_0^R \sigma_{z\theta}(r)\, r^2 dr, \tag{4.5}$$

$$N_1^{\text{sim}} = \left(1 + \frac{1}{2} \frac{d \ln F_z}{d \ln \dot{\gamma}_R} \right) \frac{2}{R^2} \int_0^R \left[\sigma_{\theta\theta}(r) - \sigma_{zz}(r) \right] r\, dr. \tag{4.6}$$

Finally, the possible impact of fluid inertia and viscous dissipation was assessed. In rotational shear flow, the complex Reynolds number Re^* is used to measure the influence of the fluid inertia and is given by (Yosick et al., 1998): $Re^* = 2\pi\rho f H^2 / \eta^*$, where ρ is the fluid density, f is the applied frequency and η^* the complex viscosity of the matrix. The largest calculated value of Re^* was for the PB20 system and was about 3.9×10^{-4}. Since Re^* was much smaller than 1, all the suspensions were considered inertialess. Furthermore, the criterion suggested by Giacomin and Dealy (1993) to investigate the effect of fluid inertia on the oscillatory shear velocity profile was verified. Inertia is negligible for a gap $H < \lambda_s / 40$, where the shear wavelength λ_s is

given by $\lambda_s = \sqrt{\rho\,\gamma_R} / f\sqrt{\sigma_1}\cos\left(\frac{\delta_1}{2}\right)$ and σ_1 and δ_1 are the fundamental harmonic amplitude of the shear stress and phase delay, respectively. In our case this approach indicated again negligible inertia for both systems. The effect of viscous dissipation that can result in a temperature increase and impact the viscosity, or in the worst case cause thermal degradation, was also verified for the polypropylene matrix. A LAOS test was performed at 200 °C under a strain deformation of 3 and a frequency of 0.005 Hz for 1500 s, then followed by a rest time of 600 s and subsequently the same LAOS test was conducted. No noticeable decrease of the shear stress and primary normal stress differences was observed, ruling out the effect of viscous dissipation for these tests.

4.3. Modeling

4.3.1. Orientation tensors

The modeling approach used in this work considers all fibers to be straight circular cylinders with uniform length and diameter, and a fiber aspect ratio $r >> 1$, and hence the influence of the fiber ends is neglected. The suspensions are further assumed to be homogeneously dispersed in the volume. Fiber orientation can be described by a unit orientation vector **p** parallel to the main axis of the fiber, while for a fiber population a statistical orientation distribution function $\psi(\mathbf{p})$ is used to describe the average state of orientation in a fluid element. Second- and fourth-order orientation tensors have been defined by Advani and Tucker (1987):

$$\mathbf{a}_2 = \int_{\mathbf{p}} \mathbf{pp}\psi(\mathbf{p})d\mathbf{p}, \tag{4.7}$$

$$\mathbf{a}_4 = \int_{\mathbf{p}} \mathbf{pppp}\psi(\mathbf{p})d\mathbf{p}, \tag{4.8}$$

where $\mathbf{a_2}$ is a positive and symmetric tensor with a constant trace equal to one, which states that the fiber length does not change under flow. Higher is the orientation tensor order, more precise is the fiber orientation state description (Advani & Tucker, 1987).

4.3.2. Fiber motion

The time derivative (D/Dt) of $\mathbf{a_2}$ can be obtained from the expression of $\mathbf{p}$ established by Jeffery (1922) for ellipsoids from prolate to oblate forms in the dilute state. For non-dilute suspensions interactions between particles may occur, and Folgar and Tucker (1984) have taken into account a randomizing effect of interactions by adding a diffusion term to the Jeffery equation. For particles suspended in a Newtonian fluid and at low Reynolds number, one obtains:

$$\dot{\mathbf{a}}_2 = \frac{D\mathbf{a}_2}{Dt} = -\frac{1}{2}(\boldsymbol{\omega}\cdot\mathbf{a}_2 - \mathbf{a}_2\cdot\boldsymbol{\omega}) + \frac{\lambda}{2}(\dot{\boldsymbol{\gamma}}\cdot\mathbf{a}_2 + \mathbf{a}_2\cdot\dot{\boldsymbol{\gamma}} - 2\dot{\boldsymbol{\gamma}}:\mathbf{a}_4) + 2C_I|\dot{\gamma}|(\boldsymbol{\delta} - 3\mathbf{a}_2), \tag{4.9}$$

where $|\dot{\gamma}| = \sqrt{\frac{1}{2}\dot{\boldsymbol{\gamma}}:\dot{\boldsymbol{\gamma}}}$ is the generalized deformation rate, $\boldsymbol{\delta}$ is the identity tensor and $\lambda = (r^2-1)/(r^2+1)$ is the form factor. For large aspect ratio prolate spheroids (or rod-like), λ tends towards 1, whereas for large aspect ratio oblate spheroids (or disked-shaped), λ tends towards -1. The quantities $\dot{\boldsymbol{\gamma}}$ and $\boldsymbol{\omega}$ are the rate of strain and vorticity tensors defined, respectively, by $\dot{\boldsymbol{\gamma}} = \boldsymbol{\kappa} + \boldsymbol{\kappa}^{\dagger}$ and $\boldsymbol{\omega} = \boldsymbol{\kappa} - \boldsymbol{\kappa}^{\dagger}$, where $\boldsymbol{\kappa}^{\dagger}$ is the velocity gradient tensor. If interactions between neighboring fibers are neglected, the interaction

coefficient C_I in Eq. (4.9) is equal to zero and the case of dilute suspensions is recovered.

4.3.3. Constitutive equation

A general constitutive equation for dilute axisymmetric particles suspended in a Newtonian fluid has been proposed by Lipscomb et al. (1988), who have derived it following the work of Jeffery (1922), Hand (1961) and Giesekus (1962). The expression is as follows:

$$\boldsymbol{\sigma} = -P\boldsymbol{\delta} + \eta_0\dot{\boldsymbol{\gamma}} + \eta_0\phi\left[A\mathbf{a}_4 : \dot{\boldsymbol{\gamma}} + B\left(\mathbf{a}_2 \cdot \dot{\boldsymbol{\gamma}} + \dot{\boldsymbol{\gamma}} \cdot \mathbf{a}_2\right) + C\dot{\boldsymbol{\gamma}} + 2F\mathbf{a}_2 D_r\right], \tag{4.10}$$

where P is the hydrostatic pressure, η_0 the Newtonian fluid viscosity, ϕ the volume fraction of particles and A, B, C and F are material parameters. D_r is the rotary diffusion coefficient related to the Brownian motion of the particles. Given that glass fibers are not subjected to Brownian motion (Chaouche & Koch, 2001), the term containing F is equal to zero. In their paper, Lipscomb et al. (1988) have presented the specific material coefficients for prolate to oblate spheroids (see also Sepehr et al. (2004c) for an interesting review of the many expressions attributed to these material coefficients). Lipscomb et al. (1988) found that for ellipsoids of large aspect ratio the geometric shape factors $A = r^2 / 2\ln(r)$, $B = 0$ and $C = 2$. For our model simulations the coefficients B and F were therefore neglected, C was fixed to 2 and the coupling and interaction coefficients A [Eq. (4.10)] and C_I [Eq. (4.9)] were used as fitting parameters, as done by Sepehr et al. (2004c).

4.3.4. Closure approximations

The set of governing equations consisting of Eqs. (4.9) and (4.10) is not totally complete as a relationship to evaluate $\mathbf{a_4}$ from $\mathbf{a_2}$, or closure approximation, is required. The early closure approximations proposed were the linear (Hand, 1961) and quadratic ones (Doi & Edwards, 1986), which are exact for random and perfectly aligned fiber orientations, respectively. Advani and Tucker (1990a) have combined them to propose the hybrid closure. Better accuracy is, however, obtained using natural (Verleye et al., 1994) and orthotropic closure approximations (Cintra & Tucker, 1995). The latter has been improved by Chung and Kwon (2001), who optimized the fit by using a 2nd order polynomial expansion of the two largest eigenvalues of $\mathbf{a_2}$. In our simulations, the ORW closure (Orthotropic fitted closure approximation for a Wide range of C_I) has been applied (Chung & Kwon, 2001).

4.4. Results and discussion

4.4.1. Preliminary tests

The first step of this work was to evaluate the two derivatives present in Eqs. (4.3) and (4.4) in order to get the correct rheological properties. For the systems based on polybutene these two derivatives are equal to 1. **Figure 4.1** shows $\ln\left(T/2\pi R^3\right)$ and $\ln F_z$ as functions of $\ln\dot{\gamma}_R$ for the neat polypropylene and its composites. Due to the shear thinning of the matrix, different slopes are necessary to describe properly the molten polymer behavior. The calculated slopes are ≤ 1 for the torque and ≤ 2 for the

normal force, with 1 and 2 being the values used by the rheometer software package. The correct values of the derivatives applied to evaluate the shear stress and the primary normal stress differences in Eqs. (4.3) and (4.4) are chosen according to the root mean square shear rate $\dot{\gamma}_{\mathrm{RMS}}$, which is defined as $\dot{\gamma}_{\mathrm{RMS}} = \sqrt{\frac{1}{T_{\mathrm{osc}}}\int_0^{T_{\mathrm{osc}}} \dot{\gamma}^2(t)\,dt} = \frac{\dot{\gamma}_R}{\sqrt{2}}$, where T_{OSC} is the input signal period. The quantity $\dot{\gamma}_{\mathrm{RMS}}$ is found to be more appropriate than the maximum shear rate $\dot{\gamma}_R$ evaluated at the rim of the parallel plates.

Figure 4.2 reports the complex viscosity as a function of deformation at different frequencies for the polybutene systems. Before the strain sweep test, the filled sample was pre-sheared at 10 s^{-1} for 1000 s in order to align the fibers in the flow direction (Sepehr et al., 2004d). As expected the neat polybutene exhibits a constant viscosity, while PB20 shows a strain hardening behavior more pronounced as the applied frequency decreases. This is attributed to a fiber re-orientation effect, from a pre-aligned state to a more disorganized structure due to the oscillatory flow, as will be shown later from the model predictions. As the strain gets very large the complex viscosity decreases, indicating that the fiber structure breaks down. It can also be seen that the lower is the applied frequency, the lower is the strain at which the fiber re-orientation process occurs.

In **Figure 4.3**, the complex viscosity of PP0 and PP30 as function of the applied strain is presented. No strain hardening is observed for the polypropylene and its 30 % composite. At higher frequency, the shear-thinning behavior is more pronounced and η^*

is found to be a strong function of the deformation amplitude even at small strain. This strain-dependence reflects a non-linear behavior and, therefore, non harmonic stress responses are expected. In contrast to the filled polybutene, the fiber reinforced polypropylene exhibits no strain overshoot, possibly indicating that the fiber rearrangement is not as important as in the case of the PB systems because of the high viscosity of the matrix and the lower strain used. The fiber rearrangement may also be hidden by the shear-thinning phenomenon. According to Hyun et al. (2002), the suspensions based on polybutene are of type III (weak strain overshoot), whereas the polypropylenes are of type I (strain thinning).

4.4.2. Polybutene suspensions in LAOS

To detect departures from linearity, we examined the Lissajous curves of $\sigma_{z\theta}$ and N_1 vs. γ_R. When the stress-strain loops are plotted, an ellipse should be obtained if the signal response is harmonic. **Figure 4.4** reports the shear stress in LAOS as a function of strain for an applied frequency of 0.1 Hz at various cycles (2nd, 125th and 250th) for PB0 and PB20. As shown in **Figure 4.4a** and as expected, the Lissajous curves (shear stress vs. strain) for PB0 are not functions of time even at large deformation, up to 7 in magnitude. On the contrary, the Lissajous curves for PB20 change with time (as indicated by the arrow in **Figure 4.4b**) until a regular shape is obtained after 250 cycles. The evolution of the shear stress is due to fiber orientation, as these samples have not been pre-sheared and as will be shown by the model predictions. At large strain amplitude, the sinusoidal stress responses of both samples remain linear with strain.

Wang et al. (2001) have reported a similar behavior for cheddar and mozzarella in LAOS, and have called it the "large strain linear regime".

The measured primary normal stress differences of PB20 are reported in **Figure 4.5** for $\gamma_R = 7$ and for samples that were not preconditioned. The normal stress signal for PB0 was too weak to be measured (values smaller than the transducer minimum) and this is indicative that the polybutene is almost inelastic as shown by Sepehr et al. (2004d). However, the presence of fibers introduces some linearity for the polybutene system. The effect of fiber addition on N_1 is illustrated in **Figure 4.5**, showing that the normal stress-strain loops exhibit a butterfly-wing-like shape. Nevertheless, in the presence of fibers the principal axis of the ellipses is always parallel to the deformation axis. It means that the phase angle remains close to 90°, suggesting that fibers have no effect on the elasticity. This has been confirmed by Sepehr et al. (2004d), who observed that the elasticity of the suspensions was the same as that of the matrix. Zirnsak et al. (1994) have related the normal stress enhancement to fiber-fiber interactions, which induce an anisotropic fiber orientation. In addition, fiber orientation causes an increase of the primary normal stress amplitude (as indicated by the arrow in **Figure 4.5**). Although the normal stress average has a positive offset, some negative values are observed just after the flow is reversed. This is coherent with observations of Sepehr et al. (2004d) who performed consecutive stress growth experiments in clockwise and counter-clockwise directions for similar model suspensions. Immediately after steady state was reached in the clockwise direction, flow reversal resulted in the normal stress differences exhibiting negative values at first, followed by positive values until reaching

the same steady state as in the clockwise direction. This was attributed to a crystalline type of structure induced by flow, and we believe that the same phenomenon is illustrated in **Figure 4.5** although the flow field is more complex than in the stress growth experiments.

Fast Fourier Transform (FFT) of the shear stress and primary normal stress difference signals between the 200th and the 250th cycle has been performed. The relative intensity of the primary normal stress differences is normalized by the maximum value, i.e. that of the second harmonic. The PB0 and PB20 shear stress responses were found to be harmonic (results not shown), confirming the elliptic shape of the Lissajous curves of **Figure 4.4**. It implies that up to a deformation of 7 at 0.1 Hz, the Lissajous curves for the shear stress were nearly independent of strain. In the case of N_1, the experimental data were shifted to zero before performing the FFT analysis in order to remove the peak introduced by the nonzero positive constant value. The FFT results for the PB20 normal stress are depicted in **Figure 4.6**. With the addition of fibers, the normal stress differences oscillate at twice the applied frequency (i.e. 0.2 Hz), as predicted by the Lodge theory on rubber-like liquids (Lodge, 1964) and observed for commercial polystyrene (Endo & Nagasawa, 1970). Nevertheless, a slight non harmonicity is noticed at 0.4 Hz. In addition, the anisotropy of the fiber orientation results in a non negligible signal response at 0.1 Hz (for low fiber content, i.e. 10 wt %, we also noted a response at 0.1 Hz). This fundamental harmonic in the N_1 spectrum may be explained by time-dependent memory effects (Manfred et al., 1998), i.e. due to fiber rotation, which is not perfectly reversible at short times (Sepehr et al., 2004d). The simultaneous presence of

the first and second harmonics explains the butterfly wing-like slight dissymmetry shown in **Figure 4.5**.

Sample PB20 was also pre-sheared at 10 s^{-1} during 1000 s before performing a LAOS test. The primary normal stress differences during some of the first cycles (2nd, 6th and 14th) are illustrated in **Figure 4.7**. While in the 2nd cycle the Lissajous curve is nearly elliptic, a well-defined butterfly wings-like shape is obtained towards the 14th cycle as expected for a second-order fluid (Endo & Nagasawa, 1970). This behavior is explained by the fact that most of the fibers which are initially aligned along the shear flow direction get disoriented by the LAOS test, therefore inducing a more isotropic structure. Furthermore, the normal stress response becomes symmetric with respect to the deformation axis. Hence, we suggest that this symmetry is characteristic of fiber orientations that are symmetric with respect to the flow direction in LAOS tests.

The viscous dissipated energy per cycle and per unit volume (E_σ) as a function of strain has been determined from the Lissajous figures. Carreau et al. (1997) present the general expression for the heat generation rate per unit volume as $\frac{1}{2}\eta\dot{\gamma}:\dot{\gamma}$. Therefore, for one cycle E_σ is:

$$\begin{aligned} E_\sigma &= \frac{1}{2}\int_0^{T_{osc}} \eta(\mathbf{a}_4,t)\dot{\gamma}(t):\dot{\gamma}(t)\,dt = \frac{1}{2}\langle\eta(\mathbf{a}_4)\rangle\int_0^{T_{osc}} 2\omega^2\gamma_R^2\cos^2(\omega t)\,dt \\ &= 4\pi^2 f^2\gamma_R^2\langle\eta(\mathbf{a}_4)\rangle\left[\frac{1}{2f}\right] = 2\pi^2\langle\eta(\mathbf{a}_4)\rangle f\,\gamma_R^2 = 4\pi^2\langle\eta(\mathbf{a}_4)\rangle f\,\gamma_{RMS}^2 \end{aligned}, \qquad (4.11)$$

where $\langle \eta(\mathbf{a}_4) \rangle$ is the viscosity of the suspension for a pre-averaged fiber orientation during a period T_{OSC}. A strain exponent close to 2 was found for the neat polybutene (as expected for Newtonian fluids) but as well for the fiber-filled PB systems, and the proportionality with the frequency as predicted by Eq. (4.11) was observed (for reason of conciseness these results are not presented, as some others in the section on polypropylene where indicated).

4.4.3. Polypropylene suspensions in LAOS

The shear stress as a function of strain for the 30 wt % filled PP is depicted in **Figure 4.8** for a frequency of 0.005 Hz and maximum deformation of 3. As for the PB in **Figure 4.4**, this sample has not been pre-sheared. Up to the 12th cycle, we observed that the Lissajous curves for the neat PP were perfectly overlapping ellipses, showing that the matrix was thermally stable. However, in the case of PP30 the stress amplitude decreases with time as shown by the arrow in **Figure 4.8**, although the stress response retains an elliptical shape. This stress drop may be attributed once more to the fiber orientation (as discussed later), and as predicted by the theory of Harlen and Koch (1997).

Figure 4.9a presents the normal stress-strain loops for PP0 at a frequency of 0.005 Hz and maximum strain of 3. As for the Lodge rubber-like liquids (Lodge, 1964), the unfilled matrix exhibits a (nearly) symmetric shape loop due to its response at twice the applied frequency, as confirmed by the slope of ≈ 2 for $\ln F_z$ versus $\ln \dot{\gamma}_R$ at low

shear rate (**Figure 4.1b**). Note that the area of the normal stress-strain loop is close to zero (due to the symmetry with the ordinate axis) indicating a pure elastic response. Moreover, the normal stress differences depict a non zero and positive offset (Lodge, 1964). **Figure 4.9b** reports the normal stress-strain loop for sample PP30 for the same conditions as PP0. The asymmetric shape is attributed to a partially pre-oriented fiber structure owing to the procedure of sample preparation by mold compression, as discussed further. The normal stress amplitude decrease seen in **Figure 4.9b** is most probably due once more to fiber orientation effects. Moreover, the normal stress-strain loops are no longer symmetric; hence, the dissipated energy is not negligible any more. Consequently, the asymmetrical fiber structure induces a "normal" dissipative energy. As for the neat polypropylene, the normal stress average of PP30 is positive. Nevertheless, some negative values for the normal stress differences are found when the flow is reversed, a behavior that is in agreement with the observations on PB20 in **Figure 4.5**. Sepehr et al. (2004c) who studied the stress growth behavior of short fiber filled polypropylenes showed similar results. In their study, a 30 wt % filled PP sample was sheared in the clockwise and counter-clockwise directions, and the normal stress differences presented negative values in flow reversal before recovering and exhibiting positive values. This behavior was attributed to a non-affine deformation or to a crystalline structure of the fiber-filled systems.

FFT performed during cycles 7 to 12 clearly demonstrated that the shear stress signal was harmonic even for the fiber-filled polypropylene. **Figure 4.10** shows the FFT results for the normal stress signal and confirms that the PP0 response oscillates at two

times the applied frequency. For PP30, however, the first and the second harmonics are the predominant frequency responses, justifying the dissymmetry shape of the normal stress-strain loops. The appearance of the first harmonic was initially believed to be due to the shear-thinning behavior of the matrix, as seen in the decreasing slope of **Figure 4.1b**. However, the same peak is observed for PB20, which depicts no important shear thinning. Therefore, as justified for PB20 the appearance of the first harmonic seems to be caused by time-dependent memory effects induced by the orientation of the fibers (Manfred et al., 1998) (the material response during the first half-cycle is different than the one in the second half-cycle). To support this hypothesis, we refer to the work of Sepehr et al. (Sepehr et al., 2004c; 2004d). These authors showed that the time required to reach steady state for the forward flow of PB- and PP-based fiber suspensions was different from that for the reverse.

To confirm that the fibers are partially pre-oriented during sample preparation under compression molding, some PP30 samples were pre-sheared at 0.08 s^{-1} during 1000 s in the clockwise (CW) and in the counter clockwise (CCW) directions, respectively, and LAOS tests were then performed. The stress versus strain curves showed similar shapes indicating that the stress signal was not very sensitive to the initial fiber orientation. However, a large effect was seen for the normal stress-strain loops, which are relatively similar except for an opposite symmetry when the flow direction for the pre-shear was changed (**Figure 4.11a** and **Figure 4.11b**). Indeed, the curves show a prominence in the strain direction depending on how the fibers were pre-aligned. This is strikingly different from the symmetrical ellipse observed previously for

sample PB20 (**Figure 4.7**). It may be explained by the difficulty of aligning the fibers in the flow direction during pre-shearing for the highly viscous PP composite, which is also more concentrated than PB20.

We also examined the viscous dissipated energy at two frequencies for the PP-based samples and it could be seen, as for the PB-based samples, that more energy was lost when the fiber content was increased. The slope for the unfilled matrix was close to 2 and decreased slightly as the fiber concentration increased. The dissipated energy was no longer a linear function of the applied frequency [Eq. (4.11)] in contrast to the results obtained with the PB system. This is explained by the shear-thinning character of the matrix.

Finally, **Figure 4.12** presents the fundamental shift angle δ_1 of the PP systems, which is defined as the difference between the stress and deformation signals (Giacomin & Dealy, 1993):

$$\delta_1 = \delta_\sigma(f) - \delta_{\gamma_R}. \tag{4.12}$$

It is found that with increasing strain, the PP systems tend to behave more as a Newtonian fluid, as observed by Sepehr et al. (2004d). Moreover, it was found that the phase angle is not affected by the pre-shearing. Also at very low deformation, the composite elasticity is not affected by the presence of the fibers (**Figure 4.12**), which confirms the results of Mobuchon et al. (2005).

4.4.4. Predictions from FTL model for PB-based systems

In order to gain insight of the effect of fiber orientation on the rheological properties, FTL model simulations were performed and compared with the results for the PB systems. The predictions in LAOS, based on Eqs. (4.9) and (4.10), are shown in **Figure 4.13** for a PB20 sample that has not been pre-sheared. **Figure 4.13a** shows the shear stress versus time, whereas **Figure 4.13b** reports the shear stress as a function of imposed deformation. The PB20 stress behavior is well described using two fitting parameters, i.e. A = 90 and C_I = 0.0005. These two parameters are then used to predict the primary normal stress differences with time, and the predictions are also quite good as shown in **Figure 4.14a**. The most interesting aspect of the modeling is the description of the evolution of the fiber orientation state, through the second-order orientation tensor components. For our simulations, we have chosen two different initial orientations, i.e. nearly planar random (**Figure 4.14a**) and fully-aligned by pre-shear (**Figure 4.14b**), given respectively by:

$$\mathbf{a}_2 = \begin{bmatrix} 0.45 & 0 & 0 \\ 0 & 0.45 & 0 \\ 0 & 0 & 0.1 \end{bmatrix}, \tag{4.13}$$

$$\mathbf{a}_2 = \begin{bmatrix} 0 & 0 & 0 \\ 0 & 1 & 0 \\ 0 & 0 & 0 \end{bmatrix}. \tag{4.14}$$

The nearly planar random orientation [Eq. (4.13)] considers that some fibers are aligned in the z-direction (flow orientation is the θ-axis). This initial orientation is

chosen because as the samples are loaded into the rheometer, they are squeezed until the desired gap is reached. The second orientation [Eq. (4.14)] corresponds to full orientation in the flow direction under a pre-shear. **Figure 4.14b** reports the simulated normal stress evolution with time in LAOS when the fibers are initially aligned in the flow (θ-) direction. The first cycles show that the normal stress contribution from the fibers is negligible, given that the suspended medium is modeled as a Newtonian matrix. The FTL model fails to predict the initial normal stress response, which oscillates at the applied frequency (explaining the elliptic shape of the normal stress-strain loop depicted in **Figure 4.7a**). After several cycles, the primary normal stress differences oscillate at twice the applied frequency and the FTL model predicts with accuracy the suspension behavior.

The simulations results for the second order orientation tensor $\mathbf{a_2}$ for the nearly planar random case [Eq. (4.13) and **Figure 4.15a**] show that most fibers tend to align in the flow direction during the oscillatory shear flow test, i.e. $a_{\theta\theta}$ increases from 0.45 to ≈ 0.67. The other simulation results performed with all fibers initially aligned with the flow direction [Eq. (4.14) and **Figure 4.15b**] indicate that the fibers loose their preferential orientation as soon as the LAOS test starts, and reach a similar final orientation as seen for the previous case (**Figure 4.15a**). This is in agreement with the conclusions drawn from **Figure 4.7** for the effect of pre-shear on sample PB20 and indicates that the LAOS test results in a fiber orientation that is between planar random and fully aligned. From the model predictions and experiments, we also suggest that the

normal stress-strain loop responses exhibit symmetric shapes for fiber orientations that are symmetric (perfectly aligned or isotropic) with respect to the flow direction. Furthermore, we note that the equilibrium orientation is reached more rapidly when fibers are initially aligned (≈ 1000 s) than for an initial planar random orientation (≈ 2000 s). This emphasizes that the LAOS test induces fiber orientation close to that of aligned fibers in the shear flow direction.

Unfortunately, the FTL model is unable to predict quantitatively the results for the PP composites, mainly because viscoelasticity is not taken into account. Nevertheless, it could predict qualitatively the decrease of the stress amplitude with time by using different initial fiber orientations than those used for the PB suspensions (i.e. planar random and fully-aligned). An initial fiber orientation with a_{rr} = 0.25, $a_{\theta\theta}$ = 0.5 and a_{zz} = 0.25, results in a decrease of the shear stress amplitude with time, as seen experimentally for the PP suspensions (**Figure 4.8**). Such an initial orientation was determined by examination of a PP-sample disk molded for rheometry, using optical microscopy (Sepehr, 2003). Using the FENE-P model instead of the Newtonian assumption for the matrix could improve the model predictions by taking into account viscoelastic effects; however, the FENE-P model overestimates the shear-thinning effect. This will result into incorrect predictions of the shear stress amplitude.

4.5. Conclusions

The rheological behavior of short glass fiber suspensions was investigated under large amplitude oscillatory shear flow. Material functions such as shear stress and

primary normal stress differences were determined from the raw signals (torque and normal force) obtained using a parallel plate rheometer. For the suspensions based on polybutene, the shear stress amplitude grows with increasing cycles of deformation to reach a constant value after more than 20 cycles. The opposite behavior, i.e. a decrease of the shear stress amplitude, was observed for the polypropylene composites. For both filled systems the evolution was attributed to fiber orientation under flow, with the differences in behavior caused by different initial fiber orientations. The primary normal stress difference was found to be more sensitive than the shear stress to the fiber orientation. The normal stress-strain loops showed symmetrical shapes if the fiber orientations were symmetric with respect to the flow direction. Fast Fourier Transform (FFT) was performed for both PB and PP-filled systems. Harmonic responses were observed for shear stresses, whereas non-harmonic signals were obtained for the primary normal stress differences. Viscous dissipation energy increased with fiber content and the behavior of the polypropylene composites became more Newtonian with increasing deformation. Finally, a model based on the Folgar-Tucker- Lipscomb (FTL) equations predicted quite well the behavior of a 20 wt % fiber filled polybutene in LAOS.

4.6. Acknowledgements

The authors would like to acknowledge financial support from the France-Québec collaboration program and the Natural Sciences and Engineering Research Council of Canada (NSERC-CIAM program). We wish to thank Dr. Manfred Wilhelm (from the Max-Planck-Institute for Polymer Research, in Mainz, Germany) who

provided us the know-how and software for operating the Fast Fourier Transform. The authors also wish to thank Dr. G. Krotkine from Basell who kindly provided the polypropylenes used in this study.

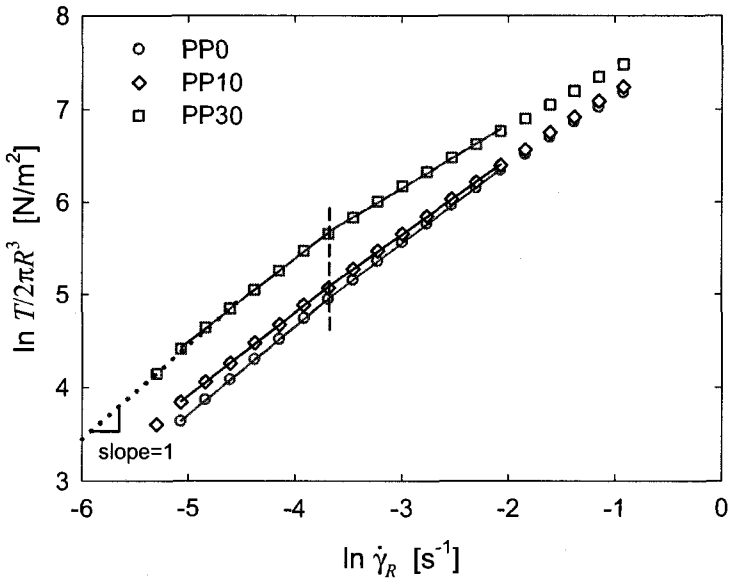

(a)

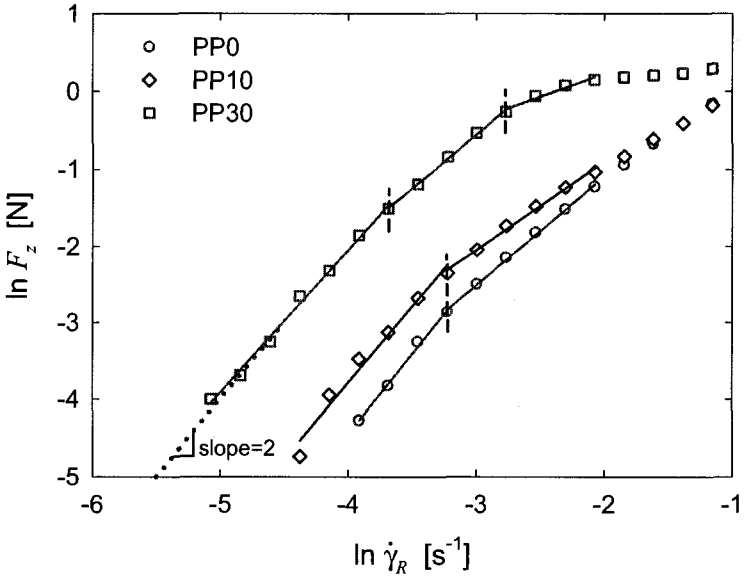

(b)

Figure 4.1 : (a) Torque and (b) normal force as functions of the rim shear rate for the neat PP and based polypropylene composites.

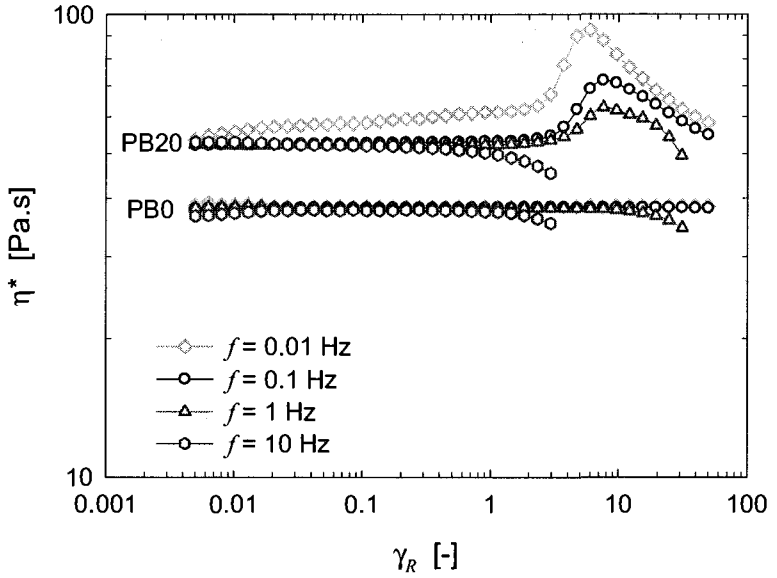

Figure 4.2 : Complex viscosity as a function of strain for PB0 and PB20. PB20 has been pre-sheared at 10 s^{-1} during 1000 s.

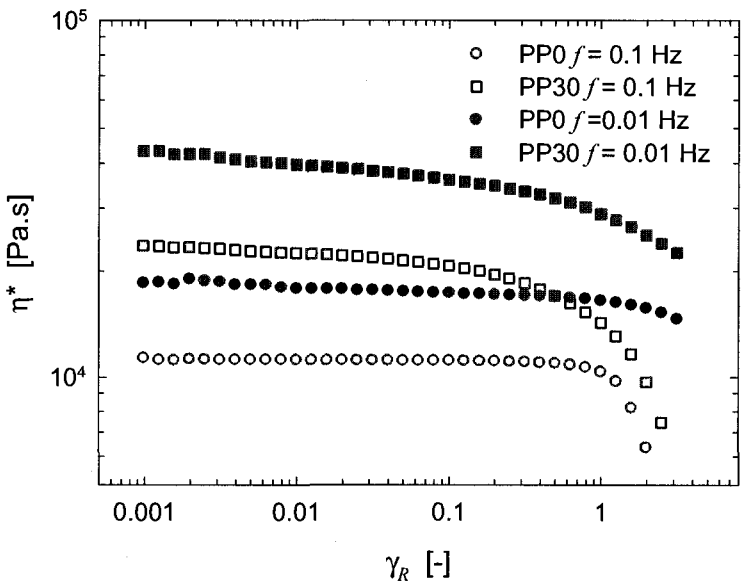

Figure 4.3 : Complex viscosity as a function of strain for PP0 and PP30.

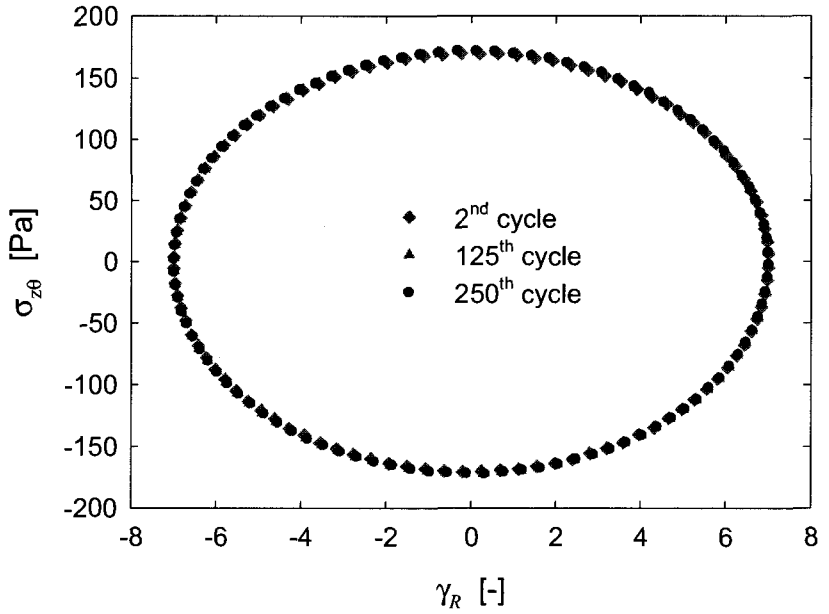

(a)

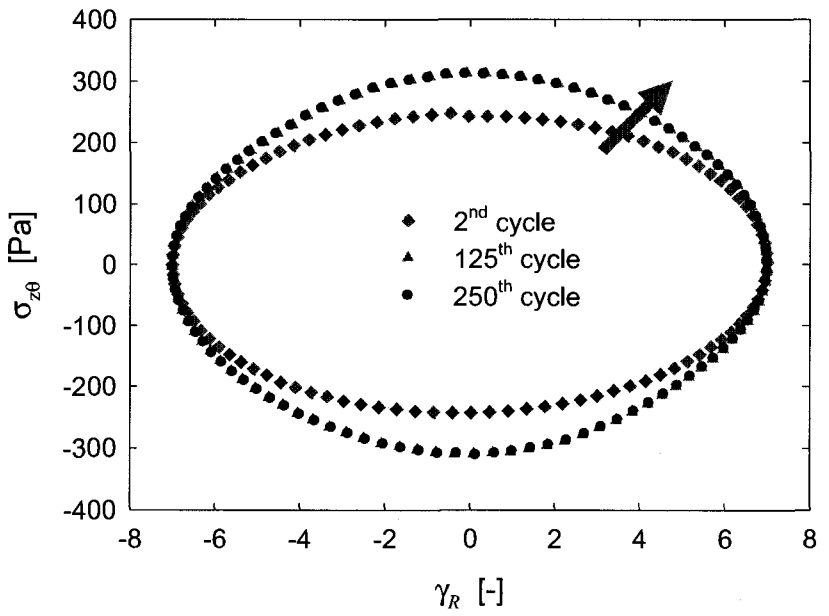

(b)

Figure 4.4 : Shear stress versus strain for 3 LAOS cycles, with $\gamma_R = 7$ and $f = 0.1$ Hz: (a) PB0; (b) PB20.

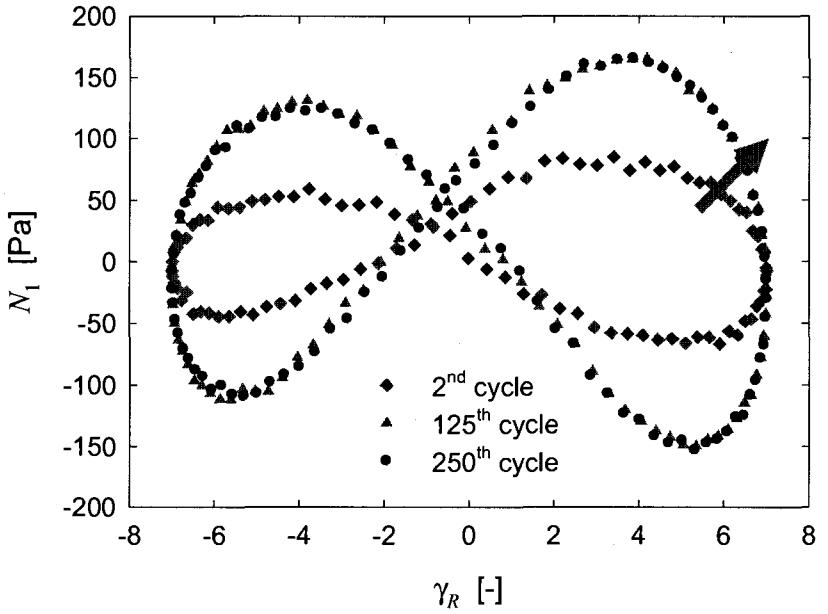

Figure 4.5 : PB20 primary normal stress differences versus strain for 3 LAOS cycles, with $\gamma_R = 7$ and $f = 0.1$ Hz.

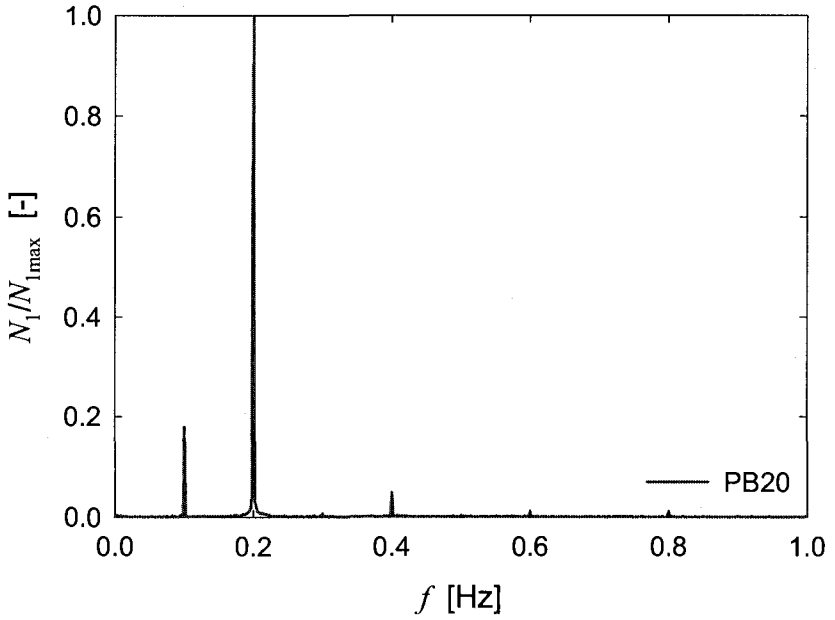

Figure 4.6 : FFT analysis at γ_R = 7 and f = 0.1 Hz of cycles 200-250: Primary normal stress difference responses for PB20.

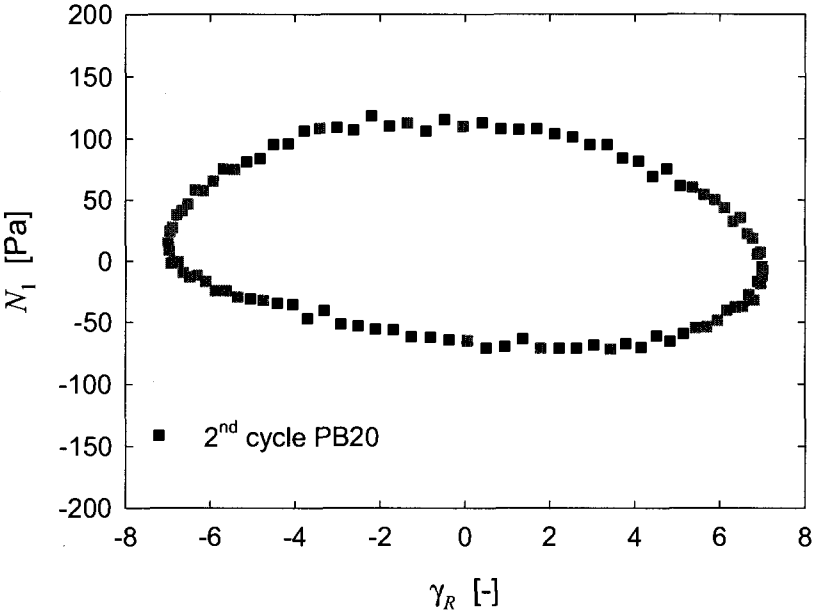
200
150
100
50
0
-50
-100
-150
-200
N_1 [Pa]
-8
-6
-4
-2
0
2
4
6
8
γ_R [-]
2nd cycle PB20

(a)

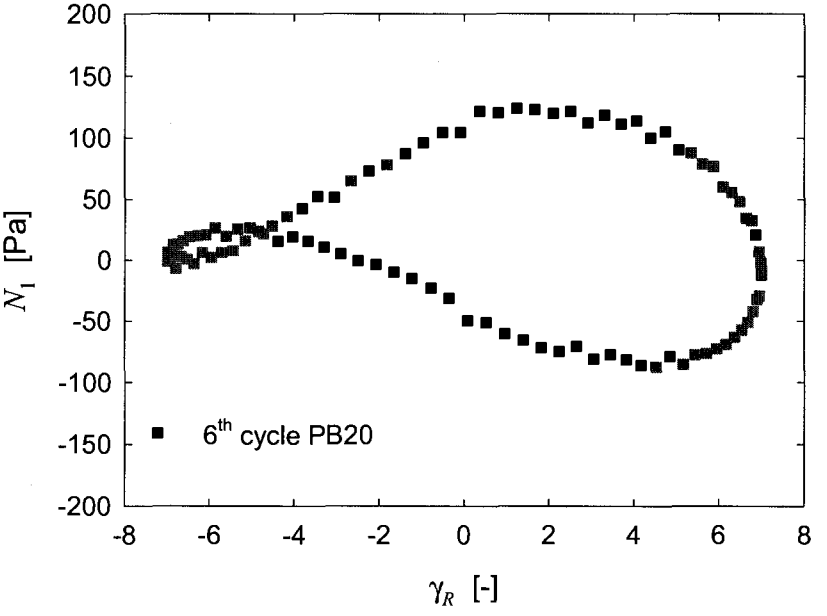
200
150
100
50
0
-50
-100
-150
-200
N_1 [Pa]
-8
-6
-4
-2
0
2
4
6
8
γ_R [-]
6th cycle PB20

(b)

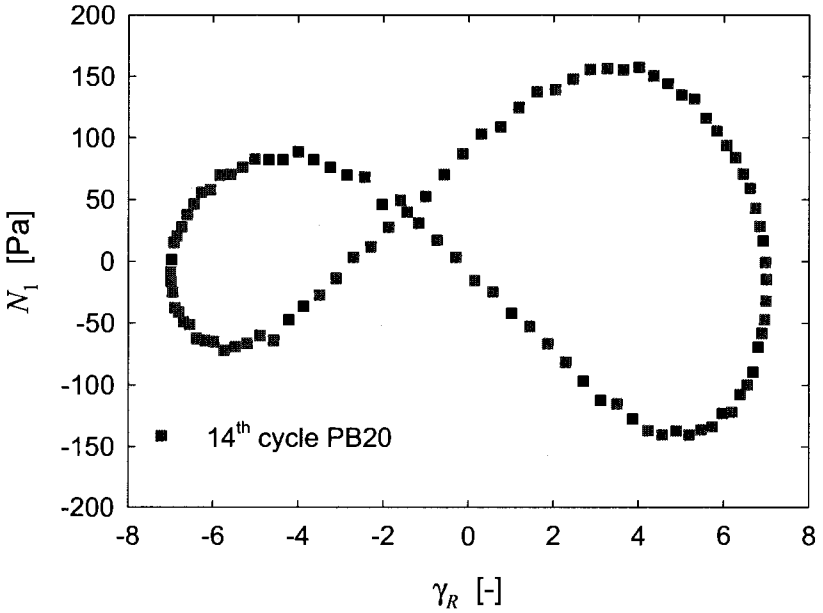

(c)

Figure 4.7 : Time evolution of the primary normal stress differences of PB20 in LAOS test (γ_R = 7 and f = 0.1 Hz), for which the sample was previously pre-sheared at 10 s^{-1} during 1000 s: (a) 2nd; (b) 6th; and (c) 14th cycles.

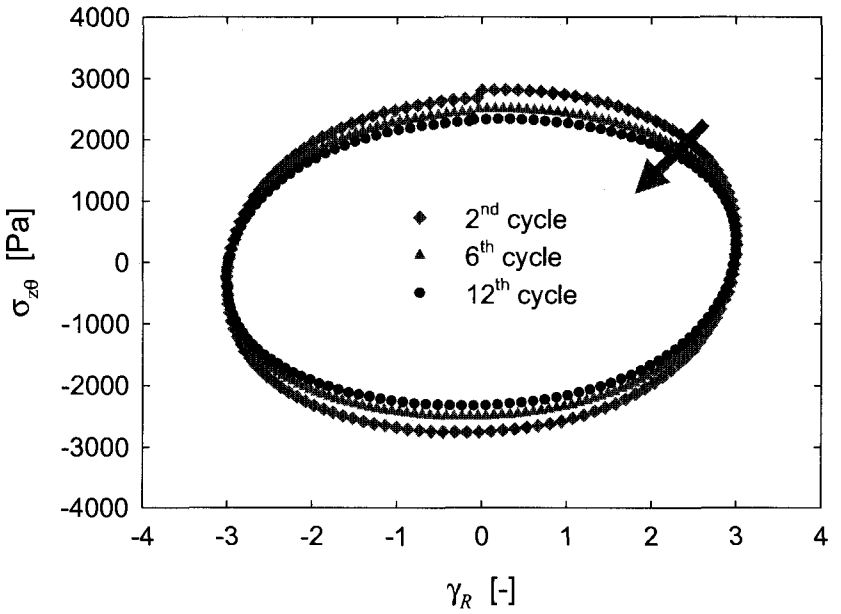

Figure 4.8 : Shear stress versus strain after 3 different LAOS cycles, where γ_R = 3 and f = 0.005 Hz for PP30.

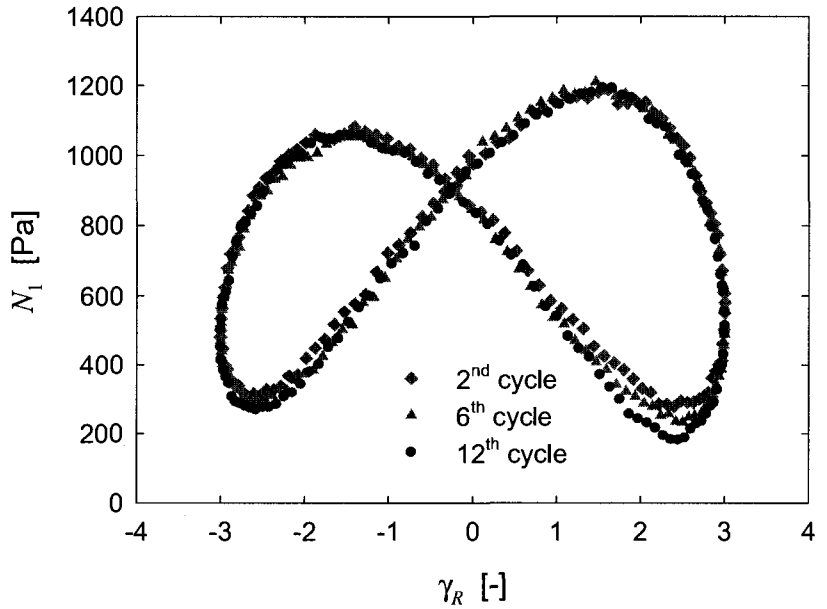

(a)

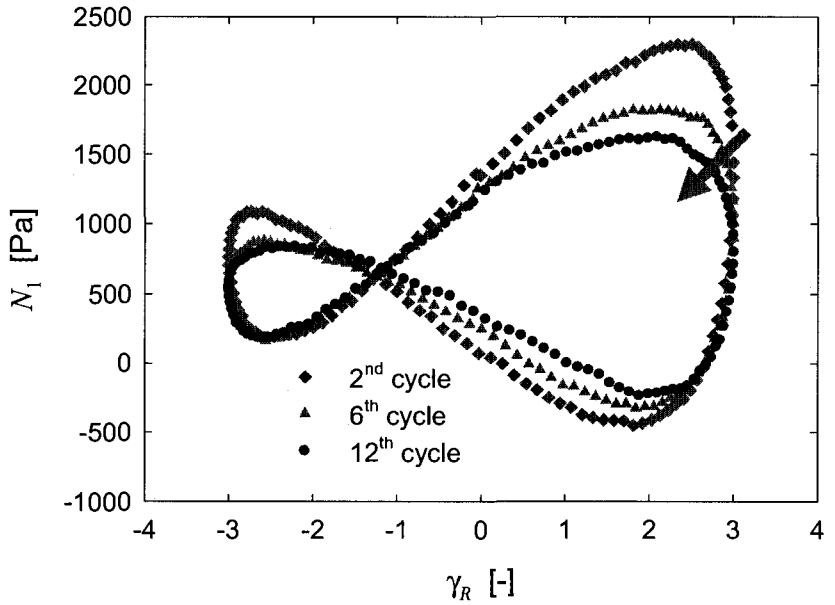

(b)

Figure 4.9 : Primary normal stress differences versus strain after 3 different LAOS cycles, where $\gamma_R = 3$ and $f = 0.005$ Hz: (a) PP0; (b) PP30.

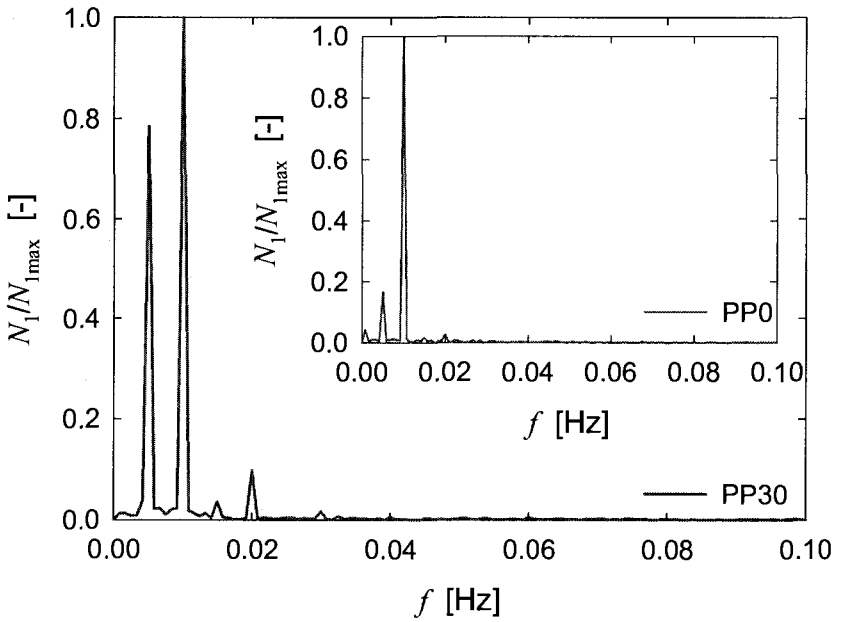

Figure 4.10 : FFT analysis of the PP30 (PP0 in insert) primary normal stress difference responses at $\gamma_R = 3$ and $f = 0.005$ Hz, cycles 7-12.

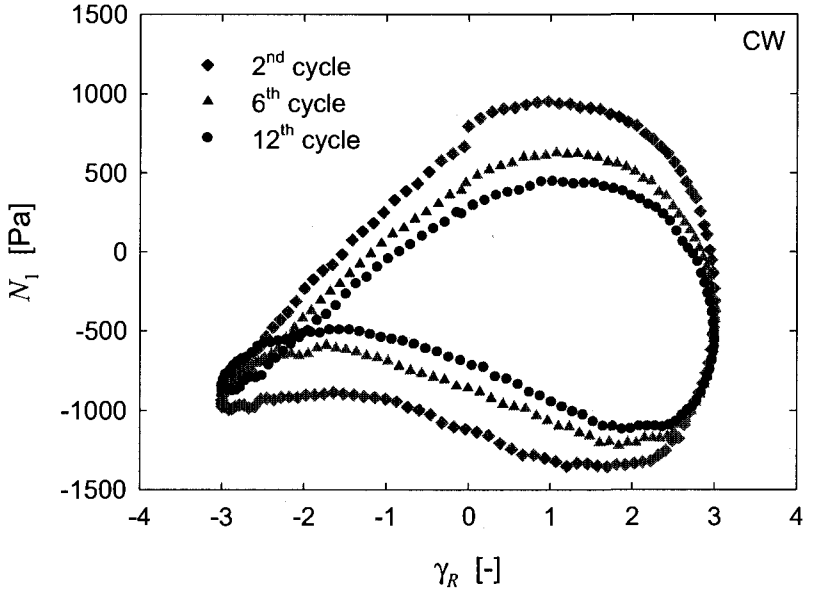

(a)

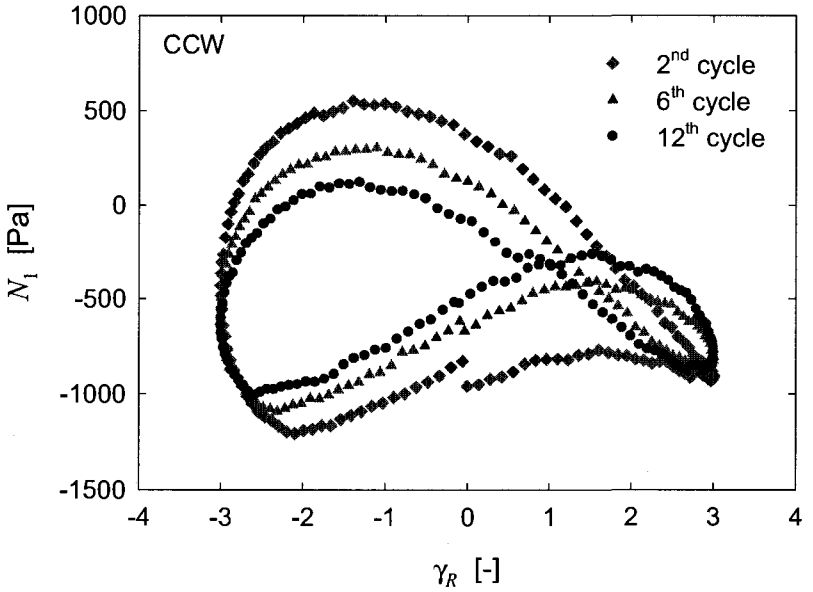

(b)

Figure 4.11 : Effect of pre-shear before LAOS tests on the normal stress Lissajous figures for PP30: (a) Pre-shear in CW direction at 0.08 s^{-1} during 1000 s; (b) Pre-shear in CCW direction at 0.08 s^{-1} during 1000 s.

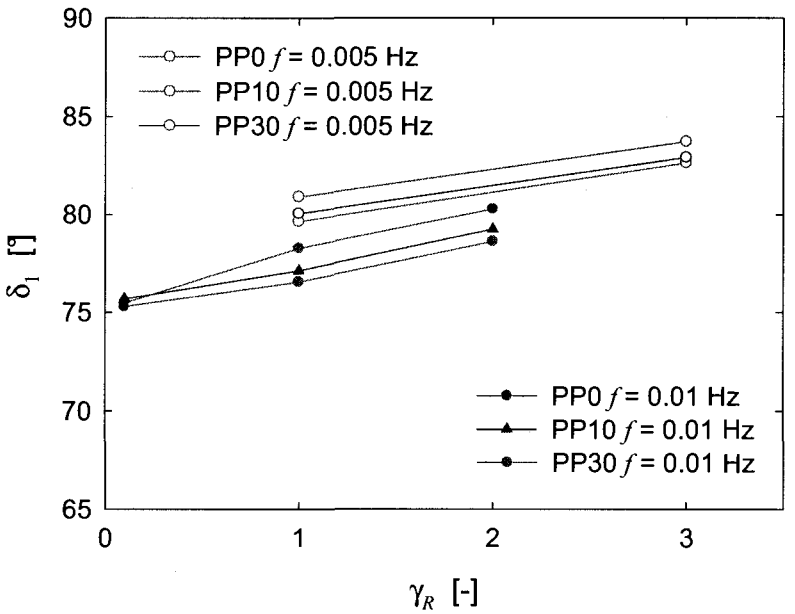

Figure 4.12 : Fundamental shift angle as a function of strain for PP0, PP10 and PP30.

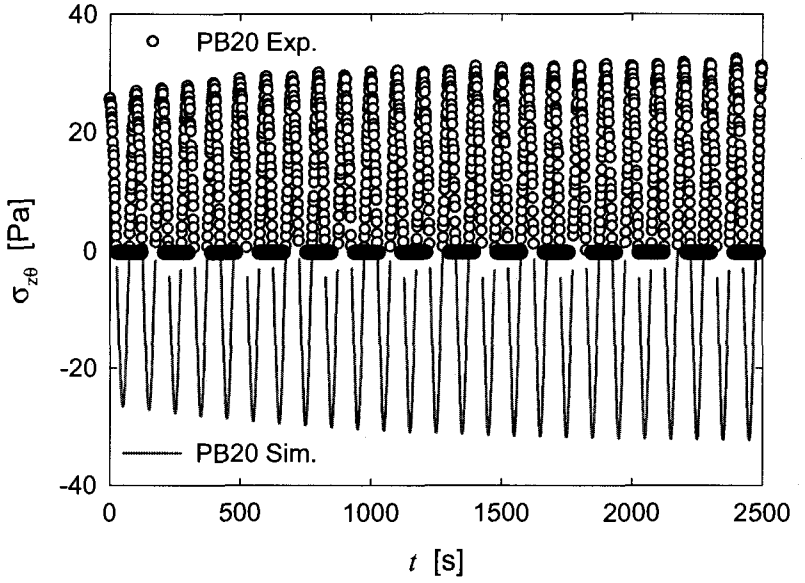

(a)

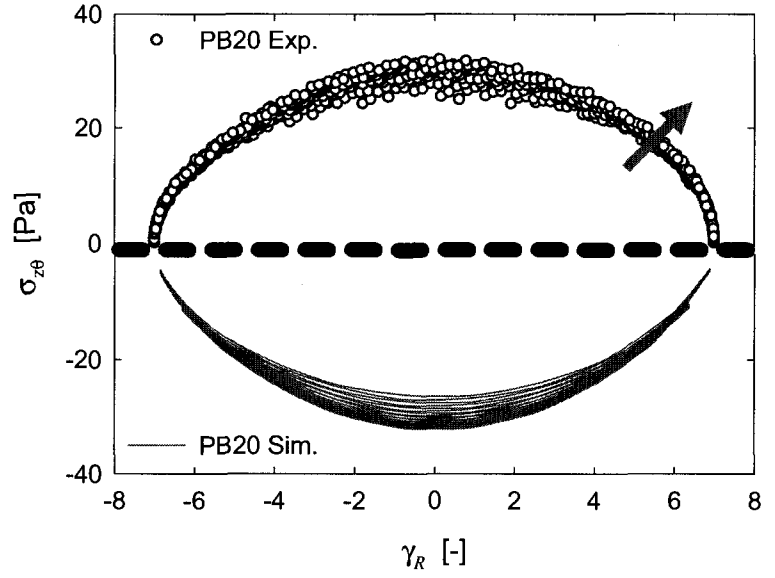

(b)

Figure 4.13 : Comparison of model predictions and shear data for PB20 in LAOS for $\gamma_R = 7$ and $f = 0.01$ Hz. The ORW closure approximation and $C_I = 0.0005$ and $A = 90$ have been used for the predictions. The initial fiber orientation is given by Eq. (13): (a) Shear stress as a function of time; (b) Shear stress as a function of deformation.

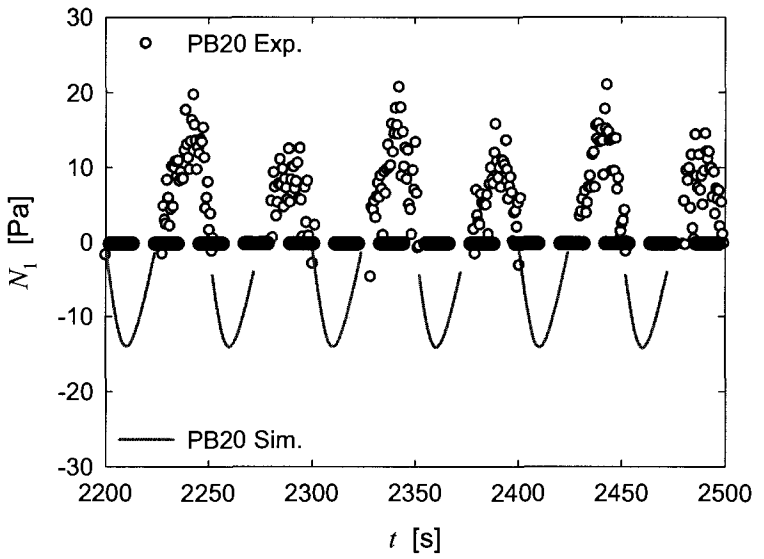

(a)

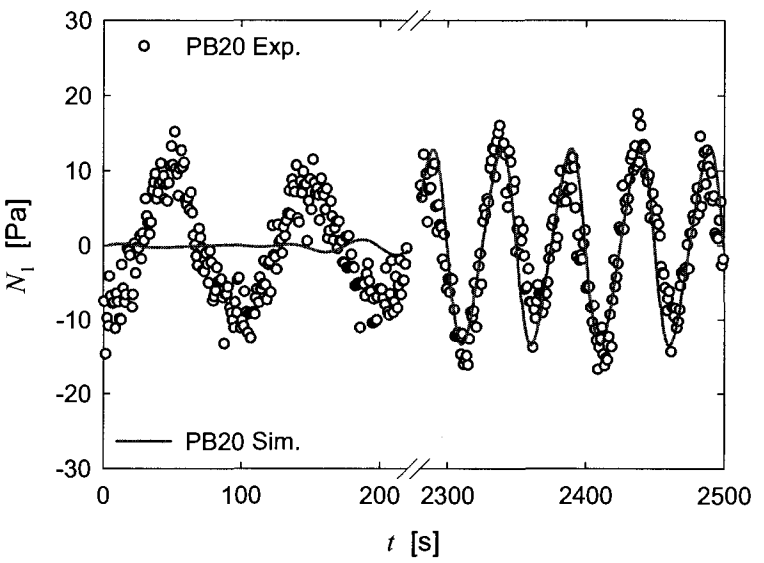

(b)

Figure 4.14 : Comparison of model predictions and normal stress data for PB20 in LAOS for $\gamma_R = 7$ and $f = 0.01$ Hz. The ORW closure approximation, $C_I = 0.0005$ and $A = 90$ have been used for the predictions: (a) Normal stress differences as a function of time for an initial planar random fiber orientation [Eq. (4.13)]; (b) Normal stress differences as a function of time for initial aligned fibers [Eq. (4.14)].

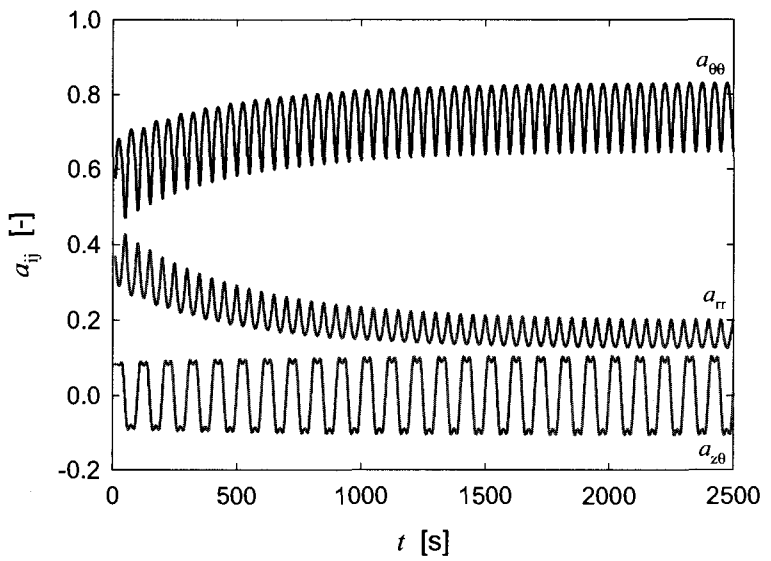

(a)

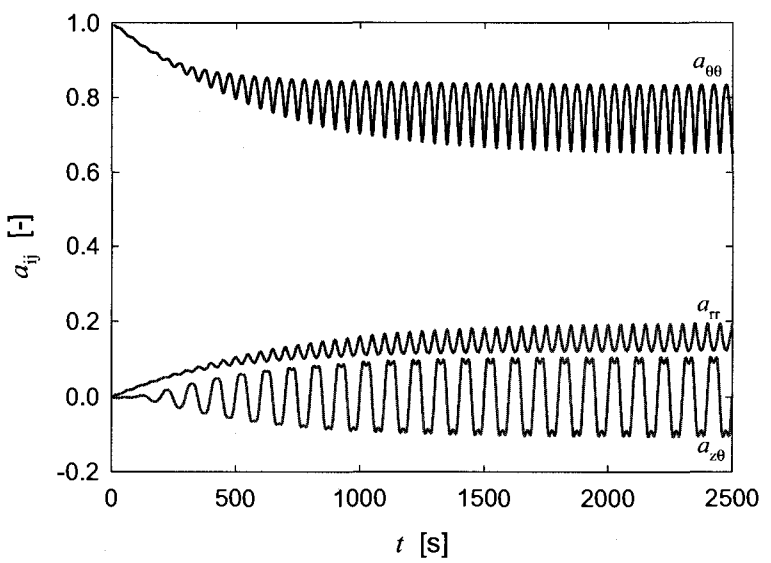

(b)

Figure 4.15 : Simulation of the second-order orientation tensor for PB20 in LAOS for $\gamma_R = 7$ and $f = 0.01$ Hz using the ORW closure approximation ($C_I = 0.0005$, $A = 90$): (a) Variations of $\mathbf{a_2}$ components with strain: initial orientation given by Eq. (4.13) ; (b) Variations of $\mathbf{a_2}$ components with strain: initial orientation given by Eq. (4.14).

CHAPITRE 5 - ARTICLE: INVESTIGATION OF THE RHEOLOGICAL PROPERTIES OF SHORT GLASS FIBER FILLED POLYPROPYLENE IN EXTENSIONAL FLOW*

J. Férec [a,c], M.C. Heuzey [a], J. Pérez-González [b], L. de Vargas [b], G. Ausias [c] and P.J. Carreau [a]

[a] *Center for Applied Research on Polymers and Composites (CREPEC), Chemical Engineering Department, École Polytechnique de Montréal, PO Box 6079, Stn Centre-Ville, Montreal, QC, Canada H3C3A7*

[b] *Laboratorio de Reología, Escuela Superior de Física y Matemáticas, Instituto Politécnico Nacional, México D. F., México*

[c] *Laboratoire d'Ingénierie des MATériaux de Bretagne (LIMATB) Université de Bretagne Sud, rue de St Maudé, 56325 Lorient, France*

Abstract

The behavior of short glass fiber - polypropylene suspensions in extensional flow was investigated using three different instruments: the SER wind-up drums geometry (Extensional Rheology System) with a strain-controlled rotational rheometer, a Meissner-type rheometer (RME) and the Rheotens. Results from uniaxial tensile testing have been compared with data previously obtained using a planar slit die with a hyperbolic entrance. The effect of three initial fiber orientations was investigated: planar random, fully aligned in the stretching flow direction and perpendicular to it. The elongational viscosity increased with fiber content and was larger for fibers initially orientated in the stretching direction. The behavior at low elongational rates showed

---

* Cet article a été soumis au journal Rheologica Acta.

differences among the various experimental setups, which are partly explained by pre-shearing history and non-homogenous strain rates. However, at moderate and high rates, the results are comparable, and the behavior is strain thinning. Finally a new constitutive equation for fibers suspended into a fluid obeying the Carreau model is used to predict the elongational viscosity, and the predictions are in good agreement with the experimental data.

5.1. Introduction

Fiber reinforced polymer materials have received attention from many researchers in the last decades. These composites improve considerably stiffness, strength and heat distortion resistance in comparison with unfilled polymers. Given that the filler particles have geometrically anisotropic shapes, the reinforcement of the solidified materials may depend also on fiber orientation. Therefore, it is of interest to develop relationships between flow properties and fiber orientation during polymer processing.

In common processing techniques such as extrusion, injection molding and blow molding, the material is subjected to a combination of shear and elongational flows. While many papers discuss the rheological properties of fiber suspensions in shear flow (Ausias et al., 1992; Kamal & Mutel, 1989; Laun, 1984; Ramazani et al., 2001; Sepehr et al., 2004c; Sepehr et al., 2004d), few reports deal with the studies of fiber-filled polymers in extensional flow, and there are many contradictions in the literature about these properties. Metzner (1985) published an interesting review on polymer suspensions, mentioning that fiber suspensions show large resistance to strain in extensional flow. One of the pioneering work was done by Chan et al. (1978), who investigated the elongational viscosity of high-density polyethylene (HDPE) and polystyrene (PS) melts filled, respectively, with 20 and 40 wt % of glass fibers. They observed that the elongational viscosity, η_E, of the composites was always larger than that of the matrices. This was confirmed by several authors (Kobayashi et al., 1995;

Laun, 1984; Ooi & Sridhar, 2004; Thomasset et al., 2005) and especially by Takahashi et al. (1999) who used a low density polyethylene (LDPE) filled with glass beads and fibers and studied the composite behavior in uniaxial elongation with a Meissner-type elongational rheometer. However, using a Göttfert tensiometer (Rheotens), Lin et al. (1997) surprisingly observed that above a critical fiber content, the elongation viscosity of a glass fiber reinforced polypropylene (PP) dropped. Also at low strain rate, Chan et al. (1978) showed that the elongational viscosity of composites showed large values but decreased with increasing deformation rates. Chan et al. (1978) noted that the Trouton ratio η_E/η_0 was close to 3 for both unfilled polymers at low strain rate (PS and HDPE), whereas it increased at high Hencky rates for a PS matrix. Moreover, the ratio $\eta_E/\eta^{composite}$ was larger for a 20 wt % fiber filled system than for a 40 wt % content. They explained this particularity by the fact that higher fiber concentrations could induce larger shear rates for the fluid trapped between fibers, and consequently result in lower shear viscosities due to the shear-thinning character of the matrix. Similar results have been published (Creasy et al., 1996a; Creasy et al., 1996b; Creasy & Advani, 1997) for long discontinuous carbon fiber in poly-ether-ketone-ketone (PEKK). For long glass fibers (L=3.1mm) suspended in a polybutene (Newtonian fluid), Mewis and Metzner (1974) showed that the elongational viscosity was independent of the strain rate and η_E/η_0^{matrix} increased by a factor of 156. Weinberger and Goddard (1974) found a constant elongational viscosity that was 26 and 23 times larger than the shear viscosity for glass fibers suspended in a highly viscous silicone oil and in a polybutene, respectively. In their paper on the resistance to uniaxial extensional flow of fibers

suspended in a Newtonian epoxy (Epikote) and Boger fluid (polyisobutylene + polybutene + kerosene) matrices, Ooi et al. (2004) found the ratio η_E/η_0^{matrix} larger than 3 for both composites at low Hencky strain. These measurements were performed using a filament stretching technique, ensuring that no necking occurred. They found that fiber addition had a marginal effect after the onset of strain hardening for the Boger fluid.

Using a Rheometrics Elongational Rheometer (RER), Kamal (Kamal et al., 1984) et al. (1984) observed that the elongational viscosity of glass fiber filled PP increased with fiber content and decreased with strain rate. From measurements in an on-line slit rheometer mounted on an injection molding press, Mobuchon et al. (2005) evaluated the apparent planar extensional viscosity of fiber-filled PP from the pressure drop in an hyperbolic die. For strain rates varying between 0.1 and 200 s^{-1}, they determined that the Trouton ratio, η_E/η^{matrix}, dropped 40 to 4 with shear rate for the unfilled PP, and from 42 to 4.2 and 54 to 5.4 for the 10 wt % and 30 wt % filled PP, respectively. Takahashi et al. (1999) found that a LDPE filled with glass beads exhibited a weak strain hardening, and showed a strain-softening behavior when filled with fibers. Kobayashi et al. (1995) investigated the influence of 10 vol % of potassium titanate whiskers suspended in a PS matrix and of their orientation during uniaxial elongational tests (using a Meissner-type elongational rheometer). They concluded that the whiskers prevented the strain-hardening behavior. Kobayashi et al. (1995) concluded that the elongational viscosity was almost independent of the filler orientation, which is in contradiction with the Batchelor theory for fibers in Newtonian fluids (Batchelor, 1971) and the Goddard

analysis in non-Newtonian fluids (Goddard, 1976). Also, Kobayashi et al. (1995) used X-ray diffraction patterns to show that the initially random oriented whiskers became remarkably aligned in the stretching direction. Zhang et al. (2001) analyzed the changes in fiber orientation using scanning electron microscopy of quenched samples of glass fiber-filled PP melts subjected to biaxial extensional flows, They found an appropriate range of strain rate, for which the degree of fiber alignment in the flow direction increased. Behavior in elongational flow is in contrast with that in the shear, where significant stress overshoots have been observed due to fiber orientation (Sepehr et al., 2004c). That is why Kobayashi et al. (1995) suggested to increase the filler content, filler length and aspect ratio in order to highlight the influence of the orientation changes of non-spherical particles on the elongational viscosity. Model predictions (made from Lipscomb (1988) constitutive equation, where the Newtonian viscosity was replaced by a Carreau expression) for isotropic and aligned fiber orientations with respect to flow have been presented by Thomasset et al. (2005). They found that their measured apparent elongational viscosity data fell between the two limiting cases (3D random and fully aligned fiber orientations). On the other hand, Wagner et al. (2003) did not observe any significant strain hardening for 12 wt % fibers in a polyamide-6 although the fibers oriented from a random state to a completely aligned orientation, as observed from selected micrographs taken during the tests. Ooi et al. (2004) assumed that fiber orientation occurred under elongational flow but no strain-hardening was observable for the suspensions in a Newtonian matrix, whereas the tensile stress for the suspensions in a Boger fluid (PIB) grew with strain from a stress free condition to a plateau and then

the behavior became strain hardening before reaching a second plateau. Takahashi et al. (1999) concluded that when particles were small and their aspect ratio large (length >> diameter), strain hardening became insignificant. For glass fiber-filled HDPE composites, Laun (1984) found that the highest tensile stress was obtained when the fibers were aligned along the elongational flow. The same value of the stress was reached when the fibers were initially oriented perpendicularly to the principal axis of the strain, suggesting that the fibers alignment most probably increased during elongation. However, no strain hardening phenomena were noticeable in the tensile stress versus strain plot. Finally, Kobayashi et al. (1995), as Wagner et al. (2003), noted that the orientation of non-spherical fillers was strain dependent.

A few theoretical expressions have been derived to predict the stress generated by non-dilute fiber suspensions in elongational flow. Batchelor (1971) derived an expression to relate the force imposed by a particle on a Newtonian surrounding medium to the particle characteristics. From first order singularities in the force distributions, the specific elongational viscosity η_E^{SP} for perfectly aligned fibers can be obtained:

$$\eta_E^{SP} = \frac{\eta_E - 3\eta_0^{matrix}}{3\eta_0^{matrix}} = \frac{4\phi r^2}{9\ln(\pi/\phi)}, \tag{5.1}$$

where ϕ is the fiber volume fraction and r is the aspect ratio, L/D (length over diameter). Batchelor (1971) extrapolated the formula to reach the dilute domain. Petrie (1999) modified this extrapolation to obtain a better correlation expressed as:

$$\eta_E^{SP} = \frac{2\phi r^2}{9\left[\ln 2r - \ln\left(1 + 2r\sqrt{\phi/\left(\pi e^3\right)}\right) - 1.5\right]}, \tag{5.2}$$

where e is an adjusting parameter. Later, Lubansky et al. (2005) extended the original Batchelor theory to take into account the cylindrical shape of fibers as higher order singularities along the principal axis. For the semi-dilute regime of constant circular cross-section particles they obtained:

$$\eta_E^{SP} = \frac{2\phi r^2\left[\ln(\pi/4\phi) + 8/3\right]}{9\ln(\pi/\phi)\left[\ln(\pi/\phi) - 3\right]}. \tag{5.3}$$

In summary, there are a lot of controversies or contradictions in the literature on the rheological behavior of fiber suspensions in polymers under elongational flow. Open questions are: do fibers cause strain hardening in elongational flow, and is fiber orientation responsible for the strain hardening? In most of the previous studies, the fibers were initially aligned in the stretching direction due to sample preparation. What would be the effect of other fiber orientations? Therefore, the main objective of this work is to determine the influence of the initial fiber orientation on the elongational behavior of short glass fiber-filled polypropylene. In addition, the Dinh and Armstrong governing equation is used to analyse the trends in the transient regime. We also report elongational data for short glass fiber-filled PP obtained using three different instruments. The results for uniaxial elongation are compared with data previously obtained in planar elongation using a slit die. Finally, an extension of the Carreau model for suspended fibers in a polymeric fluid is proposed to describe the steady uniaxial elongational data.

5.2. Modeling

In this section, the equations that describe the evolution of a fiber population with respect to the matrix flow are presented. We also propose a new constitutive equation for fibers suspended into a fluid obeying the Carreau model.

5.2.1. Orientation tensors

A unit vector **p**, directed along the principal axis of the particle, is generally used to describe the fiber orientation. A probability distribution function ψ can represent a fiber population in an elementary cell fluid, and a second- and a fourth-order orientation tensors can be defined as (Advani & Tucker, 1987):

$$\mathbf{a}_2 = \int_{\mathbf{p}} \mathbf{pp}\psi d\mathbf{p}, \tag{5.4}$$

$$\mathbf{a}_4 = \int_{\mathbf{p}} \mathbf{pppp}\psi d\mathbf{p}, \tag{5.5}$$

where $\mathbf{a_2}$ is a positive and symmetric tensor with a constant trace equals to one, which states that the fiber length does not change under flow.

5.2.2. Fiber motion

At low Reynolds numbers, Jeffery (1922) derived the ellipsoid motion $\dot{\mathbf{p}}$ in a Newtonian medium for dilute suspensions. Later, Folgar and Tucker (1984) have taken into account a randomizing effect of fiber interactions by adding a diffusion term $(-C_I|\dot{\gamma}|\nabla \ln \psi)$ to the Jeffery equation. C_I is an interaction coefficient, $|\dot{\gamma}|$ is the effective deformation rate and ∇ represents the nabla (or del) operator. Moreover, ψ may be

regarded as a convected quantity in the sense that when a fiber leaves one orientation, it must appear in another one (Bird et al., 1987b). The combination of the continuity relation with the Jeffery equation yields the equation of change for ψ:

$$\frac{D\psi}{Dt} = -\nabla \cdot \left(\dot{\mathbf{p}}_{\text{Jeffery}}\psi\right) + C_I \left|\dot{\gamma}\right| \nabla^2 \psi \,, \tag{5.6}$$

where D/Dt represents the material derivative and reduces to partial derivative in the case of homogenous flows. Defined by $\lambda = (r^2-1) / (r^2+1)$, the form factor λ appears implicitly in Equation (5.6). In the scope of this work Eq. (5.6) was discretized using a finite volume method. Hence no closure approximation for the fourth-order orientation tensor was needed. Details about this numerical procedure are presented in a forthcoming paper (Férec et al., 2008b).

5.2.3. Constitutive equation

A constitutive equation for rigid cylindrical particles suspended in a Newtonian fluid has been proposed by Dinh and Armstrong (1984). Their expression may be written as:

$$\boldsymbol{\sigma} = -P\boldsymbol{\delta} + \eta_0 \dot{\boldsymbol{\gamma}} + \eta_0 \phi \frac{r^2}{3\ln\left(2h/D\right)} \int_{\mathbf{p}} \dot{\boldsymbol{\gamma}} : \mathbf{pppp}\psi d\mathbf{p} \,, \tag{5.7}$$

where P is the hydrostatic pressure, $\boldsymbol{\delta}$ is the identity tensor, η_0 the Newtonian fluid viscosity and $\dot{\boldsymbol{\gamma}}$ is the rate of strain tensor. The average spacing h between a fiber and its neighbors is given by(Doi & Edwards, 1978a, b):

$$h = \frac{D}{2}\sqrt{\pi/\phi} \text{ , for aligned fibers,} \tag{5.8}$$

$$h = \frac{D\pi}{4\phi r}\text{, for 3D random fibers.} \tag{5.9}$$

Souloumiac and Vincent (1998) have derived a constitutive equation for rigid cylindrical particles suspended in a shear-thinning matrix with a viscosity represented by a power-law. Using a cell model approach, the total stress is the sum of the contribution of the matrix and the fibers:

$$\boldsymbol{\sigma} = -P\boldsymbol{\delta} + K\left|\dot{\gamma}\right|^{m-1}\dot{\boldsymbol{\gamma}} + K\phi\frac{r^{m+1}}{2^{m-1}(m+2)}\left[\frac{1-m}{m\left(1-(D/2h)^{\frac{1-m}{m}}\right)}\right]^{m} \cdot \int_{\mathbf{p}} \dot{\boldsymbol{\gamma}}:\mathbf{pppp}\left|\dot{\boldsymbol{\gamma}}:\mathbf{pp}\right|^{m-1}\psi d\mathbf{p}, \tag{5.10}$$

where K is the consistency index and m is the power-law index.

By considering Equations (4.10) and (5.10), it seems possible to express the total stress of fiber suspensions in a generalized Newtonian fluid (GNF) described by the Carreau model (1997). After some straightforward calculations, we obtain:

$$\boldsymbol{\sigma} = -P\boldsymbol{\delta} + \eta_0\left[1+\left(\lambda_m\left|\dot{\gamma}\right|\right)^2\right]^{\frac{m-1}{2}}\dot{\boldsymbol{\gamma}} + \eta_0\phi\mu_2\int_{\mathbf{p}}\dot{\boldsymbol{\gamma}}:\mathbf{pppp}\left[1+\left(\lambda_f\dot{\boldsymbol{\gamma}}:\mathbf{pp}\right)^2\right]^{\frac{m-1}{2}}\psi d\mathbf{p}, \tag{5.11}$$

with the coupling coefficient μ_2 expressed as:

$$\mu_2 = \frac{r^{m+1}}{2^{m-1}(m+2)}f(D/2h) = \frac{r^{m+1}}{2^{m-1}(m+2)}\left[\frac{1-m}{m\left[1-(D/2h)^{(1-m)/m}\right]}\right]^{m}. \tag{5.12}$$

We note that when m tends to 1, $\mu_2 = r^2/3\ln(2h/D)$, which is the Dinh and Armstrong expression. In their paper, Souloumiac and Vincent (1998) assumed a similar power-law index for the suspension and for the unfilled matrix. Also, as done by Yasuda with the Carreau model, an additional exponent parameter can be added to improve the fit with the experimental data (Carreau et al., 1997).

5.2.4. Extensional viscosity

To determine the transient elongational viscosity η_E^+ of a Newtonian fluid, the equation of change for ψ [Eq. (5.6)] is coupled with the expression for the bulk stress tensor [Eq. (4.10)] developed by Dinh and Armstrong (1984). It is convenient to define η_E^+ for fiber suspensions as (Batchelor, 1971; Mewis & Metzner, 1974; Mongruel & Cloitre, 2003):

$$\eta_E^+ = \frac{\sigma_{11} - \frac{1}{2}(\sigma_{22} + \sigma_{33})}{\dot{\varepsilon}}, \tag{5.13}$$

where index "1" denotes the principal stretching direction. Appendix 1 gives the transient elongational stress components for the Dinh and Armstong expression according to the fourth-order orientation tensor components. Appendix 2 presents the elongational stress components for the new Carreau-based model [Eq. (5.11)] for fibers perfectly aligned in the stretching direction.

5.3. Experiments

5.3.1. Materials

A linear unfilled polypropylene (PP0, Hostacom G3 N01L) and two filled polypropylenes, containing respectively 10 and 30 wt % glass fibers (PP10 and PP30), supplied by Basell, have been studied. An intermediate fiber content of 20 wt % (PP20) was obtained by blending equal quantities of the two last products. The filler consists of treated glass fibers with a density of $\rho_f = 2500$ kg/m^3, nominal diameter $D = 16$ μm and average length $L = 250$-320 μm (fiber breakage during sample preparation is discussed below). In order to investigate the effect of particle shape, a model suspension of micro-beads (PPB11) was prepared using the same base PP with a volume fraction corresponding to the glass fiber content of sample PP30 (i.e. $\phi = 11.5$ vol %). The micro-beads were untreated hollow glass beads ($D = 10$ μm) with a density of $\rho_b = 1100$ kg/m^3. To reduce the thermal degradation, 1 wt % of stabilizer (Irganox B225, Ciba Specialty Chemical Inc.) was added to the materials during sample preparation (Sepehr et al., 2004c). Density measurements of PP0, PP10 and PP30 were performed on a Thermo Haake PVT100 equipment. The sample nomenclature, fiber volume concentration and density of the composites are presented in **Table 5.1**. Three regimes of fiber concentrations are proposed in the literature according to fiber dimensions (Doi & Edwards, 1986): dilute, in which $\phi < D^2/L^2$; semi-dilute $D^2/L^2 < \phi < D/L$ and concentrated $\phi > D/L$. The respective regimes are also presented in **Table 5.1**. PP10 is in the semi-dilute regime whereas PP20 and 30 are in the concentrated one.

5.3.2. Elongational devices

The elongational experiments were carried out using a SER Universal Testing Platform (Xpansion Instruments LLC, model SER-HV-A01) specifically designed for a controlled rate rheometer (ARES, TA Instruments) (Sentmanat, 2004; Sentmanat et al., 2005). It is composed of two wind-up drums, which ensure a uniform extensional deformation during experiments. The device is incorporated into the oven of the ARES, and allows performing the tests at high temperature under a nitrogen atmosphere. The experiments were carried out at 200 °C. All results obtained with the SER geometry were averages of three tests.

A Göttfert Rheotens device was also used to test the composites in uniaxial extension at 200 °C for the unfilled, 10 wt % and 30 wt % filled polypropylenes. In the Rheotens experiment, a filament extruded at constant shear rate is stretched by two counter-rotating wheels whose velocity is increased with time, starting from that at which the tensile force is zero, and the resulting tensile force is recorded as a function of time. By knowing the average extrusion velocity (v_0) and that of the wheels at a given time (v), the draw ratio (D_R) is calculated as $D_R = v/v_0$. The spinline length and the acceleration factor were fixed at 0.09 m and 0.005 m/s^2, respectively. A capillary with a length to diameter (L/D) of 20 with D = 0.002 m, was used to extrude the composites using a Göttfert Rheotester 1000 capillary rheometer. The extrusion rates used in this work were in an appropriate range to avoid solidification of the extrudate along the spinline, as well as to avoid melt fracture, namely, between 200 and 300 s^{-1}.

Finally, a Meissner-type uniaxial extensional rheometer (RME, Rheometric Scientific), equipped with rotary clamping devices, was used to verify the deformation uniformity of the filled PP. Using a video acquisition system, the analysis of the sample width versus time data gives the true Hencky strain rate applied on the sample. The PP specimens were supported with an air bed, which is fed through a fritted table. The temperature chamber was set at 200 °C. As for the SER unit, the RME results were averages of three tests. A lot of care have been devoted when using the device as prescribed by Schweizer (2000).

The planar elongational results reported for the slit die with a hyperbolic entrance (Mobuchon et al., 2005) were obtained using the Binding analysis (Binding, 1988).

5.3.3. Simple shear measurements

Measurements of the shear properties were carried out using a stress controlled rheometer (CSM, Bohlin Instruments) under nitrogen atmosphere at 200 °C. The parallel-plate geometry was used instead of the cone-and-plate geometry to avoid wall effects, and the latter are not significant if the parallel-plate gap is greater than three times the fiber length (Attanasio et al., 1972). For all experiments, the gap was around 1.5 mm with a plate diameter of 25 mm. Frequency sweep tests were performed from the highest to the lowest frequency in the linear domain (γ = 0.01). Before the dynamic measurements, the samples were pre-sheared at 1000 Pa during 1000 s to pre-align the fibers in the shear direction.

5.3.4. Samples

For the SER unit, rectangular samples (1.8 cm x 1.3 cm x 0.08 cm) were used. Given that the sample length and width are larger compared to the thickness, the filler was assumed to take a 2D planar orientation. Samples for three different initial fiber orientations were prepared as shown in **Figure 5.1**:

- The first case consisted in obtaining a planar random orientation (PRO) as illustrated in **Figure 5.1a**. Firstly, the materials were mixed into a Brabender internal mixer at 40 RPM at 200 °C under a nitrogen atmosphere for 5 min. Then, the blends were compressed at 200 °C into a rectangular mold of a thickness close to that of the final samples to minimize fiber orientation during compression. For sample PP30, the average fiber length was evaluated to be L = 320 μm after blending and calcination of the matrix at 500 °C for 40 min. Consequently the fiber aspect ratio was $r \approx 20$.

- In the second case samples with nearly fully aligned fibers were prepared. Strands were produced using a Leistritz twin screw extruder (type ZSE18HP-40D) and a converging slit die. Afterwards, two layers of the extruded tape were compression molded at 200 °C. The final samples were cut parallel (PARA, **Figure 5.1b**) and perpendicular (PERP, **Figure 5.1c**) to the extrusion flow direction. For these processing conditions, the average fiber length for PP30 was reduced to $L \approx 250$ μm: therefore, the aspect ratio became $r \approx 16$. It was verified that the samples had a uniform cross-section and were free of voids.

For the RME experiments, samples of 75 mm x 7 mm x 2.1 mm were obtained by compression molding of the strands produced in twin screw extrusion. Samples with parallel (PARA, **Figure 5.1b**) and with perpendicular (PERP, **Figure 5.1c**) fiber orientations were prepared.

In the case of the Rheotens experiments, pellets were used as received. The initial fiber orientation could not be controlled, but it is expected that large extrusion shear rates in the capillary rheometer will induce a high alignment of the fibers before the sample is stretched by the Rheotens.

5.3.5. Elongational rheometry

During elongational deformation, a tensile force $F(t)$ appears in the sample. The RME measures directly $F(t)$, whereas for the SER unit mounted on the ARES rheometer, $F(t)$ is determined according to the measured torque and the drum radius. The tensile stress growth function $\eta_E^+(t)$ at a constant Hencky rate $\dot{\varepsilon}$ is expressed as:

$$\eta_E^+(t) = \frac{\sigma(t)}{\dot{\varepsilon}} = \frac{F(t)}{\dot{\varepsilon}A(t)}, \tag{5.14}$$

where $A(t)$ is the instantaneous cross-sectional area, which evolves exponentially with time as:

$$A(t) = \left(\frac{\rho_0}{\rho}\right)^{2/3} A_0 \exp(-\dot{\varepsilon}t). \tag{5.15}$$

In Equation (5.15), ρ and ρ_0 are the densities at the test and room temperature, respectively, and A_0 is the initial cross-sectional surface of the unstretched specimen before sample loading. Assuming a similar uniform deformation in the thickness and the width (w), Equation (5.15) yields the width of the specimen being stretched as a function of time:

$$w = w_0 \exp(-\dot{\varepsilon} t/2), \tag{5.16}$$

where w_0 is the initial width at the test temperature.

Figure 5.2 reports the true Hencky strain rate applied in a typical RME test by analysing the width evolution versus time obtained by video camera. The results are presented for the unfilled matrix (PP0) and the 30 wt % filled polypropylene (PP30) in the initial PARA and PERP configurations. The nominal strain rate applied is 0.1 s^{-1}, and for the unfilled matrix (PP0), it is well reproduced as two times the slope gives the true Hencky rate [cf. Eq. (5.16)]. In the case of the filled PP large differences are observed, probably due to slip between the rotary clamps and the material as the tensile force increases considerably for filled systems. Surprising, the lowest true Hencky rate is observed for the PP30 – PERP sample, while the largest tensile stress was obtained for aligned fibers in the stretching direction (PP30 – PARA sample). It seems that for PP30 – PERP, the deformation of the width was not uniform. The insert in **Figure 5.2** depicts the width decrease for sample PP30 - PERP as measured in the middle (A-B), on the left (C-D) and on the right (E-F) side of the sample, close to the rotary clamps, respectively. It indicates that the deformation along the specimen length is uniform. Moreover, a

straight mark was initially placed along the width of the PP30 – PERP sample. With time, the marker deformed non-homogeneously, showing more pronounced strains at the edges than at the center of the samples. Hence, our RME data for the PARA samples were obtained under non-uniform deformation conditions. However, it is nearly impossible to assess the effect of the non-homogeneity on the measured elongational viscosity. Finally, for the SER data we were unable to verify if the deformation was uniform for containing fibers samples.

5.4. Results and discussion

5.4.1. Transient elongational viscosity

The transient elongational viscosities, η_E^+, of the unfilled matrix PP0 as well as that of the model suspension of beads in PP (PPB11), determined with the SER unit, are shown in **Figure 5.3**. Also shown is the predicted linear viscoelastic (LVE) behavior determined from the shear relaxation modulus after a step strain for PP0 and PPB11. For PP0, the curves are superposed for all applied strain rates at short times and coincide with the predictions of the linear viscoelastic regime; no strain hardening can be observed at any strain rate. For PPB11, again a good superposition in the linear viscoelastic regime at different Hencky rates is observed. As expected, the presence of glass beads induces no strain hardening, but increases slightly the elongational viscosity as compared to the neat polypropylene.

Figure 5.4 presents the transient elongational viscosity for samples PP30 – PARA and PP30 – PERP obtained with the SER unit at Hencky strain rates of 0.05 s^{-1} and 0.1 s^{-1}. **Figure 5.4** also reports the transient elongational viscosity obtained with the RME at true Hencky rates of 0.088 s^{-1} for PP30 – PARA and 0.068 s^{-1} for PP30 – PERP, respectively. For both samples, the data from the RME are located between the boundaries delimited by the SER data, as expected considering the applied strain rates. For PP30 – PERP, both the RME and SER data show a slight strain-hardening (this behavior is explained below). Except for the initial data at 0.1 s^{-1} for PP30 – PARA, these results are in good agreement and confirm that no slip occurred in the SER unit.

Figure 5.5 reports the transient elongational viscosity of fiber-filled sample PP30 for three different initial fiber orientations (shown in **Figure 5.1**). These samples have been stretched at a constant Hencky strain rate of 0.05 s^{-1}. Independently of the initial fiber orientation, the transient viscosity of the melt is strongly increased by the presence of the fibers and the steady-state regime is reached rapidly. As expected, the largest values are observed when the fibers are oriented parallel to the principal axis of the strain (fibers resist to the stretching). A slight strain-hardening behavior is observed for the PRO and PERP initial orientations, which could be explained by fiber alignment during the elongation test. The PRO sample showed a transient behavior between that of the PARA and PERP samples, as initially some fibers were already aligned and contributed to the largest stress (Batchelor, 1971; Dinh & Armstrong, 1984). Also the value of the transient elongational viscosity for PRO sample tends to reach that of the

pre-oriented sample, i.e. PP30 – PARA, while the PERP sample needs a much longer time to reach a similar orientation. If the deformation is assumed to be uniform during the tests, as we tried to verify with the RME, this would mean that the planar random orientation is transformed into a fully aligned orientation as the elongational test is performed. However, we cannot rule out a possible effect of the non-homogeneity of the flow.

To describe the observed trend of the elongational viscosity, the equation of change for the probability distribution function [Eq. (5.6)] is combined with the Dinh and Armstrong governing equation [Eq. (4.10)] for a Newtonian matrix in the transient case (the transient case has not been developed for the Carreau-based model). Appendix 1 presents the transient elongational viscosity obtained with the Dinh and Armstrong formulation, for which no closure approximation is needed. Details for setting the three initial probability functions (i.e. PARA, PRO and PERP) are given in Appendix 3. The matrix viscosity was taken as the zero-shear viscosity of the neat polypropylene (i.e. η_0 = 27 kPa.s) and the fitting parameters, μ_2 and C_I, were chosen to be equal to 85 and $0.001/\sqrt{3} \approx 0.00058$, respectively. The results are represented in **Figure 5.5** by the short dashed lines. At short times, the effect of the matrix elasticity is not described by the model formulated for a Newtonian matrix, but the purpose of these simulations is to highlight the effect of fiber orientation at large deformations. As expected, a plateau is predicted for fully aligned fibers in the stretching direction, which is in good agreement with the PP30 – PARA data. In the case of the initial planar random (PRO) fiber

orientation, a slight strain hardening is predicted, followed by a plateau when the fibers are totally aligned at long times or large Hencky strains. This is qualitatively in agreement with the data. For the initial perpendicular orientation (PERP) case, a slight decrease in the elongational viscosity is predicted, followed by a strong strain-hardening and then the steady plateau. Except for the initial decrease, the predictions are also in qualitative agreement with the data. Therefore, the model predictions confirm the observed transient behavior of the filled polypropylenes. Interestingly, the strain hardening in the PRO and PERP samples appears at the same Hencky strain, i.e. ε_H = 0.6. Strain hardening has been observed for the initial PERP orientation at different elongational rates and appear at the same Hencky deformation (ε_H = 0.6), as shown in **Figure 5.6**. As the applied elongational rate is increased the strain hardening becomes barely visible. This is a similar strain behavior as observed for the overshoot in shear flow of fiber filled polypropylenes (Ausias et al., 1992), and for reversible shear flow of model fiber suspensions (Sepehr et al., 2004d).

5.4.2. "Steady" elongational viscosity

In this section we report "steady" elongational viscosity data as final values (plateau region) of the transient elongational viscosity curves, which may not be the real steady-state regime in elongation. **Figure 5.7** compares the shear and elongational viscosities of various samples evaluated at the effective deformation rate $\dot{\gamma} = \sqrt{3}\dot{\varepsilon}$ where $\dot{\gamma}$ and $\dot{\varepsilon}$ are, respectively, the shear and Hencky rates. The "steady" values of the fiber filled PP presented in **Figure 5.7** were obtained with PARA samples for which closest

values to steady state were obtained. For comparison, the complex viscosity and steady-shear data for the neat PP (PP0) are also reported. It can be observed that for PP0 the Cox-Merz rule applies quite well. The zero-shear viscosity was determined using the Carreau-Yasuda model, for which the best fitting parameters were η_0 = 27 kPa.s, λ_m = 0.99 s, m = 0.28 and a = 0.51. At low Hencky rates, the Trouton ratio ($Tr = \eta_E/\eta_0$) for PP0 reaches the theoretical value of 3. With increasing strain rate, the elongational viscosity of PP0 shows a strain-thinning behavior, observed as well for the fiber-filled systems. The strain-thinning appears at lower strain rate as the fiber content increases. This phenomenon has also been observed for glass beads (Poslinski et al., 1988) and short glass fibers (Crowson & Folkes, 1980) suspensions in shear flow. Also shown in **Figure 5.7** are the new Carreau-base model predictions [Eq. (5.11)], where the fiber orientation was chosen as perfectly aligned in the stretching direction. Details of the calculations for the elongational flow are reported in Appendix 2. The fits are in very good agreement with the data and allow us to extrapolate the elongational viscosity at low strain rate. **Table 5.2** presents the values of the parameters used, along with the evaluated Trouton ratios for the fiber suspensions. The presence of fibers increases considerably the Trouton ratio defined by $\eta_{E_0}/\eta_0^{composite}$ where η_{E_0} is the elongational viscosity at low Hencky rates. The zero-shear viscosity of the suspensions $\eta_0^{composite}$ was estimated by fitting frequency sweep data for pre-sheared samples with the Carreau-Yasuda model. **Table 5.2** shows that the Trouton ratio increases from 3 for unfilled PP to 19.3 and 18.6 for PP20 and PP30, respectively. The slightly smaller Trouton ratio for PP30 compared to PP20 is possibly explained by small differences in fiber alignment in

simple shear for PP30 as compared to PP20. For a similar 30 wt % filled PP in planar extension, Mobuchon et al. (2005) found a Trouton ratio of about 54 at a deformation rate of 0.2 s^{-1} that decreases to 5.4 at 200 s^{-1}.

From Eq. (5.12), it is possible to determine the average distance *h* between fibers for the different fiber volume fractions and with the model parameters used to fit the data of **Figure 5.7**. **Table 5.2** lists the determined parameters and **Table 5.3** compares the average distances between fibers calculated using Eq. (5.12) with the theoretical values for perfectly aligned fibers from Eq. (5.8) (Doi & Edwards, 1978a, b). The results show that the fitted distances *h* are much smaller than the theoretical values for perfectly aligned fibers. A plausible explanation comes from Laun (1984), who suggests that macroscopic uniaxial elongation induces a complex flow between the rigid fibers on a microscopic scale (shear and elongation), as illustrated in **Figure 5.8**. Eq. (5.8) was developed for static conditions and, in elongation the average distance *h* is strongly influenced by hydrodynamic interactions and the matrix elasticity (a strong adhesion between the matrix and the fillers is expected as glass fibers are treated with silane). Therefore, developing an appropriate and meaningful theoretical expression for the coupling coefficient μ_2 remains a challenging task.

The specific elongational viscosity, η_E^{SP}, defined as $\eta_{E_0} - 3\eta_0(\phi = 0)/3\eta_0(\phi = 0)$, is presented in **Figure 5.9**. η_E^{SP} shows a high dependence on fiber volume fraction. The Batchelor expression [Eq. (5.1)] underestimates the data in the concentrated regime. A good agreement is obtained for PP10 and PP20 when the Petrie expression [Eq. (5.2)] is

used with $e = 1.24$. The formulation of Lubansky et al. [Eq. (5.3)] deviates considerably as the fiber concentration increases. The cited theories have been developed for semi-dilute systems and additional work is required to extend them to cover the concentrated regime.

Figure 5.10 presents the new Carreau-based model parameters, i.e. characteristic time related to the matrix λ_m and power-law index m, as functions of the fiber volume fraction. A decreasing linear dependence of λ_m with ϕ is observed, which indicates that the strain-thinning behavior appears more rapidly with increasing fiber content. A quadratic correlation gives a good approximation of the variation of m with the fiber volume fraction. The variation of the coupling coefficient μ_2 as a function of the power-law index m is reported in **Figure 5.11**. As m increases μ_2 decreases, indicating that at high Hencky rates, the elongational viscosity of the filled PP tends to reach that of the neat matrix.

The Rheotens experiments were performed for different shear rates under stable extrusion conditions. The elongational viscosity was calculated from the tensile force versus draw ratio using the Wagner et al. analysis (1998). For this purpose, the tensile force versus draw ratio curves were divided into two regions, namely, a linear one characteristic of the viscoelastic behavior at low draw ratios, and a non-linear one related to a purely viscous behavior of the unfilled PP and the suspensions at high draw ratios. Results for two different extrusion rates, 200 and 300 s^{-1}, are shown in **Figure 5.12** and compared with data obtained with the SER (from PARA samples) and the

planar hyperbolic die (Mobuchon et al., 2005) for samples PP0, PP10 and PP30. The effective deformation rate based on the second invariant of the rate-of-deformation tensor is used to report the data for different flows. Also, in order to compare planar and uniaxial elongational results, the elongational viscosity is normalized according to the Trouton ratio (3 for uniaxial and 4 for planar elongation) using the zero-shear viscosity values of the materials (listed in **Table 5.2**). Firstly, we note from **Figure 5.12** that the elongational viscosity increases with increasing fiber content, as expected. Secondly, the data from the three different instruments are in very good agreement from moderate to high strain rates, while discrepancies are observed at low rates for all samples. The Rheotens data cover lower elongational rates than those from the other two rheometers, and the low rate data for the neat PP (**Figure 5.12a**) are somewhat higher than the theoretical value expected from the Trouton relation. The range for the extrusion rate when operating the Rheotens is quite limited since extrusion at shear rates lower than 200 s^{-1} would induce premature filament crystallization, while for rates larger than 300 s^{-1} extrusion instability such as draw resonance would be observed. Between these two boundaries, the influence of the shear rate in the capillary die prior to the Rheotens experiments is negligible especially at large deformation rates. The Rheotens experiments have been repeated many times for the neat PP, confirming the trend reported in **Figure 5.12a**.

Again, it is interesting to note from **Figure 5.12** that the qualitative trend of the data obtained with the Rheotens, the hyperbolic die, and the SER are very similar, except for the much larger elongational viscosity values for the unfilled PP obtained at

lower deformation rates with the planar hyperbolic die (**Figure 5.12a**) and the very large values for the PP30 data obtained at low rates with the SER unit (**Figure 5.12c**). The trends depicted by both the Rheotens and the hyperbolic die data are coherent, suggesting that the elongational behavior is first strain-hardening at low strain rates, and then becomes strain-thinning at larger strain rates. However, the SER data rule out the possible strain hardening at moderate rates (> 0.1 s^{-1}) with a smooth decrease of the elongational viscosity with strain rate. The observed discrepancies between the SER results and those of the other techniques may be explained by the different flow kinematics in the converging die and in the Rheotens experiments. Finally, we note that the trend for the elongational behavior of the suspensions is similar to that of the unfilled matrix, with an almost constant viscosity value at low extensional rates and a strain-thinning behavior at high elongation rates.

5.5. Concluding remarks

In this work, the elongational flow behavior of short glass fiber-filled polypropylenes was investigated for different fiber contents and initial fiber orientations. The presence of the fibers increased considerably the elongational viscosity, and the dynamic fiber orientation during tensile tests induced a slight strain hardening. The transient elongational viscosity was observed to be strongly dependent on the initial fiber orientation and considerably larger transient values were obtained for initially aligned fibers in the flow direction. The Dinh and Armstrong governing equations coupled with a finite volume method was used to solve the probability distribution

function and predict the transient elongational viscosity of the materials. The predictions were qualitatively in good agreement with the experimental data.

We have compared the "steady" elongational viscosity data as a function of the effective deformation rate obtained from three different rheometers: a SER unit mounted on an ARES, a slit die with a hyperbolic entrance and a Rheotens. At low strain rates, discrepancies were observed in the data from the three rheometers; however, the superposition of the data was astonishingly good at moderate to high strain rates for all materials investigated. The elongational behavior of the composites was found to be similar to that of the polymer matrix over the range of strain rates investigated, with a plateau at low elongational rates and strain-thinning at large rates. A novel constitutive equation was proposed to calculate the steady-state elongational viscosity of fiber suspensions in a generalized Newtonian fluid (GNF) described by the Carreau model. This model predicts fairly well the fiber-filled polypropylene behavior over the range of Hencky rate investigated in this study.

5.6. Acknowledgements

This work was supported by the France-Québec collaboration program and funded by NSERC (Natural Science and Engineering Research Council of Canada – CIAM program), and by CONACYT (CIAM 51837) and SIP-IPN (20060296-20070642) in México. The authors wish to thank Dr. G. Krotkine from Basell who kindly provided the materials used in this study. We are also thankful to Ms. M.J. Ramirez-Moreno, from the Instituto Politécnico Nacional in Mexico City (Mexico) for

the Rheotens measurements, to Mr. J.R. R.-Siffert, from Pontificia Universidade Católica-RJ in Rio de Janeiro (Brazil) for helpful sample preparation and preliminary tests, and to Christophe Mobuchon for the Binding analysis of the slit die data. Finally, the authors wish to acknowledge Dr. S. Dagreou and Dr. F. Leonardi at the University de Pau for the use of their RME.

5.7. Appendix 1

From the Dinh and Armstrong expression (Dinh & Armstrong, 1984), the normal stress components are defined as:

$$\sigma_{11} = 2\eta_0\dot{\varepsilon} + \eta_0\phi\mu_2\left(2a_{1111} - a_{1122} - a_{1133}\right)\dot{\varepsilon}, \tag{5.17}$$

$$\sigma_{22} = -\eta_0\dot{\varepsilon} - \eta_0\phi\mu_2\left(-2a_{1122} + a_{2222} + a_{2233}\right)\dot{\varepsilon}, \tag{5.18}$$

$$\sigma_{33} = -\eta_0\dot{\varepsilon} - \eta_0\phi\mu_2\left(-2a_{1133} + a_{2233} + a_{3333}\right)\dot{\varepsilon}. \tag{5.19}$$

According to the definition of Eq. (5.13) , the transient elongational viscosity is written as:

$$\eta_E^+ = 3\eta_0 + \eta_0\phi\mu_2\left(2a_{1111} - 2a_{1122} - 2a_{1133} + a_{2233} + \frac{1}{2}a_{2222} + \frac{1}{2}a_{3333}\right). \tag{5.20}$$

Thanks to the equation of change for ψ, the fourth-order orientation tensor components are determined easily and the transient extensional viscosity is expressed without the need of a closure approximation for the fourth-order tensor.

5.8. Appendix 2

Eq. (5.11) is used to express the steady extensional flow in the case where fibers are perfectly aligned in the principal stretching direction ($\mathbf{x}_1$). Therefore the orientation distribution function is simply a Dirac function:

$$\psi = \delta(\mathbf{p} - \mathbf{x}_1). \tag{5.21}$$

Then the normal stress components are given by:

$$\sigma_{11} = 2\dot{\varepsilon}\eta_0\left[1+\left(\lambda_m\sqrt{3}\dot{\varepsilon}\right)^2\right]^{\frac{m-1}{2}} + 2\dot{\varepsilon}\eta_0\phi\mu_2\left[1+\left(\lambda_f 2\dot{\varepsilon}\right)^2\right]^{\frac{m-1}{2}}, \tag{5.22}$$

$$\sigma_{22} = \sigma_{33} = -\dot{\varepsilon}\eta_0\left[1+\left(\lambda_m\sqrt{3}\dot{\varepsilon}\right)^2\right]^{\frac{m-1}{2}}. \tag{5.23}$$

Consequently the steady elongational viscosity is written as:

$$\eta_E = 3\eta_0\left[1+\left(\lambda_m\sqrt{3}\dot{\varepsilon}\right)^2\right]^{\frac{m-1}{2}} + 2\eta_0\phi\mu_2\left[1+\left(\lambda_f 2\dot{\varepsilon}\right)^2\right]^{\frac{m-1}{2}}, \tag{5.24}$$

where λ_m, m, μ_2 and λ_f are used as fitting parameters.

5.9. Appendix 3

In order to achieve model predictions for the transient elongational viscosity, initial orientation functions have to be defined to take into account the three initial fiber orientations of **Figure 5.1**. Following Advani and Tucker (Advani & Tucker, 1987), highly orientated states (i.e. parallel and perpendicular to the stretching direction) are obtained by a non-conventional distribution function having the form:

$$\psi(\varphi,\theta) = K_{\perp}\sin^{p}\theta\,\sin^{q}\varphi \quad \text{for PERP,} \tag{5.25}$$

$$\psi(\varphi,\theta) = K_{=}\sin^{p}\theta\,\cos^{q}\varphi \quad \text{for PARA,} \tag{5.26}$$

where $K_{\perp}$ and $K_{=}$ are constants that satisfy the normalization condition. Both p and q are taken equal to 60 to give aligned fiber orientation. The planar random orientation state (not to be confused with a bi-planar orientation obtained by adding Eqs. (5.25) and (5.26) with respect to the normalization condition) is reached with the following distribution function:

$$\psi(\varphi,\theta) = K_{\times}\delta\left(\theta - \frac{\pi}{2}\right) \quad \text{for PRO,} \tag{5.27}$$

where δ is the Dirac function and $K_{\times}$ is introduced to respect the normalization condition.

Table 5.1 : Sample nomenclature, fiber content and density.

Sample	ϕ [%]	Regime	ρ [kg/m^3]	η_0 [kPa.s]
PP0	0	-	760	27.0
PP10	3.3	semi-dilute	817	34.0**
PP20	7.1	concentrated	883*	41.0**
PP30	11.5	concentrated	961	69.0**

* calculated

** pre-sheared samples

Table 5.2 : Elongational parameter values for Eq. (5.11).

	η_0^{matrix} [kPa.s]	η_0 [kPa.s]	λ_m [s]	m [-]	λ_f [s]	μ_2 [-]	η_{E0} [kPa.s]	Tr [-]
PP0	27.0	27.0	3.64	0.71	-	-	81.0	3.0
PP10	27.0	34.0	3.06	0.59	23.96	116.9	289	8.5
PP20	27.0	41.0	2.19	0.51	38.94	185.9	793	19.3
PP30	27.0	69.4	1.30	0.46	30.95	194.3	1290	18.6

Table 5.3 : Calculated average distance between fibers.

		PP10	PP20	PP30
h	From Eq. (5.8) (aligned)	78.1	53.2	41.8
[μm]	From Eq. (5.12)	9.67	8.35	8.18

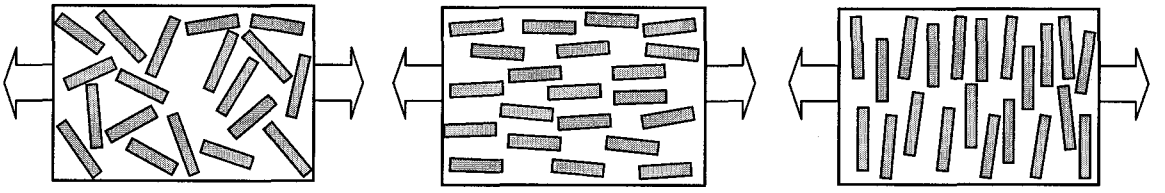

(a) (b) (c)

Figure 5.1 : Schematic representation of the three different initial fiber orientations used with the SER unit: (a) PRO: planar random orientation, (b) PARA: fibers aligned parallel to the extensional flow direction and (c) PERP: fibers oriented perpendicularly to the elongational flow direction. The arrows indicate the stretching flow direction.

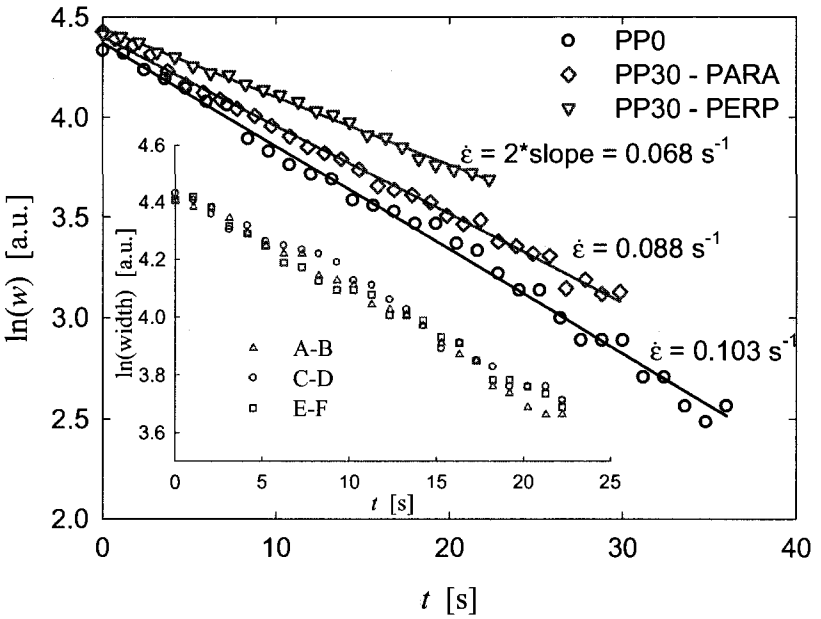

Figure 5.2 : Hencky strain rate as measured by a video camera for the unfilled matrix (PP0), for 30 wt % fiber filled polypropylene with fibers aligned parallel to the flow (PP30 – PARA) and perpendicular (PP30 – PERP) to the stretching direction. The nominal Hencky strain rate was 0.1 s^{-1}. Also shown in the insert are the width changes for PP30 - PERP in the middle of the sample (A-B), and close to the left (C-D) and right (E-F) of the rotary clamps.

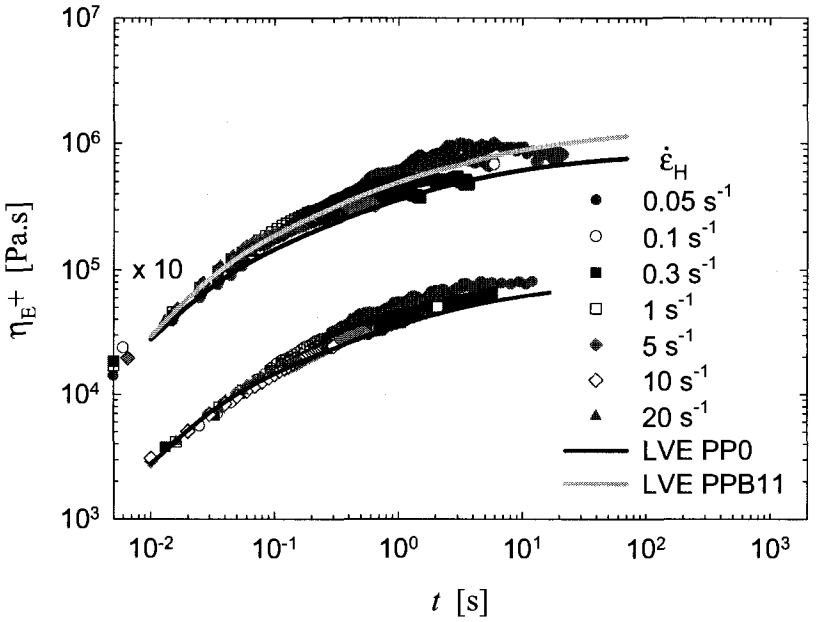

Figure 5.3 : Transient elongational viscosity of the unfilled matrix PP0 and the glass bead filled polypropylene PPB11 (values multiplied by 10) at 200 °C for Hencky strain rates ranging from 0.05 to 20 s^{-1} obtained with the SER unit. Also shown is the predicted LVE behavior as determined from the shear relaxation modulus after a step strain.

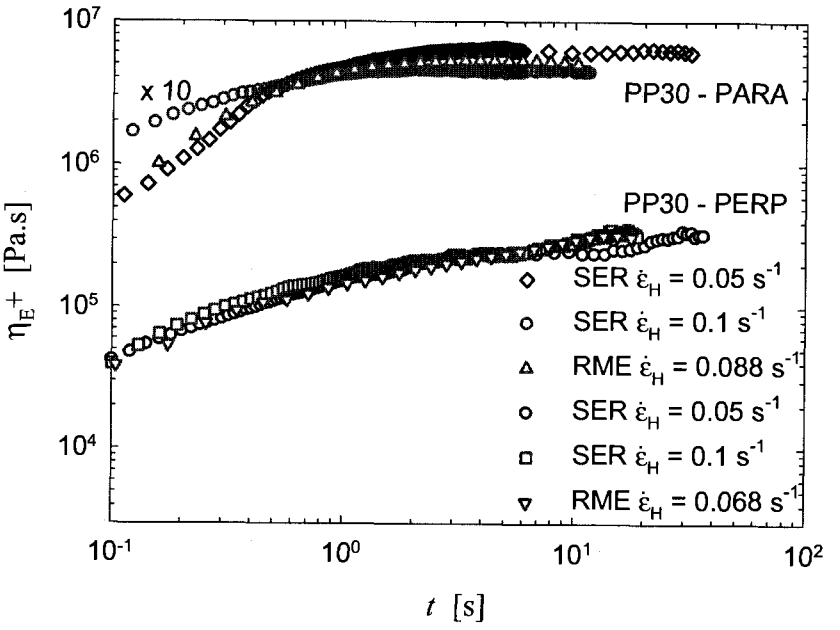

Figure 5.4 : Comparison of the transient elongational viscosity of the 30 wt % fiber filled polypropylene with fiber parallel (PP30 – PARA) and perpendicular (PP30 – PER) to the stretching direction obtained with the SER unit (at Hencky rates of 0.05 and 0.1 s^{-1}) and with the RME (at the corrected Hencky rates).

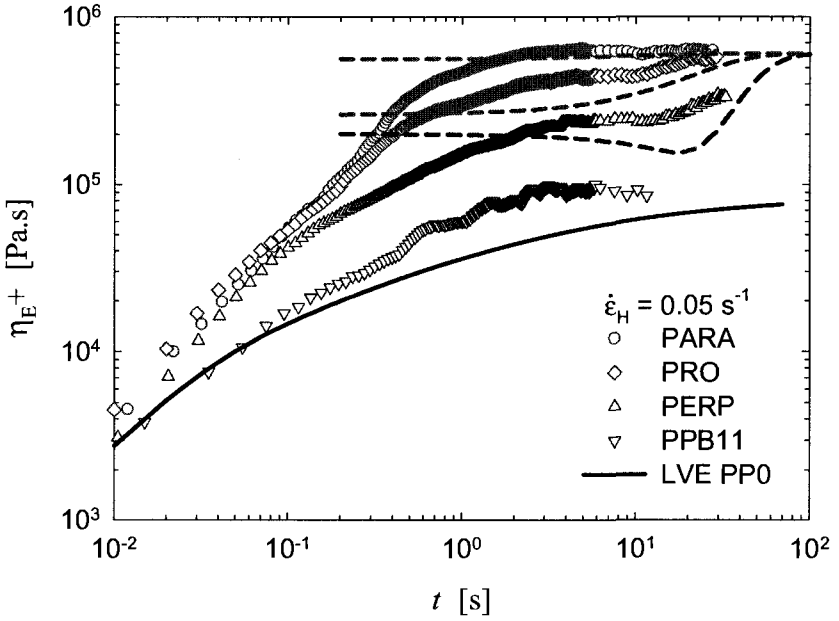

Figure 5.5 : Transient elongational viscosity at a Hencky strain rate of 0.05 s^{-1} for PP30 with different initial fiber orientations: (a) parallel to the stretching direction, PARA, (b) planar random orientation, PRO and (c) perpendicular to the stretching, PERP. Also shown is the transient elongational viscosity for PPB11 and the LVE regime of PP0 for the purpose of comparison. The dashed lines represent the model predictions (Eqs. 5, 6 and 20) for the different initial fiber orientations.

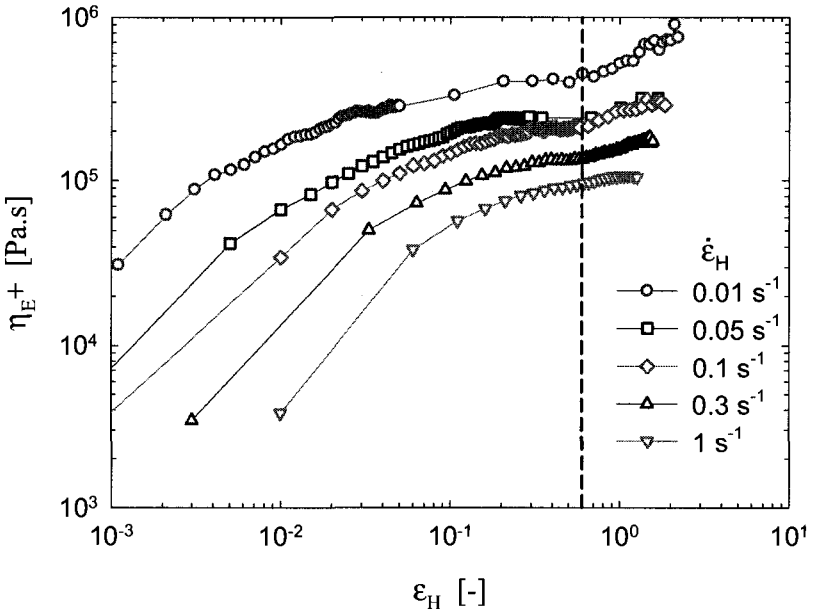

Figure 5.6 : Transient elongational viscosity as a function of Hencky deformation at different strain rates for PP30 with the initial fiber orientation perpendicular to the stretching direction.

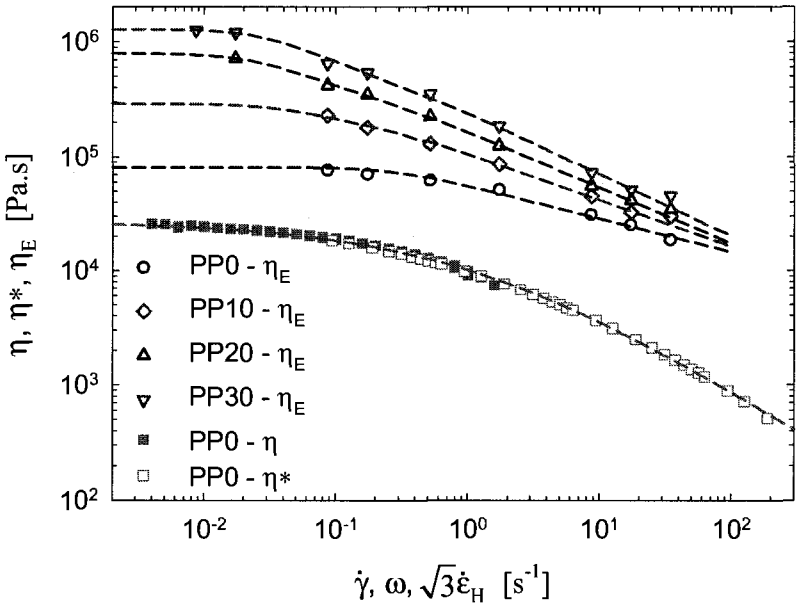

Figure 5.7 : Shear and elongational viscosities of PP0. Also shown are the elongational viscosity data of fiber filled PP when the fibers are aligned (obtained from PARA data in elongation). The dashed lines represent the model predictions.

Figure 5.8 : Schematic illustration of microscopic distortions produced by aligned fibers in uniaxial elongation: (a) initial state with length L_0 and (b) elongated state with $L = 2L_0$ [taken from Laun (1984)].

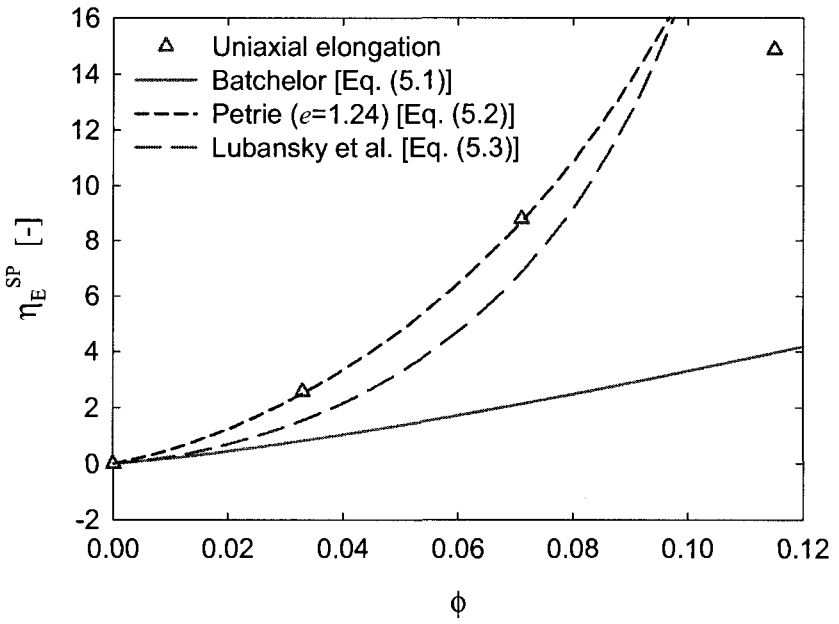

Figure 5.9 : Specific elongational viscosity of polypropylene systems. Also shown are the predictions of various models for the uniaxial elongational viscosity.

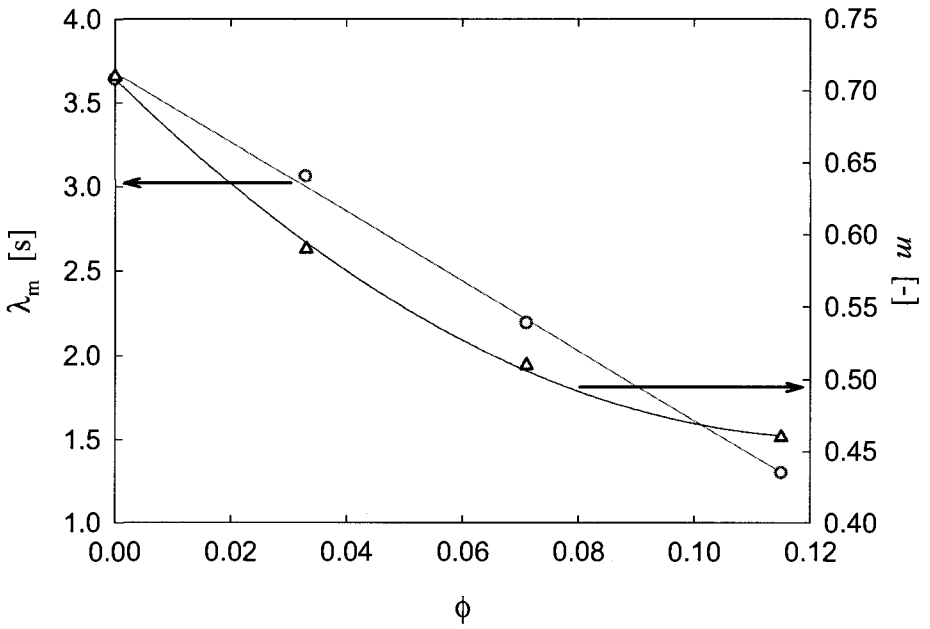

Figure 5.10 : Matrix characteristic time and power-law index as functions of fiber volume fraction. The lines represent the best fits (linear for λ_m and quadratic for m).

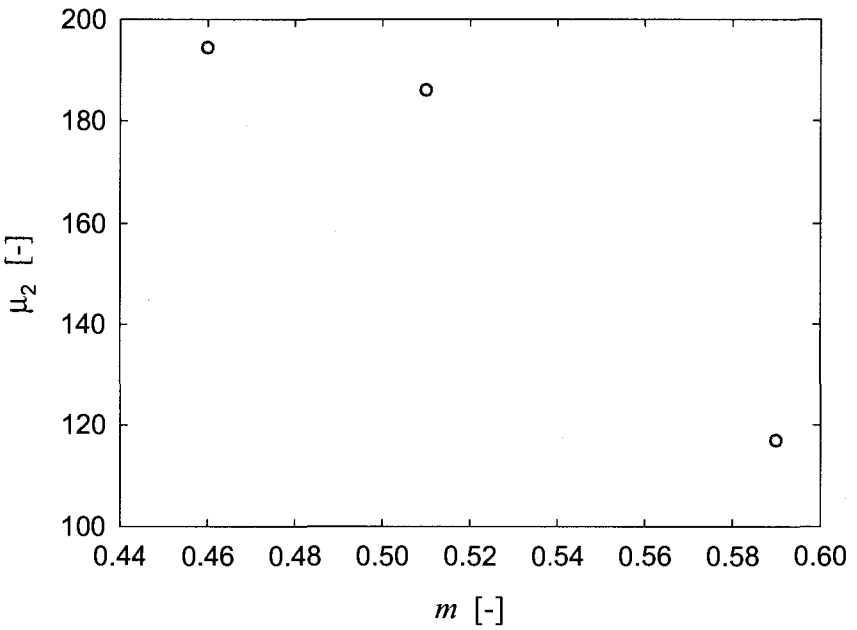

Figure 5.11 : Coupling coefficient μ_2 as a function of the power-law index m.

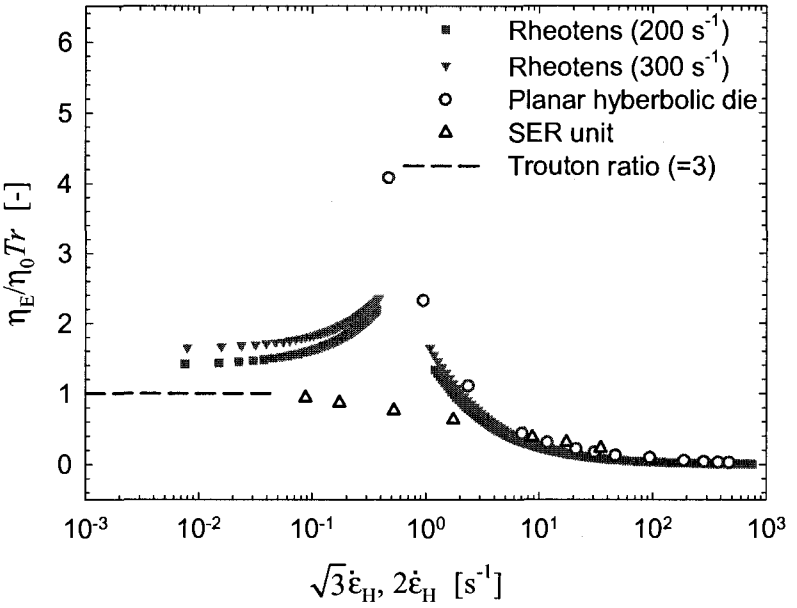
Rheotens (200 s-1)
Rheotens (300 s-1)
Planar hyberbolic die
SER unit
Trouton ratio (=3)
ηE/η0Tr [-]
√3ε̇H, 2ε̇H [s-1]

(a)

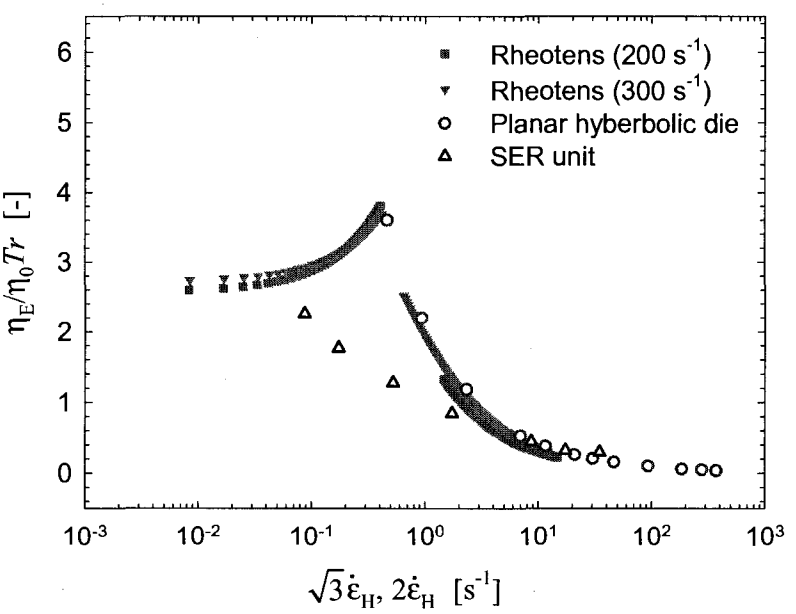
Rheotens (200 s-1)
Rheotens (300 s-1)
Planar hyberbolic die
SER unit
ηE/η0Tr [-]
√3ε̇H, 2ε̇H [s-1]

(b)

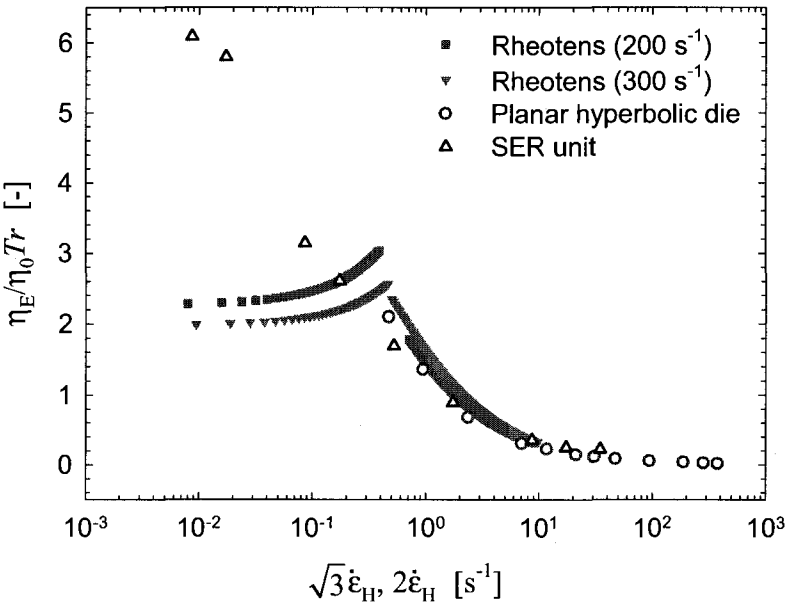

(c)

Figure 5.12 : Comparison of the reduced "steady" elongational viscosity of PP and its composites from measurements using three different instruments: (a) PP0, (b) PP10 and (c) PP30.

CHAPITRE 6 - ARTICLE: NUMERICAL SOLUTION OF THE FOKKER-PLANCK EQUATION FOR FIBER SUSPENSIONS: APPLICATION TO THE FOLGAR-TUCKER-LIPSCOMB MODEL*

J. Férec [a, b], M. Heniche [a], M.C. Heuzey [a], G. Ausias [b] and P.J. Carreau [a]

[a] *Center for Applied Research on Polymers and Composites (CREPEC), Chemical Engineering Department, École Polytechnique de Montréal, PO Box 6079, Stn Centre-Ville, Montreal, QC, Canada H3C3A7*

[b] *Laboratoire d'Ingénierie des MATériaux de Bretagne (LIMATB) Université de Bretagne Sud, rue de St Maudé, 56325 Lorient, France*

Abstract

The probability distribution function for fiber orientation under flow (Fokker-Planck equation) is numerically solved using a finite volume method. Different time and spatial schemes have been tested to reduce considerably the computational time and to cover a wide range of the Peclet (Pe) number. For $Pe \leq 10^3$, the results are compared with data available in the literature and for $Pe \geq 10^3$, the numerical schemes are assessed using an analytical solution. Excellent agreement was observed and the method allowed us to describe the evolution of the fourth order orientation tensor components of fibers in transient simple shear (forward and reverse) flows, and compare with the predictions of an orthotropic closure approximation. In addition, the Folgar-Tucker-Lipscomb (FTL) model was used with no closure approximation to predict the rheological behavior of a

---

* Cet article a été soumis à Journal of Non-Newtonian Fluid Mechanics.

short fiber-filled polypropylene in simple shear flow. The accuracy of commonly used closure approximations is discussed, and key aspects of the FTL model that still need to be improved are highlighted in the scope of this work.

6.1. Introduction

Thermoplastics reinforced by short glass fibers are widely used in the manufacturing industry as their physical properties are enhanced compared to the unfilled matrix. Fiber orientation and dispersion determine the degree of improvement. The rheological behavior of filled systems is generally quite complex due to the strong coupling between fiber orientation and flow. Understanding how fibers evolve with flow can considerably help to predict the microstructure and the ultimate properties.

The complete orientation of a single fiber can be described by a unit vector **p** directed along its principal axis, or equivalently by the spherical coordinates φ and θ. A distribution function $\psi(\mathbf{r},\mathbf{p},t)$ is introduced to take account of the specific mass center position **r** and orientation **p** at time t of a fiber. Several studies have been devoted to steady flows for $\psi(\mathbf{r},\mathbf{p})$ (Chiba et al., 2005; Chinesta et al., 2000; Chinesta et al., 2003; Mokdad et al., 2007). Here we focus on homogeneous flows in the absence of fiber concentration gradients. Therefore, the probability distribution function reduces to $\psi(\mathbf{p},t)=\psi$.

Jeffery (1922) was the first to develop an expression for the time evolution of **p** for a single spheroid suspended in a Newtonian fluid in the absence of external torque. More recently, Folgar and Tucker (1984) added to Jeffery equation a phenomenological diffusion term in order to take into account fiber interactions. Therefore, a general form of the time evolution for particles can be written as (Advani & Tucker, 1987):

$$\dot{\mathbf{p}} = \dot{\mathbf{p}}_{\mathrm{H}} - \frac{D_r}{\psi}\nabla\psi = -\frac{1}{2}\boldsymbol{\omega}\cdot\mathbf{p} + \frac{\lambda}{2}\left(\dot{\boldsymbol{\gamma}}\cdot\mathbf{p} - \dot{\boldsymbol{\gamma}}:\mathbf{ppp}\right) - \frac{D_r}{\psi}\nabla\psi, \tag{6.1}$$

where $\boldsymbol{\omega}$ and $\dot{\boldsymbol{\gamma}}$ are the vorticity and deformation rate tensors, respectively. ∇ is the differential operator $\partial/\partial\mathbf{p}$ (Bird et al., 1987b). The shape factor $\lambda = (r^2-1) / (r^2+1)$ is a parameter related to the particle aspect ratio, r ($r = L/D$ for a cylindrical particle, where L and D are its length and diameter, respectively), and D_r is the rotary diffusivity. For $D_r = 0$, the Jeffery equation ($\dot{\mathbf{p}}_{\mathrm{H}}$) is recovered; for $D_r = 0$ and $\lambda = 1$, the Dinh and Armstrong (1984) result developed for slender particles is obtained; finally for $D_r = C_I\left|\dot{\gamma}\right|$, Equation (6.1) is the Folgar and Tucker (1984) expression, where C_I is the interaction coefficient and $\left|\dot{\gamma}\right|$ the effective deformation rate.

To deal with a fiber population instead of a single fiber, the orientation distribution function ψ is introduced (Advani & Tucker, 1987). It represents the probability of finding a fiber between the angles φ and $(\varphi + d\varphi)$, and between θ and $(\theta + d\theta)$. The distribution function ψ must respect the normalization condition and must be periodic as the particle ends are indissociable. Moreover, ψ may be regarded as a convected scalar in the sense that when a fiber leaves one orientation, it must appear in another one. From Bird et al. (1987b), the continuity relation can be expressed as:

$$\frac{D\psi}{Dt} = -\nabla\cdot\left(\dot{\mathbf{p}}\psi\right), \tag{6.2}$$

where D/Dt represents the material derivative and reduces to partial derivative in the case of homogenous flows. Combining Equation (6.1) with Equation (6.2), we obtain the following time evolution of the probability distribution function:

$$\frac{D\psi}{Dt} = -\nabla \cdot \left(\dot{\mathbf{p}}_{\mathrm{H}}\psi\right) + D_r \nabla^2 \psi, \tag{6.3}$$

where the Laplacian operator, ∇^2, refers to $\partial^2/\partial\mathbf{p}^2$ (Bird et al., 1987b). This expression is known as the Fokker-Planck equation and has been the subject of numerous investigations in order to predict the fiber distributions for steady shear flows. Advani and Tucker (1990a) have solved Equation (6.3) for transient flows in order to propose accurate closure approximations. They used a finite difference technique with an implicit time derivative and a central difference formula for the φ and θ derivatives. At each time step, the solution was obtained using a Gauss-Seidel relaxation method. Nevertheless, the global conservation of the numerical method was destroyed by the use of following boundary conditions: $\psi(\varphi,\theta=0)=\psi(\varphi,\theta=\pi)=0$. The latter state that there is no probability of finding fibers oriented in the $(\varphi,\theta=0)$ and $(\varphi,\theta=\pi)$ directions, which is not always correct. Therefore, the distribution function needs to be re-normalized in a post-processing step after each time iteration (Advani, 1987), which could incorporate inaccuracies in the calculations. Strand et al. (1987) applied the Galerkin method to resolve the Fokker-Planck equation, using basis functions that were spherical harmonics. A set of ordinary differential equations in time was then obtained and solved by the spectral method. Solutions up to Peclet numbers (shear rate / rotary

diffusivity), Pe, equal to 60 were possible, as a constraint was imposed by the ill-conditioning of the modal matrix. Kamal and Mutel (1989) have adopted a finite difference algorithm to evaluate the unsteady convection – diffusion problem. To cover a wide range of Peclet number, a power-law scheme was implemented to interpolate properties between the nodes (Mutel, 1989). Periodic boundary conditions were applied and the numerical solution was obtained with a cyclic tridiagonal-matrix algorithm (C-TDMA). For various values of Pe (with a max = $2 \cdot 10^4$), Kamal and Mutel (1989) got accurate results but they did not mention the computational time required. In his work, Bay (1991) solved the Fokker-Planck equation using a finite volume method, which did not need re-normalization. The explicit time integration and the centered difference formulas did not allow to reach solutions for Pe $\geq 10^2$ except by reducing the time step, which required very long CPU times (Bay, 1991). Han and Im (1999) were able to solve numerically the Fokker-Planck equation with a finite element method using triangular elements, but only for a maximum Peclet number of 10^3. In a recent investigation by Mandal (2004), Equation (6.3) was also cast into a finite difference technique using a Crank-Nicholson time scheme. The solution at each time step was obtained by a LU decomposition, where L and U are lower and upper triangular matrices, and its efficiency was verified with the normalization condition. The author showed results up to Pe = 10^2.

Advani and Tucker (1987) defined the moments of the probability distribution function, known as the orientation tensors. They are formed by the dyadic products of **p** averaged over the orientation space, with ψ as the weighting function. The second- and

fourth-order orientation tensors $\mathbf{a}_2$ and $\mathbf{a}_4$, which are generally used in rheological modeling, are given by Advani and Tucker (1987) as:

$$\mathbf{a}_2 = \int_{\mathbf{p}} \mathbf{pp}\psi \, d\mathbf{p}, \tag{6.4}$$

$$\mathbf{a}_4 = \int_{\mathbf{p}} \mathbf{pppp}\psi \, d\mathbf{p}. \tag{6.5}$$

These orientation tensors are symmetric and respect the normalization conditions (i.e. $\mathbf{a}_2$ has five independent components). From the two previous definitions and with the help of Equation (6.3), Advani and Tucker (1987) obtained the following time evolution for the second orientation tensor:

$$\frac{D\mathbf{a}_2}{Dt} = -\frac{1}{2}(\boldsymbol{\omega}\cdot\mathbf{a}_2 - \mathbf{a}_2\cdot\boldsymbol{\omega}) + \frac{1}{2}\lambda(\dot{\boldsymbol{\gamma}}\cdot\mathbf{a}_2 + \mathbf{a}_2\cdot\dot{\boldsymbol{\gamma}} - 2\dot{\boldsymbol{\gamma}}:\mathbf{a}_4) + 2C_I|\dot{\gamma}|(\boldsymbol{\delta} - 3\mathbf{a}_2), \tag{6.6}$$

where $\boldsymbol{\delta}$ represents the identity tensor. The fourth-order orientation tensor $\mathbf{a}_4$ appears in this expression. In order to determine $\mathbf{a}_4$, the sixth-order tensor has to be known, and so forth. That is why a closure approximation is needed to express the $\mathbf{a}_4$ components as a function of $\mathbf{a}_2$. Different hypothesis for closure approximations have been suggested in the literature. The earliest ones were based on the linear (Hand, 1961) and quadratic (Doi & Edwards, 1986) assumptions. Advani and Tucker (1990a) have proposed a combination known as the hybrid closure. However, better accuracy is obtained by using natural (Verleye et al., 1994) and orthotropic closure approximations (Cintra & Tucker, 1995). The first one is based on the invariant of $\mathbf{a}_2$, whereas the second one is constructed using the eigenvalues of $\mathbf{a}_2$. Cintra and Tucker (1995) have developed the ORS (orthotropic smooth closure) approximation, which consists of a linear

interpolation between extreme cases (isotropic, planar random and fully oriented) of fiber orientation. This was found to predict a very poor behavior when modeling flow-induced orientation. Then, Cintra and Tucker (1995) used a second order polynomial interpolation, where the coefficients were fitted from five different flow data and the orientation distribution function was numerically solved for $C_I = 0.01$ and $|\dot{\gamma}| = 1\ s^{-1}$. The solution obtained from the derived ORF (orthotropic fitted closure) predicted non-physical oscillations when C_I became small. By solving the orientation distribution function for $C_I = 10^{-3}$, the fitting procedure led to the ORL (orthotropic closure, fitted for low C_I). Chung and Kwon (2001) optimized the fit by using a 2nd order polynomial expansion of the two largest eigenvalues of $\mathbf{a_2}$ over a wide range of C_I. They increased from five to eight the number of flow situations fitted and proposed the ORW closure (orthotropic fitted closure for a wide range of C_I). Recently, improvements were obtained with the ORW3 (orthotropic fitted closure for a wide range of C_I with a 3rd order polynomial expansion) (Chung & Kwon, 2001).

In the present work, we have developed a robust and fast numerical method to solve the probability distribution function. The overall objective of this work is divided into three distinct parts. The first one consists in solving the Fokker-Planck equation over a wide range of values of the interaction coefficient C_I. The computational time required for various conditions should not depend on the values of the shear rate and the interaction coefficient used, and should be reasonable. In the second part, the performance of the most recent orthotropic closure approximation (ORW3) is tested for

transient forward stress growth and especially reverse flows, for which the initial orientation is not isotropic (the development of the closure approximation was done for the forward direction with an initial isotropic orientation). Finally, the probability distribution function is used to predict the rheological behavior of a 30 wt % fiber filled polypropylene under shear flow. In this case, no closure approximation is needed and it allows to assess the real performance of the Folgar-Tucker-Lipscomb (FTL) model (Sepehr et al., 2004c).

6.2. Calculation of the orientation distribution function

The Fokker-Planck equation [Eq. (6.3)] has to be solved numerically except under specific conditions, where some analytical solutions are available. A dimensionless form for Eq. (6.3) by using the following notation changes: $\dot{\gamma} = \dot{\gamma}\,\dot{\gamma}^*$, $\boldsymbol{\omega} = \dot{\gamma}\,\boldsymbol{\omega}^*$, $\tau = tD_r$ and the Peclet number Pe = $\dot{\gamma}/D_r$., is:

$$\frac{D\psi}{D\tau} = -\mathrm{Pe}\nabla\cdot\left(\dot{\mathbf{p}}_{\mathrm{H}}^{*}\psi\right) + \nabla^2\psi, \tag{6.7}$$

where $\dot{\mathbf{p}}_{\mathrm{H}}^{*}$ is the dimensionless hydrodynamic contribution given by the Jeffery equation (Strand et al., 1987).

6.2.1. Discretization by the finite volume method

When the effects of diffusion are important (Pe $\neq \infty$), there is no analytical solution of the Fokker-Planck equation and then, the recourse to a numerical solution is required. Following the work of Bay (1991), a finite volume method is chosen because it

is well known for its local conservativeness property needed to respect the normalization condition, which is included in the formalism of the model. The surface of the unit sphere is discretized with incremental areas $\Delta A = \sin\theta\,\Delta\varphi\,\Delta\theta$, where $\Delta\theta$ and $\sin\theta\,\Delta\varphi$ are the edge lengths. **Figure 6.1** depicts the control volume used to perform the flux balance. As ψ is symmetric, only one half of the sphere is meshed in order to reduce the computational time. Consequently, the node number in the θ-direction is the same as the one in the φ-direction. Also, to evaluate the probability distribution function and the derivatives appearing in the diffusion terms at the four boundaries, a central differencing approach is employed as the variations are assumed linear (different schemes for the discretization of Eq. (6.7) have been implemented in the past, namely central, upwind, hybrid differencing and power-law (Versteeg & Malalasekera, 1995)). Therefore, the discretized form of the Fokker-Planck equation [Eq. (6.7)] is:

$$\begin{aligned}&(a_M+\alpha a_P)\psi_P^{\tau+\Delta\tau}-\alpha a_E\psi_E^{\tau+\Delta\tau}-\alpha a_W\psi_W^{\tau+\Delta\tau}-\alpha a_N\psi_N^{\tau+\Delta\tau}-\alpha a_S\psi_S^{\tau+\Delta\tau}=\\&(1-\alpha)a_E\psi_E^{\tau}+(1-\alpha)a_W\psi_W^{\tau}+(1-\alpha)a_N\psi_N^{\tau}+(1-\alpha)a_S\psi_S^{\tau}+\left[a_M-(1-\alpha)a_P\right]\psi_P^{\tau}\end{aligned} \tag{6.8}$$

When $\alpha = 0$, the explicit scheme is recovered (Bay, 1991); $\alpha = 1$ gives the fully implicit scheme and the Crank-Nicholson scheme is obtained for $\alpha = 0.5$. The appendix details the expressions for the coefficient a_E, a_W, a_N, a_S, a_M and a_P. As done by Bay (1991), the following periodic boundary conditions are applied to calculate the distribution function (**Figure 6.2**):

$$\psi(\varphi,\theta)=\psi(\varphi,\theta+\pi), \tag{6.9}$$

$$\psi(\varphi,\theta)=\psi(\varphi+\pi,\pi-\theta). \tag{6.10}$$

Most frequently in the literature the initial orientation was assumed to be isotropic, or $\psi(\varphi,\theta) = 1/4\pi$. Given that most of the distanced off diagonal entries are zeros, the global matrix is stored with the skyline scheme (Dhatt & Touzot, 1984). Therefore, the whole matrix is factorized with a LU decomposition only once (at the first time iteration) because the matrix remains unchanged. At each time iteration, the right-hand side of Eq. (6.8) is updated and the transient solution is then obtained by a forward-backward resolution procedure. The appropriate time step $\Delta\tau$ is the minimum value chosen between $\Delta\tau = 0.1/\mathrm{Pe}$ (user setting) (Han & Im, 1999), $\Delta\tau = \mathrm{Cr}\Delta\theta/\dot{\theta}$ or $\Delta\tau = \mathrm{Cr}\Delta\varphi/\dot{\varphi}$ in order to ensure scheme stability. Cr is the Courant number (ratio of a time step to a cell residence time: it is ≤ 1 when convection dominates) and is set equal to 1. Fortran 90 programming language was used to write the distribution function computational code. All the simulation results presented hereafter were computed on a Linux PC (series 6219-38, Pentium IV, 2.8 GHz, 1 Go RAM).

6.2.2. Accuracy of the numerical method

At each time step the distribution function was computed, and the orientation tensor components of $\mathbf{a_2}$ and $\mathbf{a_4}$ could be evaluated using Equations (6.4) and (6.5). **Figure 6.3** depicts the computed non-zero components of $\mathbf{a_2}$ (except the a_{33} component that can be obtained from the trace of $\mathbf{a_2} = a_{11} + a_{22} + a_{33} = 1$) for simple shear flow (1, 2 and 3 are the velocity, gradient and vorticity directions, respectively). The central scheme was applied and a 40x40 cell grid was used. For the numerical solution, the shape factor was set to $\lambda = 1$. **Figure 6.3** also shows the results of Advani (1987) and

Bay (1991) obtained using finite difference and finite volume methods, respectively. Globally, our numerical predictions are in very good agreement with the results of the two previous investigations. Solutions up to a Peclet number, Pe = 10^3 were obtained and for all cases the CPU time was less than one minute. This is to be compared with the work of Bay (1991), where few days of CPU time were required for Pe = 10^2. In fact, even with modern computers the program used by Bay and tested in the scope of our work would require very long calculation times.

Different time and spatial schemes were employed and **Table 6.1** shows the required CPU times for various combinations. The time step was fixed as $\Delta\tau = 0.1/\mathrm{Pe}$ for a total flow time, t_{max}, = 100 s. With the explicit scheme, no solution was reached due to time instability. Refined time steps were needed, which increased considerably the calculation time as mentioned by Bay (1991). For the Crank-Nicholson and the fully implicit schemes, accurate solutions were obtained in less than 2 s of CPU time except for Pe = 10^4 with the central scheme, where spurious oscillations appeared (**Figure 6.4**). As the discretization error of the fully explicit scheme is $O(\Delta\tau)$ compared to $O(\Delta\tau^2)$ for the Crank-Nicholson, the latter was preferred.

6.2.3. Validation

When Peclet number tends towards infinity (Pe $\rightarrow \infty$), the diffusion term in the Fokker-Planck equation becomes insignificant and convection dominates. In this case an analytical solution exists as the Jeffery equation can be solved in terms of an initial unit vector and a deformation gradient **E**. For different value of λ, the solution of the Fokker-

Planck equation for an initially isotropic fiber orientation becomes (Lipscomb, 1986; Lipscomb et al., 1988):

$$\psi = \frac{1}{4\pi}\left[1 + \boldsymbol{\gamma}^{[0]} : \mathbf{pp}\right]^{-3/2}, \tag{6.11}$$

where $\boldsymbol{\gamma}^{[0]}$ is the finite strain tensor and is related to the deformation gradient by $\boldsymbol{\gamma}^{[0]} = \left(\mathbf{E}^{-1}\right)^{\dagger} \cdot \mathbf{E}^{-1} - \boldsymbol{\delta}$ (Dinh & Armstrong, 1984). The deformation gradient $\mathbf{E}$ must satisfy the following differential equation (Lipscomb, 1986; Lipscomb et al., 1988):

$$\frac{D\mathbf{E}}{Dt} = \frac{1}{2}\left(-\boldsymbol{\omega} + \lambda\dot{\boldsymbol{\gamma}}\right) \cdot \mathbf{E}. \tag{6.12}$$

In equilibrium (no flow), an isotropic fiber orientation is obtained for $\mathbf{E} = \boldsymbol{\delta}$. The Fokker-Planck equation [Eq. (6.11)], can be solved for unsteady convection flows to obtain the following expression of the time evolution of $\mathbf{a_2}$ for an initially 3D random distribution:

$$\mathbf{a}_2 = \frac{1}{4\pi}\int_{\mathbf{p}} \mathbf{pp}\left[1 + \boldsymbol{\gamma}^{[0]} : \mathbf{pp}\right]^{-3/2} d\mathbf{p}. \tag{6.13}$$

A similar result could be easily obtained for $\mathbf{a_4}$ and higher order tensors, since they are even.

In order to test our finite volume method at high Peclet numbers, Equation (6.13) was used and the analytical results are compared to the numerical results in **Figure 6.4** for the a_{11}, a_{12} and a_{22} components, obtained using both the central and power-law schemes. At high Peclet numbers, all downstream fluxes are immediately transported following the flow direction. Therefore, the central scheme fails to predict the correct

behavior as spurious oscillations appear at large deformation. Accurate solutions are predicted only with the power-law scheme as it is an upwind type method.

These benchmark tests allowed us to completely validate the code used for the solution of the Fokker-Planck equation on a wide range of the Peclet number. Moreover, by increasing the number of cell grids, a study of the normalization condition versus the number of nodes showed that the order of accuracy is $O(\Delta\theta^2, \Delta\varphi^2)$. Consequently, the global discretization error varies as $O(\Delta\tau^2, \Delta\theta^2, \Delta\varphi^2)$.

6.3. Investigation of the fourth-order orientation tensor components in simple shear flow

Lipscomb et al. (1988) have proposed a general constitutive equation for axisymmetric particles suspended in a Newtonian fluid by following the ideas of Jeffery (1922), Hand (1961) and Giesekus (1962). The total stress in the composite is expressed as:

$$\boldsymbol{\sigma} = -P\boldsymbol{\delta} + \eta_0\dot{\boldsymbol{\gamma}} + \eta_0\phi\left[A\mathbf{a}_4 : \dot{\boldsymbol{\gamma}} + B\left(\mathbf{a}_2 \cdot \dot{\boldsymbol{\gamma}} + \dot{\boldsymbol{\gamma}} \cdot \mathbf{a}_2\right) + C\dot{\boldsymbol{\gamma}} + 2F\mathbf{a}_2 D_r\right], \tag{6.14}$$

where P is the hydrostatic pressure, η_0 the Newtonian fluid viscosity, ϕ the particle volume fraction and A, B, C and F are material parameters. D_r is the rotary diffusion coefficient related to the Brownian motion of the particles. In their paper, Lipscomb et al. (1988) have presented the specific material coefficients for spheroids. For a large fiber aspect ratio, the geometric shape factors B, C and F are equal to 0, 2 and 0,

respectively and A is used as a fitting parameter. Consequently, the shear stress, the primary and the secondary normal stress differences in simple shear flow are given by:

$$\sigma_{12} = \eta_0 \left[1 + 2\phi \left(1 + A a_{1212} \right) \right] \dot{\gamma}, \tag{6.15}$$

$$N_1 = 2\phi\eta_0 A \left(a_{1211} - a_{1222} \right) \dot{\gamma}, \tag{6.16}$$

$$N_2 = 2\phi\eta_0 A \left(a_{1222} - a_{1233} \right) \dot{\gamma}, \tag{6.17}$$

where 1 and 2 denote the velocity and gradient directions, respectively We note that the rheological functions are directly related to the a_{1212}, a_{1211}, a_{1222} and a_{1233} components of the fourth order orientation tensor.

Figure 6.5 presents the evolution of selected components of $\mathbf{a_4}$ in simple shear flow as functions of strain and for different values of the Peclet number, with an initial isotropic fiber orientation. The linear closure approximation, which is exact for this initial conformation, yields a_{1212} = 1/15 and zero for a_{1211}, a_{1222} and a_{1233}. This result is confirmed by the numerical solution of the distribution function (**Figure 6.5a**). For the lowest Peclet number (Pe = 1) diffusion is the dominant phenomenon. That is why there is little change of a_{1212} and a very weak evolution is observed as a function of strain. When the Peclet number increases, the hydrodynamic convection becomes predominant and a_{1212}, a_{1211}, a_{1222} and a_{1233} exhibit increasing overshoots up to Pe = 10^4 (**Figure 6.5a** to **Figure 6.5d**). For Pe > 50, important decreases are depicted after the overshoots, then undershoots are predicted before reaching the steady regime; these predictions are strongly dependent on the Peclet number. Similar undershoots were experimentally observed by Sepehr et al. (2004d) for fiber-filled Boger fluids. Also **Figure 6.5** presents

the a_{1212}, a_{1211}, a_{1222} and a_{1233} components as predicted using the ORW3 closure approximation (Chung & Kwon, 2001). In the transient state the ORW3 closure approximation tends to either overpredict or underpredict the behavior calculated by the numerical solution of the Fokker-Planck equation. However, the steady-state values are fairly well predicted by the ORW3 closure approximation apart from the a_{1212} component, where the deviation increases at large Peclet numbers. Nevertheless, these general good agreements confirm that this closure approximation was indeed developed to represent this type of flow. It is interesting to investigate what happens for reverse flows with a non-isotropic fiber orientation as the initial conformation, and this is achieved in the following paragraph.

Figure 6.6 reports the a_{1212}, a_{1211}, a_{1222} and a_{1233} components determined by the computation of the probability distribution function for reverse simple shear flows (a negative constant shear rate was considered). For these, the initial orientation is set by the final orientation reached during the previous forward flow. The results are reported for different values of the Peclet number and as functions of the absolute deformation. As previously noted, high diffusion (lowest Pe) induces no huge changes on the key components of $\mathbf{a}_4$ and, therefore, on fiber conformation. At large Pe convection becomes more significant, which causes a_{1212} to exhibit an overshoot before reaching steady state. For the largest Peclet numbers (Pe = 10^3 and 10^4), convection is the dominant phenomenon under the investigated deformation range and again, a_{1212} exhibits a large overshoot before reaching the steady-state regime. Similar overshoots have been observed experimentally for fiber suspensions in reverse flows (Sepehr et al., 2004c;

Sepehr et al., 2004d). The components related to the normal stress differences (Eqs. (6.16) and (6.17)) exhibit positive to negative values and slight undershoots are depicted. For reverse flows, negative normal stress differences followed by slight positive overshoots have also been observed experimentally for short fiber-filled polypropylene (30 wt % of glass fiber, r = 20 and $\dot{\gamma} = 0.1\text{s}^{-1}$) (Sepehr et al., 2004c) and in polybutene and Boger model fluids (20 wt % of glass fiber, r = 20 and $5\text{s}^{-1} \leq \dot{\gamma} \leq 10\text{s}^{-1}$) (Sepehr et al., 2004d). **Figure 6.6** also shows the results obtained from the ORW3 closure approximation. Again in the transient state, the closure approximation tends to smooth out the curves. Components of $\mathbf{a}_4$ related to the normal stress differences are well predicted, but some significant deviations are observed for a_{1212}. As for **Figure 6.5** (forward flow), the steady-state values of a_{1211}, a_{1222} and a_{1233} numerically calculated from the probability distribution function and the ORW3 closure relation are very similar in reverse flow, except again for the a_{1212} component.

6.4. Comparison of experimental data with Folgar-Tucker-Lipscomb model predictions

We can now assess the performance of the Folgar-Tucker-Lipscomb (FTL) model without the use of any closure approximations. This is achieved by numerically solving the fiber distribution function ψ [Eq. (6.7)]; then, the fourth order orientation components are calculated using Equation (6.5) while the stresses are determined by expression (6.14), where A and Pe are used as fitting parameters. **Figure 6.7** and **Figure 6.8** compare the model predictions for an isotropic initial fiber orientation with

experimental data obtained on suspensions containing 30 wt % of short glass fibers in polypropylene (PP30) provided by Basell (Sepehr et al., 2004c). The average fiber length, L, is close to 260 μm and its diameter D = 14 μm. The fiber weight fraction of 30 wt % corresponds to a volume fraction, ϕ, of 11.5 %, which is in the concentrated regime (Doi & Edwards, 1978a). Stress growth measurements were performed at a shear rate of 0.1 s^{-1} with a strain controlled ARES rheometer (Rheometric Scientific) using a parallel plate geometry with a 25 mm diameter. The gap was set to 1.5 mm, which allowed fibers to rotate freely at least in the shear plane. In order to correct for variations of the shear rate with plate radius, the predicted rheological functions (shear stress, primary and secondary normal stress differences) were calculated as follows:

$$\sigma_{12}(\gamma_R) = \eta_0 \left[1 + 2\phi \left(1 + A \frac{4}{\gamma_R^4} \int_0^{\gamma_R} a_{1212}\, \gamma^3 d\gamma \right) \right] \dot{\gamma}, \tag{6.18}$$

$$N_1(\gamma_R) = 2\phi\eta_0 A\dot{\gamma} \frac{2}{\gamma_R^2} \int_0^{\gamma_R} (a_{1211} - a_{1222})\, \gamma\, d\gamma, \tag{6.19}$$

$$N_2(\gamma_R) = 2\phi\eta_0 A\dot{\gamma} \frac{2}{\gamma_R^2} \int_0^{\gamma_R} (a_{1222} - a_{1233})\, \gamma\, d\gamma, \tag{6.20}$$

where γ_R is the strain at the disk rim and γ is the deformation at a radial position r.

Figure 6.7a compares the reduced viscosity growth PP30 data for the forward direction with the predictions of the FTL model for an isotropic initial fiber orientation numerically computed for Pe = 3200, A = 30 and Pe = 10^5, A = 25 and predictions using the ORW3 closure approximation for Pe = 770 and A = 30. The corresponding comparisons for the reduced normal stress differences are presented in **Figure 6.7b**. It is

interesting to note that the FTL model qualitatively describes the rheological behavior of the fiber filled PP. Nevertheless, it fails to predict the width of the viscosity overshoot (**Figure 6.7a**) and also the width and the position of the normal stress difference overshoot (**Figure 6.7b**). Furthermore, no important deviations are observed in the stress growth predictions using the distribution function computation (DFC) or using the ORW3 closure approximation. However, different values for the parameters Pe and A have to be used to obtain best fits. Surprisingly, the best fit of the viscosity overshoot is obtained for the largest Pe number (**Figure 6.7a**), indicating that the diffusion part due to fiber interaction is negligible. A light viscosity undershoot at a deformation close to 20 strain units is predicted by the numerical solution obtained with Pe = 3200 and or using the ORW3 closure approximation. For fiber reinforced polypropylene, no undershoot was observed as reported by Sepehr et al. (2004c), whereas for fiber filled Boger fluids an undershoot appeared at a strain close to 30 (Sepehr et al., 2004d).

Figure 6.8a and **Figure 6.8b** compare the stress growth PP30 data in reverse flow with the predictions of the FTL model using the DFC solution or the ORW3 closure approximation. Globally the FTL model using the DFC or the ORW3 closure approximation qualitatively predicts the reduced rheological properties (i.e. a reverse overshoot for the viscosity and a negative undershoot followed by a positive overshoot for the normal stress differences). Nevertheless, the quantitative predictions using the ORW3 closure approximation are quite poor. A better behavior (but the fit remains poor) could be obtained by using DFC with a large Peclet number (Pe = 10^5): the width of the viscosity and normal stress difference overshoots increases.

6.5. Discussion

In previous papers, the probability distribution function was not numerically solved to predict the rheological behavior of fiber suspensions in shear flows, due to the huge CPU times required. The Moore law specifies that the CPU velocity doubles every 18 months (Moore, 1965). Therefore, the CPU time of the present code would have been approximately 20 min as apposed to a few days as in the work of Bay (1991), would the tests have been performed about 15 years ago. This explains why many closure approximations were derived to avoid the large CPU times. However, the errors induced by these closure relations were not clearly highlighted. Sepehr et al. (Sepehr et al., 2004a; 2004c) have mentioned that multiple behaviors were predicted when using different closures. Hence, the choice of an appropriate closure approximation still remains arbitrary and until now, the FTL model was assessed solely using closure approximations.

The use of closure approximations has saved a lot of computation time especially in the finite element/finite volume framework. Numerous studies have been performed to derive better closure relations. The recent closure approximations (orthotropic and natural) generally describe quite well the behavior in transient and steady flows. In this work, the CPU time required to estimate $\mathbf{a}_4$ using the more reliable DFC approach is comparable to the one needed to solve the FTL model using closure approximations. In the case of the orthotropic closure, the CPU time required to calculate the eigenvalues of $\mathbf{a}_2$ and to rotate the fourth order orientation tensor from its principal axis to laboratory

coordinates can be very long. The same observation is made for natural closure approximations such as IBOF (invariant-based optimal fitting (Chung & Kwon, 2002b)) that can be costly when it requires calculating the symmetric part of a fourth order tensor. Moreover, using the DFC numerical solution avoids the implicit errors induced by a closure approximation and gives a better description of the fiber orientation in space.

The FTL model qualitatively describes the rheological behavior of fiber suspensions in polypropylene in transient forward and reverse flows, despite the fact that in the model the matrix is assumed to be Newtonian whereas polypropylene is viscoelastic. However, the FTL model fails to predict the widths and positions of the transient viscosity and normal stress difference overshoots. For large Peclet numbers, the FTL model appears to be more accurate suggesting that the Jeffery equation is a key base to develop a new model. Efforts have to be devoted to better model fiber-fiber interactions, which are believed to play a major role in concentrated regimes. This has been partly achieved by the modeling of fiber direct contacts with neighboring fibers (Férec et al., 2008a).

6.6. Concluding remarks

A finite volume method has been used to solve numerically the time evolution of the orientation probability distribution function in simple shear flow. The focus has been on reducing considerably the CPU time and to cover a large range of the Peclet number, from pure diffusion ($Pe = 0$) to pure convection ($Pe \rightarrow \infty$). The new method allows

solving the Fokker-Planck equation with a short CPU time, similar to the one required with the use of closure approximations. Compared to closure relations, the solution of DFC does not induce approximations or errors, apart from those of numerical nature. Moreover, the probability distribution function results in a superior description of fiber orientation as opposed to the use of orientation tensors. This work has allowed testing the performance of a recent closure approximation (ORW3), especially for predictions in reverse flow and over a wide range of the Peclet number. Results have shown that the ORW3 closure approximation gives reasonable results although discrepancies still exist with respect to experimental data for a fiber suspension based on polypropylene.

The solution of the probability distribution function has also been used to assess the FTL model with regards to experimental data for a short fiber filled polypropylene. The predictions are then not biased by the use of closure approximations. It is found that the Jeffery equation, which is the base of the FTL model, catches the main physic behind the rheological behavior of fiber suspensions, but efforts have to be devoted to better describe fiber-fiber interactions.

6.7. Acknowledgements

The authors would like to acknowledge financial support from the France-Québec collaboration program and the Natural Sciences and Engineering Research Council of Canada (NSERC-CIAM program).

6.8. Appendix

The coefficient a_E, a_W, a_N, a_S, a_M and a_P are expressed as:

$$
\begin{aligned}
a_M &= \frac{\sin\theta_P \, \Delta\varphi \, \Delta\theta}{\Delta t} \\
a_E &= D_e - F_e/2 \\
a_W &= D_w + F_w/2 \\
a_N &= D_n - F_n/2 \\
a_S &= D_s + F_s/2 \\
a_P &= a_E + a_W + a_N + a_S + F_e - F_w + F_n - F_s
\end{aligned}
\quad , \tag{6.21}
$$

where the fluxes are evaluated as:

$$
\begin{aligned}
D_e &= D_r \sin\theta_e \frac{\Delta\varphi}{\Delta\theta} \\
D_w &= D_r \sin\theta_w \frac{\Delta\varphi}{\Delta\theta} \\
D_n &= D_r \frac{\Delta\theta}{\sin\theta_P \, \Delta\varphi} \\
D_s &= D_r \frac{\Delta\theta}{\sin\theta_P \, \Delta\varphi}
\end{aligned}
\tag{6.22}
$$

$$
\begin{aligned}
F_e &= \dot{\theta}_e \sin\theta_e \Delta\varphi \\
F_w &= \dot{\theta}_w \sin\theta_w \Delta\varphi \\
F_n &= \sin\theta_P \dot{\varphi}_n \, \Delta\theta \\
F_s &= \sin\theta_P \dot{\varphi}_s \, \Delta\theta
\end{aligned}
\quad . \tag{6.23}
$$

Table 6.1 : Calculation CPU time for different spatial schemes, time schemes and Peclet numbers.

Time scheme	Spatial scheme	$Pe \leq 10^3$	$Pe = 10^4$
Explicit scheme	Central differencing	N.A.	N.A.
	Power law	N.A.	N.A.
Fully implicit scheme	Central differencing	2 s	N.A.
	Power law	2 s	2 s
Crank-Nicolson scheme	Central differencing	2 s	N.A.
	Power law	2 s	2 s

N.A. = Not Available

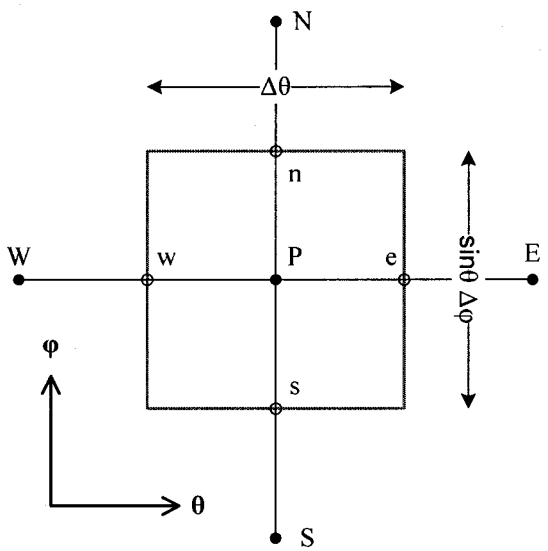

Figure 6.1 : Control volume used to perform flux balances for the probability distribution function. The faces of the control volume labelled as *e*, *w*, *n* and *s* refers to east, west, north and south directions.

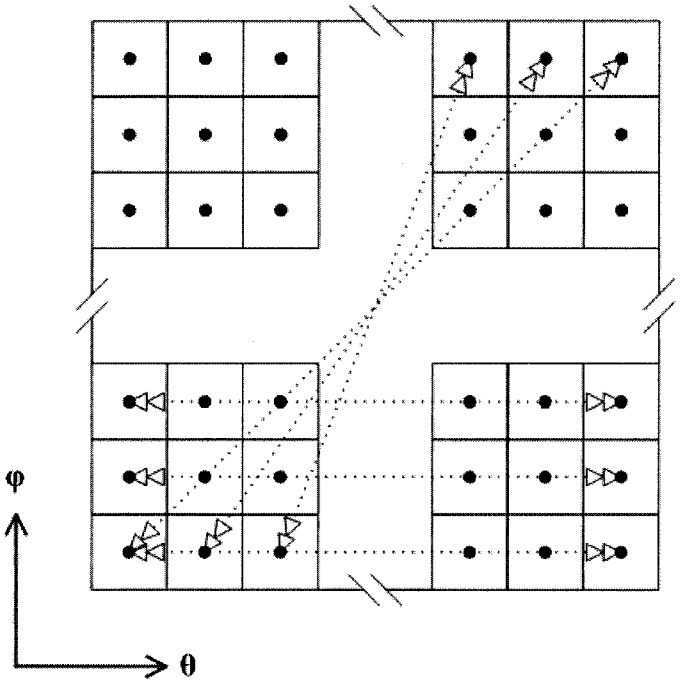

Figure 6.2 : Schematic representation of the periodic boundary conditions on the total meshed domain.

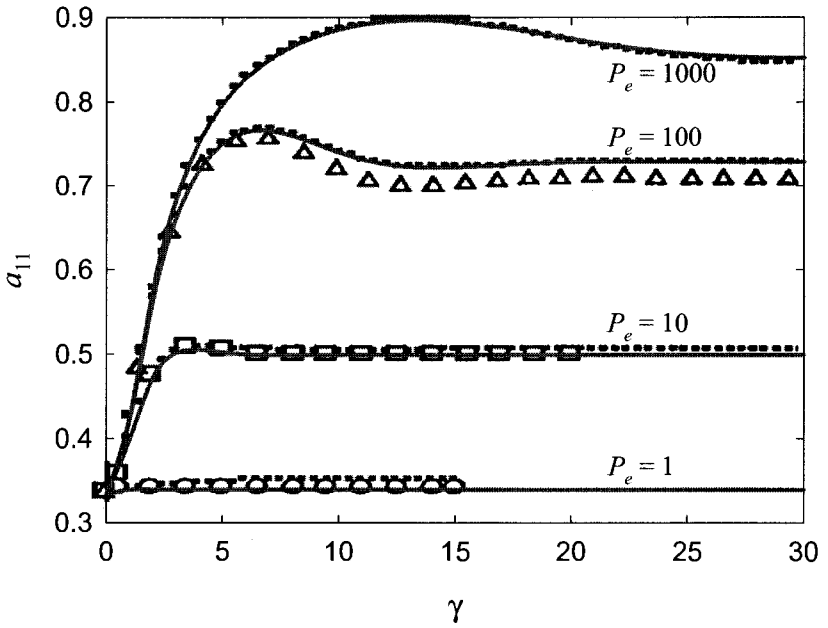
0.9
0.8
0.7
0.6
0.5
0.4
0.3
a_{11}
$P_e = 1000$
$P_e = 100$
$P_e = 10$
$P_e = 1$
0
5
10
15
20
25
30
γ

(a)

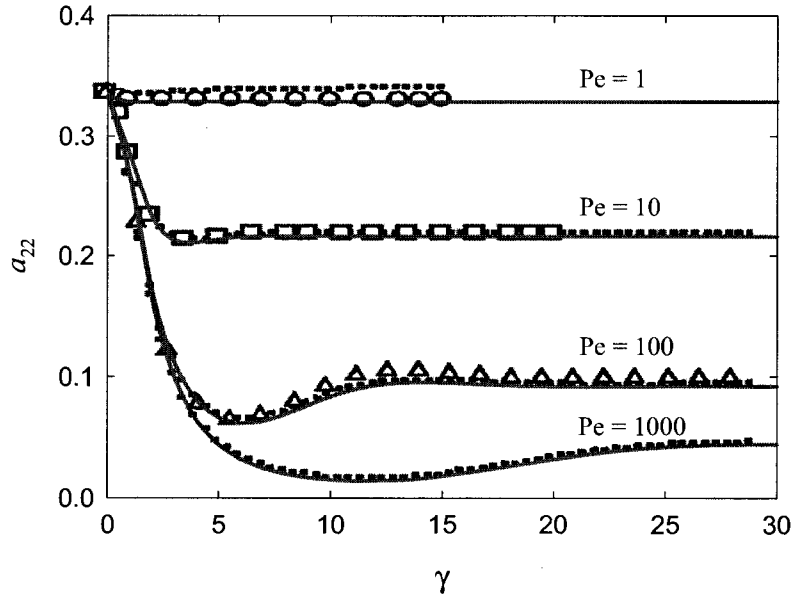
0.4
0.3
0.2
0.1
0.0
a_{22}
Pe = 1
Pe = 10
Pe = 100
Pe = 1000
0
5
10
15
20
25
30
γ

(b)

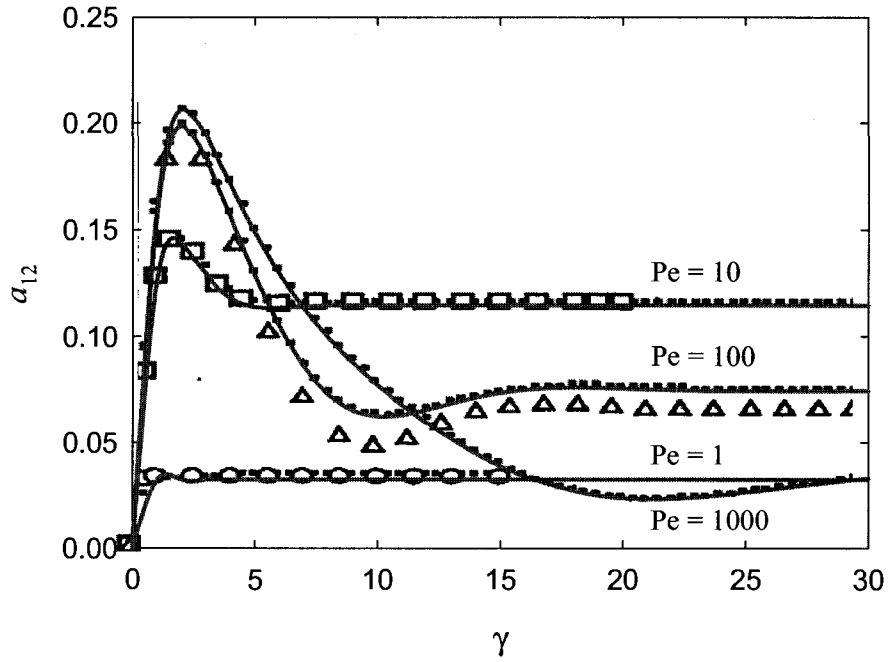

(c)

Figure 6.3 : Comparison of calculation results in simple shear flow (1: velocity direction; 2: gradient direction) with $r = \infty$; (▪▪) Advani results; (○) Bay results; (□) Bay results; (△) Bay results (r = 10 instead of infinity for all previous cases), adapted from Advani (1987) and Bay (1991): (a) a_{11} component; (b) a_{22} component; and (c) a_{12} component vs. deformation.

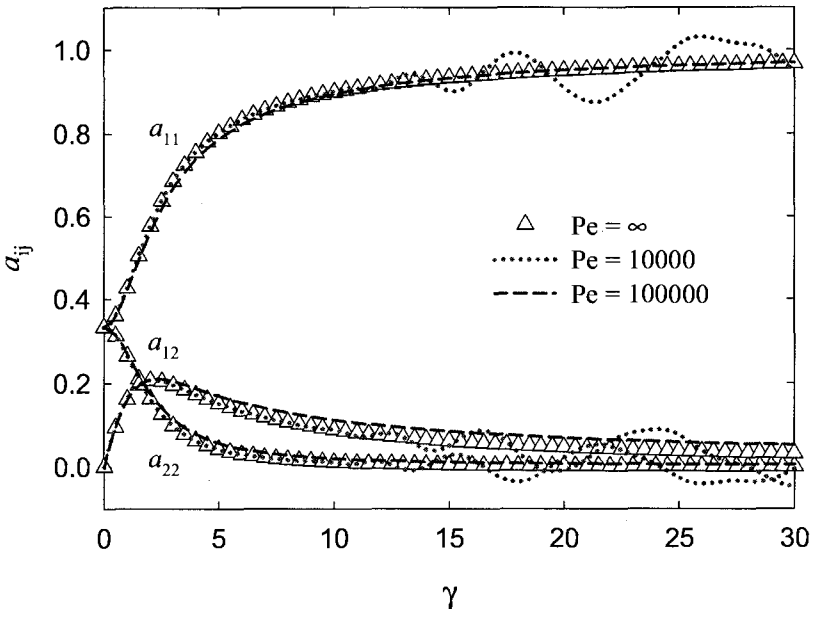

Figure 6.4 : Comparison of calculated results in simple shear flow (1: velocity direction; 2: gradient direction, $r = \infty$) for the attractive components of $\mathbf{a_2}$: (△) Fokker-Planck analytical solution without diffusion [Eq. (6.13)]; (·····) Central scheme; (------) Power law scheme.

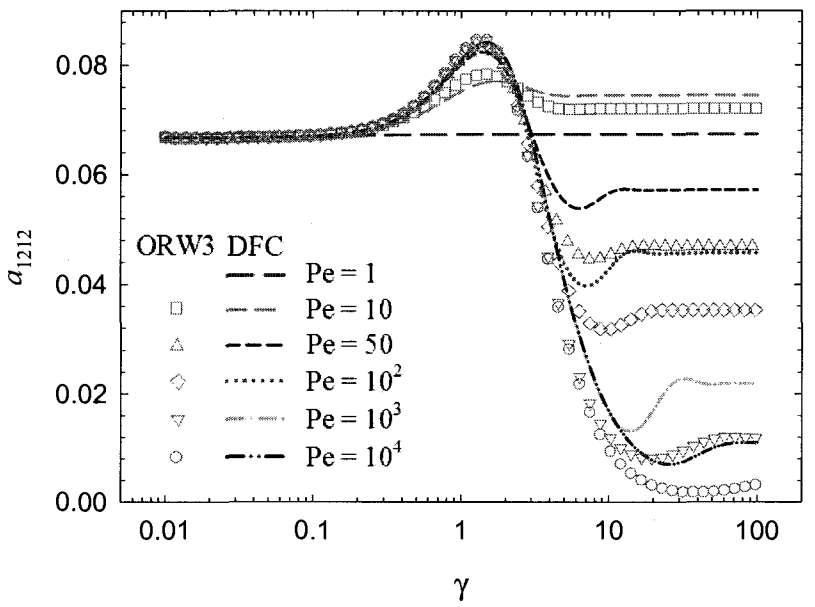
ORW3 DFC
Pe = 1
Pe = 10
Pe = 50
Pe = 10^2
Pe = 10^3
Pe = 10^4
a1212
γ
0.00
0.02
0.04
0.06
0.08
0.01
0.1
1
10
100

(a)

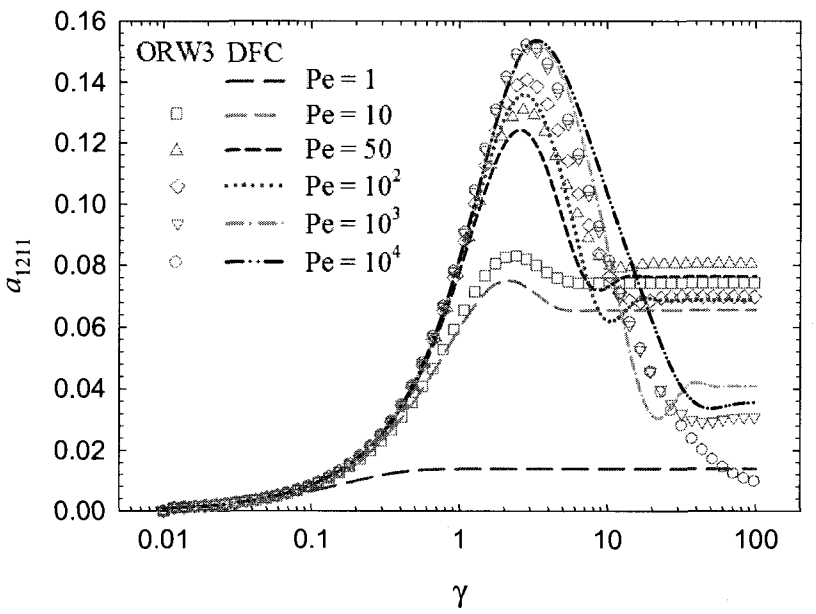
ORW3 DFC
Pe = 1
Pe = 10
Pe = 50
Pe = 10^2
Pe = 10^3
Pe = 10^4
a1211
γ
0.00
0.02
0.04
0.06
0.08
0.10
0.12
0.14
0.16
0.01
0.1
1
10
100

(b)

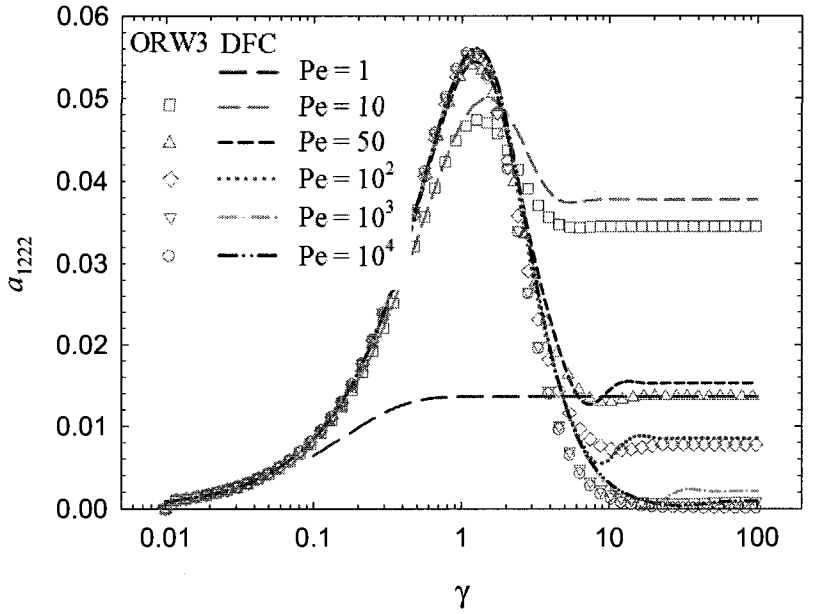

(c)

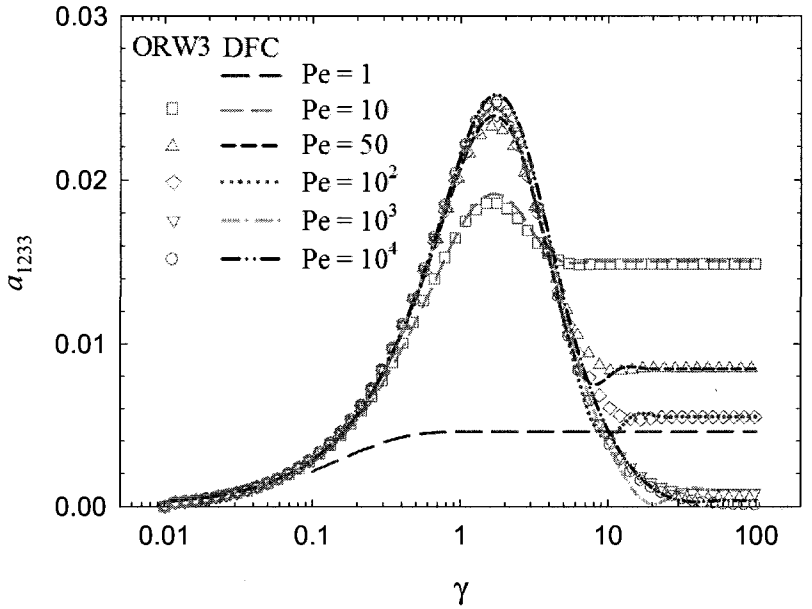

(d)

Figure 6.5 : Comparisons of a_{1212}, a_{1112}, a_{1222} and a_{1233} components obtained by solving the orientation distribution function and the ORW3 closure approximation in simple shear (forward direction) at different Pe numbers.

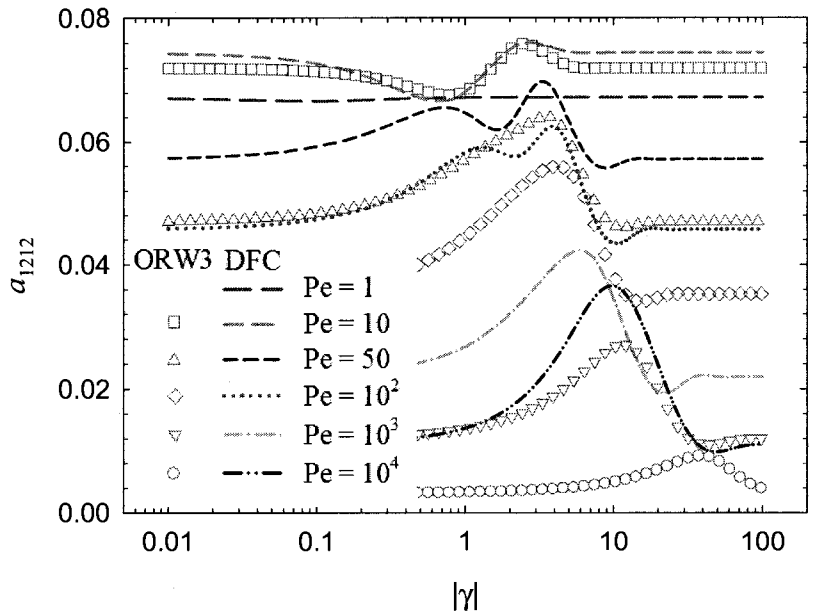
0.08
0.06
0.04
0.02
0.00
a_{1212}
ORW3 DFC
Pe = 1
Pe = 10
Pe = 50
Pe = 10^2
Pe = 10^3
Pe = 10^4
0.01
0.1
1
10
100
|γ|

(a)

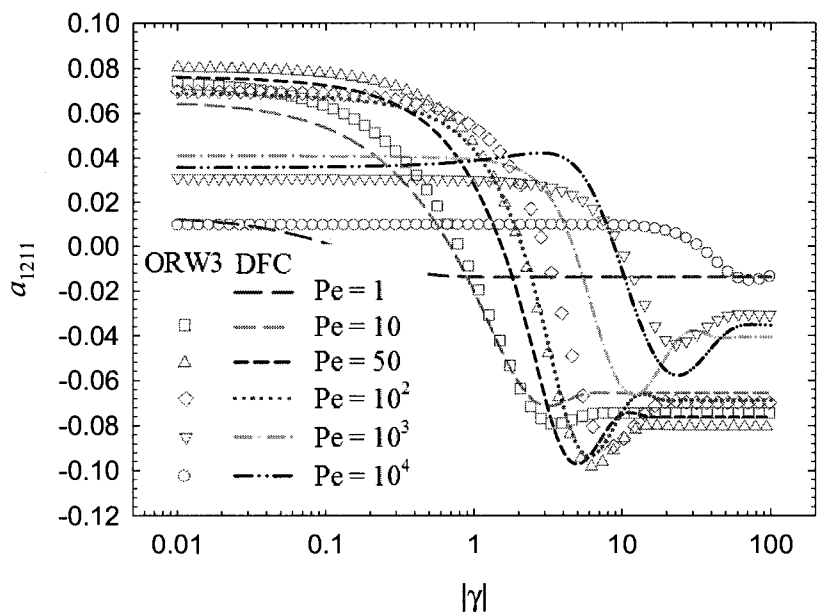
0.10
0.08
0.06
0.04
0.02
0.00
-0.02
-0.04
-0.06
-0.08
-0.10
-0.12
a_{1211}
ORW3 DFC
Pe = 1
Pe = 10
Pe = 50
Pe = 10^2
Pe = 10^3
Pe = 10^4
0.01
0.1
1
10
100
|γ|

(b)

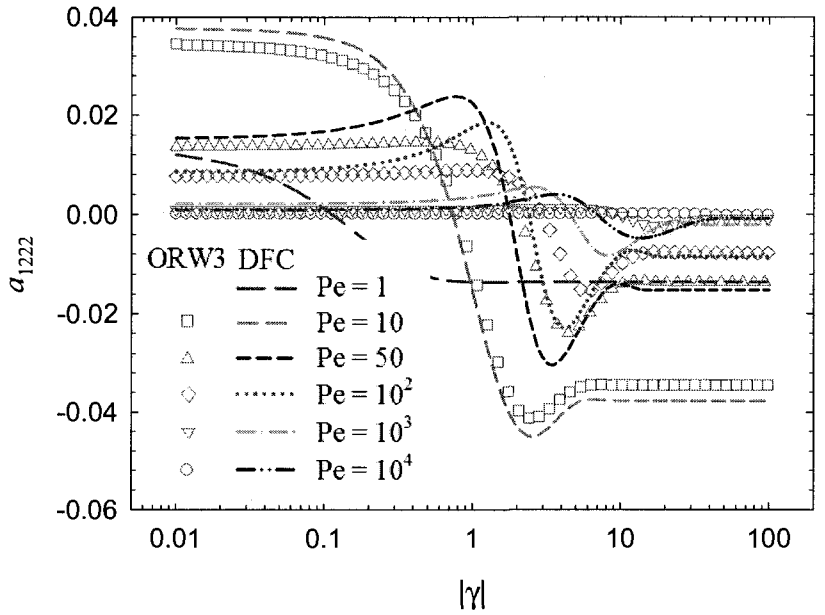

(c)

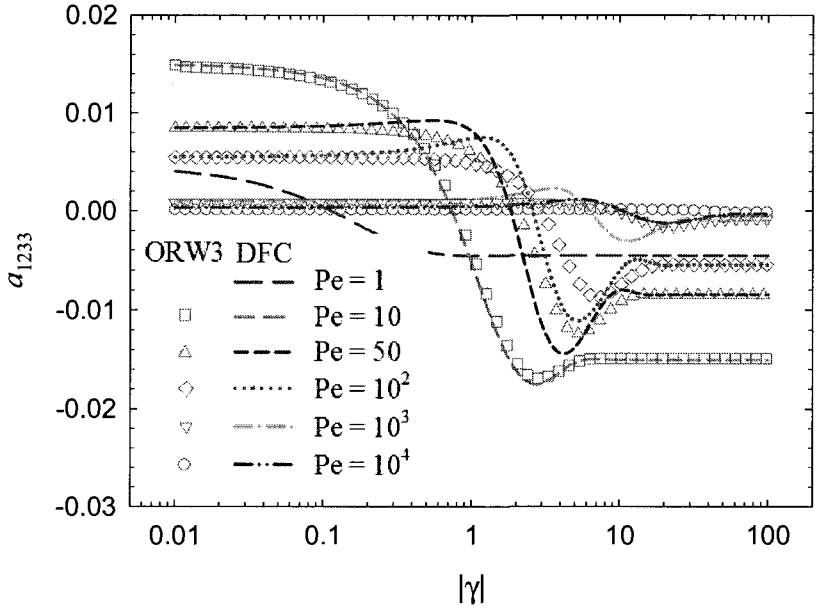

(d)

Figure 6.6 : Comparisons of a_{1212}, a_{1112}, a_{1222} and a_{1233} components obtained by solving the orientation distribution function computation or the ORW3 closure approximation in simple shear (reverse direction) for different Pe numbers.

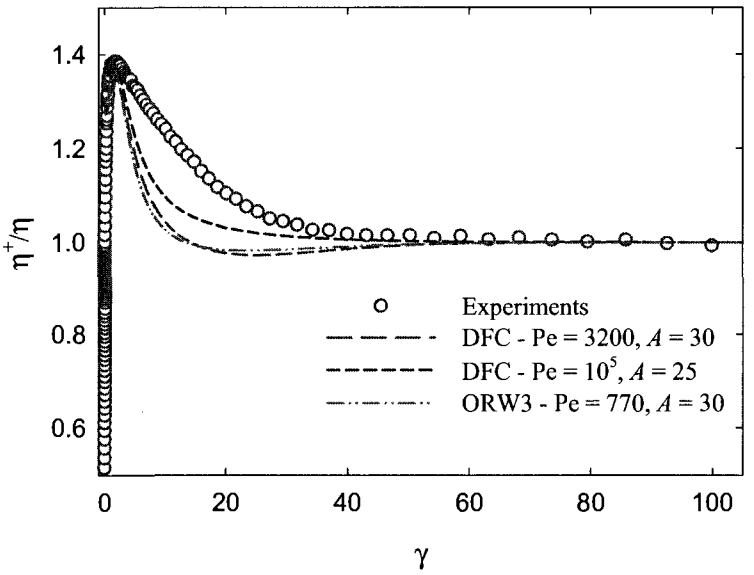

(a)

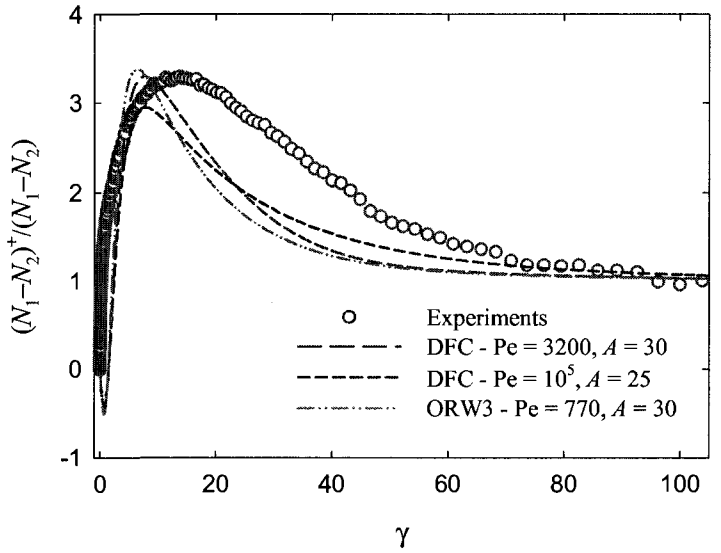

(b)

Figure 6.7 : Experimental stress growth data for PP30 as compared to model predictions from the orientation distribution function computation (DFC) and from the ORW3 closure approximation for forward flow (CW) at $\dot{\gamma}$ = 0.1 s^{-1}: (a) Transient viscosity, and (b) transient normal stress difference as functions of strain.

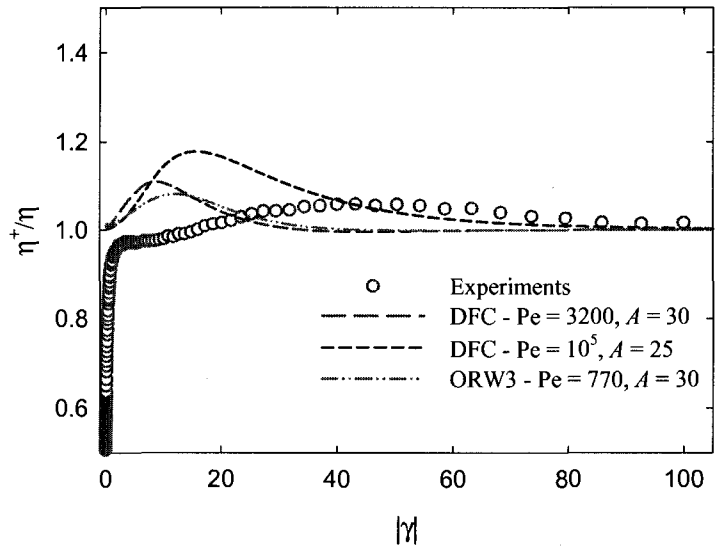

(a)

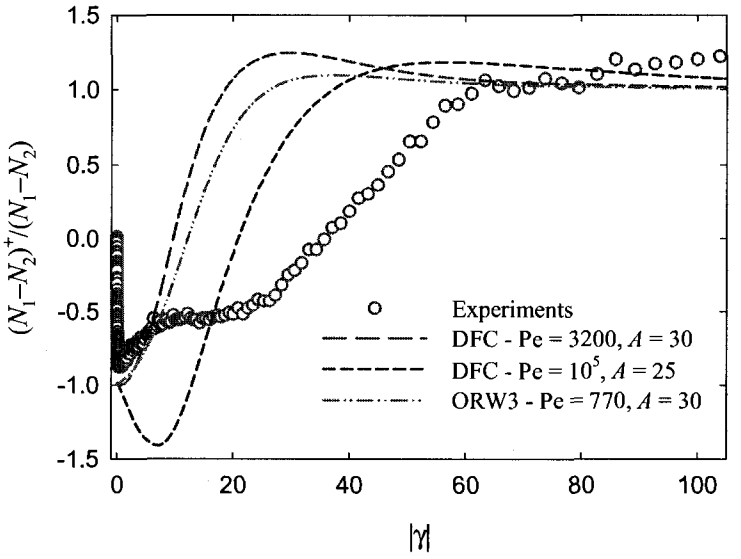

(b)

Figure 6.8 : Experimental stress growth data for PP30 as compared to model predictions from the orientation distribution function computation (DFC) and from the ORW3 closure approximation for reverse flow (CCW) at $\dot{\gamma}$ = 0.1 s^{-1}: (a) Transient viscosity and (b) transient normal stress differences as functions of strain.

CHAPITRE 7 - ARTICLE: MODELING FIBER INTERACTIONS IN NON-DILUTE FIBER SUSPENSIONS*

J. Férec [a, b], G. Ausias [b], M.C. Heuzey [a] and P.J. Carreau [a]

[a] *Center for Applied Research on Polymers and Composites (CREPEC), Chemical Engineering Department, École Polytechnique de Montréal, PO Box 6079, Stn Centre-Ville, Montreal, QC, Canada H3C3A7*

[b] *Laboratoire d'Ingénierie des MATériaux de Bretagne (LIMATB) Université de Bretagne Sud, rue de St Maudé, 56325 Lorient, France*

Abstract

A set of rheological equations is developed for non dilute suspensions of rigid fibers in a Newtonian fluid taking into account hydrodynamic and fiber-fiber interactions. The force generated by the fiber interactions is modeled using a linear hydrodynamic friction coefficient proportional to the relative velocity at the contact point, and weighted by the probability for contacts to occur. The equation of evolution of the second-order orientation tensor, containing advection and diffusion terms due to fiber interactions, is derived to predict fiber orientation under flow. The well known fourth-order orientation tensor, related to the hydrodynamic contribution, and a newly proposed fourth-order interaction tensor are used to evaluate the total stress in the composite. A linear and a quadratic closure approximation are proposed to describe the fourth-order interaction tensor. Results are presented using the quadratic form, which is found to be more accurate than the linear one. The model is shown to describe well

---

* Cet article est a été soumis au Journal of Rheology

simple shear data of suspensions of glass fibers in a Newtonian polybutene. Moreover, fiber orientation and the average number of contacts per fiber are predicted. The newly proposed interaction coefficient varies with fiber orientation, which appears to be realistic.

7.1. Introduction

Thermoplastic polymer composites containing short fibers can be extruded or molded into the desired shape without any significant modification of conventional processing equipment. Owing to flow, the fiber orientation changes dynamically during processing and the final orientation pattern is retained in the part following solidification. From this orientation state, it is possible to determine the mechanical and other physical properties of the final product. However, this is not a simple task since fiber motion and rotation are affected by fluid flow and vice versa.

Many investigations have been carried out to elucidate the rheological behavior of suspensions of elongated particles. Some pioneering theoretical developments have been presented by Jeffery (1922), who developed a model for a single dilute spheroid suspended in a Newtonian fluid. He calculated the stress around a particle in the absence of external torque and derived the evolution equation of the unit vector **p** directed along the particle principal axis.

Generally, fiber suspensions are concentrated systems and fibers can not be considered as individual particles. Therefore, a reference cell that contains a large number of fibers needs to be defined (Batchelor, 1971). The orientation state of this fiber population in the reference cell can be represented by a probability distribution function, from which Advani and Tucker (1987) have defined orientation tensors, second- and fourth-order tensors, $\mathbf{a}_2$ and $\mathbf{a}_4$, respectively. These describe more easily the fiber orientation state than the probability distribution function, without significant losses.

Fiber suspensions can be characterized according to the volumetric fraction of solid particles in the fluid. Depending on the fiber volume fraction ϕ, some quantities such as hydrodynamic or fiber-fiber interaction forces dominate the system. Typically, the number of fibers per unit volume n is divided into three distinct regimes (Doi & Edwards, 1978a). In the dilute regime defined by $n << 1/L^3$, where L is the length of the particle, the fibers are allowed to move without interference from other particles. By increasing the number of fibers, $1/L^3 < n < 1/DL^2$ (D = particle diameter), the semi-dilute domain is reached and non-negligible hydrodynamic interactions between fibers are encountered. Furthermore, some fiber contacts are possible. Finally, the concentrated regime is characterized by the numerous contacts of a fiber with its neighbors, and in this state, $n > 1/DL^2$.

From experimental observations in concentrated systems the primary fiber orientation is that of the flow direction, but some deviations appear in injection parts (Bay, 1991) and extruded tubes (Ausias et al., 1994). The modeling of these effects represents a challenging task. Folgar and Tucker (1984) and then Advani and Tucker (1987) included into the Jeffery equation an empirical diffusional term that accounts for particle interactions. This phenomenological term is proportional to the effective deformation rate $|\dot{\gamma}| = \sqrt{\dot{\gamma} : \dot{\gamma}/2}$ and to a constant diffusion coefficient C_I, as shown below in the time evolution equation for the second-order orientation tensor (Advani & Tucker, 1987):

$$\frac{D\mathbf{a}_2}{Dt} = -\frac{1}{2}(\boldsymbol{\omega}\cdot\mathbf{a}_2 - \mathbf{a}_2\cdot\boldsymbol{\omega}) + \frac{1}{2}\lambda(\dot{\boldsymbol{\gamma}}\cdot\mathbf{a}_2 + \mathbf{a}_2\cdot\dot{\boldsymbol{\gamma}} - 2\mathbf{a}_4 : \dot{\boldsymbol{\gamma}}) + 2C_I|\dot{\boldsymbol{\gamma}}|(\boldsymbol{\delta} - 3\mathbf{a}_2), \qquad (7.1)$$

where $\boldsymbol{\omega}$ and $\dot{\boldsymbol{\gamma}}$ are the vorticity and deformation rate tensors, respectively. $\boldsymbol{\delta}$ is the identity tensor and the shape factor $\lambda = (r^2-1) / (r^2+1)$ is a parameter related to the particle aspect ratio $r = L/D$. Several authors have tried to express the diffusion coefficient C_I as functions of the fiber aspect ratio and volume fraction. Based on experimental data, Bay (1991) proposed the following exponential function:

$$C_I = 0.0184\exp(-0.7148r\phi). \qquad (7.2)$$

Phan-Thien et al. (2002) also suggested an empirical expression, where the numerical parameters were obtained by best fits of the direct simulation predictions with experimental data:

$$C_I = 0.03\left[1 - \exp(-0.224r\phi)\right]. \qquad (7.3)$$

Finally, Ranganathan and Advani (1991) assumed a simple relationship between the diffusion coefficient and the average inter-fiber spacing a_c for non dilute suspensions, with $C_I = KL/a_c$, where K is a constant.

In terms of constitutive equations, Hand (1961) and then Giesekus (1962) derived expressions for dilute ellipsoid suspensions in a Newtonian fluid of viscosity η_0. Lipscomb et al. (1988) have extended the previous work to propose a more general governing equation with corresponding material coefficients (A, B, C and F) for dilute ellipsoid suspensions, represented by:

$$\boldsymbol{\sigma} = -P\boldsymbol{\delta} + \eta_0\dot{\boldsymbol{\gamma}} + \eta_0\phi\left[A\mathbf{a}_4 : \dot{\boldsymbol{\gamma}} + B\left(\mathbf{a}_2 \cdot \dot{\boldsymbol{\gamma}} + \dot{\boldsymbol{\gamma}} \cdot \mathbf{a}_2\right) + C\dot{\boldsymbol{\gamma}} + 2F\mathbf{a}_2 D_r\right], \tag{7.4}$$

where P is the total hydrostatic pressure and D_r the rotary diffusivity due to Brownian motion. For slender particles (i.e. $r >> 1$), the fibers are large enough that the Brownian motion can be omitted (Chaouche & Koch, 2001). For semi-concentrated fiber suspensions, Dinh and Armstrong (1984) have calculated the forces induced by the fluid on cylinders of an infinite aspect ratio and derived the particle motion and rotation. Using the cell model approach developed by Batchelor (1970b), they expressed the stress contribution of the fibers by averaging the fiber contribution with the orientation distribution function. Eq. (7.4) reduces to that of the Dinh and Armstrong (1984) result if A is the only non zero coefficient.

More recently, fiber interactions have been modeled by direct simulation methods. These techniques have been used for rigid fibers by Yamamoto and Matsuoka (1996) and Ausias (2006) who took also into account a fiber length distribution. Schmid et al. (2000) and Joung et al. (2001) did similar investigations for flexible fibers. Although of considerable interest, these direct simulations can not be easily introduced into commercial software packages owing to their large computational time.

Finally, Sandstrom (1993) and Sandstrom and Tucker (1993) have presented a theory for concentrated fiber suspensions with strong fiber interactions. The inter-fiber contact forces are modeled as linear lubrication forces between particles and are weighted by the probability distribution function. Le Corre et al. (2005) used a numerical analysis based on the homogenization of discrete and periodic structures to

investigate the relationships between the microstructure and the macroscopic rheological properties of concentrated suspensions of fiber bundles having an average planar orientation. More developments have been achieved by Djalili-Moghaddam and Toll (2005) who considered the total stress as the sum of the contributions of the matrix, the hydrodynamic forces acting on the particles and the interaction forces between fibers.

In this paper we present a rheological model for non dilute fiber suspensions, in which interactions between fibers are taken into account. The approach uses the fiber orientation distribution function from which new conformation tensors, called interaction tensors, are constructed. An evolution equation for the orientation is derived, and a constitutive law is developed by adding a fiber-fiber contribution to the total stress equation proposed by Dinh and Armstrong (1984). Closure approximations required to evaluate the fourth-order interaction tensor are also proposed. The new model contains a few adjustable parameters that are determined by fitting experimental data for short glass fiber-filled reinforced polybutene.

7.2. Model formulation

7.2.1. Definitions

The test fiber is denoted by the superscript α, whereas the superscript β refers to the neighboring fiber (**Figure 7.1**). The location of the mass center of the test fiber is $\mathbf{r}_C^\alpha$, and s^α is an arc length measured along the fiber axis with $s^\alpha = 0$ at the center. The unit vector $\mathbf{p}^\alpha$ along the major axis of the fiber describes its orientation. The vector $\mathbf{r}_C^\alpha$ is

expressed with respect to a fixed coordinate system **R** (the velocity of the coordinate origin is set to zero) and a particle coordinate system $\mathbf{R}^{\alpha}$ (where the 1-direction is taken collinear to $\mathbf{p}^{\alpha}$) on the fiber element. Similar definitions are used for the neighboring fiber using the superscript β. The surrounding fluid angular velocity is defined by $\mathbf{\Omega}^{\infty} = \frac{1}{2}\nabla \times \mathbf{v}^{\infty}$.

7.2.2. Hypotheses

(1) All fibers are considered as straight and rigid cylinders of uniform length L, constant diameter D and large aspect ratio $r >> 1$ (absence of Brownian motion).

(2) The bulk flow is assumed to be homogeneous, whereas the velocity gradient is constant over the fiber length ($\nabla \mathbf{v}^{\infty} = \boldsymbol{\kappa}^{\dagger}$), so the fluid velocity is given by $\mathbf{v}^{\infty} = \boldsymbol{\kappa} \cdot \mathbf{r}_{\mathbf{C}}^{\alpha}$.

(3) The suspended fibers are assumed to be distributed uniformly, i.e. there is no concentration gradient. Therefore, for homogeneous flows the probability distribution functions $\psi_{\mathbf{p}\alpha}$ and $\psi_{\mathbf{p}\beta}$ are independent on the spatial location of the fibers and n becomes a constant.

(4) The translational and rotational inertia of particles are neglected. Furthermore, gravitational effects are negligible.

(5) The suspending fluid is assumed to be incompressible and a continuous Newtonian medium. The fluid motion is determined by the Stokes equation (negligible translational and rotational fluid inertia).

(6) The particle-particle interaction force is linear with respect to the relative velocity at the contact point (hydrodynamic friction).

(7) In dilute or semi-dilute suspensions, the particle extra stress consists mostly of the hydrodynamic stress and fiber-fiber interactions are less significant. Affine motion and rotation are then assumed.

7.2.3. Equations for fiber motion

From Kim and Karrila (1991), the time evolution for the change of orientation of a test prolate spheroid α yields:

$$\dot{\mathbf{p}}_{\mathrm{H}}^{\alpha} = \boldsymbol{\varpi}^{\alpha} \times \mathbf{p}^{\alpha} = \left(\boldsymbol{\Omega}^{\infty} + \mathbf{C}^{-1} \cdot \mathbf{H} : \dot{\boldsymbol{\gamma}}\right) \times \mathbf{p}^{\alpha} = -\frac{1}{2}\boldsymbol{\omega} \cdot \mathbf{p}^{\alpha} + \frac{1}{2}\frac{Y_H}{Y_C}\left(\dot{\boldsymbol{\gamma}} \cdot \mathbf{p}^{\alpha} - \dot{\boldsymbol{\gamma}} : \mathbf{p}^{\alpha}\mathbf{p}^{\alpha}\mathbf{p}^{\alpha}\right), \quad (7.5)$$

where $\boldsymbol{\varpi}^{\alpha}$ is the angular velocity of fiber α. Expressed in **R**, the resistance tensors are, $\mathbf{C} = \eta_0 L^3 \left[Y_C \boldsymbol{\delta} + \left(X_C - Y_C\right)\mathbf{p}^{\alpha}\mathbf{p}^{\alpha} \right]$ and $\mathbf{H} = -\frac{1}{2}\eta_0 L^3 Y_H \left(\boldsymbol{\varepsilon} \cdot \mathbf{p}^{\alpha}\right)\mathbf{p}^{\alpha}$, respectively where $\boldsymbol{\varepsilon}$ is the third order permutation tensor and X_C, Y_C and Y_H are resistance functions. For the dilute regime, we find that the rotational drag coefficients are $X_C = 4\pi/r^2$ and $Y_C = 1/6$. Expression (7.5) is equivalent to the Jeffery (1922) equation, when Y_H / Y_C is the form

factor (Kim & Karrila, 1991). In the limit of infinite aspect ratio (i.e. the form factor, $\lambda = 1$), the slender body theory is recovered, which reduces the Jeffery equation to:

$$\dot{\mathbf{p}}_{\mathrm{H}}^{\alpha} = -\frac{1}{2}\boldsymbol{\omega}\cdot\mathbf{p}^{\alpha} + \frac{1}{2}\left(\dot{\boldsymbol{\gamma}}\cdot\mathbf{p}^{\alpha} - \dot{\boldsymbol{\gamma}}:\mathbf{p}^{\alpha}\mathbf{p}^{\alpha}\mathbf{p}^{\alpha}\right) = \boldsymbol{\kappa}\cdot\mathbf{p}^{\alpha} - \boldsymbol{\kappa}:\mathbf{p}^{\alpha}\mathbf{p}^{\alpha}\mathbf{p}^{\alpha}. \tag{7.6}$$

For the case of fiber motion with interactions, we assume that the test fiber α suspended in a Newtonian fluid is subjected to an external force caused by a neighboring interacting fiber β. Using the previous development, the equation for the change of orientation for any fiber α becomes:

$$\dot{\mathbf{p}}^{\alpha} = \boldsymbol{\varpi}^{\alpha}\times\mathbf{p}^{\alpha} = \left[\boldsymbol{\Omega}^{\infty} + \mathbf{C}^{-1}\cdot\left(\mathbf{H}:\dot{\boldsymbol{\gamma}} + \mathbf{T}_{\mathrm{I}}\right)\right]\times\mathbf{p}^{\alpha}, \tag{7.7}$$

where $\mathbf{T}_{\mathrm{I}}$ represents the global torque produced by all neighboring fibers, which act on the test fiber α. To determine $\mathbf{T}_{\mathrm{I}}$, the differential interaction moment $d\mathbf{T}_{\mathrm{I}}$ has to be used, which is given by $d\mathbf{T}_{\mathrm{I}} = s^{\alpha}\mathbf{p}^{\alpha}\times d\mathbf{f}_{\mathrm{I}}$. It is simply the lever arm times the applied differential force $d\mathbf{f}_{\mathrm{I}}$. The general form for the force due to short range fiber-fiber interactions has been proposed by several authors (Djalili-Moghaddam & Toll, 2005; Gibson & Toll, 1999; Sandstrom, 1993). If a linear lubrication is assumed, it gives:

$$\mathbf{f}_{\mathrm{I}} = D\eta_0 k\Delta\dot{\mathbf{r}}, \tag{7.8}$$

where k is a dimensionless geometric factor and the relative velocity between two fibers at the interaction point $\Delta\dot{\mathbf{r}}$ is expressed as:

$$\begin{aligned}\Delta\dot{\mathbf{r}} &= \dot{\mathbf{r}}_{\mathrm{C}}^{\beta} + s^{\beta}\dot{\mathbf{p}}^{\beta} - \dot{\mathbf{r}}_{\mathrm{C}}^{\alpha} - s^{\alpha}\dot{\mathbf{p}}^{\alpha} \\ &= \dot{\mathbf{r}}_{\mathrm{C}}^{\beta} - \dot{\mathbf{r}}_{\mathrm{C}}^{\alpha} + \frac{s^{\beta}}{2}\left(\dot{\boldsymbol{\gamma}}\cdot\mathbf{p}^{\beta} - \dot{\boldsymbol{\gamma}}:\mathbf{p}^{\beta}\mathbf{p}^{\beta}\mathbf{p}^{\beta}\right) - \frac{s^{\alpha}}{2}\left(\dot{\boldsymbol{\gamma}}\cdot\mathbf{p}^{\alpha} - \dot{\boldsymbol{\gamma}}:\mathbf{p}^{\alpha}\mathbf{p}^{\alpha}\mathbf{p}^{\alpha}\right)\end{aligned}. \tag{7.9}$$

$\Delta\dot{\mathbf{r}}$ is taken to be a simple function of the rate-of-deformation tensor. It means that only fluid deformation modifies the distance $\Delta\mathbf{r}$ between the two fibers at the interaction point. The next step considers that the short-range interaction force is function of the fiber contact probability. As the average inter-fiber spacing increases, one would expect the effect of interaction to decrease and vice versa. The inter-fiber spacing is a physical parameter that directly indicates the available space for fiber rotation. The interacting fiber β modifies the test fiber α rotation through the force weighted by the probability that the neighboring fiber interacts with the test fiber. This quantity is proportional to the probability $\psi_{\mathbf{p}^\beta}$ to find a fiber with an orientation $\mathbf{p}^\beta$. The orientation of the neighboring fiber is independent of that of the test fiber, which means that the orientations of neighboring fibers are not correlated. We used the following classical assumptions: a contact occurs if the distance between the nearest points of the two fibers is shorter than the fiber diameter D and there is no excluded volume effect. The positions along the test fiber and the interacting fiber of this nearest point are s^α and s^β, respectively (see **Figure 7.1**). Doi and Edwards (1978a), and then Sandstrom (1993) have proposed an evaluation of this probability as:

$$P_C = 2nD\left|\mathbf{p}^\alpha \times \mathbf{p}^\beta\right| \psi_{\mathbf{p}^\beta} d\mathbf{p}^\beta ds^\alpha ds^\beta . \tag{7.10}$$

The interaction force [Eq. (7.8)] is weighted by this contact probability P_C to give the elementary interaction force:

$$d\mathbf{f}_I = 2k\eta_0 nD^2 \Delta\dot{\mathbf{r}}\left|\mathbf{p}^\alpha \times \mathbf{p}^\beta\right| \psi_{\mathbf{p}^\beta} d\mathbf{p}^\beta ds^\alpha ds^\beta . \tag{7.11}$$

Then, the above expression is used to express the global torque $\mathbf{T}_I$. Integration over the neighboring and test fiber lengths gives all the possible interaction positions. It implies that all the contact point positions (described by the arc lengths s^α and s^β) will have the same probability to occur. An extra integration over all directions of $\mathbf{p}^\beta$ takes into account all the possible orientations of the neighboring fiber. With these considerations, the global torque $\mathbf{T}_I$ is evaluated to result in the expression of the orientation time evolution for the test fiber α:

$$\dot{\mathbf{p}}^\alpha = \dot{\mathbf{p}}_H^\alpha - \phi\tilde{M}\int_{\mathbf{p}^\beta}\left|\mathbf{p}^\alpha \times \mathbf{p}^\beta\right|\left(\frac{1}{2}\dot{\gamma}\cdot\mathbf{p}^\alpha - \frac{1}{2}\dot{\gamma}:\mathbf{p}^\alpha\mathbf{p}^\alpha\mathbf{p}^\alpha\right)\psi_{\mathbf{p}^\beta}\mathrm{d}\mathbf{p}^\beta\,, \tag{7.12}$$

where the dimensionless scalar $\tilde{M} = 2k/3\pi Y_C$. The term in brackets represents the fiber rotation induced by fluid deformation only. Since interactions modify also fiber rotation, a perturbation velocity is introduced similarly as done by Folgar and Tucker (1984), which is proportional to the effective deformation rate $|\dot{\gamma}|$. This diffusional term is not due to the Brownian motion, but represents the rotational fluctuations undergoing by the test fiber, when the suspension is flowing. Therefore, the test fiber evolution can be expressed as:

$$\dot{\mathbf{p}}^\alpha = \dot{\mathbf{p}}_H^\alpha - \phi\tilde{M}\int_{\mathbf{p}^\beta}\left|\mathbf{p}^\alpha \times \mathbf{p}^\beta\right|\left(\frac{1}{2}\dot{\gamma}\cdot\mathbf{p}^\alpha - \frac{1}{2}\dot{\gamma}:\mathbf{p}^\alpha\mathbf{p}^\alpha\mathbf{p}^\alpha + q|\dot{\gamma}|\frac{\partial \ln \psi_{\mathbf{p}^\alpha}}{\partial \mathbf{p}^\alpha}\right)\psi_{\mathbf{p}^\beta}\mathrm{d}\mathbf{p}^\beta\,, \tag{7.13}$$

where q is a dimensionless interaction coefficient. We notice that when the fiber volume fraction ϕ is small, Eq. (7.13) reduces to the time evolution equation for slender particles [Eq. (7.6)].

7.2.4. Time evolution of the second order orientation tensor

From Bird et al. (1987b), the probability distribution function may be regarded as a convected quantity. Then, the dynamic change of the second orientation tensor is derived from Eq. (7.13) as:

$$\begin{aligned}\frac{D\mathbf{a}_2}{Dt} &= -\frac{1}{2}(\boldsymbol{\omega}\cdot\mathbf{a}_2 - \mathbf{a}_2\cdot\boldsymbol{\omega}) + \frac{1}{2}(\dot{\boldsymbol{\gamma}}\cdot\mathbf{a}_2 + \mathbf{a}_2\cdot\dot{\boldsymbol{\gamma}} - 2\dot{\boldsymbol{\gamma}}:\mathbf{a}_4) \\ &\quad -\frac{1}{2}\phi\tilde{M}(\dot{\boldsymbol{\gamma}}\cdot\mathbf{b}_2 + \mathbf{b}_2\cdot\dot{\boldsymbol{\gamma}} - 2\dot{\boldsymbol{\gamma}}:\mathbf{b}_4) \\ &\quad -\phi\tilde{M}q|\dot{\gamma}|\int_{\mathbf{p}^\alpha}\frac{\partial\psi_{\mathbf{p}^\alpha}}{\partial\mathbf{p}^\alpha}\int_{\mathbf{p}^\beta}|\mathbf{p}^\alpha\times\mathbf{p}^\beta|\psi_{\mathbf{p}^\beta}d\mathbf{p}^\beta\cdot\frac{\partial\mathbf{p}^\alpha\mathbf{p}^\alpha}{\partial\mathbf{p}^\alpha}\,d\mathbf{p}^\alpha\end{aligned} \tag{7.14}$$

Some already known tensors appear, such as the second- and fourth-order orientation tensors $\mathbf{a}_2$ and $\mathbf{a}_4$ (Advani & Tucker, 1987). New tensors are also introduced, the second- and fourth-order tensors $\mathbf{b}_2$ and $\mathbf{b}_4$, called interaction tensors. They are defined by forming the dyadic products of the vector $\mathbf{p}^\alpha$, weighted by the potential $|\mathbf{p}^\alpha\times\mathbf{p}^\beta|$, and then twice integrating the product with respect to the distribution function over all possible directions (Djalili-Moghaddam & Toll, 2005). Because the distribution function is even, the odd-order integrals are zero, so only the even-order tensors are of interest:

$$\mathbf{b}_2 = \int_{\mathbf{p}^\alpha}\int_{\mathbf{p}^\beta}\mathbf{p}^\alpha\mathbf{p}^\alpha|\mathbf{p}^\alpha\times\mathbf{p}^\beta|\psi_{\mathbf{p}^\beta}\psi_{\mathbf{p}^\alpha}d\mathbf{p}^\beta d\mathbf{p}^\alpha, \tag{7.15}$$

$$\mathbf{b}_4 = \int_{\mathbf{p}^\alpha}\int_{\mathbf{p}^\beta}\mathbf{p}^\alpha\mathbf{p}^\alpha\mathbf{p}^\alpha\mathbf{p}^\alpha|\mathbf{p}^\alpha\times\mathbf{p}^\beta|\psi_{\mathbf{p}^\beta}\psi_{\mathbf{p}^\alpha}d\mathbf{p}^\beta d\mathbf{p}^\alpha. \tag{7.16}$$

The interaction tensors are completely symmetric. Moreover, all the terms in Eq. (7.14) have been averaged easily except the last term on the right hand side, which

requires an approximate solution. To achieve a simplest form, we follow the approach done for the FENE-P model by Peterlin (1955), Bird et al. (1987b), and Carreau et al. (1997) who consider the average macromolecule length as a characteristic length. In our case, the pre-averaging of the scalar quantity $\int_{\mathbf{p}^\beta} \left|\mathbf{p}^\alpha \times \mathbf{p}^\beta\right| \psi_{\mathbf{p}^\beta} d\mathbf{p}^\beta$ with respect to the distribution $\psi_{\mathbf{p}^\alpha}$ indicates that the average contact number is representative of all the contact points. Hence we obtain the following scalar function:

$$f = \text{trace}\, \mathbf{b}_2 = \int_{\mathbf{p}^\alpha} \int_{\mathbf{p}^\beta} \left|\mathbf{p}^\alpha \times \mathbf{p}^\beta\right| \psi_{\mathbf{p}^\beta} \psi_{\mathbf{p}^\alpha} d\mathbf{p}^\beta d\mathbf{p}^\alpha \,. \tag{7.17}$$

Toll (1998) referred to f as the average number of contacts per fiber. Moreover, he defined a second scalar invariant g of the fiber orientation distribution, defined as:

$$g = \int_{\mathbf{p}^\alpha} \int_{\mathbf{p}^\beta} \left|\mathbf{p}^\alpha \cdot \mathbf{p}^\beta\right| \psi_{\mathbf{p}^\beta} \psi_{\mathbf{p}^\alpha} d\mathbf{p}^\beta d\mathbf{p}^\alpha \,. \tag{7.18}$$

Some generic values of f and g for different fiber orientations are listed in **Table 7.1**. According to Toll (1998), the scalar quantities f and g are related to the average number of contacts per fiber N_C as:

$$N_C = \frac{8}{\pi} r\phi f + 4\phi(g+1) \,. \tag{7.19}$$

For slender fibers, the average number of contacts per fiber reduces to:

$$N_C = \frac{8}{\pi} r\phi f \,. \tag{7.20}$$

Using the pre-averaging, the equation of change for $\mathbf{a}_2$ becomes:

$$\frac{D\mathbf{a}_2}{Dt} = -\frac{1}{2}(\boldsymbol{\omega}\cdot\mathbf{a}_2 - \mathbf{a}_2\cdot\boldsymbol{\omega}) + \frac{1}{2}(\dot{\boldsymbol{\gamma}}\cdot\mathbf{a}_2 + \mathbf{a}_2\cdot\dot{\boldsymbol{\gamma}} - 2\dot{\boldsymbol{\gamma}}:\mathbf{a}_4) \\ -\frac{1}{2}\phi\tilde{M}(\dot{\boldsymbol{\gamma}}\cdot\mathbf{b}_2 + \mathbf{b}_2\cdot\dot{\boldsymbol{\gamma}} - 2\dot{\boldsymbol{\gamma}}:\mathbf{b}_4) + 2f\phi\tilde{M}q|\dot{\boldsymbol{\gamma}}|(\boldsymbol{\delta} - 3\mathbf{a}_2) \quad , \tag{7.21}$$

where the last term is a diffusion term. If we refer to Equation (7.13), which gives the average angular velocity of a particle in a concentrated suspension, the variance is equal to $2f\phi\tilde{M}q|\dot{\gamma}|$ compared to $2C_I|\dot{\gamma}|$ for the Folgar and Tucker (1984) model. This quantity evolves with time: it is maximum for a random orientation state and tends to zero for perfectly aligned fibers (see f values in **Table 7.1**). The variance in this model is a function of the number of fiber contacts, not accounted for in the Folgar and Tucker model.

In Appendix 1, it is proven that the average mass center of a fiber moves affinely with the bulk flow.

7.3. Stress determination

The total stress for slender fiber supensions has been derived by Dinh and Armstrong (1984) as:

$$\boldsymbol{\sigma} = -P\boldsymbol{\delta} + \eta_0\dot{\boldsymbol{\gamma}} + \eta_0\phi\frac{r^2}{6\pi}X_A\dot{\boldsymbol{\gamma}}:\mathbf{a}_4 . \tag{7.22}$$

For non dilute suspensions, there is an additional stress contribution due to the contact forces acting on the fibers. From the previous development, the deviatoric stress $\boldsymbol{\tau}$ becomes:

$$\boldsymbol{\tau} = \eta_0 \dot{\boldsymbol{\gamma}} + \eta_0 \phi \frac{r^2}{6\pi} X_A \dot{\boldsymbol{\gamma}} : \mathbf{a}_4 + n \int_{\mathbf{p}^\alpha} \int s^\alpha \mathbf{p}^\alpha d\mathbf{f}_I \psi_{\mathbf{p}^\alpha} d\mathbf{p}^\alpha , \tag{7.23}$$

where the stress contribution comes from the Newtonian matrix, the hydrodynamic forces (same as previously) and the fiber interactions (Toll & Manson, 1994), respectively [hypothesis (7)]. In order to simplify the development, we use Eq. (7.6) to represent the motion of the test fiber. Combining Eqs. (7.11) and (7.23) yields the stress induced by fiber interactions:

$$\boldsymbol{\tau}_I = \eta_0 \phi^2 \frac{4r^2}{3\pi^2} k \dot{\boldsymbol{\gamma}} : \mathbf{b}_4 . \tag{7.24}$$

We note that the fluid velocity at any contact point is close to that of the fluid velocity at a neighboring contact point. Hence, using the assumption that particles do not perturb the fluid flow, the velocity at the contact point is $\dot{\mathbf{r}}_C^\beta + s^\beta \boldsymbol{\kappa} \cdot \mathbf{p}^\beta \approx \dot{\mathbf{r}}_C^\alpha + s^\alpha \boldsymbol{\kappa} \cdot \mathbf{p}^\alpha$. Finally, the total stress tensor including fiber–fiber interactions is given by:

$$\boldsymbol{\sigma} = -P\boldsymbol{\delta} + \eta_0 \dot{\boldsymbol{\gamma}} + \eta_0 \phi \frac{r^2}{6\pi} X_A \dot{\boldsymbol{\gamma}} : \mathbf{a}_4 + \eta_0 \phi^2 \frac{4r^2}{3\pi^2} k \dot{\boldsymbol{\gamma}} : \mathbf{b}_4 . \tag{7.25}$$

Expression (7.25) reduces to that proposed by Djalili-Moghaddam and Toll (2005) for short range interactions (concentrated regime), if the slender-body coefficients (used here) are replaced by the Shaqfeh-Fredrickson coefficients (Shaqfeh & Fredrickson, 1990). Furthermore, in the work of Djalili-Moghaddam and Toll (2005) the interaction distance is arbitrary, whereas in this work it is taken as the fiber diameter, as already done by Sandstrom (1993). Again, we note that for very low fiber volume

fraction, the term in ϕ^2 becomes insignificant and the total stress [Eq. (7.25)] reduces to the Dinh and Armstrong (1984) result [Eq. (7.22)].

7.4. Approximations

Equations (7.21) and (7.25) do not represent a complete set of rheological equations yet. To achieve this, we need to state some approximations. The first one has to relate the fourth-order orientation tensor to the second order one. Many closure approximations have been proposed in the literature, but will not be reported further in this paper (see (Chung & Kwon, 2001) and (Sepehr et al., 2004c) for more details). The ORW3 closure approximation (Orthotropic fitted closure approximation for wide C_I values with 3rd order polynomial expansions) developed by Chung and Kwon (2001) is used to evaluate the fourth-order orientation tensor. This closure has been chosen as the diffusion coefficient in Eq. (7.21) evolves with time and it has been shown to give reliable results for a wide range of C_I (Chung & Kwon, 2001, 2002a). In the next development, a relationship between the second-order orientation tensor and the second-order interaction tensor is proposed. Finally, we suggest closure approximations for the fourth-order interaction tensor.

7.5. Onsager and Maier-Saupe potentials

First, we note that the scalar quantity $\left|\mathbf{p}^{\alpha}\times\mathbf{p}^{\beta}\right|$ known as the Onsager potential (Onsager, 1949) cannot be expressed in a simple form without the use of a closure approximation. Nevertheless, it is possible to relate the interaction tensor $\mathbf{b_2}$ to the

orientation tensors (second and fourth) by correctly approximating the Onsager potential. It is often replaced by the Maier-Saupe potential (Maier & Saupe, 1959) expressed as $\left|\mathbf{p}^{\alpha}\times\mathbf{p}^{\beta}\right|^{2}$. These two potentials are obviously different, but they share the essential properties that their maximum are reached when the fibers are orthogonal and then decrease when the fibers orient (Grmela & Dlugogorski, 1996). By performing some straightforward algebraic calculations (see Appendix 2), we obtain:

$$\mathbf{b}_2 = \frac{3\pi}{8}\left(\mathbf{a}_2 - \mathbf{a}_4 : \mathbf{a}_2\right), \tag{7.26}$$

where the numerical pre-factor $3\pi/8$ is introduced to reach the exact value of $f = \pi/4$ for an isotropic fiber orientation, as already done by Dhont and Briels (2003) who evaluated the Onsager potential using a Ginzburg-Landau expansion.

7.5.1. Interaction closure approximations

As initial simple approximations we propose two closures, one based on the quadratic formulation and the second one formulated with a linear combination. The quadratic closure, called IQUA, has the following form:

$$b^{Q}_{ijkl} = \frac{1}{f} b_{ij} b_{kl}, \tag{7.27}$$

whereas the linear closure (ILIN) can be written as:

$$\begin{aligned} b^{L}_{ijkl} = &-\frac{f}{35}\left(\delta_{ij}\delta_{kl} + \delta_{ik}\delta_{jl} + \delta_{il}\delta_{jk}\right) \\ &+\frac{1}{7}\left(b_{ij}\delta_{kl} + b_{ik}\delta_{jl} + b_{il}\delta_{jk} + b_{kl}\delta_{ij} + b_{jl}\delta_{ik} + b_{jk}\delta_{il}\right) \end{aligned} \tag{7.28}$$

It was shown by Sepehr et al. (2004b) that linear orientation closures produced oscillations, while quadratic orientation approximations were not efficient to predict the correct behavior for reverse flows. Results obtained with the quadratic form (IQUA) seem to be more relevant than the ones obtained with the linear interaction closure (ILIN). Hence, for simplicity, we chose the IQUA approximation for the interaction tensor in the following comparison with experimental results. Other closure approximations will be examined in another investigation.

7.6. Predictions and comparison with experimental data

7.6.1. Model predictions

The present model, formed by Equations (7.21), (7.25), (7.26) and (7.27), has been tested in simple shear flow for forward and reverse stress growth experiments. The deformation is calculated as $\gamma = \dot{\gamma} t$, where the applied shear rate is set at 1 s^{-1}. All predictions are obtained with the following conditions: η_0 = 1 Pa·s, ϕ = 10 % and r = 20. The closure approximation for the 4th order interaction tensors is the IQUA [Eq. (7.27)]. The only adjustable parameters are the dimensionless numbers k and q, with k taking into account the intensity of the friction force and q proportional to the diffusion term. The resistance functions X_A and Y_C are set to 1 and 1/6, respectively, from the dilute regime. Results from the Folgar-Tucker-Dinh-Armstrong (FTDA) model are also compared. The FTDA model consists of Equations (7.1) and (7.22), where the interaction coefficient C_I is set to 0.01. For both models, the initial fiber orientation is assumed to be 3D random (isotropic) and the closure approximation for the 4th order

orientation tensor is the ORW3 (Chung & Kwon, 2001). The system of equations of each model is solved using the Matlab® software.

Figure 7.2 and **Figure 7.3** report the predictions for the shear stress growth coefficient η^+ and the first normal stress growth function N_1^+ in forward (clock-wise (CW) direction) and reverse (counterclock-wise (CCW) direction) flows, respectively, for different values of k. In comparison to the FTDA predictions, the results show that by increasing k the steady-state values are reached more rapidly. In addition, the relative amplitude of the overshoots for the stress growth functions in the forward direction (**Figure 7.2a** and **b**) depends on the k value, especially for the first normal stress growth function. We note some oscillations in the predicted functions. For the reverse direction (**Figure 7.3a** and **b**), the overshoots are predicted at lower strain values as k increases. It is a reasonable result since fewer fibers are aligned in the flow direction for large k. All of these observations confirm that fiber interactions prevent fiber orientation, which is physically realistic. As in **Figure 7.2a** and **b**, we note oscillations in the predicted functions for the reverse (counterclock) flow: the local undershoots followed by a slight overshoot, observed at strains larger than 10 are probably due to the quadratic closure approximation used for the 4th order interaction tensor.

Effects of different values of q on η^+ and N_1^+ are presented in **Figure 7.4** and **Figure 7.5** for forward and reverse flow experiments, respectively. In the forward direction (**Figure 7.4a** and **b**), q does not affect the strain at which the overshoots of the stress growth functions are predicted. In addition, as q increases the maximum value of

the stress growth coefficient η^+ is unchanged, whereas the maximum of the first normal stress growth function N_1^+ slightly decreases. However, the relative amplitude of the overshoots with respect to the steady-state values is a strong function of q and the steady values become larger as q is increased. In analogy with results of **Figure 7.3a** and **b**, the overshoots for reverse flows (**Figure 7.5a** and **b**) occur at lower strain values as q increases. Similar results have been reported by (Sepehr et al., 2004c) using the Folgar-Tucker-Lipcomb model and different values of the interaction coefficient C_I. Since parameter q is related to diffusion, it is reasonable to expect that q and C_I produce similar effects.

Key components of $\mathbf{a_2}$ and the trace of $\mathbf{b_2}$, f, have been also calculated for forward (**Figure 7.6**) and reverse (**Figure 7.7**) stress growth experiments, both for k = 0.3 and q = 0.5. **Figure 7.6** indicates that for an initial 3D random state most of the fibers orient in the shear direction. The scalar f depicts a decrease from $f = \pi/4$ to a steady value of f = 0.4588, with a small undershoot at a strain close to 10. For the reverse flow (**Figure 7.7**), fiber tumbling is predicted by the model, as illustrated by the $\mathbf{a_2}$ components. Also, f exhibits an overshoot before reaching the same steady state of 0.4588 indicating that fiber contacts increase during tumbling.

7.6.2. Comparison with experimental data

Experiments have been performed on suspensions of short glass fibers in a Newtonian polybutene matrix (PB Indopol H100, η_0=35.1 Pa·s at 20°C). The fibers were obtained from the calcination at 600°C for 40 min of a 30 wt % filled

polypropylene provided by Basell. The average fiber length, L, was close to 320 μm and its diameter D = 16 μm. Four different weight fractions of fibers were used (10 % (PB10), 15 % (PB15), 20 % (PB20) and 25 % (PB25), corresponding to volume fractions, ϕ, of 3.8, 5.8, 8.1 and 10.5 %, respectively). Sample PB10 was in the semi-dilute regime whereas PB15, PB20 and PB25 were in the concentrated one. The composites were prepared manually by gently mixing the fibers in the matrix in order to avoid fiber breakage. Measurements were performed with an Anton Paar Physica MCR501 rheometer using a parallel plate geometry with a 25 mm radius. The gap was fixed at 1.5 mm, which allowed fibers to rotate freely at least in the shear plane. Stress growth experiments were carried out at a shear rate of 10 s^{-1}. The torque and the normal force exerted by the material on the disks are respectively given by Carreau et al. (1997):

$$T = \int_0^{2\pi}\int_0^{R} \sigma_{\theta z}(r)\, r^2 dr\, d\theta, \tag{7.29}$$

$$F = \int_0^{2\pi}\int_0^{R} \sigma_{zz}(r)\, r\, dr\, d\theta. \tag{7.30}$$

These quantities are dependent on the strain γ and different values are obtained at different radius r. To compare the experimental data with the model predictions, the predicted rheological functions have to be evaluated under the same conditions, i.e. same deformation. Using straightforward calculations, the model predictions are calculated as:

$$\eta(\gamma_R) = \frac{4}{\gamma_R^4}\int_0^{\gamma_R} \eta(\gamma)\, \gamma^3 d\gamma, \tag{7.31}$$

$$N_1(\gamma_R) - N_2(\gamma_R) = \frac{2}{\gamma_R^2}\int_0^{\gamma_R} \left[N_1(\gamma) - N_2(\gamma)\right] \gamma\, d\gamma, \tag{7.32}$$

where γ_R is the strain at the disk rim and γ is the deformation at the radius r. Furthermore, the IQUA [Eq. (7.27)] approximation is employed for the interaction tensor. The three quantities X_A, k and q are chosen as fitting parameters. A simple optimization technique was applied to determine the suitable coefficients, which were fixed for the four fiber concentrations.

The predicted reduced steady-state viscosity and normal stress difference as functions of the fiber volume fraction are compared to the data in **Figure 7.8** for a shear rate of 10 s^{-1}. The fitting parameters are found to be X_A = 17.116, k = 0.112 and q = 0.220. The viscosity and normal stress data describe linear dependences at low fiber concentrations as observed by Sepehr et al. (2004d) for similar suspensions, but exhibit quadratic trends as fiber contents increase. The largest fiber volume fraction that was used by Sepehr et al. (2004d) was ϕ = 7.06 %, as compared to ϕ = 10.5 % in our work. The quadratic dependences for both the reduced viscosity and normal stress difference are well predicted by the model. Kitano and Kataoka (1981a) have also reported quadratic behaviors with vinylon and nylon fibers in silicone oil. Also shown are the reduced normal stress difference, which also exhibits a quadratic dependence.

Figure 7.9 reports the transient shear viscosity and normal stress difference as functions of deformation for an applied shear rate of 10 s^{-1}. The stress growth data were obtained in reverse flow (counterclock-wise (CCW) direction) following a first stress growth in the clockwise (CW) direction, since they have been observed to be more reproducible (Sepehr et al., 2004d). The data and model predictions for the four

composites are presented in **Figure 7.9** using a semi-log scale to highlight the behavior at low strain. In **Figure 7.9a**, we can see that the magnitude and the width of the stress growth overshoot, which have been related to fiber tumbling (Laun, 1984; Sepehr et al., 2004c), are fairly well described by the model. In **Figure 7.9b**, for the normal stress difference, the model predictions are in good qualitative agreement with the data. The model predicts correctly that under reverse flow the normal stress difference takes initially negative values (nevertheless underestimated) before rising and depicting a positive overshoot. However, the amplitude of the overshoots is slightly underestimated. Obviously, better fits would be obtained if different values for the parameters were used for each suspension.

Another interesting point is to compare the values obtained for the interaction coefficient C_I using the new model with those of the literature, namely of Bay (1991) and Phan-Thien et al. (2002). Comparing Eq. (7.1) and Eq. (7.21), we can express our interaction coefficient as:

$$C_I = f\phi\tilde{M}q\,. \tag{7.33}$$

In contrast to the empirical Phan-Thien et al. expression [Eq. (7.3)], which is only dependent on the particle aspect ratio r and the fiber volume fraction ϕ, the new C_I is proportional to ϕ and the scalar f, which is a function of the inter-fiber spacing, as suggested by Ranganathan and Advani (1991). It implies that the proposed diffusion coefficient evolves with time as f depends on fiber orientation, contrarily to Bay model [Eq. (7.2)], and Phan-Thien et al model [Eq. (7.3)]. **Figure 7.10** presents the computed

values for large deformation (steady-state regime) of C_I [Eq. (7.3)], just as the Bay and Phan-Thien et al. models. Our results show the same tendency as the Phan-Thien et al. expression, which supports the validity of Eq. (7.33). (Bay, 1991) obtained their numerical coefficients from measurement of fiber orientation in injection, as compared to transient shear flow in your case. Phan-Thien et al. (2002) proposed the empirical expression [Eq. (7.3)] by comparing simulations with the experimental data of Folgar and Tucker (1984) for nylon fibers (non rigid fibers as in your case) in silicone oil. All this could explain the observed deviation of one decade. In addition to being related to diffusivity as suggested by Folgar and Tucker (1984), the proposed C_I is dependent on fiber orientation. This affects considerably the transient fiber orientation and is of major importance for the modeling of processes.

Finally, with the trace of the second-order interaction tensor, it is possible to predict the average contact number per fiber as a function of the material deformation using Eq. (7.20). This is given in **Figure 7.11** for reverse flow (CCW). As expected, a maximum of fiber interactions occurs at a given deformation and then the average fiber contacts decrease to reach a steady value. Moreover, the effective contact number per fiber is similar to the one obtained by Ausias (2006) from direct simulations. For their largest concentrated suspensions (ϕ = 11.5 %), their computed average contact number was close to 2.0, similarly to what we find for ϕ = 10.5%. To justify the trends in **Figure 7.11**, we have computed the average spacing between fibers (h) according to Dinh and Armstrong (1984). For PB25, it is found that $h = (nL)^{-1/2} \approx 44$ μm for totally aligned

fibers and $h = (nL^2)^{-1} \approx 6$ μm for isotropic orientation. Consequently, more contacts are expected when fibers disorient, as predicted by the model. The small oscillations, that appear at large deformation, as already observed in **Figure 7.2** to **Figure 7.5**, are attributed to the used of the quadratic closure approximation for the 4th order interaction tensor.

Our first observations show that the physics from which the model is derived is of a great relevance. The proposed approximations seem to be quite reasonable but further efforts are necessary, mainly concerning the closure approximations. The orientation probability distribution function should be numerically solved in order to suggest better closure approximations dealing with the new fourth order interaction tensor. Improvement of the present work can also be accomplished by modeling the interacting force with a nonlinear lubrication expression such as a power law instead of a linear one. Finally, the obtained diffusivity is isotropic and improvement could be achieved by using an anisotropic diffusivity.

7.7. Conclusions

A new mathematical formulation has been proposed to describe the rheological behavior of fiber suspensions in the non dilute regime and can be considered as an extension of the Dinh and Armstrong (1984) model. It takes into account fiber-fiber interactions with linear lubrication forces. In addition to the orientation tensors, this development allowed to introduce interaction tensors. A new equation of change for the second-order orientation tensor was derived, and an additional extra stress term was

developed to take into account the contribution induced by the interacting forces. Closure approximations were proposed to estimate the fourth-order interaction tensors and the most accurate one is based on a quadratic derivation.

In order to validate the model, a rheological study of suspensions with fiber volume fractions close to those encountered in industrial applications have been performed using a Newtonian polybutene matrix and glass fibers. Despite the simple assumptions postulated at the fiber scale, start-up flow results showed a fairly good agreement in terms of the predicted viscosity and normal stress difference. The measured reduced viscosity and normal stress difference were found to be quadratic functions of the fiber volume fraction, as predicted by the model. Moreover, the interaction coefficient C_I derived from the model described most of the observations found in the literature. Finally, the new model requires only a small set of constitutive parameters (3), which are all directly linked to the physics and geometry at the fiber scale. In the present study, the same three parameters have been used to predict all the investigated fiber suspensions at different volume fractions, ranging from the semi-dilute to the concentrated regimes.

7.8. Acknowledgements

This work was supported by the France-Québec collaboration program and funded by NSERC (Natural Science and Engineering Council of Canada) – CIAM (Inter-American Collaboration in Materials) program.

7.9. Appendix 1: Fiber mass center velocity

The global hydrodynamic force $\mathbf{F}_{\mathrm{H}}$ applied along the fiber length in the dilute regime is expressed as:

$$\mathbf{F}_{\mathrm{H}} = \mathbf{A} \cdot \left(\mathbf{v}^{\infty} - \dot{\mathbf{r}}_{\mathrm{C}}^{\alpha} \right), \tag{7.34}$$

where $\dot{\mathbf{r}}_{\mathrm{C}}^{\alpha}$ is the mass center velocity of the test particle. $\mathbf{A}$ is a second order hydrodynamic resistance tensor, which contains fluid drag coefficients, and is expressed by $\mathbf{A} = \eta_0 L \left[Y_A \boldsymbol{\delta} + \left(X_A - Y_A \right) \mathbf{p}^{\alpha} \mathbf{p}^{\alpha} \right]$ in the $\mathbf{R}$ coordinate systems (**Figure 7.1**). Coefficients X_A and Y_A describe the drag exerted on the fiber from the axial and transverse fluid motion, respectively. For dilute suspensions of fibers in a Newtonian fluid, the slender body theory results in $Y_A = 2X_A = 2$ (Dinh & Armstrong, 1984). A force balance for negligible fiber inertia gives $\dot{\mathbf{r}}_{\mathrm{C}}^{\alpha} = \boldsymbol{\kappa} \cdot \mathbf{r}^{\alpha}$ as derived by Dinh and Armstrong (1984), and it shows that the fiber centroid moves affinely with the effective medium in the absence of any other forces besides those imparted by the suspending fluid.

Furthermore, in the case where contacts between fibers are taken into account, the total force on the test fiber is now the sum of the global hydrodynamic and interaction force. Again, a force balance for negligible fiber inertia gives the motion of the center mass:

$$\dot{\mathbf{r}}_{\mathrm{C}}^{\alpha} = \boldsymbol{\kappa} \cdot \mathbf{r}_{\mathrm{C}}^{\alpha} + 2k\eta_0 n D^2 L^2 \mathbf{A}^{-1} \cdot \left(\dot{\mathbf{r}}_{\mathrm{C}}^{\beta} - \dot{\mathbf{r}}_{\mathrm{C}}^{\alpha} \right) \int_{\mathbf{p}^{\beta}} \left| \mathbf{p}^{\alpha} \times \mathbf{p}^{\beta} \right| \psi_{\mathbf{p}^{\beta}} d\mathbf{p}^{\beta}, \tag{7.35}$$

where $\dot{\mathbf{r}}_{\mathbf{C}}^{\beta}$ is the mass center velocity of the neighboring fiber. Consequently, the center mass deforms non-affinely if the interactions are present. The Dinh and Armstrong (1984) expression is recovered when the number of fibers per unit volume (n) is small.

However, if we suppose that $\dot{\mathbf{r}}_{\mathbf{C}}^{\beta}$ is close to $\dot{\mathbf{r}}_{\mathbf{C}}^{\alpha}$ plus a perturbation velocity, as done for $\dot{\mathbf{p}}^{\alpha}$ in section C, the next result is obtained after simplification:

$$\dot{\mathbf{r}}_{\mathbf{C}}^{\alpha} = \boldsymbol{\kappa} \cdot \mathbf{r}_{\mathbf{C}}^{\alpha} - 2knD^2 L \frac{D_t}{Y_A \psi_{\mathbf{p}^{\alpha}}} \mathbf{A}^{-1} \cdot \frac{\partial \psi_{\mathbf{p}^{\alpha}}}{\partial \mathbf{r}_{\mathbf{C}}^{\alpha}} \int_{\mathbf{p}^{\beta}} \left| \mathbf{p}^{\alpha} \times \mathbf{p}^{\beta} \right| \psi_{\mathbf{p}^{\beta}} d\mathbf{p}^{\beta} , \tag{7.36}$$

where the parameter D_t is expressed in m/s. According to hypothesis (3), it implies that:

$$\dot{\mathbf{r}}_{\mathbf{C}}^{\alpha} = \boldsymbol{\kappa} \cdot \mathbf{r}_{\mathbf{C}}^{\alpha} . \tag{7.37}$$

This result clearly shows that the mass center of the fibers moves affinely with the bulk fluid.

7.10. Appendix 2: Evaluation of interaction tensors with Maier-Saupe approximation

The scalar quantity can be extended as follow:

$$
\begin{aligned}
\left|\mathbf{p}^{\alpha}\times\mathbf{p}^{\beta}\right| &\Rightarrow \left|\mathbf{p}^{\alpha}\times\mathbf{p}^{\beta}\right|^{2} = \left(\mathbf{p}^{\alpha}\times\mathbf{p}^{\beta}\right)^{2} = \left(\mathbf{p}^{\alpha}\times\mathbf{p}^{\beta}\right)_{i}\left(\mathbf{p}^{\alpha}\times\mathbf{p}^{\beta}\right)_{i} \\
&= \left(\varepsilon_{ijk}p_{j}^{\alpha}p_{k}^{\beta}\right)\left(\varepsilon_{imn}p_{m}^{\alpha}p_{n}^{\beta}\right) = \left(\varepsilon_{ijk}\varepsilon_{imn}\right)\left(p_{j}^{\alpha}p_{k}^{\beta}p_{m}^{\alpha}p_{n}^{\beta}\right) \\
&= \left(\delta_{jm}\delta_{kn} - \delta_{jn}\delta_{km}\right)\left(p_{j}^{\alpha}p_{k}^{\beta}p_{m}^{\alpha}p_{n}^{\beta}\right) \\
&= \delta_{jm}\delta_{kn}p_{j}^{\alpha}p_{k}^{\beta}p_{m}^{\alpha}p_{n}^{\beta} - \delta_{jn}\delta_{km}p_{j}^{\alpha}p_{k}^{\beta}p_{m}^{\alpha}p_{n}^{\beta} \\
&= p_{j}^{\alpha 2}p_{k}^{\beta 2} - p_{j}^{\alpha}p_{j}^{\beta}p_{k}^{\alpha}p_{k}^{\beta} \\
&= 1 - \mathbf{p}^{\alpha}\mathbf{p}^{\alpha} : \mathbf{p}^{\beta}\mathbf{p}^{\beta}
\end{aligned}
\quad . \tag{7.38}
$$

Moreover, we introduce a numerical pre-factor of $3\pi/8$ to reach the exact value of $\pi/4$ for the isotropic average value. After replacing expression (7.38) into Eq. (7.15), we get:

$$
\begin{aligned}
\mathbf{b}_{2} &= \int_{\mathbf{p}^{\alpha}}\int_{\mathbf{p}^{\beta}} \mathbf{p}^{\alpha}\mathbf{p}^{\alpha}\left|\mathbf{p}^{\alpha}\times\mathbf{p}^{\beta}\right|\psi_{\mathbf{p}^{\alpha}}\psi_{\mathbf{p}^{\beta}}\, d\mathbf{p}^{\alpha}d\mathbf{p}^{\beta} \\
&= \frac{3\pi}{8}\int_{\mathbf{p}^{\alpha}}\int_{\mathbf{p}^{\beta}} \mathbf{p}^{\alpha}\mathbf{p}^{\alpha}\left(1 - \mathbf{p}^{\alpha}\mathbf{p}^{\alpha} : \mathbf{p}^{\beta}\mathbf{p}^{\beta}\right)\psi_{\mathbf{p}^{\alpha}}\psi_{\mathbf{p}^{\beta}}\, d\mathbf{p}^{\alpha}d\mathbf{p}^{\beta} \\
&= \frac{3\pi}{8}\int_{\mathbf{p}^{\alpha}}\int_{\mathbf{p}^{\beta}} \left(\mathbf{p}^{\alpha}\mathbf{p}^{\alpha} - \mathbf{p}^{\alpha}\mathbf{p}^{\alpha}\mathbf{p}^{\alpha}\mathbf{p}^{\alpha} : \mathbf{p}^{\beta}\mathbf{p}^{\beta}\right)\psi_{\mathbf{p}^{\alpha}}\psi_{\mathbf{p}^{\beta}}\, d\mathbf{p}^{\alpha}d\mathbf{p}^{\beta} \\
&= \frac{3\pi}{8}\int_{\mathbf{p}^{\alpha}} \left(\mathbf{p}^{\alpha}\mathbf{p}^{\alpha} - \mathbf{p}^{\alpha}\mathbf{p}^{\alpha}\mathbf{p}^{\alpha}\mathbf{p}^{\alpha} : \mathbf{a}_{2}\right)\psi_{\mathbf{p}^{\alpha}}\, d\mathbf{p}^{\alpha} \\
&= \frac{3\pi}{8}\left(\mathbf{a}_{2} - \mathbf{a}_{4} : \mathbf{a}_{2}\right)
\end{aligned}
\quad . \tag{7.39}
$$

Table 7.1 : Calculated values of f and g for different fiber orientations.

Orientation	f	g
Unidirectional	0	1
2-D random	$2/\pi$	$2/\pi$
2-D (½→1; ½→2)*	1/2	1/2
3-D random	$\pi/4$	1/2
3-D (⅓→1; ⅓→2; ⅓→3)**	2/3	1/3

* ½→1 ≡ 50% of fibers aligned in the 1-direction

** ⅓→1 ≡ 1/3 of fibers aligned in the 1-direction

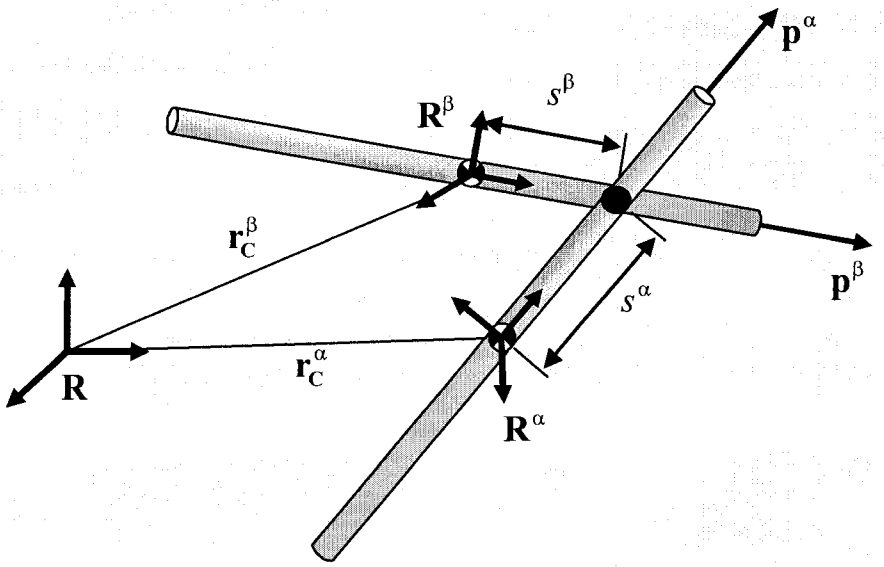

Figure 7.1 : Schematic representation of two interacting fibers. Superscript α represents the test fiber, superscript β refers to the neighboring fiber.

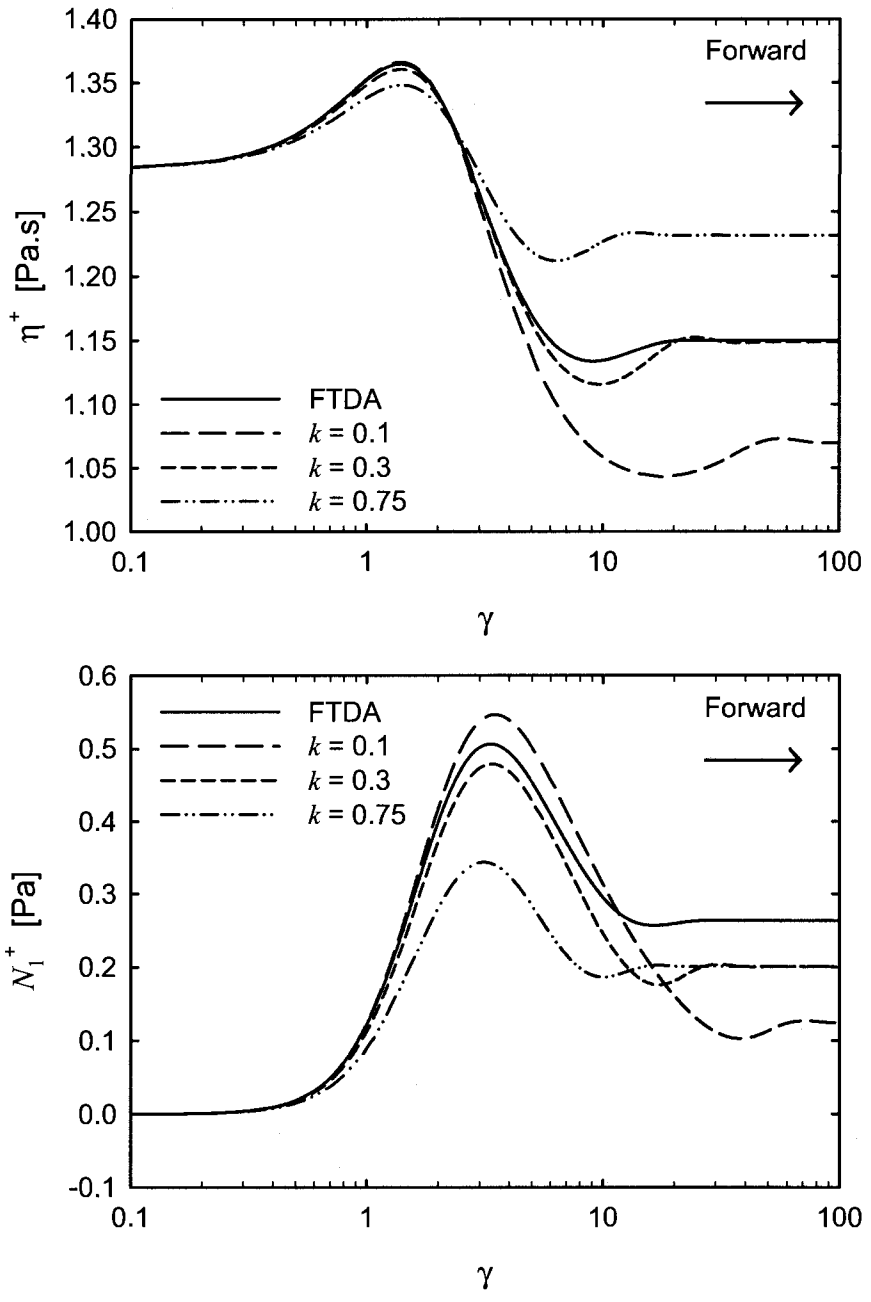

Figure 7.2 : Predicted stress growth functions for forward flow (CW); ORW3 and IQUA closure approximations, $\dot{\gamma}$ = 1 s-1 and q = 0.5: (a) transient viscosity; (b) transient primary normal stress differences as functions of strain.

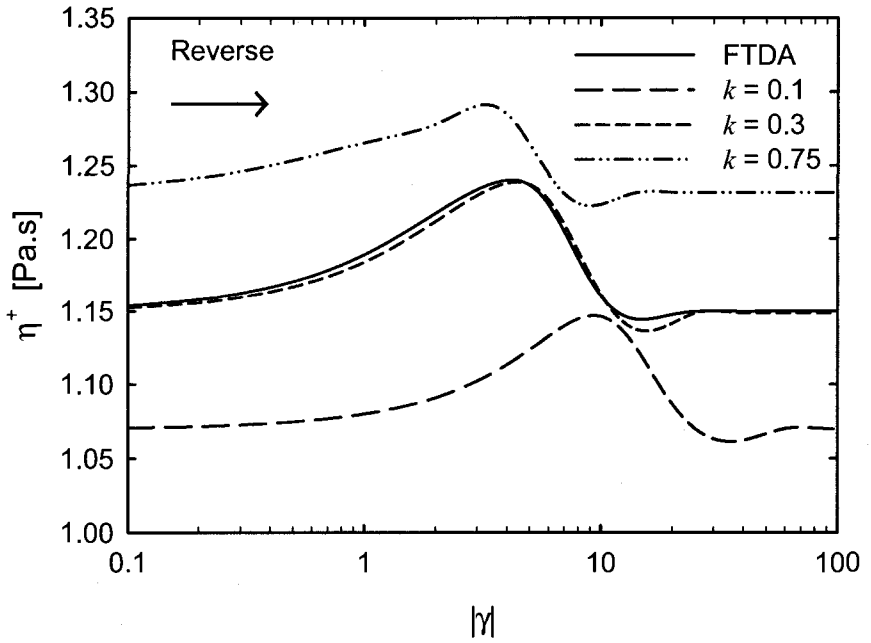

(a)

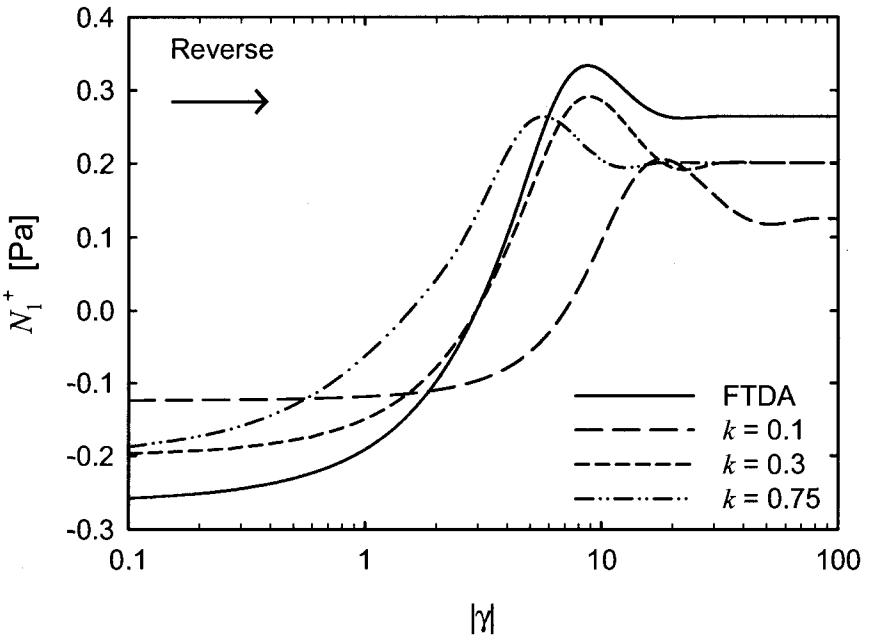

(b)

Figure 7.3 : Predicted stress growth functions for reverse flow (CCW); ORW3 and IQUA closure approximations, $|\dot{\gamma}| = 1\ s^{-1}$ and $q = 0.5$: (a) transient viscosity; (b) transient primary normal stress differences as functions of strain.

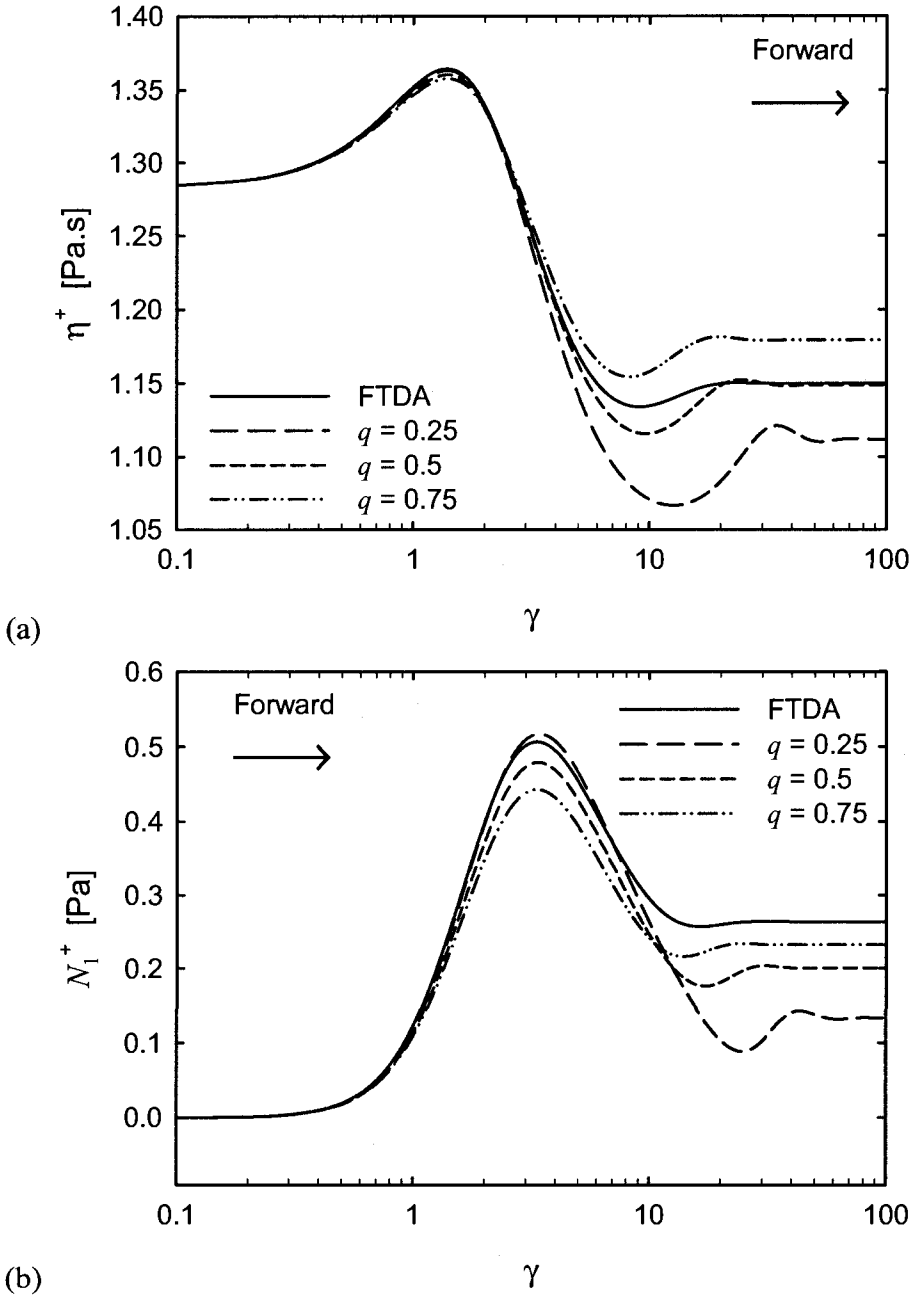

Figure 7.4 : Predicted stress growth functions for forward flow (CW); ORW3 and IQUA closure approximations, $\dot{\gamma}$ = 1 s^{-1} and k = 0.3: (a) transient viscosity; (b) transient primary normal stress differences as functions of strain.

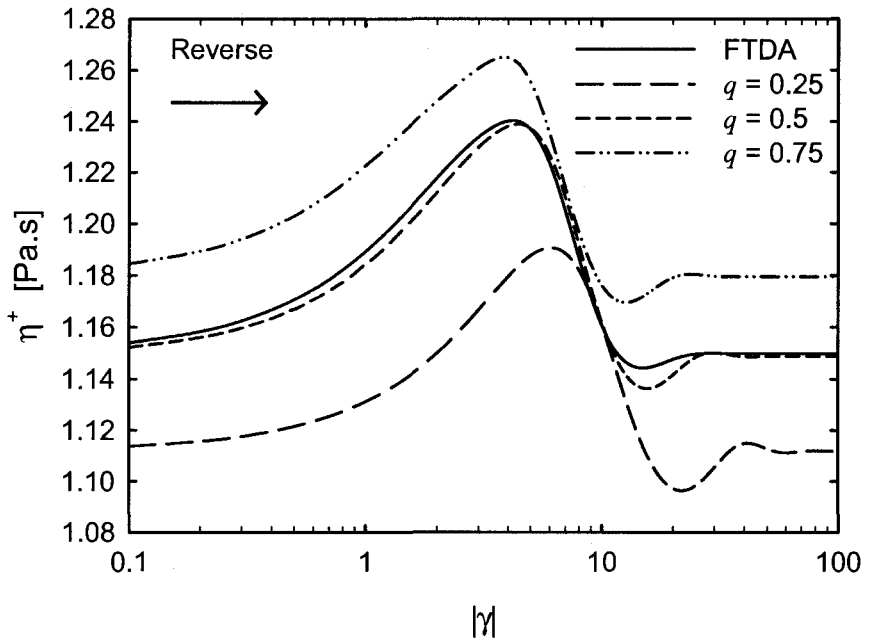

(a)

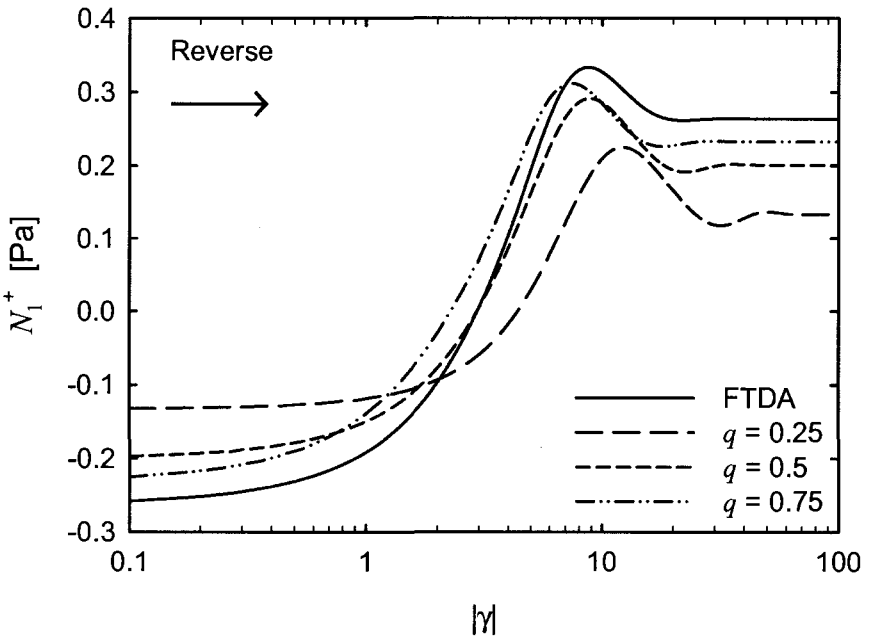

(b)

Figure 7.5 : Predicted stress growth functions for reverse flow (CCW); ORW3 and IQUA closure approximations, $|\dot{\gamma}| = 1\ s^{-1}$ and k= 0.3: (a) transient viscosity; (b) transient primary normal stress differences as functions of strain.

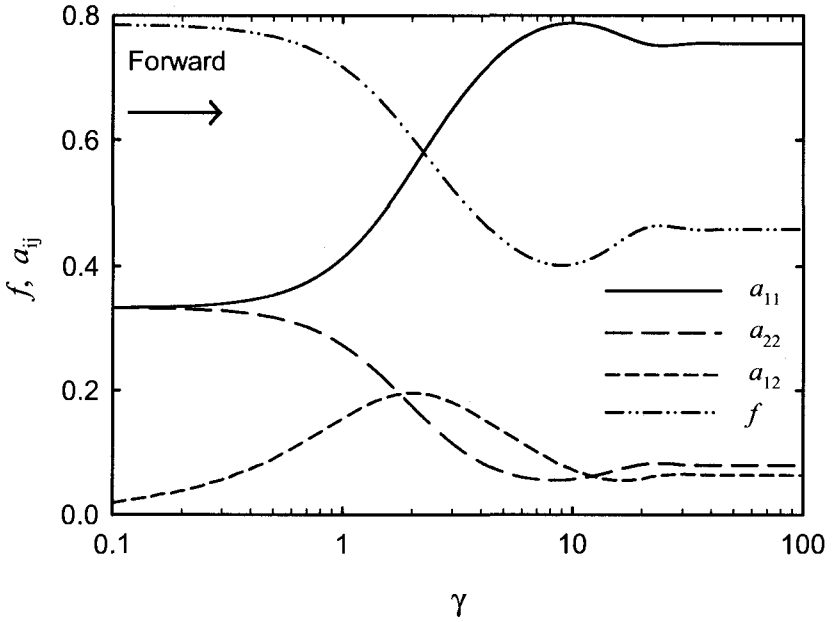

Figure 7.6 : Predicted variations for key components of $\mathbf{a_2}$ (a_{11}, a_{22} and a_{12}) and for the scalar f as functions of deformation for forward flow (ORW3 and IQUA closure approximations, $\dot{\gamma} = 1\ s^{-1}$, $X_A = 1$, $k = 0.3$ and $q = 0.5$).

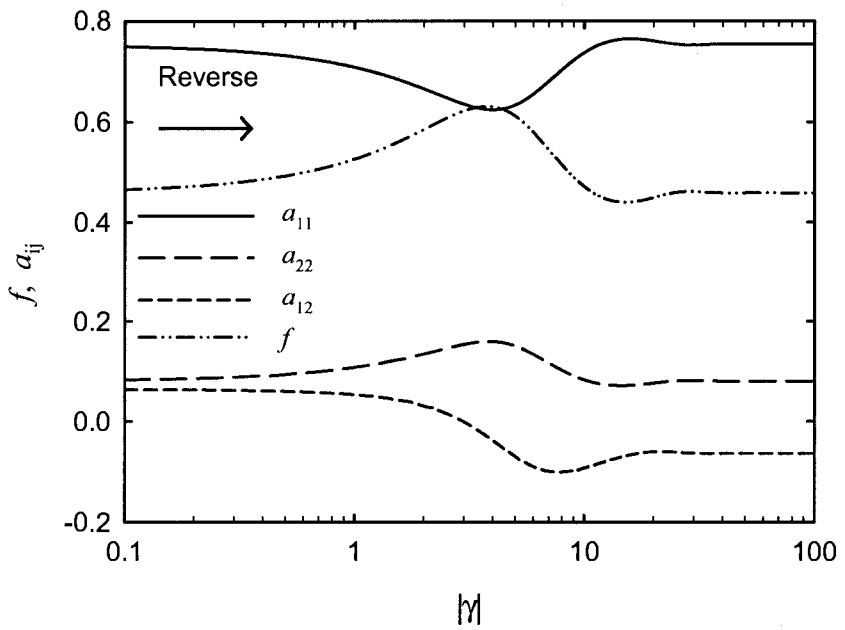

Figure 7.7 : Predicted variations for key components of $\mathbf{a_2}$ (a_{11}, a_{22} and a_{12}) and for the scalar f as functions of deformation for reverse flow (ORW3 and IQUA closure approximations, $|\dot{\gamma}| = 1\ \mathrm{s}^{-1}$, $X_A = 1$, $k = 0.3$ and $q = 0.5$).

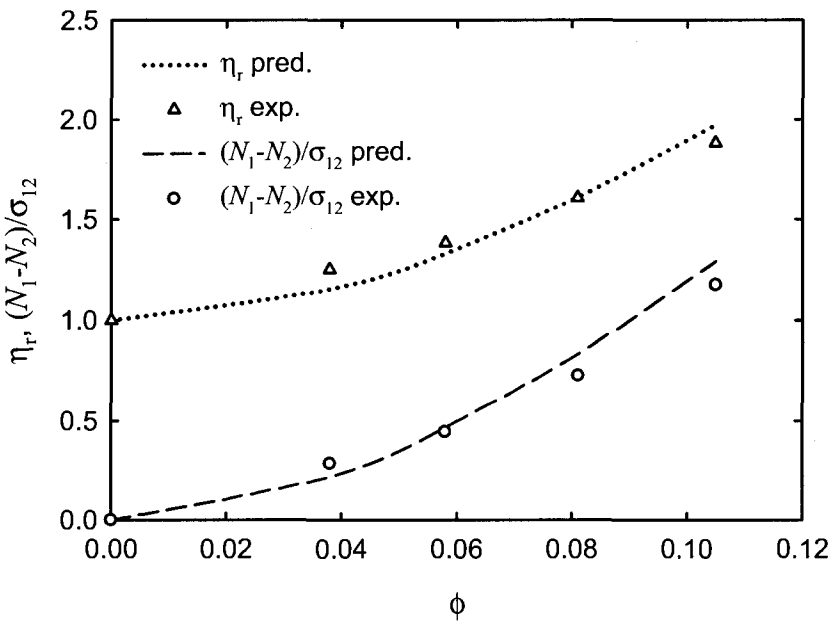

Figure 7.8 : Predicted reduced steady shear viscosity and normal stress differences compared to experimental data as functions of fiber volume fraction (ORW3 and IQUA closure approximations). ($|\dot{\gamma}| = 10\ s^{-1}$, $X_A = 17.116$, $k = 0.112$ and $q = 0.220$). σ_{12} represents the shear stress component of the matrix.

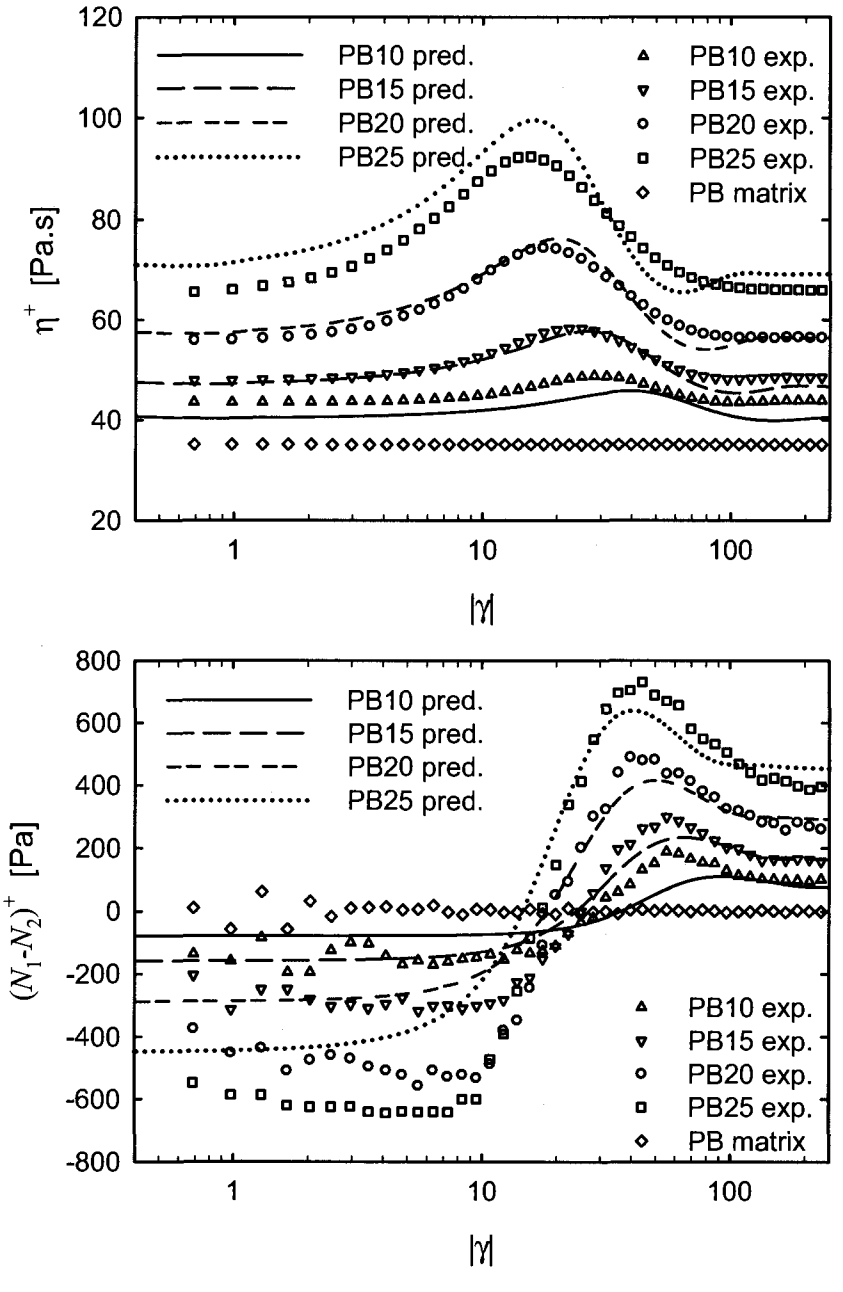

Figure 7.9 : Stress growth data compared to model predictions for reverse flow (CCW) performed with the ORW3 and IQUA closure approximations. ($|\dot{\gamma}|$ = 10 s^{-1}, X_A = 17.116, k = 0.112 and q = 0.220): (a) transient viscosity; (b) transient normal stress differences as a functions of strain.

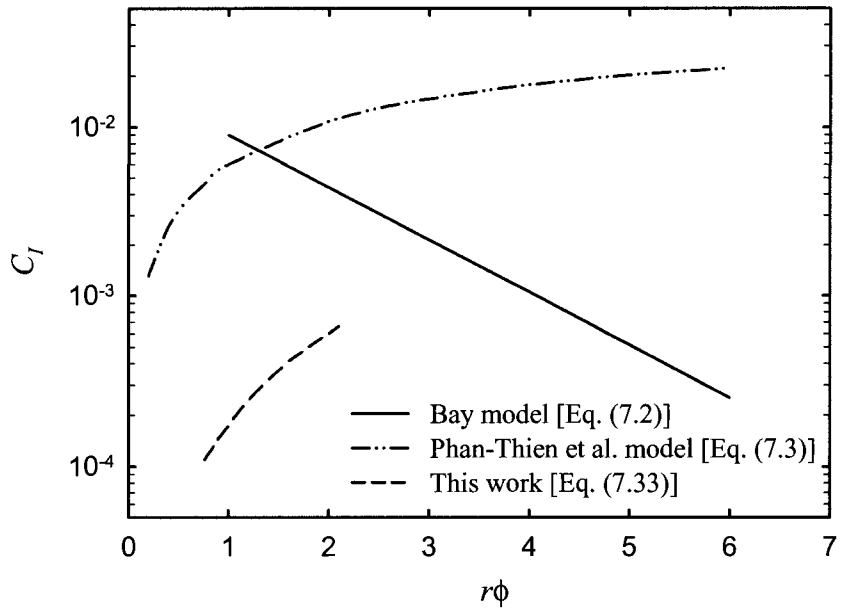

Figure 7.10 : Comparison of values of C_I obtained with the new model (ORW3 and IQUA closure approximations) with Bay model and Phan-Thien et al. model.

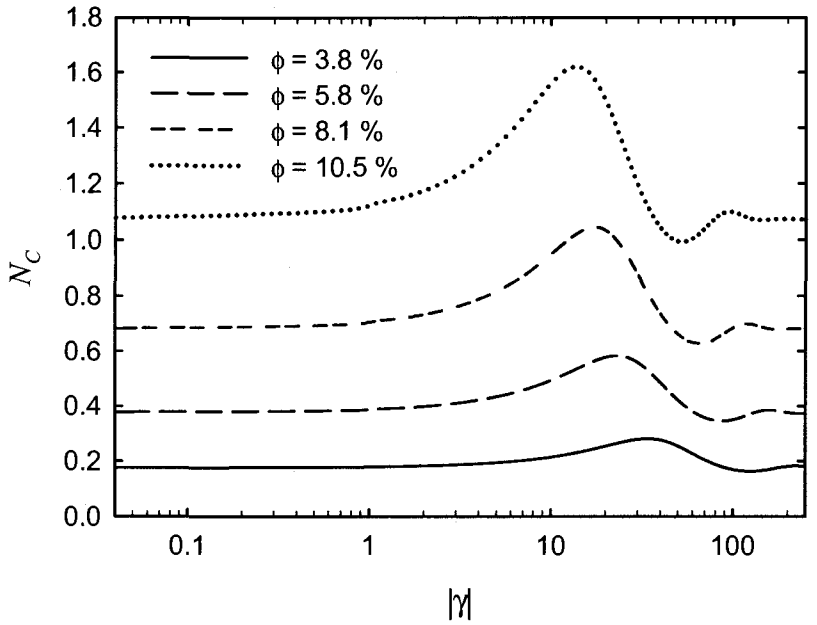

Figure 7.11 : Predictions of the average contact number per fiber as a function of deformation in reverse flow (CCW) at a shear rate of 10 s^{-1} (ORW3 and IQUA closure approximations).

CHAPITRE 8 - DISCUSSION GÉNÉRALE

Ce chapitre présente une discussion générale au regard des aspects méthodologiques et des résultats en lien avec la revue de la littérature.

8.1. Dégradation et stabilité thermique

Afin de réaliser les essais rhéologiques sur les polypropylènes à de hautes températures (200 °C), une quantité de 1 % en masse d'antioxydant (Irganox B225, Ciba) a été additionnée à tous les échantillons pendant leurs préparations. Cet ajout a été jugé suffisant pour stabiliser les différents polypropylènes pendant la durée des expérimentations qui n'excédent généralement pas plus de quatre heures.

Également, tous les essais rhéologiques à hautes températures ont été effectués sous une atmosphère d'azote, hormis ceux réalisés à l'aide du rhéomètre RME. En effet, le volume assez important de la chambre opératoire, le long temps de stabilisation de la température et la courte durée du test en élongation ont fait que l'utilisation d'azote n'a pas été jugée nécessaire. C'est de l'air qui a été employé comme substitut.

Le polybutène est quant à lui stable à la température ambiante mais reste sensible à une variation de température. Durant les essais expérimentaux, le contrôle en température a été opéré par l'emploi d'un système Peltier.

8.2. Conditionnement initial des échantillons

Que ce soit pour les systèmes à base de polybutène ou de polypropylène, l'orientation initiale des fibres après l'installation des échantillons dans la géométrie du rhéomètre reste aléatoire, dans le sens d'inconnue. Le moulage par compression des pastilles à base de PP et la fixation de l'entrefer de la géométrie des plaques parallèles pour les composites à base de PB ne garantissent pas une orientation initiale isotrope des fibres.

Ainsi en cisaillement, la majorité des tests commence par un pré-cisaillement des fibres afin d'aligner la majorité des fibres suivant la direction de l'écoulement. Ce test sert à donc à conditionner l'échantillon pour une meilleure répétatibilité des résultats.

Contrairement aux échantillons destinés à des mesures en cisaillement, ceux préparés pour effectuer des mesures en élongation ont suscité de nombreuses précautions pour contrôler l'orientation initiale des fibres (orientation aléatoire des fibres dans un plan, fibres parallèles et perpendiculaires à la direction de l'étirement).

8.3. Homogénéité dans la déformation

Les mesures en élongation sont et restent des mesures difficiles à réaliser bien que de nouveaux dispositifs sont récemment apparus sur le marché. En particulier, la géométrie SER montée sur un rhéomètre à vitesse en fait partie. Pour des systèmes chargés, la difficulté réside principalement dans l'uniformité de la déformation des échantillons. À l'aide de l'acquisition video disponible sur le RME, il a été démontré des

déformations non uniformes des échantillons chargés mais la complexité de l'appareillage peut être aussi à l'origine de ces problèmes (glissement de l'échantillon entre les chenilles...). Grâce au dispositif simplifié du SER, il faudrait à nouveau vérifier l'homogénéité de la déformation de l'échantillon à l'aide d'une acquisition video notamment. Dans le cas le plus défavorable, il serait intéressant d'essayer de quantifier cette non-homogénéité.

8.4. Programme Fortran de la résolution numérique de la fonction de distribution d'orientation

Le programme résolvant la fonction de distribution d'orientation des fibres est écrit en Fortran 90. Initialement, il est fortement inspiré du listing du programme de Bay (1991) disponible dans sa thèse (une dizaine de pages). Après l'incorporation de toutes les modifications effectuées au programme et présentées au chapitre 6, le programme final est composé de plus de 2000 lignes de commande. Il ne sera pas donc consultable comme listing dans cette thèse mais pourra être fourni sur demande.

8.5. Modèle rhéologique

Au vu des recherches effectuées dans la littérature, le modèle de Folgar-Tucker-Lipscomb et ses variantes ont suscité de nombreuses attentions. Le modèle proposé au chapitre 7 présente une autre alternative bien qu'il existe de nombreuses similitudes. Ce dernier a été testé uniquement en cisaillement simple pour des régimes transitoires et établis. Ses performances ou bien ses lacunes devront être mises en évidence sous

d'autres types de sollicitation (élongation, oscillation dynamique...). Il a aussi été uniquement testé pour des suspensions à base de polybutène : il serait intéressant de l'utiliser pour prédire le comportement d'autres matériaux composites. Finalement, le modèle proposé pourra faire l'objet de nombreuses recherches futures tout comme l'a été celui de Folgar-Tucker-Lipscomb au cours du dernier quart de siècle.

CHAPITRE 9 - CONCLUSIONS

Cette thèse intitulée « Étude et modélisation du comportement rhéologique de suspensions de fibres rigides en régime non-dilué » apporte une contribution majeure à la compréhension de ces systèmes. L'originalité de ce travail consiste en :

- La caractérisation rhéologique de suspensions de fibres dans des écoulements de type industriel, à savoir les grandes déformations oscillatoires et l'élongation.

- Une contribution numérique sur la réduction du temps de calcul de la fonction de distribution d'orientation des fibres par la méthode des volumes finis.

- La proposition d'un modèle rhéologique qui prend en compte une meilleure description des contacts fibre-fibre par l'introduction de tenseurs d'interaction.

Comme son titre l'indique, cette thèse intéressera certainement les industriels qui utilisent les procédés d'injection de type « push-pull ». En effet, des mesures rhéologiques ont été effectuées en grandes déformations oscillatoires (« Large Amplitude Oscillatory Shear ») sur deux matrices distinctes, l'une en polybutène (PB, quasi newtonien) et l'autre en polypropylène (PP, viscoélastique), toutes deux renforcées par des fibres de verre (même distribution en longueur et en diamètre). Les résultats expérimentaux montrent que pour les composites à base de PB, l'amplitude de la contrainte en cisaillement augmente graduellement pour atteindre une constante après plusieurs cycles, ce qui est attribué à une orientation des fibres suivant la direction de l'écoulement. Cette observation a été validée par les prédictions du modèle de Folgar-

Tucker-Lipscomb (FTL) pour un PB chargé à 20% en masse de fibres. Pour les composites en PP, l'amplitude de la contrainte en cisaillement diminue progressivement au cours des cycles étudiés. Phénomène opposé à celui du PB, l'orientation des fibres est toujours à l'origine de ce comportement. Pour les deux systèmes, les courbes de Lissajous (contrainte en cisaillement vs. déformation) conserve une forme constante et les transformées de Fourier confirment ces réponses harmoniques. À de grandes déformations, les premières différences de contraintes normales mesurées sont plus sensibles aux phénomènes d'orientation des fibres que les contraintes en cisaillement. Les figures de contrainte normales vs déformation exhibent des formes symétriques si la configuration d'orientation des fibres est elle-même symétrique suivant la direction de l'écoulement. De plus, le spectre des transformées de Fourier montre des réponses non harmoniques. L'aire des courbes de Lissajous indique que l'énergie de dissipation visqueuse augmente avec le taux de fibres et les composites à base du PP présentent un caractère plus newtonien avec une déformation croissante.

Également cette thèse suscitera l'attention des industriels en ce qui attrait aux observations réalisées en écoulement élongationnel. Ces dernières indiquent que la présence des fibres dans un polypropylène augmente considérablement sa viscosité élongationnelle. En régime transitoire, différentes orientations initiales des fibres ont été préparées : planaire aléatoire, perpendiculaire et parallèle à la direction d'étirement. Ce dernier cas génère la viscosité élongationnelle transitoire la plus élevée à cause de la résistance des fibres à l'étirement. Pour les deux autres cas, la dynamique d'orientation des charges provoque un léger comportement rhéoépaississant sous déformation. Ces

observations sont confortées par le modèle Folgar-Tucker-Lipscomb (FTL), qui prédit de façon qualitative ces phénomènes de rhéoépaississement sous déformation. En régime établi, la viscosité élongationnelle en fonction du taux effectif de déformation a été comparée pour trois appareillages différents (l'unité SER montée sur un rhéomètre rotationnel ARES, un système rhéomètre capillaire Rheotens et l'entrée convergente d'une filière hyperbolique planaire). Le comportement à de faibles taux d'élongation montre des désaccords entre les trois appareils. Cependant à des taux d'élongation modérés et élevés, les résultats sont très comparables pour les trois matériaux (PP0, PP10 et PP30). Le comportement élongationnel des composites est très similaire à celui de la matrice : un plateau est observé pour des faibles taux d'élongation et une rhéofluidifiance apparait pour des taux d'élongation plus élevés. De plus, une nouvelle équation constitutive est proposée pour déterminer la viscosité élongationnelle en régime établi d'une suspension de fibres dans un fluide Newtonien généralisé décrit par le modèle de Carreau. Ainsi, de bonnes prédictions sont obtenues sur toute la plage de taux d'élongation étudiés.

Afin d'utiliser les principaux modèles rhéologiques applicables aux suspensions de fibres disponibles dans la littérature, dont le modèle Folgar-Tucker-Lipscomb (FTL), il est nécessaire de connaître le tenseur d'orientation d'ordre quatre $\mathbf{a}_4$. Les approximations de fermeture entrainent généralement des erreurs implicites et la résolution numérique de la fonction de distribution d'orientation ψ, qui donne de meilleurs résultats, consomme énormément de temps de calcul. Dans ce travail, une méthode basée sur les volumes finis a été utilisée pour résoudre numériquement

l'équation de Fokker-Planck pour ψ. Les résultats sont tels que les temps de calcul sont considérablement réduits et comparables à ceux utilisant les approximations de fermeture. De plus, une large gamme du nombre de Péclet est maintenant envisageable sans que les résultats ne soient altérés, ceci n'étant pas possible avec l'emploi des relations de fermeture.

Finalement cette thèse propose une nouvelle loi de comportement pour des suspensions de fibres, inspirée des modèles de Folgar-Tucker-Lipscomb (FTL) et de Dinh et Armstrong (DA). Un jeu d'équations rhéologiques a été développé pour des suspensions non diluées de fibres rigides dans un fluide newtonien en prenant en compte les interactions hydrodynamiques et fibre-fibre. La force générée par les interactions des fibres est modélisée en utilisant un coefficient de friction hydrodynamique linéaire proportionnel à la vitesse relative des deux fibres au point de contact, et est ensuite pondérée par la probabilité que ce contact ait lieu. L'équation d'évolution du tenseur d'orientation d'ordre deux, composée de termes convectif et diffusif causé par les interactions des fibres, est dérivée pour prédire l'orientation des fibres sous écoulement. Le bien connu tenseur d'orientation d'ordre quatre, relié à la contribution hydrodynamique, et un tenseur d'interaction d'ordre quatre, proposé dans cet article, sont utilisés pour déterminer la contrainte totale dans le composite. Des approximations de fermeture linéaire et quadratique ont été formulées pour décrire le tenseur d'interaction du quatrième ordre. Les résultats sont présentés en utilisant la forme quadratique qui a été trouvée plus précise que la relation linéaire. Le modèle décrit correctement l'évolution de la viscosité et de la différence de contraintes normales dans

un écoulement retour en cisaillement simple. De plus, l'orientation des fibres et le nombre moyen de contacts par fibre sont prédictibles.

Le travail de cette thèse est une avancée sur la compréhension du comportement rhéologique des suspensions de fibres rigides, notamment par ces deux études approfondies sur leurs caractérisations rhéologiques en grandes déformations oscillatoires et en élongation. Il apporte également une solution concrète sur la résolution numérique de la fonction de distribution d'orientation, qui a auparavant suscité de nombreux problèmes. Finalement, il a été proposé un modèle rhéologique permettant une meilleure description des contacts fibre-fibre par l'introduction de tenseurs d'interaction.

Perspectives

Les travaux effectués dans cette thèse laissent envisager de nouvelles perspectives de recherches.

En grandes déformations oscillatoires, l'utilisation d'un rhéomètre rotationnel a restreint l'étude à des déformations plutôt modérées. De plus, la géométrie de plaques parallèles ne garantit pas un taux de cisaillement uniforme. Il serait alors intéressant d'utiliser un rhéomètre à glissière composé de plaques parallèles « sliding plate rheometer » (Giacomin et al., 1989) pour approfondir l'étude. Pour une meilleure analyse, le rhéomètre devra être équipé d'un dispositif permettant de mesurer les forces normales, puisque cette étude a démontrée que la première différence des contraintes

normales était très sensible à l'orientation des fibres. C'est ainsi que des essais orthogonaux (oscillations dynamiques selon la direction de la force normale) pourront aussi apporter des informations complémentaires sur l'état d'orientation des fibres. L'idéal serait de coupler ce mouvement à un cisaillement simple ou dynamique. Aussi et dépendamment des systèmes à étudier, l'utilisation d'une géométrie couette permettrait d'investiguer leur comportement à des déformations plus importantes que celle des plaques parallèles. La sollicitation couverte dans ce travail était sinusoïdale : il serait intéressant d'envisager une sollicitation en créneaux avec des déformations croissantes pour tenter de faire un lien avec des essais transitoires consécutifs dans des directions opposées.

En élongation, l'utilisation du RME avec le système d'acquisition vidéo a montré que la déformation n'était pas uniforme. Pour la géométrie SER montée sur un rhéomètre à vitesse contrôlée, un appareillage similaire permettrait de valider les résultats et d'obtenir pourquoi pas des informations quant à l'évolution de l'état d'orientation des fibres. Dans un autre registre, l'emploi de capteurs de pression plus sensibles sur la filière hyperbolique convergente montée sur une presse à injection serait d'un grand intérêt : il serait alors envisageable d'aller chercher à obtenir la viscosité plateau en élongation du matériel. Également dans ce chapitre, il a été proposé une équation constitutive pour des fibres en suspension dans un fluide obéissant au modèle de Carreau. À date, elle a été utilisée pour prédire la viscosité élongationnelle en régime établi et peut tout autant s'appliquer en cisaillement. Aussi en se basant notamment sur

les travaux de Jeffery (1922), il serait fort intéressant de proposer une équation d'évolution de l'orientation des fibres en suspension dans un fluide de Carreau.

Le temps de calcul pour la résolution numérique de la fonction de distribution d'orientation est maintenant nettement comparable à celui de l'emploi des dernières approximations de fermeture et ceci sans générer d'erreurs significatives. Son implantation dans un logiciel de simulation numérique de l'écoulement tel que Fluent® ou Moldflow® devient alors envisageable.

Pour le modèle rhéologique proposé, la force d'interaction est linéaire mais rien n'empêche d'investiguer le cas non linéaire. Également, il a été suggéré que les positions des points de contact le long de la fibre était équiprobable, chose qui n'est vraisemblablement pas réaliste. Il serait aussi intéressant d'effectuer des modifications mineures sur le programme de la résolution numérique de la fonction de distribution d'orientation pour tenir compte des nouvelles considérations du modèle. À partir de là, il sera possible de proposer une relation plus précise entre les tenseurs d'interaction et d'orientation et aussi de générer une approximation de fermeture plus précise pour $\mathbf{b}_4$. Mais un des défis majeur consiste à déterminer une équation d'évolution pour le tenseur d'interaction du second ordre. Certains coefficients restent également indéterminés et nécessitent des expressions analytiques en fonction des paramètres des matériaux. Finalement ce modèle a été développé pour des corps minces et il serait fort intéressant de le réécrire pour des sphéroïdes, des disques ou des plaquettes par exemple.

RÉFÉRENCES

Advani, S. G. (1987). *Prediction of fiber orientation during processing of short fiber composites.* Ph.D. thesis inédit, University of Illinois, Urbana-Champaign, IL.

Advani, S. G., & Tucker, C. L. (1987). The use of tensors to describe and predict fiber orientation in short fiber composites. *Journal of Rheology, 31*(8), 751-784.

Advani, S. G., & Tucker, C. L. (1990a). Closure approximations for 3-dimensional structure tensors. *Journal of Rheology, 34*(3), 367-386.

Advani, S. G., & Tucker, C. L. (1990b). A numerical-simulation of short fiber orientation in compression molding. *Polymer Composites, 11*(3), 164-173.

Advani, S. G. (1994). *Flow and rheology in polymer composites manufacturing.* Amsterdam - Pays-Bas: Elsevier.

Ait-Kadi, A., & Grmela, M. (1994). Modelling the rheological behaviour of fibre suspensions in viscoelastic media. *Journal of Non-Newtonian Fluid Mechanics, 53*, 65-81.

Akay, M., & Barkley, D. (1993). Flow-aberrations and weld lines in glass-fibre reinforced thermoplastic injection mouldings. *Plastics, Rubber and Composites Processing and Applications, 20*(3), 137-149.

Altan, M. C., Advani, S. G., Guceri, S. I., & Pipes, R. B. (1989). On the description of the orientation state for fiber suspensions in homogeneous flows. *Journal of Rheology, 33*(7), 1129-1155.

Attanasio, A., Bernini, U., Galloppe, P., & Segre, G. (1972). Significance of viscosity measurement in macroscopic suspensions of elongated particles. *Transactions of the Society of Rheology, 16*(1), 147-154.

Ausias, G., Agassant, J. F., Vincent, M., Lafleur, P. G., Lavoie, P. A., & Carreau, P. J. (1992). Rheology of short glass-fiber reinforced polypropylene. *Journal of Rheology, 36*(4), 525-542.

Ausias, G., Agassant, J. F., & Vincent, M. (1994). Flow and fiber orientation calculations in reinforced thermoplastic extruded tubes. *International Polymer Processing, IX*(1), 51-59.

Ausias, G., Fan, X. J., & Tanner, R. I. (2006). Direct simulation for concentrated fibre suspensions in transient and steady state shear flows. *Journal of Non-Newtonian Fluid Mechanics, 135*(1), 46-57.

Azaiez, J. (1996). Constitutive equations for fiber suspensions in viscoelastic media. *Journal of Non-Newtonian Fluid Mechanics, 66*(1), 35-54.

Azaiez, J., Guenette, R., & Ait-Kadi, A. (1997). Investigation of the abrupt contraction flow of fiber suspensions in polymeric fluids. *Journal of Non-Newtonian Fluid Mechanics, 73*, 289–316.

Azaiez, J. (2000). Stability of the mixing layer of fiber suspensions: role of the closure approximation and off-plane orientation. *Journal of Non-Newtonian Fluid Mechanics, 95*(2-3), 253-276.

Barbosa, S. E., Ercoli, D. R., Bibbo, M. A., & Kenny, J. M. (1994). Rheology of short-fiber composites: A systematic approach. *Composite Structures, 27*(1-2), 83-91.

Batchelor, G. K. (1970a). Slender-body theory for particles of arbitrary cross-section in Stokes flow. *Journal of Fluid Mechanics, 44*(3), 419-440.

Batchelor, G. K. (1970b). The stress system in a suspension of force-free particles. *Journal of Fluid Mechanics, 41*(3), 545-570.

Batchelor, G. K. (1971). The stress generated in a non-dilute suspension of elongated particles by pure straining motion. *Journal of Fluid Mechanics, 46*(4), 813-829.

Bay, R. S. (1991). *Fiber orientation in injection-molded composites: A comparison of theory and experiment.* Ph.D. dissertation inédit, University of Illinois at Urbana-Champaign, Illinois, United States.

Becraft, M. L., & Metzner, A. B. (1992). The rheology, fiber orientation, and processing behavior of fiber-filled fluids. *Journal of Rheology, 36*(1), 143-174.

Bibbo, M. A., Dinh, S. M., & Armstrong, R. C. (1985). Shear flow properties of semiconcentrated fiber suspensions. *Journal of Rheology, 29*(6), 905-929.

Binding, D. M. (1988). An approximate analysis for contraction and converging flows. *Journal of Non-Newtonian Fluid Mechanics, 27*(2), 173-189.

Bird, R. B., Armstrong, R. C., & Hassager, O. (1987a). *Dynamics of polymeric liquids. Volume 1, Fluid mechanics* (2nd éd.). New York: Wiley.

Bird, R. B., Curtiss, C. F., Armstrong, R. C., & Hassager, O. (1987b). *Dynamics of polymeric liquids. Volume 2, Kinetic theory* (2nd éd.). New York: Wiley.

Boger, D. V., & Binnington, R. (1977). Separation of elastic and shear thinning effects in the capillary rheometer. *Journal of Rheology, 21*(4), 515-534.

Burgers, J. M. (1938). On the motion of small particles of elongated form suspended in a viscous liquid. In K. N. A. Wet. (éd.), *Second report on viscosity and plasticity, Ch. III.* Amsterdam.

Carreau, P. J., De Kee, D., & Chhabra, R. P. (1997). *Rheology of polymeric systems: Principles and applications*. Munich: Hanser.

Chan, Y., White, J. L., & Oyanagi, Y. (1978). A fundamental study of the rheological properties of glass-fiber-reinforced polyethylene and polystyrene melts. *Journal of Rheology, 22*(5), 507-524.

Chaouche, M., & Koch, D. L. (2001). Rheology of non-Brownian rigid fiber suspensions with adhesive contacts. *Journal of Rheology, 45*(2), 369-382.

Chiba, K., Ammar, A., & Chinesta, F. (2005). On the fiber orientation in steady recirculating flows involving short fibers suspensions. *Rheologica Acta, 44*(4), 406-417.

Chinesta, F., Poitou, A., & Torres, R. (2000). A semi-lagrangian strategy to predict the fiber orientation in the steady flows of reinforced thermoplastics. *Computer Methods in Applied Mechanics and Engineering, 189*(1), 233-247.

Chinesta, F., Chaidron, G., & Poitou, A. (2003). On the solution of Fokker-Planck equations in steady recirculating flows involving short fiber suspensions. *Journal of Non-Newtonian Fluid Mechanics, 113*(2-3), 97-125.

Chung, D. H., & Kwon, T. H. (2001). Improved model of orthotropic closure approximation for flow induced fiber orientation. *Polymer Composites, 22*(5), 636-649.

Chung, D. H., & Kwon, T. H. (2002a). Fiber orientation in the processing of polymer composites. *Korea-Australia Rheology Journal, 14*(4), 175-188.

Chung, D. H., & Kwon, T. H. (2002b). Invariant-based optimal fitting closure approximation for the numerical prediction of flow-induced fiber orientation. *Journal of Rheology, 46*(1), 169-194.

Chung, S. T., & Kwon, T. H. (1995). Numerical simulation of fiber orientation in injection molding of short-fiber-reinforced thermoplastics. *Polymer Engineering & Science, 35*(7), 604-618.

Cintra, J. S., & Tucker, C. L. (1995). Orthotropic closure approximations for flow-induced fiber orientation. *Journal of Rheology, 39*(6), 1095-1122.

Cox, R. G. (1971). The motion of long slender bodies in a viscous fluid. Part 2. Shear flow. *Journal of Fluid Mechanics, 45*(4), 625-657.

Cox, W. P., & Merz, E. H. (1958). Correlation of dynamic and steady flow viscosities. *Journal of Polymer Science, 28*(118), 619-622.

Creasy, T. S., Advani, S. G., & Okine, R. K. (1996a). Non-linear response of a long, discontinuous fiber/melt system in elongational flows. *Rheologica Acta, 35*(4), 347-355.

Creasy, T. S., Advani, S. G., & Okine, R. K. (1996b). Transient rheological behavior of a long discontinuous fiber-melt system. *Journal of Rheology, 40*(4), 497-519.

Creasy, T. S., & Advani, S. G. (1997). A model long-discontinuous-fiber filled thermoplastic melt in extensional flow. *Journal of Non-Newtonian Fluid Mechanics, 73*(3), 261-278.

Crowson, R. J., Folkes, M. J., & Bright, P. F. (1980). Rheology of short glass fiber-reinforced thermoplastics and its application to injection molding I. Fiber motion and viscosity measurement. *Polymer Engineering & Science, 20*(14), 925-933.

Crowson, R. J., & Folkes, M. J. (1980). Rheology of short glass fiber-reinforced thermoplastics and its application to injection molding II. The effect of material parameters. *Polymer Engineering & Science, 20*(14), 934-940.

Currie, P. K. (1982). Constitutive equations for polymer melts predicted by the Doi-Edwards and Curtiss-Bird kinetic theory models. *Journal of Non-Newtonian Fluid Mechanics, 11*(1-2), 53-68.

Czarnecki, L., & White, J. L. (1980). Shear flow rheological properties, fiber damage, and mastication characteristics of aramid-, glass-, and cellulose-fiber-reinforced polystyrene melts. *Journal of Applied Polymer Science, 25*(6), 1217-1244.

Dhatt, G., & Touzot, G. (1984). *The finite element method displayed.* New-York: John Wiley & Sons Inc.

Dhont, J. K. G., & Briels, W. J. (2003). Viscoelasticity of suspensions of long, rigid rods. *Colloids and Surfaces A: Physicochemical and Engineering Aspects, 213*(2-3), 131-156.

Dinh, S. M. (1981). *On the rheology of concentrated fiber suspensions.* S.C.D.C. inédit, Massachusetts Institute of Technology, United States - Massachusetts.

Dinh, S. M., & Armstrong, R. C. (1984). A rheological equation of state for semiconcentrated fiber suspensions. *Journal of Rheology, 28*(3), 207-227.

Djalili-Moghaddam, M., & Toll, S. (2005). A model for short-range interactions in fibre suspensions. *Journal of Non-Newtonian Fluid Mechanics, 132*(1-3), 73-83.

Doi, M., & Edwards, S. F. (1978a). Dynamics of rod-like macromolecules in concentrated solution. Part 1. *Journal of the Chemical Society, Faraday Transactions 2, 74*, 560-570.

Doi, M., & Edwards, S. F. (1978b). Dynamics of rod-like macromolecules in concentrated solution. Part 2. *Journal of the Chemical Society, Faraday Transactions 2, 74*, 918-932.

Doi, M., & Edwards, S. F. (1986). *The Rheology of Polymer Dynamics*. New York: Oxford Science Publications.

Dupret, F., & Verleye, V. (1999). Modeling the flow of fiber suspensions in narrow gaps. In D. A. Siginer, D. De Kee & R. P. Chhabra (éds.), *Advances in the Flow*

and Rheology of Non-Newtonian Fluids (Rheology Ser 8e éd., Vol. 2, pp. 19-29). Armsterdam: Elsevier.

Endo, H., & Nagasawa, M. (1970). Normal stress and shear stress in a viscoelastic liquid under oscillatory shear flow. *Journal of Polymer Science: Part A-2, 8*(3), 371-381.

Ericsson, K. A., Toll, S., & Manson, J. A. E. (1997). Sliding plate rheometry of planar oriented concentrated fiber suspension. *Rheologica Acta, 36*(4), 397-405.

Fan, X. J., Phan-Thien, N., & Zheng, R. (1998). A direct simulation of fibre suspensions. *Journal of Non-Newtonian Fluid Mechanics, 74*(1-3), 113-135.

Férec, J., Ausias, G., Heuzey, M. C., & Carreau, P. J. (2008a). Modeling fiber interactions in non-dilute fiber suspensions. *Journal of Rheology, In revision.*

Férec, J., Heniche, M., Heuzey, M. C., Ausias, G., & Carreau, P. J. (2008b). Numerical solution of the Fokker-Planck equation for fiber suspensions: Application to the Folgar-Tucker-Lipscomb model. *Journal of Non-Newtonian Fluid Mechanics, Submitted.*

Ferry, J. D. (1980). *Viscoelastic properties of polymers* (3d éd.). New York: Wiley.

Folgar, F. P., & Tucker, C. L. (1984). Orientation behavior of fibers in concentrated suspensions. *Journal of Reinforced Plastics and Composites, 3*(2), 98-119.

Franzen, B., Klason, C., Kubat, J., & Kitano, T. (1989). Fibre degradation during processing of short fibre reinforced thermoplastics. *Composites, 20*(1), 65-76.

Ganani, E., & Powell, R. L. (1985). Suspensions of rodlike particles: Literature review and data correlations. *Journal of Composite Materials, 19*(3), 194-215.

Ganani, E., & Powell, R. L. (1986). Rheological properties of rodlike particles in a Newtonian and a non-Newtonian fluid. *Journal of Rheology, 30*(5), 995-1013.

Ghosh, T. (1993). *Rheological modeling of complex polymeric fluids.* Ph.D. inédit, Ecole Polytechnique, Montreal, Canada.

Ghosh, T., Grmela, M., & Carreau, P. J. (1995). Rheology of short-fiber filled thermoplastics. *Polymer Composites, 16*(2), 144-153.

Giacomin, J. A., Samurkas, T., & Dealy, J. M. (1989). A novel sliding plate rheometer for molten plastics. *Polymer Engineering & Science, 29*(8), 499-504.

Giacomin, J. A., & Dealy, J. M. (1993). Large-amplitude oscillatory shear. In A. A. Collyer (éd.), *Techniques in rheological measurement* (Chapter 4). London New York: Chapman & Hall.

Gibson, A. G., & Toll, S. (1999). Mechanics of the squeeze flow of planar fibre suspensions. *Journal of Non-Newtonian Fluid Mechanics, 82*, 1-24.

Giesekus, H. (1962). Elasto-viskose flüssigkeiten, für die in stationären schichtströmungen sämtliche normalspannungskomponenten verschieden gross sind. *Rheologica Acta, 2*(1), 50-62.

Goddard, J. D. (1976). The stress field of slender particles oriented by a non-Newtonian extensional flow. *Journal of Fluid Mechanics, 78*(01), 177-206.

Goto, S., Nagazono, H., & Kato, H. (1986a). The flow behavior of fiber suspensions in Newtonian fluids and polymer solutions. I Mechanical properties. *Rheologica Acta, 25*(2), 119-129.

Goto, S., Nagazono, H., & Kato, H. (1986b). The flow behavior of fiber suspensions in Newtonian fluids and polymer solutions. II Capillary flow. *Rheologica Acta, 25*(3), 246-256.

Greene, J. P., & Wilkes, J. O. (1995). Steady-state and dynamic properties of concentrated fiber-filled thermoplastics. *Polymer Engineering & Science, 35*(21), 1670-1681.

Grmela, M. (1986). Bracket formulation of diffusion-convection equations. *Physica D: Nonlinear Phenomena, 21*(2-3), 179-212.

Grmela, M., & Carreau, P. J. (1987). Conformation tensor rheological models. *Journal of Non-Newtonian Fluid Mechanics, 23*, 271-294.

Grmela, M., & Dlugogorski, B. Z. (1996). Hamiltonian modelling of liquid crystal polymers and blends. In D. Acierno & A. A. Collyer (éds.), *Rheology and Procesing of Liquid Crystal Polymers* (pp. 49-85). London: Chapman & Hall.

Guo, R., Azaiez, J., & Bellehumeur, C. (2005). Rheology of fiber filled polymer melts: role of fiber-fiber interactions and polymer-fiber coupling. *Polymer Engineering and Science*, 385-399.

Gupta, V. K., Krishnamoorti, R., Chen, Z. R., Kornfield, J. A., Smith, S. D., Satkowski, M. M., et al. (1996). Dynamics of shear alignment in a lamellar diblock copolymer: Interplay of frequency, strain amplitude, and temperature. *Macromolecules, 29*(3), 875-884.

Han, K. H., & Im, Y. T. (1999). Modified hybrid closure approximation for prediction of flow-induced fiber orientation. *Journal of Rheology, 43*(3), 569-589.

Hand, G. L. (1961). A theory of dilute suspensions. *Archive for Rational Mechanics and Analysis, 7*(1), 81-86.

Hand, G. L. (1962). A theory of anisotropic fluids. *Journal of Fluid Mechanics, 13*(1), 33-46.

Harlen, O. G., & Koch, D. L. (1997). Orientational drift of a fibre suspended in a dilute polymer solution during oscillatory shear flow. *Journal of Non-Newtonian Fluid Mechanics, 73*(1-2), 81-93.

Hinch, E. J., & Leal, L. G. (1972). The effect of Brownian motion on the rheological properties of a suspension of non-spherical particles. *Journal of Fluid Mechanics, 52*(4), 683-712.

Hinch, E. J., & Leal, L. G. (1973). Time-dependent shear flows of a suspension of particles with weak Brownian rotations. *Journal of Fluid Mechanics, 57*(4), 753-767.

Huq, A. M. A., & Azaiez, J. (2005). Effects of length distribution on the steady shear viscosity of semiconcentrated polymer-fiber suspensions. *Polymer Engineering & Science, 45*(10), 1357-1368.

Hyun, K., Kim, S. H., Ahn, K. H., & Lee, S. J. (2002). Large amplitude oscillatory shear as a way to classify the complex fluids. *107*(1-3), 51-65.

Iso, Y., Koch, D. L., & Cohen, C. (1996a). Orientation in simple shear flow of semi-dilute fiber suspensions 1. Weakly elastic fluids. *Journal of Non-Newtonian Fluid Mechanics, 62*(2-3), 115-134.

Iso, Y., Cohen, C., & Koch, D. L. (1996b). Orientation in simple shear flow of semi-dilute fiber suspensions 2. Highly elastic fluids. *Journal of Non-Newtonian Fluid Mechanics, 62*(2-3), 135-153.

Jack, D. A., & Smith, D. E. (2005). An invariant based fitted closure of the sixth-order orientation tensor for modeling short-fiber suspensions. *Journal of Rheology, 49*(5), 1091-1115.

Jack, D. A., & Smith, D. E. (2006). Sixth-order fitted closures for short-fiber reinforced polymer composites. *Journal of Thermoplastic Composite Materials, 19*(2), 217-246.

Jeffery, G. B. (1922). The motion of ellipsoidal particles immersed in a viscous fluid. *Proceedings of the Royal Society of London Serie A, 102*, 161-179.

Joung, C. G., Phan-Thien, N., & Fan, X. J. (2001). Direct simulation of flexible fibers. *Journal of Non-Newtonian Fluid Mechanics, 99*(1), 1-36.

Joung, C. G., Phan-Thien, N., & Fan, X. J. (2002). Viscosity of curved fibers in suspension. *Journal of Non-Newtonian Fluid Mechanics, 102*(1), 1-17.

Kalaprasad, G., Mathew, G., Pavithran, C., & Thomas, S. (2003). Melt rheological behavior of intimately mixed short sisal-glass hybrid fiber-reinforced low-density polyethylene composites. I. Untreated fibers. *Journal of Applied Polymer Science, 89*(2), 432-442.

Kamal, M. R., Mutel, A. T., & Utracki, L. A. (1984). Elongational behavior of short glass fiber reinforced polypropylene melts. *Polymer Composites, 5*(4), 289-298.

Kamal, M. R., & Mutel, A. T. (1985). Rheological properties of suspensions in Newtonian and non-Newtonian fluids. *Journal of Polymer Engineering, 5*(4), 293-382.

Kamal, M. R., & Mutel, A. T. (1989). The prediction of flow and orientation behavior of short fiber reinforced melts in simple flow systems. *Polymer Composites, 10*(5), 337-343.

Kim, J. K., & Song, J. H. (1997). Rheological properties and fiber orientations of short fiber-reinforced plastics. *Journal of Rheology, 41*(5), 1061-1085.

Kim, S., & Karrila, S. J. (1991). *Microdynamics: Principles and selected applications*. Boston: Butterworth - Heinemann.

Kitano, T., & Kataoka, T. (1980). The effect of the mixing methods on viscous properties of polyethylene melts filled with fibers. *Rheologica Acta, 19*(6), 753-763.

Kitano, T., Kataoka, T., Nishimura, T., & Sakai, T. (1980). Relative viscosities of polymer melts filled with inorganic fillers. *Rheologica Acta, 19*(6), 764-769.

Kitano, T., & Kataoka, T. (1981a). The rheology of suspensions of vinylon fibers in polymer liquids. I. Suspensions in silicone oil. *Rheologica Acta, 20*(4), 390-402.

Kitano, T., & Kataoka, T. (1981b). The rheology of suspensions of vinylon fibers in polymer liquids. II. Suspensions in polymer solutions. *Rheologica Acta, 20*(4), 403-415.

Kitano, T., Kataoka, T., & Nagatsuka, Y. (1984a). Dynamic flow properties of vinylon fibre and glass fiber reinforced polyethylene melts. *Rheologica Acta, 23*(4), 408-416.

Kitano, T., Kataoka, T., & Nagatsuka, Y. (1984b). Shear flow rheological properties of vinylon- and glass-fiber reinforced polyethylene melts. *Rheologica Acta, 23*(1), 20-30.

Knutsson, A. B., White, J. L., & Abbas, K. B. (1981). Rheological and extrusion characteristics of glass fiber-reinforced polycarbonate. *Journal of Applied Polymer Science, 26*(7), 2347-2362.

Kobayashi, M., Takahashi, T., Takimoto, J., & Koyama, K. (1995). Flow-induced whisker orientation and viscosity for molten composite systems in a uniaxial elongational flow field. *Polymer, 36*(20), 3927-3933.

Koch, D. L. (1995). A model for orientational diffusion in fiber suspensions. *Physics of Fluids, 7*(8), 2086-2088.

Kumar, K. S., Bhatnagar, N., & Ghosh, A. K. (2007). Development of long glass fiber reinforced polypropylene composites: Mechanical and morphological characteristics. *Journal of Reinforced Plastics and Composites, 26*(3), 239-249.

Laun, H. M. (1984). Orientation effects and rheology of short glass fiber-reinforced thermoplastics. *Colloid & Polymer Science, 262*(4), 257-269.

Le Corre, S., Dumont, P., Orgeas, L., & Favier, D. (2005). Rheology of highly concentrated planar fiber suspensions. *Journal of Rheology, 49*(5), 1029-1058.

Lin, G.-G., & Hu, M.-C. (1997). Measurement of elongation viscosity for polymer melts by fiber spinning. *Advances in Polymer Technology, 16*(3), 199-207.

Lipscomb, G. G. (1986). *Analysis of suspension rheology in complex flows.* Ph.D. thesis inédit, University of California, Berkeley.

Lipscomb, G. G., Denn, M. M., Hur, D. U., & Boger, D. V. (1988). The flow of fiber suspensions in complex geometries. *Journal of Non-Newtonian Fluid Mechanics, 26*(3), 297-325.

Lodge, A. S. (1964). *Elastic liquids: an introductory vector treatment of finite-strain polymer rheology.* London: Academic Press.

Lubansky, A. S., Boger, D. V., & Cooper-White, J. J. (2005). Batchelor's theory extended to elongated cylindrical or ellipsoidal particles. *Journal of Non-Newtonian Fluid Mechanics, 130*(1), 57-61.

Mackaplow, M. B., & Shaqfeh, E. S. G. (1996). A numerical study of the rheological properties of suspensions of rigid, non-Brownian fibres. *Journal of Fluid Mechanics, 329*(1), 155-186.

Maier, W., & Saupe, A. (1959). Eine einfache molekular-statistische Theorie des nematischen kristallinflüssigen Zustandes. *Zeitschrift fur Naturforschung, 14a*, 882.

Malamataris, N., & Papanastasiou, T. C. (1991). Closed-form material functions for semidilute fiber suspensions. *Journal of Rheology, 35*(3), 449-464.

Mandal, D. K. (2004). *Simulation of flow-induced fiber orientation with a new closure model using the finite element method.* Ph.D. inédit, Michigan State University, United States -- Michigan.

Manfred, W., Daniel, M., & Spiess, H. W. (1998). Fourier-transform rheology. *Rheologica Acta, V37*(4), 399-405.

Metzner, A. B. (1985). Rheology of suspensions in polymeric liquids. *Journal of Rheology, 29*(6), 739-775.

Mewis, J., & Metzner, A. B. (1974). The rheological properties of suspensions of fibres in Newtonian fluids subjected to extensional deformations. *Journal of Fluid Mechanics, 62*(3), 593-600.

Milliken, W. J., Gottlieb, M., Graham, A. L., Mondy, L. A., & Powell, R. L. (1989). The viscosity-volume fraction relation for suspensions of rod-like particles by falling-ball rheometry. *Journal of Fluid Mechanics, 202*(1), 217-232.

Mobuchon, C. (2002). *Propriétés rhéologiques en cisaillement et en élongation d'un polypropylène chargé de fibres de verre courtes.* M.Sc.A. inédit, Ecole Polytechnique de Montréal, Québec, Canada.

Mobuchon, C., Carreau, P. J., Heuzey, M. C., Sepehr, M., & Ausias, G. (2005). Shear and extensional properties of short glass fiber reinforced polypropylene. *Polymer Composites, 26*(3), 247-263.

Mokdad, B., Pruliere, E., Ammar, A., & Chinesta, F. (2007). On the simulation of kinetic theory models of complex fluids using the Fokker-Planck approach. *Applied Rheology, 17*(2), 26494-26414p.

Mondy, L. A., Morrison, T. G., Graham, A. L., & Powell, R. L. (1990). Measurements of the viscosities of suspensions of oriented rods using falling ball rheometry. *International Journal of Multiphase Flow, 16*(4), 651-662.

Mongruel, A., & Cloitre, M. (2003). Axisymmetric orifice flow for measuring the elongational viscosity of semi-rigid polymer solutions. *Journal of Non-Newtonian Fluid Mechanics, 110*(1), 27-43.

Moore, G. E. (1965). Cramming more components onto integrated circuits. *Electronics, 38*(8), 114-117.

Mutel, A. T., & Kamal, M. R. (1984). The effect of glass fibers on the rheological behavior of polypropylene melts between rotating parallel plates. *Polymer Composites, 5*(1), 29-35.

Mutel, A. T., & Kamal, M. R. (1986). Characterization of the rheological behavior of fiber-filled polypropylene melts under steady and oscillatory shear using cone-and-plate and rotational parallel plate rheometry. *Polymer Composites, 7*(5), 283-294.

Mutel, A. T., & Kamal, M. R. (1987). Measurement of fiber orientation distributions in simple flows of fiber reinforced melts. *Society of Plastics Engineers, Los Angeles, CA, USA* (pp. 732-737)Soc of Plastics Engineers, Brookfield Center, CT, USA.

Mutel, A. T. (1989). *Rheological behavior and fiber orientation in simple flows of glass fiber filled polypropylene melts.* Ph.D. inédit, McGill University, Canada.

Nawab, M. A., & Mason, S. G. (1958). Viscosity of dilute suspensions of thread-like particles. *The Journal of Physical Chemistry, 62*(10), 1248-1253.

Nicodemo, L., & Nicolais, L. (1974). Viscosity of concentrated fiber suspensions. *The Chemical Engineering Journal, 8*(2), 155-156.

Onogi, S., Mikami, Y., & Matsumoto, T. (1977). The rheology of suspensions of titanate fibers in polymer solution. *Polymer Engineering and Science, 17*(1), 1-8.

Onsager, L. (1949). The effects of shape on the interaction of colloidal particles. *Annals of the New York Academy of Sciences, 51*, 627-659.

Ooi, Y. W., & Sridhar, T. (2004). Resistance to uniaxial extensional flow of fibre suspensions. *Rheologica Acta, 43*(3), 223-231.

Peterlin, A. (1955). Excluded volume effect on light scattering of the coiled linear macromolecule. *Journal of Chemical Physics, 23*(2), 2464-2465.

Petrich, M. P., Koch, D. L., & Cohen, C. (2000a). An experimental determination of the stress-microstructure relationship in semi-concentrated fiber suspensions. *Journal of Non-Newtonian Fluid Mechanics, 95*(2-3), 101-133.

Petrich, M. P., Chaouche, M., Koch, D. L., & Cohen, C. (2000b). Oscillatory shear alignment of a non-Brownian fiber in a weakly elastic fluid. *91*(1), 1-14.

Petrie, C. J. S. (1999). The rheology of fibre suspensions. *Journal of Non-Newtonian Fluid Mechanics, 87*(2-3), 369-402.

Phan-Thien, N., Fan, X. J., Tanner, R. I., & Zheng, R. (2002). Folgar-Tucker constant for a fibre suspension in a Newtonian fluid. *Journal of Non-Newtonian Fluid Mechanics, 103*(2-3), 251-260.

Poslinski, A. J., Ryan, M. E., Gupta, R. K., Seshadri, S. G., & Frechette, F. J. (1988). Rheological behavior of filled polymeric systems I. Yield stress and shear-thinning effects. *Journal of Rheology, 32*(7), 703-735.

Ramazani, A., Ait-Kadi, A., & Grmela, M. (1997). Rheological modelling of short fiber thermoplastic composites. *Journal of Non-Newtonian Fluid Mechanics, 73*(3), 241-260.

Ramazani, A., Ait-Kadi, A., & Grmela, M. (2001). Rheology of fiber suspensions in viscoelastic media: Experiments and model predictions. *Journal of Rheology, 45*(4), 945-962.

Ranganathan, S., & Advani, S. G. (1991). Fiber-fiber interactions in homogeneous flows of nondilute suspensions. *Journal of Rheology, 35*(8), 1499-1522.

Ross, R. F., & Klingenberg, D. J. (1997). Dynamic simulation of flexible fibers composed of linked rigid bodies. *Journal of Chemical Physics, 106*(7), 2949-2960.

Sandstrom, C. R. (1993). *Interactions and orientation in concentrated suspensions of rigid rods: theory and experiment.* Ph.D. thesis inédit, University of Illinois, Urbana-Champaign.

Sandstrom, C. R., & Tucker, C. L. (1993). A theory for concentrated fiber suspensions with strong fiber-fiber interactions. *Makromolekulare Chemie-Macromolecular Symposia, 68*, 291-300.

Schmid, C. F., Switzer, L. H., & Klingenberg, D. J. (2000). Simulations of fiber flocculation: Effects of fiber properties and interfiber friction. *Journal of Rheology, 44*(4), 781-809.

Schweizer, T. (2000). The uniaxial elongational rheometer RME - six years of experience. *Rheologica Acta, 39*(5), 428-443.

Sentmanat, M. L. (2004). Miniature universal testing platform: from extensional melt rheology to solid-state deformation behavior. *Rheologica Acta, 43*(6), 657-669.

Sentmanat, M. L., Wang, B. N., & McKinley, G. H. (2005). Measuring the transient extensional rheology of polyethylene melts using the SER universal testing platform. *Journal of Rheology, 49*(3), 585-606.

Sepehr, M. (2003). *Étude rhéologique des composites chargés de fibres de verre courtes.* Ph.D. inédit, École polytechnique de Montréal, Québec, Canada.

Sepehr, M., Carreau, P. J., Grmela, M., Ausias, G., & Lafleur, P. G. (2004a). Comparison of rheological properties of fiber suspensions with model predictions. *Journal of Polymer Engineering, 24*(6), 579-610.

Sepehr, M., Ausias, G., & Carreau, P. J. (2004b). Rheological behavior in transient shear flows for concentrated short fiber filled polymer. *Mecanique et Industries, 5*(4), 419-428.

Sepehr, M., Ausias, G., & Carreau, P. J. (2004c). Rheological properties of short fiber filled polypropylene in transient shear flow. *Journal of Non-Newtonian Fluid Mechanics, 123*(1), 19-32.

Sepehr, M., Carreau, P. J., Moan, M., & Ausias, G. (2004d). Rheological properties of short fiber model suspensions. *Journal of Rheology, 48*(5), 1023-1048.

Servais, C., & Manson, J. A. E. (1999). The relationship between steady-state and oscillatory shear viscosity in planar randomly oriented concentrated fiber suspensions. *Journal of Rheology, 43*(4), 1019-1031.

Shaqfeh, E. S. G., & Fredrickson, G. H. (1990). The hydrodynamic stress in a suspension of rods. *Physics of Fluids a-Fluid Dynamics, 2*(1), 7-24.

Souloumiac, B., & Vincent, M. (1998). Steady shear viscosity of short fibre suspensions in thermoplastics. *Rheologica Acta, 37*(3), 289-298.

Strand, S. R., Kim, S., & Karrila, S. J. (1987). Computation of rheological properties of suspensions of rigids rods: Stress growth after inception of steady shear flow. *Journal of Non-Newtonian Fluid Mechanics, 24*(3), 311-329.

Switzer, L. H., & Klingenberg, D. J. (2003). Rheology of sheared flexible fiber suspensions via fiber-level simulations. *Journal of Rheology, 47*(3), 759-778.

Takahashi, T., Takimoto, J.-I., & Koyama, K. (1999). Uniaxial elongational viscosity of various molten polymer composites. *Polymer Composites, 20*(3), 357-366.

Thomasset, J., Carreau, P. J., Sanschagrin, B., & Ausias, G. (2005). Rheological properties of long glass fiber filled polypropylene. *Journal of Non-Newtonian Fluid Mechanics, 125*(1), 25-34.

Toll, S., & Manson, J. A. E. (1994). Dynamics of a planar concentrated fiber suspension with nonhydrodynamic interaction. *Journal of Rheology, 38*(4), 985-997.

Toll, S. (1998). Packing mechanics of fiber reinforcements. *Polymer Engineering and Science, 38*(8), 1337-1350.

Trevelyan, B. J., & Mason, S. G. (1951). Particle motions in sheared suspensions. I. Rotations. *Journal of Colloid Science, 6*(4), 354-367.

Verleye, V., Couniot, A., & Dupret, F. (1994). Numerical prediction of fiber orientation in complex injection molded parts. *ASME Winter Annual Meeting* (Vol. 49, pp. 265-279.

Versteeg, H. K., & Malalasekera, W. (1995). *An introduction to computational fluid dynamics: the finite volume method.* Harlow; Toronto: Pearson Prentice Hall.

VerWeyst, B. E. (1998). *Numerical simulations of flow-induced fiber orientation in three dimensional geometries.* Ph.D. thesis inédit, University of Illinois at Urbana-Champaign, Urbana, IL.

Vincent, M. (2003). Orientation des fibres courtes dans les pièces en thermoplastique renforcé. *Techniques de l'ingénieur*, AM 3 729 pp. 721-710. Consulté le 14 décembre 2007, tiré de Techniques de l'ingénieur.

Wagner, A. H., Kalyon, D. M., Yazici, R., & Fiske, T. J. (2003). Uniaxial Extensional Flow Behavior of a Glass Fiber-Filled Engineering Plastic. *Journal of Reinforced Plastics and Composites, 22*(4), 327-337.

Wagner, M. H., Bernnat, A., & Schulze, V. (1998). The rheology of the rheotens test. *Journal of Rheology, 42*(4), 917-928.

Wang, Y.-C., Gunasekaran, S., & Giacomin, J. A. (2001). The Lodge rubberlike liquid behavior for cheese in large amplitude oscillatory shear. *Applied Rheology, 11*(6), 312-319.

Weinberger, C. B., & Goddard, J. D. (1974). Extensional flow behavior of polymer solutions and particle suspensions in a spinning motion. *International Journal of Multiphase Flow, 1*(3), 465-486.

Wetzel, E. D., & Tucker, C. L. (1999). Area tensors for modeling microstructure during laminar liquid-liquid mixing. *International Journal of Multiphase Flow, 25*, 35.

Wetzel, E. D. (1999). *Modeling flow-induced microstructure of inhomogeneous liquid-liquid mixtures.* Ph.D. inédit, University of Illinois at Urbana-Champaign, United States -- Illinois.

Yamamoto, S., & Matsuoka, T. (1996). Dynamic simulation of microstructure and rheology of fiber suspensions. *Polymer Engineering and Science, 36*(19), 2396-2403.

Yosick, J. A., Giacomin, J. A., Stewart, W. E., & Ding, F. (1998). Fluid inertia in large amplitude oscillatory shear. *Rheologica Acta, 37*(4), 365-373.

Zhang, W., Komoto, S., Yamane, H., Takahashi, M., & White, J. L. (2001). Biaxial extensional flow behavior and fiber dispersion and orientation in short glass fiber filled polypropylene melts. *Journal of the Society of Rheology, Japan, 29*(3), 111-120.

Zirnsak, M. A., Hur, D. U., & Boger, D. V. (1994). Normal stresses in fibre suspensions. *Journal of Non-Newtonian Fluid Mechanics, 54*, 153-193.

ANNEXE A : ÉTUDE MORPHOLOGIQUE

Le **Tableau A.1** ci-après liste les caractéristiques dimensionnelles des fibres pour les différents polypropylènes chargés (PP10 et PP30). La mention « granulé » indique que les dimensions des renforts sont mesurées dans l'état de livraison tandis que la mention « pastille » donne les mesures dimensionnelles après la préparation des échantillons avant les mesures rhéologiques. Les fibres sont obtenues par calcination de la matrice et un microscope optique a été utilisé pour effectuer les mesures sur une population de plus de 500 fibres.

Tableau A.1 : Caractéristiques dimensionnelles des fibres dans les polypropylènes.

Type	$\overline{L}$ [μm]	L_σ [μm][1]	$\overline{L}_n$ [μm][2]	$\overline{L}_w$ [μm][3]	$\overline{L}_w / \overline{L}_n$	D [μm]	r
PP10 (granulé)	404	142	424	472	1.11	16	25
PP10 (pastille)	375	132	394	439	1.11	16	23
PP30 (granulé)	326	159	346	420	1.21	16	20
PP30 (pastille)	317	136	337	392	1.16	16	20

où $\overline{L}$ est la longueur moyenne des fibres, L_σ est l'écart-type, $\overline{L}_n = \sum n_i L_i / \sum n_i$ est la longueur moyenne en nombre et $\overline{L}_w = \sum n_i L_i^2 / \sum n_i L_i$ est la longueur moyenne en masse. n_i représente le nombre de fibres ayant la longueur L_i.

ANNEXE B : COURBES DE VISCOSITÉ

La **Figure B.1** montre les courbes de viscosité du polypropylène vierge (PP0) et de ses composites (PP10, PP20 et PP30). Les mesures ont été effectuées par un rhéomètre à contrainte impose (CSM, Bohlin Instruments) sous une atmosphère d'azote à 200 °C. Pour tous les essais, l'entrefer de la géométrie des plaques parallèles, de diamètre 25 mm, a été fixée autour de 1.5 mm. Les tests de balayage en fréquence ont été réalisés des hautes jusqu'aux basses fréquences dans le domaine linéaire ($\gamma = 0.01$). Également avant chaque mesure, les échantillons ont été pré-cisaillés à 1000 Pa pendant 1000 s pour aligner les fibres dans la direction du cisaillement.

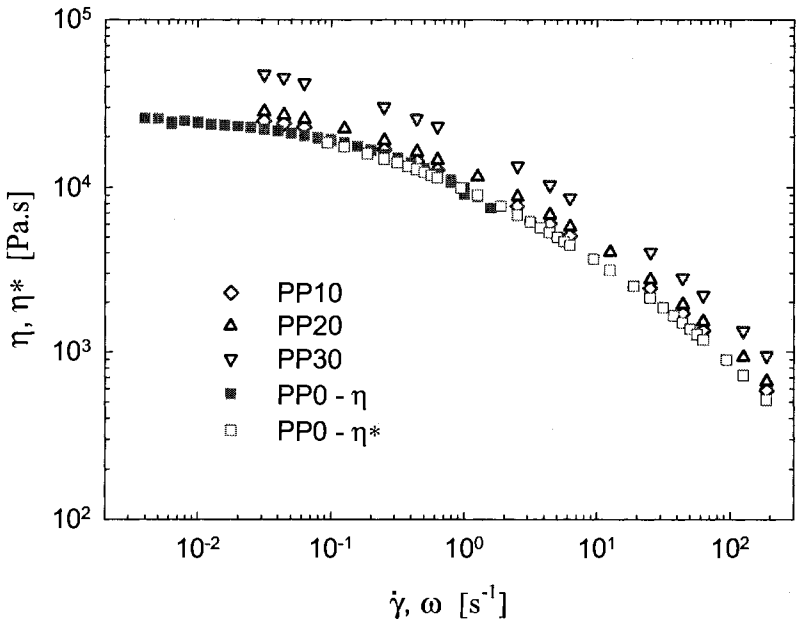

Figure B.1 : Courbes de viscosité du PP0, PP10, PP20 et PP30.